Channel Simulation Models for Mobile Broadband Communication Systems

Carlos A. Gutiérrez

Channel Simulation Models for Mobile Broadband Communication Systems

Doctoral Dissertation

University of Agder
Faculty of Engineering and Science
2009

Doctoral Dissertations at the University of Agder 16
ISBN : 978-82-7117-658-7
ISSN: 1504-9272

Printed by the Printing Office, University of Agder
Kristiansand

To my wife and child, Andrea and Pablo
and to my parents, Imelda and Carlos

Contents

Summary **xi**

Acknowledgments **xiii**

List of Figures **xix**

List of Tables **xxi**

Acronyms **xxiii**

1 Introduction **1**
1.1 Mobile Broadband Wireless Communication Systems 1
1.2 Channel Simulation Models 2
1.2.1 The Need for Channel Simulation Models 2
1.2.2 The Sum-of-Cisoids Channel Simulation Approach 4
1.3 Goals of the Doctoral Project 5
1.4 Organization of the Manuscript 6

2 The Reference Model **7**
2.1 Introduction 7
2.2 The Narrowband Rician Fading Channel Model 7
2.3 Statistical Characterization of the Reference Channel Model 9
2.3.1 ACFs 9
2.3.2 PSDs 11
2.3.3 Average Doppler Shift and Doppler Spread 11
2.4 Statistical Characterization of the Signal Fading 13
2.4.1 PDFs of the Channel's Envelope and Phase 13
2.4.1.1 First-Order PDF of the Envelope 13
2.4.1.2 First-Order PDF of the Phase 14
2.4.2 LCR and ADF 15
2.4.2.1 LCR 16
2.4.2.2 ADF 17
2.4.3 ACF of the Channel's Squared Envelope 17
2.5 Distributions of the AOA and Particular Cases 18
2.5.1 The von Mises PDF of the AOA and the Associated ACF and DPSD of the Channel's Diffuse Component 18

2.5.2 The Laplacian PDF of the AOA and the Associated ACF and DPSD of the Diffuse Component 20
2.6 Chapter Summary and Conclusions 23

3 Narrowband SOC-Based Simulation Models 25
3.1 Introduction 25
3.2 SOC-Based Channel Simulators: General Structure and Classes . . 26
3.3 The Stochastic SOC-Based Simulation Model 27
3.3.1 Structure and Considerations 27
3.3.2 Mean Value, Variance, and Average Power 28
3.3.3 Correlation Properties and Spectral Characteristics 28
3.3.3.1 ACFs 28
3.3.3.2 DPSDs 30
3.3.3.3 Average Doppler Shift and Doppler Spread 30
3.3.4 PDFs of the Stochastic SOC Model's Envelope and Phase . 31
3.3.4.1 First-Order PDF of the Envelope 32
3.3.4.2 First-Order PDF of the Phase 32
3.3.5 A Note on the LCR and ADF of the Stochastic SOC Model's Envelope 34
3.3.6 ACF of the Stochastic SOC Model's Squared Envelope . . . 35
3.4 The Deterministic SOC-Based Simulation Model 35
3.4.1 Structure 35
3.4.2 Mean Value and Average Power 36
3.4.3 Correlation Properties and Spectral Characteristics 37
3.4.3.1 Time-averaged ACFs 37
3.4.3.2 DPSDs 38
3.4.3.3 Average Doppler Shift and Doppler Spread 38
3.4.4 ACF of the Deterministic Squared Envelope 39
3.5 On the Ergodicity of the Stochastic SOC-Based Simulation Model 40
3.6 Chapter Summary and Conclusions 42

4 Parameter Computation Methods 43
4.1 Introduction 43
4.2 Overview of the Existing Parameter Computation Methods for SOC-Based Channel Simulators 44
4.2.1 The EMEDS 44
4.2.2 The LPNM 45
4.3 The GMEA 46
4.3.1 Description 46
4.3.2 Differences Between the GMEA and Other Versions of the MEA 48
4.3.3 Implementation 49
4.3.3.1 von Mises Distributed AOAs 49
4.3.3.2 Laplacian Distributed AOAs 51
4.4 The RSAM 53
4.4.1 Description 53

4.4.1.1 Basic Approach . . . 53
4.4.1.2 Problems of the Basic Approach . . . 54
4.4.1.3 Improved Approach . . . 56
4.4.2 Implementation . . . 57
4.4.2.1 von Mises Distributed AOAs . . . 57
4.4.2.2 Laplacian Distributed AOAs . . . 58
4.5 Performance Analysis . . . 59
4.5.1 Emulation of the Correlation and Spectral Characteristics of the Reference Model's Random Component . . . 61
4.5.1.1 ACF . . . 61
4.5.1.2 Average Doppler Shift and Doppler Spread . . . 67
4.5.2 Emulation of the Fading Statistics of the Reference Model . 70
4.5.2.1 PDF of the Envelope . . . 70
4.5.2.2 PDF of the Phase . . . 74
4.5.2.3 ACF of the Squared Envelope . . . 79
4.6 Chapter Summary and Conclusions . . . 90

5 Simulation of Mobile MIMO Fading Channels Under Single-Bounce Non-Isotropic Scattering Conditions 91
5.1 Introduction . . . 91
5.2 Reference Model . . . 92
5.2.1 The Geometrical One-Ring Scattering Model . . . 92
5.2.2 Narrowband MIMO Rayleigh Fading Channel Model . . . 94
5.2.3 Correlation Properties of the Reference Model . . . 95
5.2.3.1 ACF and DPSD of the MIMO Channel Gains . . 95
5.2.3.2 Space-Time CCF of the MIMO Channel Gains . . 96
5.3 The Simulation Model . . . 96
5.3.1 The Stochastic SOC Simulation Model . . . 96
5.3.2 Correlation Properties of the SOC Simulation Model . . . 97
5.4 Parameter Computation Methods . . . 97
5.4.1 The GMEA . . . 98
5.4.2 The RSAM . . . 99
5.5 Performance Analysis . . . 100
5.5.1 Considerations . . . 100
5.5.2 Emulation of the ACF . . . 101
5.5.3 Emulation of the SCCF . . . 101
5.6 Simulation of Wideband MIMO Fading Channels . . . 106
5.6.1 Modeling and Statistical Characterization of Wideband Mobile MIMO Fading Channels . . . 106
5.6.2 Simulation Approach . . . 107
5.7 Chapter Summary and Conclusions . . . 109

6 Design of TDL Models for WSSUS Channels with Diffuse Impulse Responses 111
6.1 Introduction . . . 111
6.2 About the Validity of SSTDL Models . . . 113

6.2.1 The SSTDL Modeling Approach . . . 113
6.2.2 The Validity of SSTDL Models . . . 114
6.3 Statistical Behavior of SSTDL Models . . . 116
6.3.1 Statistical Description of the Reference Channel Model . . 116
6.3.2 Statistical Description of Δ_η-Spaced TDL Models . . . 117
6.4 Numerical Examples . . . 119
6.4.1 The Truncated-Exponential-Decay PDP . . . 119
6.4.2 Effects of Aliasing on the FCF . . . 120
6.4.3 The Influence of the FCF on the System Performance . . . 120
6.5 Avoiding the Problems Caused by SSTDL Models . . . 123
6.6 Chapter Summary and Conclusions . . . 125

7 Summary of Contributions and Open Problems 129
7.1 Contributions . . . 129
7.2 Open Problems . . . 130

A Derivation of the Squared Envelope ACF of the Reference Model 131

B Derivation of the Squared Envelope ACF of the Stochastic SOC-Based Simulation Model 135

C Derivation of the Squared Envelope ACF of the Deterministic SOC-Based Simulation Model 137

D Closed-Form Expression for the Squared Envelope ACF of the Sample Functions of the Stochastic Homogeneous SOC Model with Uncorrelated IQ Components 141

E Theorems About the Design of SOC-Based Simulation Models with Uncorrelated IQ Components 145

F Validation of the Expressions Obtained for the Squared Envelope ACF of the Deterministic SOC-Based Simulation Model 149

Summary

Mobile broadband wireless communication systems (MBWCS) are emerging as a solution to provide broadband services to users on the move. These systems are expected to operate in a wide variety of propagation scenarios, at different mobile speeds, and at various frequency bands. Under such a variety of requirements, flexible and efficient channel simulation models will prove fundamental for the laboratory analysis of MBWCS. Currently, most of the existing channel simulation models are either too complex as to allow for an efficient performance investigation of MBWCS, or they cannot be applied to the simulation of some relevant classes of mobile fading channels. To overcome these limitations, we present in this doctoral a flexible and efficient methodology for the design of channel simulation models for MBWCS. Such a methodology is based on the sum-of-cisoids (SOC) approach, an approach that is closely in line with the electromagnetic plane-wave propagation model.

We build our channel simulators upon a class of ergodic SOC simulation models. For the computation of the SOC model parameters, we introduce two simple methods that enable the design of simulation models for mobile fading channels characterized by any type of Doppler power spectral densities (DPSDs). The proposed methods are well-suited for the simulation of both single-input single-output (SISO) and multiple-input multiple-output (MIMO) channels. We evaluate the methods' performance with respect to their accuracy for emulating important statistical functions of the channel, such as the autocorrelation function (ACF), the envelope probability density function (PDF), and the ACF of the squared envelope. In the case of MIMO channels, we evaluate the methods' performance in terms of the approximation of the channel temporal ACF and spatial cross-correlation function (SCCF). The obtained results demonstrate the excellent performance of the proposed methods.

This dissertation is also intended to provide a comprehensive treatise of the theory behind the design of SOC simulation models for mobile fading channels. In this respect, the statistical properties of SOC channel simulators are thoroughly analyzed. Important contribution are given concerning the correlation properties of the square envelope of SOC simulators. Such contributions include the derivation of closed-form expressions for the squared envelope ACF of the

SOC simulation model, and the analysis of the ergodicity properties of the SOC model's squared envelope.

We also revisit here the concept of the symbol-spaced tapped line model (SSTDL) for WSSUS channels. In this regard, we present a discussion on the problems of SSTDL models, and we propose a simple solution to avoid them. The usefulness of such a solution is exemplary demonstrated by analyzing the bit error probability of a multi-carrier code division multiple access (MC-CDMA) system.

Acknowledgments

The completion of this Dissertation was a monumental task that I would not have been able to accomplish without the help and the support of many individuals and institutions to whom I want to express my gratitude.

I am very grateful to my advisor, Prof. Matthias Pätzold. I learned a lot working with him and his guidance was decisive to achieve the goals of my PhD project. I am also thankful to the members of the evaluation committee, Profs. Dongwoo Kim, Neji Youssef, and José J. Gonzalez. My gratitude goes also to the Doctoral Fellows from the ICT Department, specially to Ali Chelli, Batool Talha, Bjørn Olav Hogstad, Dmitry Umansky, Gulzaib Rafiq, Martin Choux, Ram Kumar, Sigurd Eskeland, and Yuanyuan Ma. They made my stay in Grimstad something pleasant to remember and I benefited so much from their technical knowledge and expertise. Thanks go to my teachers Prof. Andreas Prinz and Prof. Vladimir Oleshchuk. I am thankful too to the Project Secretary of the Mobile Communications Group, Mrs. Katharina Pätzold, and the Coordinator of the PhD Program in Mobile Communication Systems, Mrs. Trine Tonnessen.

I kindly acknowledge the financial support that the Mexican National Council of Science and Technology (CONACyT) gave me to pursue the PhD degree in Norway. I also acknowledge the opportunity given to me by the University of Agder to make my PhD in a topic I feel so passionate about.

I was lucky to enjoy the friendship of Ahmed A. A. S. AbouGhonim, Fanny Paris, Mikael Snaprud, and Morten Goodwin Olsen. Thanks go to all of them. I am thankful too to my friends and teachers from CICESE, specially to Paul Medina, Prof. Jaime Sánchez, Prof. Roberto Conte, and Prof. José R. Gallardo.

My deepest thanks to my parents, Imelda and Carlos; my brothers, Luis and Aaron; my sisters-in-law, Monica and Eli; my parents-in-law, Guadalupe and Ramiro; and to my brother-in-law, Ramiro. They sacrificed a lot in order for me to make my PhD in Norway. There are no words I can use to express my gratefulness to my wife, Andrea. She gave me the heart to complete this enterprise. I am also grateful to Pablo, my son. He was my motivation during the final and decisive stage of my doctoral work.

Last but not least, I thank the Lord. Bringing my doctoral studies to a good end has been another of the many gifts he has given to me.

Carlos A. Gutiérrez
June 11, 2009
Aguascalientes, Ags., Mexico

List of Figures

2.1 Channel's envelope and its first-order PDF for different Rician factors. . . . 14
2.2 Channel's phase and its first-order PDF for different Rician factors. 15
2.3 The von Mises PDF of the AOA. . . . 20
2.4 ACF of the channel's diffuse component by considering the von Mises PDF of the AOA. . . . 20
2.5 DPSD of the channel's diffuse component by considering the von Mises PDF of the AOA. . . . 21
2.6 The Laplacian PDF of the AOA. . . . 22
2.7 ACF of the channel's diffuse component by considering the Laplacian PDF of the AOA. . . . 23
2.8 DPSD of the channel's diffuse component by considering the Laplacian PDF of the AOA. . . . 23

3.1 Block diagram of an SOC-based simulation model for Rician fading channels. . . . 27
3.2 Comparison between the theoretical envelope PDF of the stochastic SOC-based simulation model and the Rice PDF by considering different values for both the Rician factor and the number of cisoids. 33
3.3 Comparison between the theoretical phase PDF of the stochastic SOC-based simulation model and the phase PDF of reference model by considering different values for both the Rician factor and the number of cisoids. . . . 34

4.1 Comparison between the ACF of the channel's diffuse component and the ACF of the SOC-based simulation model's random component by considering the von Mises PDF of the AOA and the generalization of the MEA proposed by other authors. . . . 50
4.2 Comparison between the DPSD of the channel's diffuse component and the DPSD of the SOC-based simulation model's random component by considering the von Mises PDF of the AOA and the GMEA. . . . 52
4.3 Comparison between the DPSD of the channel's diffuse component and the DPSD of the SOC-based simulation model's random component by considering the Laplacian PDF of the AOA and the GMEA. . . . 53

4.4 Relationship between the gains and AOAs of the SOC-based simulation model's random component by applying the BRSAM to the von Mises PDF of the AOA. 55

4.5 Comparison between the Rayleigh PDF and the first-order PDF of the envelope of the simulation model's random component by applying the BRSAM to the von Mises PDF of the AOA. 55

4.6 Comparison between the DPSD of the channel's diffuse component and the DPSD of the SOC-based simulation model's random component by considering the von Mises PDF of the AOA and the RSAM. 60

4.7 Comparison between the DPSD of the channel's diffuse component and the DPSD of the SOC-based simulation model's random component by considering the Laplacian PDF of the AOA and the RSAM. 61

4.8 Comparison among the GMEA, RSAM, and LPNM I in terms of the emulation of the ACF of channel's diffuse component by considering the von Mises PDF of the AOA. 62

4.9 Comparison among the GMEA, RSAM, and LPNM II in terms of the emulation of the ACF of channel's diffuse component by considering the von Mises PDF of the AOA. 63

4.10 Comparison among the GMEA, RSAM, and LPNM III in terms of the emulation of the ACF of channel's diffuse component by considering the von Mises PDF of the AOA. 64

4.11 Root mean square error between the ACF of the channel's diffuse component and the ACF of the SOC-based simulation model's random component by considering the von Mises PDF of the AOA with different pairs of parameters. 66

4.12 Absolute error between the average Doppler shift of the channel's diffuse component and the average Doppler shift of the SOC-based simulation model's random component by considering the von Mises PDF of the AOA and the GMEA, RSAM, and LPNM. . 68

4.13 Relative error between the Doppler spread of the channel's diffuse component and the Doppler spread of the SOC-based simulation model's random component by considering the von Mises PDF of the AOA and the GMEA, RSAM, and LPNM. 69

4.14 Comparison between the first-order PDF of the reference model's envelope and the first-order PDF of the envelope of the SOC-based simulation model by applying the GMEA to the von Mises PDF of the AOA. 71

4.15 Comparison between the first-order PDF of the reference model's envelope and the first-order PDF of the envelope of the SOC-based simulation model by applying the LPNM I to the von Mises PDF of the AOA. 71

4.16 Comparison between the first-order PDF of the reference model's envelope and the first-order PDF of the envelope of the SOC-based simulation model by applying the LPNM II to the von Mises PDF of the AOA. 72
4.17 Comparison between the first-order PDF of the reference model's envelope and the first-order PDF of the envelope of the SOC-based simulation model by applying the LPNM III to the von Mises PDF of the AOA. 73
4.18 Comparison between the first-order PDF of the reference model's envelope and the first-order PDF of the envelope of the SOC-based simulation model by applying the RSAM to the von Mises PDF of the AOA. 74
4.19 Root mean square error between the envelope distributions of the channel's diffuse component and SOC-based simulation model's random component by considering the von Mises PDF of the AOA with different pairs of parameters. 75
4.20 Comparison between the first-order PDF of the reference model's phase and the first-order PDF of the phase of the SOC-based simulation model by applying the GMEA to the von Mises PDF of the AOA. 76
4.21 Comparison between the first-order PDF of the reference model's phase and the first-order PDF of the phase of the SOC-based simulation model by applying the LPNM I to the von Mises PDF of the AOA. 76
4.22 Comparison between the first-order PDF of the reference model's phase and the first-order PDF of the phase of the SOC-based simulation model by applying the LPNM II to the von Mises PDF of the AOA. 77
4.23 Comparison between the first-order PDF of the reference model's phase and the first-order PDF of the phase of the SOC-based simulation model by applying the LPNM III to the von Mises PDF of the AOA. 78
4.24 Comparison between the first-order PDF of the reference model's phase and the first-order PDF of the phase of the SOC-based simulation model by applying the RSAM to the von Mises PDF of the AOA. 79
4.25 Comparison among the GMEA, RSAM, and LPNM I in terms of the emulation of the ACF of the reference model's squared envelope by considering a Rician factor equal to zero and the von Mises PDF of the AOA. 81
4.26 Comparison among the GMEA, RSAM, and LPNM II in terms of the emulation of the ACF of the reference model's squared envelope by considering a Rician factor equal to zero and the von Mises PDF of the AOA. 82

4.27 Comparison among the GMEA, RSAM, and LPNM III in terms of the emulation of the ACF of the reference model's squared envelope by considering a Rician factor equal to zero and the von Mises PDF of the AOA. 83
4.28 Comparison among the GMEA, RSAM, and LPNM I in terms of the emulation of the ACF of the reference model's squared envelope by considering a Rician factor equal to two and the von Mises PDF of the AOA. 84
4.29 Comparison among the GMEA, RSAM, and LPNM II in terms of the emulation of the ACF of the reference model's squared envelope by considering a Rician factor equal to two and the von Mises PDF of the AOA. 85
4.30 Comparison among the GMEA, RSAM, and LPNM III in terms of the emulation of the ACF of the reference model's squared envelope by considering a Rician factor equal to two and the von Mises PDF of the AOA. 86
4.31 Comparison among the GMEA, RSAM, and LPNM I in terms of the emulation of the ACF of the reference model's squared envelope by considering a Rician factor equal to four and the von Mises PDF of the AOA. 87
4.32 Comparison among the GMEA, RSAM, and LPNM II in terms of the emulation of the ACF of the reference model's squared envelope by considering a Rician factor equal to four and the von Mises PDF of the AOA. 88
4.33 Comparison among the GMEA, RSAM, and LPNM III in terms of the emulation of the ACF of the reference model's squared envelope by considering a Rician factor equal to four and the von Mises PDF of the AOA. 89

5.1 The geometrical one-ring scattering propagation model 93
5.2 Comparison between the ACF of the MIMO channel gains and the ACF of the simulation model by applying the GMEA and the RSAM to the von Mises PDF of the AOA. 102
5.3 Absolute value of the SCCF of the MIMO channel model by considering the von Mises PDF of the AOA. 103
5.4 Error between the SCCF of the MIMO channel gains and the SCCF of the simulation model by applying the GMEA to the von Mises PDF of the AOA. 104
5.5 Error between the SCCF of the MIMO channel gains and the SCCF of the simulation model by applying the RSAM to the von Mises PDF of the AOA. 105

6.1 Comparison between the absolute value of the FCF of the reference model and the absolute value of the FCF of the SSTDL by considering the TED-PDP. 121

6.2 Comparison between the theoretical and the empirical BEPs of a MUI-free downlink MC-CDMA system with MRC by considering the SSTDL model and the TED-PDP with a falling factor = 30 ns. In the figure, SF stands for the spreading factor. 124
6.3 Comparison between the absolute value of the FCF of the reference model and the absolute value of the FCF of the HSSTDL by considering the TED-PDP. 126
6.4 Comparison between the theoretical and the empirical BEPs of a MUI-free downlink MC-CDMA system with MRC by considering the HSSTDL model and the TED-PDP with a falling factor = 30 ns. In the figure, SF stands for the spreading factor. 127

F.1 Comparison between the theoretical and the empirical squared envelope ACFs of the SOC-based simulation model's sample functions by considering a Rician factor equal to zero and applying the RSAM to the von Mises PDF of the AOA. 150
F.2 Comparison between the theoretical and the empirical squared envelope ACFs of the SOC-based simulation model's sample functions by considering a Rician factor equal to two and applying the RSAM to the von Mises PDF of the AOA. 151
F.3 Comparison between the theoretical and the empirical squared envelope ACFs of the SOC-based simulation model's sample functions by considering a Rician factor equal to four and applying the RSAM to the von Mises PDF of the AOA. 152

List of Tables

1.1 Air Interface Specifications of LTE, UMB, and Mobile WiMAX . . 3
1.2 Air Interface Specifications of the standards IEEE 802.16e, IEEE 802.16m, and IEEE 802.20 3

2.1 Average Doppler shift and Doppler spread of the channel's diffuse component by considering the von Mises PDF of the AOA. 21
2.2 Average Doppler shift and Doppler spread of the channel's diffuse component by considering the Laplacian PDF of the AOA. 24

3.1 Classification of SOC-based simulation models for Rician fading channels according to the nature of the cisoids' parameters. 27

Acronyms

3G:	third generation
3GPP:	third generation partnership project
3GPP2:	third generation partnership project
ACF:	autocorrelation function
ADF:	average duration of fades
AOA:	angle of arrival
AOD:	angle of departure
AWGN:	additive white Gaussian noise
BPSK:	binary phase shift keying
BRSAM:	basic Riemann sum approximation method
BS:	base station
CCF:	cross-correlation function
CDF:	cumulative distribution function
CDMA:	code division multiple access
CIR:	channel impulse response
CNR:	carrier-to-noise-ratio
DPSD:	Doppler power spectral density
DS-SS:	direct sequence spread spectrum
EMEDS:	extended method of exact Doppler spread
ETSI:	European Telecommunication Standards Institute
FCF:	frequency correlation function
GMEA:	generalized method of equal areas
GSM:	global system for mobile communications
HSSTDL:	half-symbol spaced tapped delay line
i.i.d.:	independent and identically distributed
IP:	Internet protocol
IQ:	Inphase and quadrature
ISI:	inter-symbol interference
LCR:	level-crossing rate
LPNM:	L_p-norm method
LOS:	line of sight
LTE:	long term evolution
MBWCS:	mobile broadband wireless communication systems
MC-CDMA:	multicarrier code division multiple access
MEA:	method of equal areas

MEDS:	method of exact Doppler spread
MIMO:	multiple-input multiple-output
MRC:	maximal ratio combining
MT:	mobile terminal
MUI:	multi-user interference
NLOS:	non-line of sight
OFDM:	orthogonal frequency division multiplexing
OFDMA:	orthogonal frequency division multiple access
PDF:	probability density function
PDP:	power delay profile
PSD:	power spectral density
QAM:	quadrature amplitude modulation
RSAM:	Riemann sum approximation method
SC-FDMA:	single carrier frequency division multiple access
SCCF:	spatial cross-correlation function
SDMA:	spatial division multiple access
SISO:	single-input single-output
SOC:	sum-of-cisoids
SOS:	sum-of-sinusoids
SSTDL:	symbol-spaced tapped-delay-line
STCCF:	space-time cross-correlation function
SSS:	strict-sense stationary
TACF:	temporal autocorrelation function
TDL:	tapped-delay-line
TED-PDP:	truncated-exponential-decay power delay profile
TF-ACF:	time-frequency autocorrelation function
TVLF:	time-variant linear filter
UMB:	ultra-mobile broadband
UMTS:	universal mobile telecommunication system
US:	uncorrelated scattering
VoIP:	voice over IP
WCDMA:	wideband code division multiple access
WiFi:	wireless fidelity
WiMAX:	worldwide interoperability for microwave access
WSS:	wide-sense stationary
WSSUS:	wide-sense stationary uncorrelated scattering

Chapter 1

Introduction

1.1 Mobile Broadband Wireless Communication Systems

In the opinion of many technology analysts, such as the authors of [Lee07, Orti07], the next revolution in the wireless communications industry will be triggered by the emerging mobile broadband wireless communication systems (MBWCS). These novel systems will combine the best of modern fixed broadband wireless access networks [Abic06, Stal04] and third generation (3G) cellular telephony systems [Rapp02, Robe06] with the aim of providing broadband multimedia services to users on the move. MBWCS are expected to deliver high-data-rate services, such as voice over IP (VoIP) and video on demand, to users moving at speeds as high as those of fast trains [Li07, Bolt07].

Among the initiatives that are currently ongoing toward the standardization of MBWCS, we can distinguish those carried out within the third-generation partnership project (3GPP), the 3GPP 2 (3GPP2), the WiMAX Forum^{TM}, and the IEEE 802 group. The 3GPP [3Gweb1] is working on the standardization of an advanced 3G cellular system called Long-Term Evolution (LTE). LTE is an evolutionary upgrade of the Global System for Mobile Communications (GSM) and the 3G Wideband Code Division Multiple Access (WCDMA) cellular system [Robe06]. Its air interface utilizes an orthogonal frequency division multiple access (OFDMA) scheme on the downlink, and a single-carrier frequency division multiple access (SC-FDMA) scheme on the uplink [Orti07, Schu05]. LTE employs multiple-input multiple-output (MIMO) transceivers to achieve data rates of up to 277 Mbps on the downlink and 75 Mbps on the uplink, within a 20 MHz bandwidth. It uses spatial division multiple access (SDMA) techniques to increase cell capacity [Qua08a].

The 3GPP2 [3Gweb2] recently published the specifications of the Ultra Mobile Broadband (UMB) standard for beyond-3G cellular systems [3gpUMB]. UMB is

an upgrade of the CDMA2000 standard for 3G cellular networks [Robe06]. The air interface of UMB is based on an OFDMA scheme, and it incorporates MIMO transceivers to achieve data transfer rates of up to 288 Mbps on the downlink and 75 Mbps on the uplink, within a 20 MHz bandwidth [3gpUMB]. UMB includes beamforming and transmission modes basing on SDMA.

The WiMAX Forum, an industry-led nonprofit organization, is developing the Mobile WiMAX standard. Mobile WiMAX is a trimmed version of the IEEE 802.16e standard for fixed and mobile broadband wireless access networks [IEEE06]. It defines an OFDMA-based air interface able to deliver information at peak data rates of 60 Mbps on the downlink and 23 Mbps on the uplink over a 10 MHz bandwidth [Teo07]. A 2×2 MIMO configuration is required in order to achieve such high data rates. Even though the Mobile WiMAX standard has not yet been released, several trial networks basing on Mobile WiMAX have already been deployed in several countries around the world, such as USA, Pakistan, Korea, and Colombia [Goza06, Lee07].

The IEEE 802.20 Task Group is developing a new standard for MBWCS which will specify an efficient packet-based air interface optimized for the transport of Internet-Protocol- (IP)-based services [Bolt07]. In turn, the IEEE 802.16m Task Group is working on a high throughput enhancement for licensed cellular bands of the 802.16e standard.

We summarize the main features of LTE, UMB, and Mobile WiMAX in Table 1.1, whereas Table 1.2 overviews the target characteristics of the IEEE 802.16m and IEEE 802.20 standards. An overview of the 802.16e standard is also shown in Table 1.2.

1.2 Channel Simulation Models

1.2.1 The Need for Channel Simulation Models

In order to get insights into the problems that affect the performance of MBWCS, or any other type of wireless communication systems, one often has to resort in practice to the use of computer simulators. Computer simulators provide a powerful, reproducible, and affordable way to assess the system performance. They can be used as well to verify the correctness of results obtained analytically.

Choosing a proper channel simulation model is fundamental for the laboratory analysis of MBWCS, as most of the problems affecting the performance of mobile communication systems, e.g., path loss, shadowing, and signal fading, are caused by the channel [Skla88]. The importance of channel simulation models is such that the European Telecommunications Standards Institute (ETSI) has recently issued a document with specifications for the design of channel simulators for MBWCS [3gpSCM]. In view of the recommendations in [3gpSCM], and taking into account

Table 1.1: Air Interface Specifications of LTE, UMB, and Mobile WiMAX

Characteristics	**LTE**	**UMB**	**Mobile WiMAX**
Transmission modes	OFDMA on the uplink and SC-FDMA on the downlink	OFDMA and an alternative mode based on CDMA	OFDMA
Bands	Licensed bands below 2.6 GHz	Licensed bands below 2.6 GHz	Licensed bands between 2.3 and 3.5 GHz
Bandwidth	Various, ranging from 1.25 MHz to 20 MHz	Various, ranging from 1.25 MHz to 20 MHz	Various, ranging from 1.25 MHz to 10 MHz
Smart antenna techniques	MIMO (2×2, 4×4), SDMA*, and beamforming	MIMO (2×2, 4×4), SDMA*, and beamforming	MIMO (2×2)
Compatibility with other systems	Scalable from GSM and WCDMA cellular networks	1xEV-DO and CDMA2000 1X cellular networks	—
Standard status	Currently ongoing	Released in 2007	Currently ongoing

Sources: [3gpUMB, Goza06, Li07, Qua08a, Teo07].
* SDMA and MIMO are complementary to each other. They are not used together.

Table 1.2: Air Interface Specifications of the standards IEEE 802.16e, IEEE 802.16m, and IEEE 802.20

Characteristics	**IEEE 802.16e**	**IEEE 802.16m**	**IEEE 802.20**
Transmission modes	Three alternatives: single-carrier, OFDM, and OFDMA	OFDMA	OFDMA
Bands	Licensed bands suitable for mobility below 6 GHz	Licensed bands below 6 GHz	Licensed bands below 3.5 GHz
Bandwidth	Various, ranging from 1.25 MHz to 20 MHz	Various, ranging from 5 MHz to 20 MHz	Various, ranging from 1.25 MHz to 20 MHz
Smart antenna techniques	MIMO (2×2)	MIMO (2×2, 4×4) and beamforming	MIMO (different configurations) and beamforming
Compatibility	—	802.16e networks operating in OFDMA mode	802.11a/g standard
Standard status	Released in 2006	Currently ongoing	Currently ongoing

Sources: [Bolt07, Goza06, IEEE06].

the characteristics of standardized channel models for MBWCS [Alme07], such as the COST 259 [Corr01, Moli06] and the COST 273 [Corr06], we have that a channel simulation model for MBWCS should meet the following:

- They should be able to reproduce the statistical properties of direction-selective mobile fading channels.
- They should be adequate for the simulation of macrocell and microcell mobile fading channels.
- They should be flexible and simple enough as to allow for the evaluation of MBWCS operating in environments that exhibit propagation conditions that change quite often during active sessions.
- They should be well-suited for the performance assessment of narrowband and wideband MIMO systems.
- They should be well-suited for the performance assessment of multicarrier single-input single-output (SISO) and MIMO systems.

1.2.2 The Sum-of-Cisoids Channel Simulation Approach

Several different models exist that allow for a proper simulation of mobile fading channels, including:

- Models based on the Cholesky decomposition algorithm [Erte98, Beau04].
- Models based on the IFFT algorithm [Youn00].
- Models based on the autorregresive filtering concept[Badd05, Badd04].
- Models based on ray tracing [Cora97].

However, simulation models based on the SOS principle introduced by Rice [Rice44, Rice45] are particularly attractive for the performance evaluation of MBWCS. In addition to providing an excellent basis for the simulation of temporally correlated narrowband channels [Jake74, Pae02a, Pate05], the SOS principle can easily be applied to the simulation of frequency-selective [Hohe92, Yip95, Wang07] and space-selective [Han02, Paet01, Pae04a, Pae08a] radio channels.

The design of accurate and efficient SOS-based simulators for mobile fading channels has been a topic of research of several books and papers, e.g., [Jake74, p. 70], [Pae02a, ch. 5], and [Pate05, Hohe92, Yip95, Wang07, Han02]. Nevertheless, most of the existing SOS-based simulators have been developed on the assumption that the channel's Doppler power spectral density (DPSD) is symmetrical with respect to the origin. This poses a serious restriction, since

it has been observed that the DPSD of real-world channels is in general non-symmetrical [Kott04, Abd02a, Zhao03, Blau06]. Moreover, simulation models for fading channels having asymmetrical DPSDs are necessary to assess the performance of mobile communication systems under non-isotropic scattering conditions [Pae04a, Miti04]. To close this gap, a new class of SOS channel simulators that are able to produce complex-valued waveforms with cross-correlated inphase and quadrature (IQ) components—as required for the synthesis of channels characterized by asymmetrical DPSDs—was introduced in [Paet01]. SOS models of such a class, which are known as sum-of-cisoids (SOC) models [Paet07], are closely in line with the plane-wave propagation model [Saun07], and have already been adopted as the core structure of several space-selective channel simulators [Paet01, Pae04a, Pae08a]. Unfortunately, the existing parameter computation methods for SOC fading channel simulators with asymmetrical DPSD rely upon optimization techniques that make the determination of the model parameters a complex and time-consuming task. The development of new methods, under the constraint of simplicity and accuracy, is therefore desirable to facilitate the performance analysis of MBWCS.

1.3 Goals of the Doctoral Project

In this Doctoral thesis, we aim at developing accurate and efficient SOC channel simulators for MBWCS. The proposed simulators should fulfill the following requirements:

- They should enable the simulation of mobile fading channels characterized by symmetrical and asymmetrical DPSDs.
- They should be adequate for the simulation of fading channels under line-of-sight (LOS) and non-line-of-sight (NLOS) conditions.
- They should be suitable for the performance analysis of MBWCS based on SISO and MIMO technology.
- The determination of the model parameters should be done in a simple and efficient manner.

To accomplish these goals, we propose two simple and effective parameter computation methods for the design of SOC simulation models for mobile fading channels with arbitrary DPSDs. We will show that the proposed methods emulate the statistical properties of SISO and MIMO channels with high accuracy.

It is also the objective of this dissertation to provide a comprehensive treatise of the theory behind the design of SOC simulators for mobile fading channels. In this respect, we present a thorough analysis of the statistical properties of

SOC channel simulators for mobile Rician fading channels having a time-variant LOS component. So far, the statistical properties of SOC Rician fading channel simulators have been studied by considering a time-invariant LOS component. Particularly, important contributions are given regarding the correlation properties of the squared envelope of SOC simulation models for Rician fading channels. This includes closed-form solutions for the squared envelope autocorrelation function (ACF) of SOC channel simulators, and a detailed analysis on the ergodicity properties of the squared envelope of the simulation model.

1.4 Organization of the Manuscript

The outline to the rest of the manuscript is as follows. In Chapter 2, we review the characteristics and the statistical properties of a narrowband mobile Rician fading channel that we will consider as a reference model to design the parameters computation methods proposed in this dissertation. In addition to the correlation and spectral properties of the channel model, the review presented in Chapter 2 includes information about the fading statistics, including the envelope probability density function (PDF), the level crossing rate (LCR), the average duration of fades (ADF), and the squared envelope ACF. In Chapter 3, we present a stochastic SOC simulation model suitable for the simulation of the reference model described in Chapter 2. Then, in Chapter 4, we introduce our parameter computation methods. In Chapter 5, we show that such parameter computation methods can be applied to the simulation of narrowband mobile MIMO fading channels. We demonstrate in that chapter that the proposed methods produce excellent results concerning the emulation of the correlation properties of MIMO channels. The design of simulation models for wideband MIMO channels is also discussed in Chapter 5. In Chapter 6, we deal with the simulation of wideband channels. Finally, we summarize the main contributions of this dissertation in Chapter 7.

Chapter 2

The Reference Model

2.1 Introduction

This chapter describes the characteristics and statistical properties of a narrowband mobile Rician fading channel model that we will consider as reference model in subsequent chapters to design our channel simulators. The chapter reviews important statistical functions of the model, such as its ACF, DPSD, envelope PDF, LCR, and ADF. In addition, it reviews the channel's average Doppler shift and Doppler spread, as well as the ACF of the channel's squared envelope.

The channel model herein described is based on the assumption that in a microcellular/macrocellular small-scale propagation scenario, the narrowband signal seen by the mobile terminal (MT) is composed of a specular plane wave and a collection of scattered plane waves that reached the MT's antenna at the same time but through different paths. Such a modeling approach was originally proposed by Clarke in [Clar68] for characterizing non-frequency-selective mobile SISO channels, and it was extended afterwards by other researchers to describe narrowband mobile MIMO channels [Chen00, Shiu00, Abd02b], as well as to characterize three-dimensional mobile SISO channels [Auli79, Pars00].

The statistical properties of the aforementioned Rician fading channel model are studied in a number of papers and books, but mostly under the assumption of isotropic scattering, e.g., [Jake74, Rapp02, Auli79, Pars00]. In contrast, the review presented here covers both isotropic and non-isotropic scattering scenarios.

2.2 The Narrowband Rician Fading Channel Model

We model the non-frequency-selective mobile fading channel in the equivalent complex baseband by a complex Gaussian process[1] $\boldsymbol{\nu}(t)$, which characterizes a

[1] Throughout this dissertation, we will make use of bold symbols and letters to denote random variables and stochastic processes, whereas we will employ normal symbols and letters for constants and deterministic processes.

two-dimensional small-scale propagation environment where the scattering is not necessarily isotropic. We in turn model the process $\boldsymbol{\nu}(t)$ by a superposition of a stationary zero-mean complex Gaussian process $\boldsymbol{\mu}(t)$ and a time-variant deterministic process $m_\rho(t)$, i.e., $\boldsymbol{\nu}(t) = \boldsymbol{\mu}(t) + m_\rho(t)$, where the random process $\boldsymbol{\mu}(t)$ describes the diffuse part of the channel due to scattering and $m_\rho(t)$ characterizes its specular part.

On the basis of the central limit theorem [Papo02, p. 278], and following Clarke's scattering propagation model [Clar68], we can express the channel's diffuse part in terms of a sum of scattered azimuthal plane waves as follows:

$$\boldsymbol{\mu}(t) = \lim_{\mathcal{N}\to\infty} \sum_{n=1}^{\mathcal{N}} \boldsymbol{c}_n \exp\left\{j\big(2\pi \boldsymbol{f}_n t + \boldsymbol{\theta}_n\big)\right\} \tag{2.1}$$

where the nth plane wave is characterized by a cisoid with a random gain $\boldsymbol{c}_n$, a random phase $\boldsymbol{\theta}_n$, and a random Doppler frequency $\boldsymbol{f}_n$. According to Clarke's model [Clar68], the cisoids' phases $\boldsymbol{\theta}_n$ are independent and identically distributed (i.i.d.) random variables, each having a uniform distribution over $[-\pi, \pi)$, while the gains $\boldsymbol{c}_n$ are given such that $E\{\boldsymbol{c}_n^2\} = \sigma_{\boldsymbol{\mu}}^2/\mathcal{N}$ for all $n = 1, \ldots, \mathcal{N}$, where $\sigma_{\boldsymbol{\mu}}^2$ is the mean power of the channel due to scattering ($0 < \sigma_{\boldsymbol{\mu}}^2 < \infty$); $E\{\cdot\}$ denotes statistical expectation. In turn, the Doppler frequencies $\boldsymbol{f}_n$ are defined as

$$\boldsymbol{f}_n \;\triangleq\; f_{\max}\cos(\boldsymbol{\alpha}_n), \quad \forall n = 1, \ldots, \mathcal{N} \tag{2.2}$$

where $\boldsymbol{\alpha}_n$ is the random AOA of the nth incoming wave, and $f_{\max}$ stands for the maximum Doppler frequency shift induced on the channel's multipath components by the Doppler effect ($f_{\max} > 0$). The AOAs $\boldsymbol{\alpha}_n$ introduced above are assumed to be i.i.d. random variables having some given PDF $p_{\boldsymbol{\alpha}}(\alpha)$, $\alpha \in [-\pi, \pi)$. The gains $\boldsymbol{c}_n$, phases $\boldsymbol{\theta}_n$, and AOAs $\boldsymbol{\alpha}_n$ are furthermore considered as being mutually independent.

On the other hand, we model the specular component $m_\rho(t)$ through a single cisoid with a deterministic gain ρ, phase θ_ρ, and Doppler frequency $f_\rho \triangleq f_{\max}\cos(\alpha_\rho)$, where $\theta_\rho, \alpha_\rho \in [-\pi, \pi)$, and $0 \le \rho < \infty$.

Under such considerations, the channel model can be written in the form

$$\boldsymbol{\nu}(t) = \underbrace{\lim_{\mathcal{N}\to\infty} \sum_{n=1}^{\mathcal{N}} \boldsymbol{c}_n \exp\left\{j\big(2\pi \boldsymbol{f}_n t + \boldsymbol{\theta}_n\big)\right\}}_{\boldsymbol{\mu}(t)} + \underbrace{\rho \exp\left\{j(2\pi f_\rho t + \theta_\rho)\right\}}_{m_\rho(t)}. \tag{2.3}$$

One can easily verify from the expression above that the mean value $m_{\boldsymbol{\nu}}(t) \triangleq E\{\boldsymbol{\mu}(t)\}$ of $\boldsymbol{\nu}(t)$ is equal to $m_\rho(t)$, that is, $m_{\boldsymbol{\nu}}(t) = m_\rho(t)$, whereas its variance $\mathrm{Var}\{\boldsymbol{\nu}(t)\} \triangleq E\{|\boldsymbol{\nu}(t) - m_{\boldsymbol{\nu}}(t)|^2\}$ equals $\sigma_{\boldsymbol{\mu}}^2$, i.e., $\mathrm{Var}\{\boldsymbol{\nu}(t)\} = \sigma_{\boldsymbol{\mu}}^2$. In turn, the power

of $\boldsymbol{\nu}(t)$ is given by $\mathcal{P}_{\boldsymbol{\nu}}(t) \triangleq E\{|\boldsymbol{\nu}(t)|^2\} = \sigma_{\boldsymbol{\nu}}^2$, where $\sigma_{\boldsymbol{\nu}}^2 = \sigma_{\boldsymbol{\mu}}^2 + \rho^2$; $|\cdot|$ indicates complex absolute value. We refer the reader to [Clar68, Jake74] for details on the physics behind (2.3). There, the suitability of the model for describing real-world channels is also discussed.

2.3 Statistical Characterization of the Reference Channel Model

2.3.1 ACFs

The complex Gaussian process $\boldsymbol{\nu}(t)$, which acts in this dissertation as a reference channel model, can be characterized by means of its ACF $r_{\boldsymbol{\nu\nu}}(t_1, t_2) \triangleq E\{\boldsymbol{\nu}^*(t_1)\boldsymbol{\nu}(t_2)\}$. It is straightforward to verify that the ACF of $\boldsymbol{\nu}(t)$ satisfies

$$\begin{aligned} r_{\boldsymbol{\nu\nu}}(t_1, t_2) &= r_{\boldsymbol{\nu\nu}}(\tau) && (2.4)\\ &= r_{\boldsymbol{\mu\mu}}(\tau) + \rho^2 \exp\{j2\pi f_\rho \tau\} && (2.5) \end{aligned}$$

where $\tau = t_2 - t_1$, and $r_{\boldsymbol{\mu\mu}}(\tau)$ is the ACF of the channel's diffuse component $\boldsymbol{\mu}(t)$; the notation $r_{\boldsymbol{xx}}(\tau)$ stands for the time-origin independent ACF $r_{\boldsymbol{xx}}(\tau) \triangleq E\{\boldsymbol{x}^*(t)\boldsymbol{x}(t+\tau)\}$ of a stationary random process $\boldsymbol{x}(t)$, and the operator $(\cdot)^*$ indicates complex conjugation. One can easily show for the latter ACF that

$$r_{\boldsymbol{\mu\mu}}(\tau) = \sigma_{\boldsymbol{\mu}}^2 E\big\{\exp(j2\pi f_{\max}\cos(\boldsymbol{\alpha})\tau)\big\} \quad (2.6)$$

where $\boldsymbol{\alpha}$ is any arbitrary AOA in $\{\boldsymbol{\alpha}_n\}_{n=1}^{\mathcal{N}}$. Furthermore, since the cisoid $\exp(j2\pi \cdot f_{\max}\cos(\boldsymbol{\alpha})\tau)$ is an even function of $\boldsymbol{\alpha}$, we can present (2.6) in the form

$$r_{\boldsymbol{\mu\mu}}(\tau) = 2\sigma_{\boldsymbol{\mu}}^2 \int_0^\pi g_{\boldsymbol{\alpha}}(\alpha)\exp(j2\pi f_{\max}\cos(\alpha)\tau)d\alpha \quad (2.7)$$

with $g_{\boldsymbol{\alpha}}(\alpha) \triangleq [p_{\boldsymbol{\alpha}}(\alpha) + p_{\boldsymbol{\alpha}}(-\alpha)]/2$ denoting the even part of the PDF $p_{\boldsymbol{\alpha}}(\alpha)$ of $\boldsymbol{\alpha}$. Alternatively, we can write

$$r_{\boldsymbol{\mu\mu}}(\tau) = \sigma_{\boldsymbol{\mu}}^2 \int_{-f_{\max}}^{f_{\max}} p_{\boldsymbol{f}}(f)\exp\{j2\pi f\tau\}df \quad (2.8)$$

where $p_{\boldsymbol{f}}(f)$ is the PDF of the random Doppler frequencies $\boldsymbol{f}_n$ defined in (2.2). Such a PDF is found to be equal to

$$p_{\boldsymbol{f}}(f) = 2\,\mathrm{rect}(f)\cdot\frac{g_{\boldsymbol{\alpha}}(\arccos(f/f_{\max}))}{f_{\max}\sqrt{1-(f/f_{\max})^2}}. \quad (2.9)$$

The function rect(f) in (2.9) stands for the rectangular function, which we define as rect(f) = 1 for $|f| < f_{\max}$, and rect(f) = 0 for $|f| \geq f_{\max}$. It is worth noticing that the ACF of the diffuse component $\boldsymbol{\mu}(t)$ meets

$$\begin{aligned} r_{\boldsymbol{\mu}\boldsymbol{\mu}}(\tau) &= \big[r_{\boldsymbol{\mu}_I\boldsymbol{\mu}_I}(\tau) + r_{\boldsymbol{\mu}_Q\boldsymbol{\mu}_Q}(\tau)\big] + j\big[r_{\boldsymbol{\mu}_I\boldsymbol{\mu}_Q}(\tau) - r_{\boldsymbol{\mu}_Q\boldsymbol{\mu}_I}(\tau)\big] \\ &= 2\big[r_{\boldsymbol{\mu}_I\boldsymbol{\mu}_I}(\tau) + j r_{\boldsymbol{\mu}_I\boldsymbol{\mu}_Q}(\tau)\big] \end{aligned} \tag{2.10}$$

where

$$r_{\boldsymbol{\mu}_I\boldsymbol{\mu}_I}(\tau) = r_{\boldsymbol{\mu}_Q\boldsymbol{\mu}_Q}(\tau) = \sigma_{\boldsymbol{\mu}}^2 \int_0^{\pi} g_{\boldsymbol{\alpha}}(\alpha) \cos\left(2\pi f_{\max} \cos(\alpha)\tau\right) d\alpha \tag{2.11a}$$

$$r_{\boldsymbol{\mu}_I\boldsymbol{\mu}_Q}(\tau) = -r_{\boldsymbol{\mu}_Q\boldsymbol{\mu}_I}(\tau) = \sigma_{\boldsymbol{\mu}}^2 \int_0^{\pi} g_{\boldsymbol{\alpha}}(\alpha) \sin\left(2\pi f_{\max} \cos(\alpha)\tau\right) d\alpha \tag{2.11b}$$

are the ACFs and cross-correlation functions (CCFs) of the IQ components of $\boldsymbol{\mu}(t)$, denoted by $\boldsymbol{\mu}_I(t)$ and $\boldsymbol{\mu}_Q(t)$, respectively. The CCF of any pair of random processes $\boldsymbol{x}(t)$ and $\boldsymbol{y}(t)$ is defined here as $r_{\boldsymbol{x}\boldsymbol{y}}(\tau) \triangleq E\{\boldsymbol{x}^*(t)\boldsymbol{y}(t+\tau)\}$. It becomes evident from (2.10) and (2.11) that if $\boldsymbol{\mu}_I(t)$ and $\boldsymbol{\mu}_Q(t)$ are uncorrelated, then the ACF $r_{\boldsymbol{\mu}\boldsymbol{\mu}}(\tau)$ of $\boldsymbol{\mu}(t)$ will be an even and a real-valued function; otherwise, it will be complex-valued and hermitian symmetric.

From the results presented in (2.5) and (2.8), we obtain

$$r_{\boldsymbol{\nu}\boldsymbol{\nu}}(\tau) = \sigma_{\boldsymbol{\mu}}^2 \int_{-f_{\max}}^{f_{\max}} p_{\boldsymbol{f}}(f) \exp\left\{j2\pi f\tau\right\} df + \rho^2 \exp\{j2\pi f_\rho \tau\}. \tag{2.12}$$

We recall that a random process is wide-sense stationary (WSS) when its mean value is constant and its ACF depends only on the time difference τ [Leon94, p. 356]. Since the mean value of $\boldsymbol{\nu}(t)$ is equal to $m_{\boldsymbol{\nu}}(t) = m_\rho(t) = \rho \exp\{j(2\pi f_\rho t + \theta_\rho)\}$ [cf. Sec. 2.2], and $r_{\boldsymbol{\nu}\boldsymbol{\nu}}(t_1, t_2) = r_{\boldsymbol{\nu}\boldsymbol{\nu}}(\tau)$, it follows that the reference model is WSS process if any of the conditions stated below is fulfilled[2]:

Condition 2.1 *The received signal is solely composed of scattered waves, so that* $\boldsymbol{\nu}(t) = \boldsymbol{\mu}(t)$*, and therefore* $m_{\boldsymbol{\nu}}(t) = 0$*.*

Condition 2.2 *The AOA of the specular component is equal to* $\pm\pi/2$*, i.e.,* $\alpha_\rho = \pm 90°$*. In such a case, we obtain* $m_{\boldsymbol{\nu}}(t) = \rho \exp\left\{j\theta_\rho\right\}$*, which is a time-independent quantity.*

Condition 2.1 leads in fact to the well-known Rayleigh fading channel model [Pae02a, Chap. 3]—a model that is widely used for assessing the performance of

[2]The reference model will be strict-sense stationary (SSS) indeed, since $\boldsymbol{\nu}(t)$ is a Gaussian process [Leon94, p. 360].

mobile communication systems [Hou04, Choi01]. We will pay special attention to such a particular case—which we will refer to as the NLOS case—because of its relevance. Condition 2.2, on the other hand, is related to very specific scenarios, and we will not devote further attention to that case.

2.3.2 PSDs

The channel model described by $\boldsymbol{\nu}(t)$ can alternatively be characterized through its PSD $S_{\boldsymbol{\nu\nu}}(f)$. It is shown in [Mill04, pp. 373–375] that the PSD and the ACF of a random process form a Fourier transform pair provided that the ACF depends only on the time difference τ. Since this is the case for the ACF $r_{\boldsymbol{\nu\nu}}(\tau)$ of $\boldsymbol{\nu}(t)$ [see (2.12)], we find by substituting $r_{\boldsymbol{\nu\nu}}(\tau)$ from (2.12) into $S_{\boldsymbol{\nu\nu}}(f) = \int_{-\infty}^{\infty} r_{\boldsymbol{\nu\nu}}(\tau)\exp\{-j2\pi f\tau\}d\tau$ that

$$S_{\boldsymbol{\nu\nu}}(f) = \sigma^2_{\boldsymbol{\mu}} p_{\boldsymbol{f}}(f) + \rho^2\delta(f - f_\rho) \tag{2.13}$$

$$= 2\sigma^2_{\boldsymbol{\mu}}\mathrm{rect}(f) \cdot \frac{g_{\boldsymbol{\alpha}}(\arccos(f/f_{\max}))}{f_{\max}\sqrt{1-(f/f_{\max})^2}} + \rho^2\delta(f - f_\rho) \tag{2.14}$$

where $\delta(\cdot)$ is the Dirac delta function. This result implies that the PSD of $\boldsymbol{\nu}(t)$ is confined to a bandwidth of $2f_{\max}$, as $|f_\rho| \leq f_{\max}$ and $p_{\boldsymbol{f}}(f) = 0$ for $|f| \geq f_{\max}$. The channel's PSD is often referred to as the DPSD due to the relationship between $S_{\boldsymbol{\nu\nu}}(f)$ and the distribution of the signal power in the Doppler frequency domain. We will adopt such a terminology from this point onwards.

For the special case $m_\rho(t) = 0$, $S_{\boldsymbol{\nu\nu}}(f)$ reduces to the DPSD

$$S_{\boldsymbol{\mu\mu}}(f) = 2\sigma^2_{\boldsymbol{\mu}}\mathrm{rect}(f) \cdot \frac{g_{\boldsymbol{\alpha}}(\arccos(f/f_{\max}))}{f_{\max}\sqrt{1-(f/f_{\max})^2}} \tag{2.15}$$

of $\boldsymbol{\mu}(t)$. For this case, we can observe from classic Fourier theory (see [Brig88, Sec. 3.6]) that if the IQ components of $\boldsymbol{\mu}(t)$ are uncorrelated, meaning that $r_{\boldsymbol{\mu\mu}}(\tau)$ is even and real-valued, then $S_{\boldsymbol{\mu\mu}}(f)$ will be symmetrical with respect to the origin. On the contrary, if $\boldsymbol{\mu}_I(t)$ and $\boldsymbol{\mu}_Q(t)$ are mutually correlated, then $S_{\boldsymbol{\mu\mu}}(f)$ will be asymmetrical. In this respect, it is worth noticing that measurement campaigns carried out in different propagation scenarios have shown that the DPSDs of real-world NLOS channels are in general asymmetrical [Kott04, Zhao03, Blau06].

2.3.3 Average Doppler Shift and Doppler Spread

The first moment and the squared-root second central moment of $S_{\boldsymbol{\nu\nu}}(f)$ define the channel's average Doppler shift $A_{\boldsymbol{\nu\nu}}$ and Doppler spread $D_{\boldsymbol{\nu\nu}}$, respectively. These two quantities play an important role in the investigation of problems related to the time-variant behavior of the channel, such as speed estimation [Moha05] and frequency synchronization [Cai06, Niss06]. One can show by taking

account of the Fourier transform relationship between $S_{\boldsymbol{\nu\nu}}(f)$ and $r_{\boldsymbol{\nu\nu}}(\tau)$ that

$$\begin{aligned} A_{\boldsymbol{\nu\nu}} &\triangleq \frac{\int_{-\infty}^{\infty} f S_{\boldsymbol{\nu\nu}}(f) df}{\int_{-\infty}^{\infty} S_{\boldsymbol{\nu\nu}}(f) df} \\ &= \frac{1}{j2\pi} \frac{\dot{r}_{\boldsymbol{\nu\nu}}(0)}{r_{\boldsymbol{\nu\nu}}(0)} \end{aligned} \tag{2.16}$$

$$\begin{aligned} D_{\boldsymbol{\nu\nu}} &\triangleq \sqrt{\frac{\int_{-\infty}^{\infty} S_{\boldsymbol{\nu\nu}}(f)\big[f - A_{\boldsymbol{\nu\nu}}\big]^2 df}{\int_{-\infty}^{\infty} S_{\boldsymbol{\nu\nu}}(f) df}} \\ &= \frac{1}{2\pi} \sqrt{\left(\frac{\dot{r}_{\boldsymbol{\nu\nu}}(0)}{r_{\boldsymbol{\nu\nu}}(0)}\right)^2 - \frac{\ddot{r}_{\boldsymbol{\nu\nu}}(0)}{r_{\boldsymbol{\nu\nu}}(0)}} \end{aligned} \tag{2.17}$$

where the single and double overdots denote the first and second derivatives with respect to τ, respectively. Interestingly, (2.16) and (2.17) indicate that the average Doppler shift and Doppler spread of $\boldsymbol{\nu}(t)$ can unequivocally be determined from the value, slope, and curvature of $r_{\boldsymbol{\nu\nu}}(\tau)$ at the origin ($\tau = 0$).

In a similar way, one can show that the average Doppler shift $A_{\boldsymbol{\mu\mu}}$ and Doppler spread $D_{\boldsymbol{\mu\mu}}$ of the diffuse component $\boldsymbol{\mu}(t)$ are equal to

$$\begin{aligned} A_{\boldsymbol{\mu\mu}} &\triangleq \frac{\int_{-\infty}^{\infty} f S_{\boldsymbol{\mu\mu}}(f) df}{\int_{-\infty}^{\infty} S_{\boldsymbol{\mu\mu}}(f) df} \\ &= \frac{\dot{r}_{\boldsymbol{\mu}_I\boldsymbol{\mu}_Q}(0)}{\pi\sigma_{\boldsymbol{\mu}}^2} \end{aligned} \tag{2.18}$$

$$\begin{aligned} D_{\boldsymbol{\mu\mu}} &\triangleq \sqrt{\frac{\int_{-\infty}^{\infty} S_{\boldsymbol{\mu\mu}}(f)\big[f - A_{\boldsymbol{\mu\mu}}\big]^2 df}{\int_{-\infty}^{\infty} S_{\boldsymbol{\mu\mu}}(f) df}} \\ &= \sqrt{-\left(A_{\boldsymbol{\mu\mu}}^2 + \frac{\ddot{r}_{\boldsymbol{\mu}_I\boldsymbol{\mu}_I}(0)}{2\pi^2\sigma_{\boldsymbol{\mu}}^2}\right)}. \end{aligned} \tag{2.19}$$

We took account of the relationships $\dot{r}_{\boldsymbol{\mu\mu}}(0) = 2j\dot{r}_{\boldsymbol{\mu}_I\boldsymbol{\mu}_Q}(0)$ and $\ddot{r}_{\boldsymbol{\mu\mu}}(0) = 2\ddot{r}_{\boldsymbol{\mu}_I\boldsymbol{\mu}_I}(0)$ in writting the previous expressions, where

$$\dot{r}_{\boldsymbol{\mu}_I\boldsymbol{\mu}_Q}(0) = 2\pi\sigma_{\boldsymbol{\mu}}^2 f_{\max} \int_0^{\pi} g_{\boldsymbol{\alpha}}(\alpha)\cos(\alpha) d\alpha \tag{2.20a}$$

$$\ddot{r}_{\boldsymbol{\mu}_I\boldsymbol{\mu}_I}(0) = -\sigma_{\boldsymbol{\mu}}^2 (2\pi f_{\max})^2 \int_0^{\pi} g_{\boldsymbol{\alpha}}(\alpha)\cos^2(\alpha) d\alpha. \tag{2.20b}$$

It becomes evident from (2.18) that if the IQ components of $\boldsymbol{\mu}(t)$ are uncorrelated, meaning that $r_{\boldsymbol{\mu}_I\boldsymbol{\mu}_Q}(\tau) = 0$, then $A_{\boldsymbol{\mu\mu}} = 0$. This was to be expected, since the DPSD of $\boldsymbol{\mu}(t)$ is symmetrical under such conditions.

2.4 Statistical Characterization of the Signal Fading

The design of robust transceivers for mobile communication systems requires knowledge on the statistics of the signal fading. In this regard, explicit information about the distributions of the channel's envelope and phase, LCR, and ADF is of utmost interest, as these statistical functions play an important role in the design of carrier detection/tracking [Brow96], channel codification [Edba89], and diversity techniques [Rapp02, Sec. 7.10], [Jake74, Sec. 6.3], just to give a few examples. Information about the ACF of the channel's squared envelope is also relevant, since this function gives insights into the carrier-to-noise-ratio (CNR) fluctuations produced by noisy fading channels [Pars00, p. 129].

2.4.1 PDFs of the Channel's Envelope and Phase

2.4.1.1 First-Order PDF of the Envelope

Concerning the distribution of the reference model's envelope $\boldsymbol{\xi}(t) \triangleq |\boldsymbol{\nu}(t)|^2$, one can show by proceeding as in [Pae02a, Sec. 6.1.1] and [Auli79] that irrespective of the channel's correlation properties, the first-order PDF $p_{\boldsymbol{\xi}}(z;t)$ of $\boldsymbol{\xi}(t)$ equals

$$p_{\boldsymbol{\xi}}(z) = \frac{2z}{\sigma_{\boldsymbol{\mu}}^2} e^{-\frac{z^2+\rho^2}{\sigma_{\boldsymbol{\mu}}^2}} I_0\left(\frac{2z\cdot\rho}{\sigma_{\boldsymbol{\mu}}^2}\right), \qquad z \geq 0 \tag{2.21}$$

where $I_0(\cdot)$ is the modified Bessel function of the first kind and order zero. Equation (2.21) can be identified as the Rice distribution [Proa01, p. 46], and it indicates that the channel's envelope $\boldsymbol{\xi}(t)$ is a first-order stationary process, since $p_{\boldsymbol{\xi}}(z;t) = p_{\boldsymbol{\xi}}(z)$. The PDF given above can be rewritten in terms of the ratio between the powers of the specular and diffuse components as follows

$$p_{\boldsymbol{\xi}}(z) = \frac{2z(c_R+1)}{\sigma_{\boldsymbol{\nu}}^2} \cdot \exp\left\{-c_R - \frac{z^2(c_R+1)}{\sigma_{\boldsymbol{\nu}}^2}\right\} \cdot I_0\left(\frac{2z}{\sigma_{\boldsymbol{\nu}}}\sqrt{c_R(c_R+1)}\right) \tag{2.22}$$

for $z \geq 0$, where $\sigma_{\boldsymbol{\nu}}^2 = \sigma_{\boldsymbol{\mu}}^2 + \rho^2$ is the total power of the channel, and $c_R \triangleq \rho^2/\sigma_{\boldsymbol{\mu}}^2$ is the so-called Rician factor, which is an indicator of the link quality (the higher the Rician factor, the higher the quality of the wireless link).

For the NLOS case ($c_R = 0$), the PDF in (2.22) reduces to the PDF $p_{\boldsymbol{\zeta}}(z)$ of the envelope $\boldsymbol{\zeta}(t) \triangleq |\boldsymbol{\mu}(t)|$ of the diffuse component. Such a PDF is given by

$$p_{\boldsymbol{\zeta}}(z) = \frac{2z}{\sigma_{\boldsymbol{\mu}}^2} e^{-\frac{z^2}{\sigma_{\boldsymbol{\mu}}^2}}, \qquad z \geq 0. \tag{2.23}$$

Equation (2.23) can in turn be recognized as the Rayleigh PDF [Proa01, p. 44].

Figure 2.1 shows graphs of the channel's envelope obtained by considering $c_R \in \{0, 2, 4\}$, $\sigma_{\boldsymbol{\nu}}^2 = 1$, and $f_{\max} = 91$ Hz (corresponding to a carrier frequency

of 1.8 GHz and a MT traveling at around 54 km/h). The PDF of $\boldsymbol{\xi}(t)$ defined in (2.22) is plotted also in that figure for the same values of c_R and $\sigma^2_{\boldsymbol{\nu}}$.

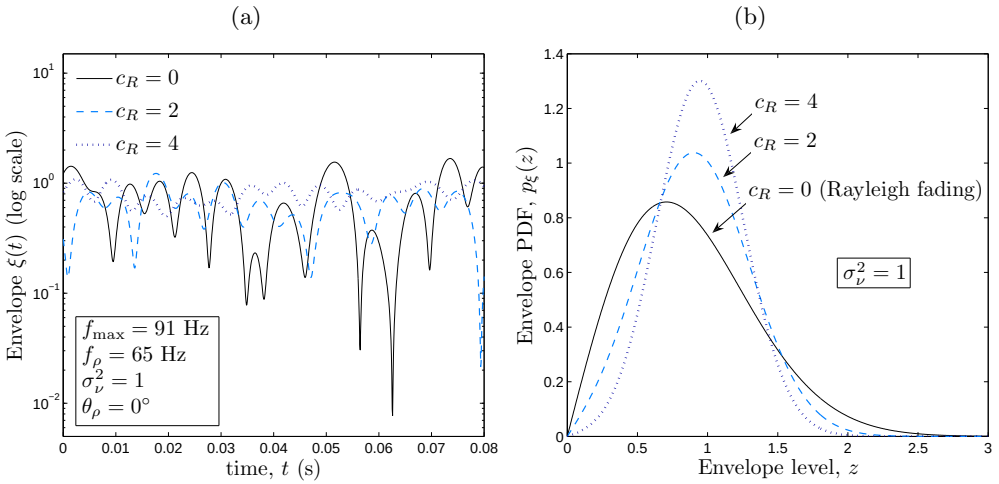

Figure 2.1: (a) Channel's envelope $\boldsymbol{\xi}(t)$ (b) and its first-order PDF $p_{\boldsymbol{\xi}}(z)$ for different Rician factors c_R.

2.4.1.2 First-Order PDF of the Phase

In a similar way, one can show that the first-order PDF $p_{\boldsymbol{\psi}}(\theta;t)$ of the channel's phase $\boldsymbol{\psi}(t) \triangleq \arg\{\boldsymbol{\nu}(t)\}$ is given by [Pae02a, Sec. 6.1.1.1], [Auli79]

$$\begin{aligned} p_{\boldsymbol{\psi}}(\theta;t) &= \frac{e^{-\frac{\rho^2}{\sigma^2_{\boldsymbol{\mu}}}}}{2\pi} + \frac{\rho}{\sqrt{4\pi}\sigma_{\boldsymbol{\mu}}} \cos\left(\theta - 2\pi f_\rho t - \theta_\rho\right) e^{-\frac{\rho^2}{\sigma^2_{\boldsymbol{\mu}}}\sin^2(\theta - 2\pi f_\rho t - \theta_\rho)} \\ &\quad \cdot \operatorname{erfc}\Big(-\frac{\rho}{\sigma_{\boldsymbol{\mu}}}\cos(\theta - 2\pi f_\rho t - \theta_\rho)\Big), \qquad -\pi \le \theta \le \pi \end{aligned} \tag{2.24}$$

where $\operatorname{erfc}(x)$ denotes the complementary error function, which is defined as

$$\operatorname{erfc}(x) \triangleq \frac{2}{\sqrt{\pi}} \int_x^\infty \exp\left\{-y^2\right\} dy. \tag{2.25}$$

Such a PDF can alternatively be presented in terms of the Rician factor as follows

$$\begin{aligned} p_{\boldsymbol{\psi}}(\theta;t) &= \frac{e^{-c_R}}{2\pi} + \sqrt{\frac{c_R}{4\pi}} \cos\left(\theta - 2\pi f_\rho t - \theta_\rho\right) e^{-c_R \sin^2(\theta - 2\pi f_\rho t - \theta_\rho)} \\ &\quad \cdot \operatorname{erfc}\left(-\sqrt{c_R}\cos(\theta - 2\pi f_\rho t - \theta_\rho)\right), \qquad -\pi \le \theta \le \pi. \end{aligned} \tag{2.26}$$

An inspection to (2.26) reveals that the correlation properties of $\boldsymbol{\nu}(t)$ do not influence the PDF of $\boldsymbol{\psi}(t)$. Besides, (2.26) shows that the channel's phase is not

a first-order stationary process, because the PDF $p_{\boldsymbol{\psi}}(\theta;t)$ of $\boldsymbol{\psi}(t)$ is in general time-dependent. Nevertheless, the PDF of $\boldsymbol{\psi}(t)$ happens to be time-independent if either Condition 2.1 or Condition 2.2 [see Sec. 2.3.1] is observed. In particular, if Condition 2.1 is met, so that $c_R = 0$, then

$$p_{\boldsymbol{\psi}}(\theta;t) = p_{\boldsymbol{\varphi}}(\theta) \tag{2.27}$$

$$= \frac{1}{2\pi}, \qquad -\pi \leq \theta \leq \pi \tag{2.28}$$

where $p_{\boldsymbol{\varphi}}(\theta)$ is the first-order PDF of the diffuse component's phase $\boldsymbol{\varphi}(t) \triangleq \arg\{\boldsymbol{\mu}(t)\}$.

The phase of the channel and its first-order distribution $p_{\boldsymbol{\psi}}(\theta;t)$ are depicted in Fig. 2.2 for $\sigma_\nu^2 = 1$ and $c_R \in \{0, 2, 4\}$. The graphs of $p_{\boldsymbol{\psi}}(\theta;t)$ presented there correspond to the time instants $t = 0$ s and $t = 0.25$ s.

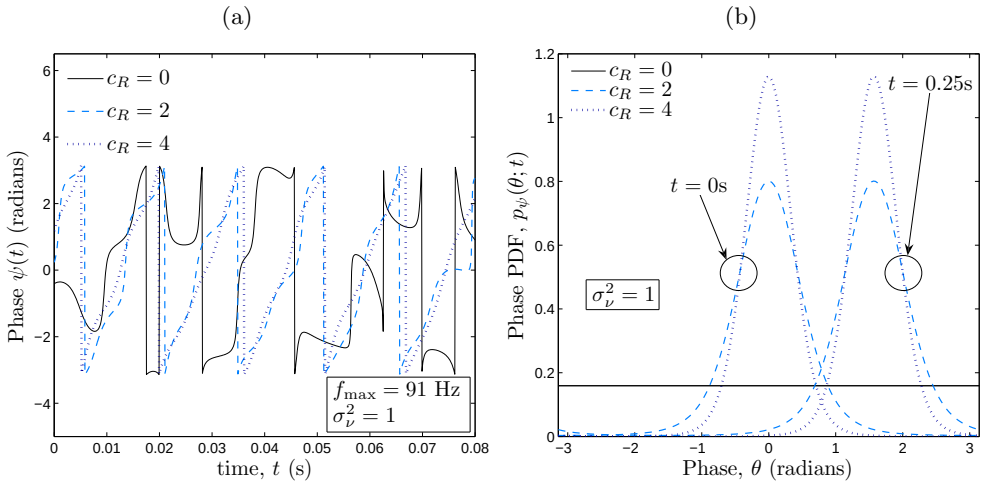

Figure 2.2: (a) Channel's phase $\boldsymbol{\psi}(t)$ (b) and its first-order PDF $p_{\boldsymbol{\psi}}(\theta;t)$ for different Rician factors c_R ($f_\rho = 65$ Hz and $\theta_\rho = 0°$).

2.4.2 LCR and ADF

The first-order PDFs of the envelope and phase of $\boldsymbol{\nu}(t)$ do not provide information about the coherence or rapidity of the signal fades, as both PDFs are blind to the channel's correlation properties. Such an information, which is fundamental for the design of bit and symbol interleaving schemes [Proa01, pp. 467–470], should instead be acquired from the LCR and ADF of the channel's envelope. The LCR gives a measure of the number of times the channel's envelope crosses a given level r with positive (or negative) slope within one second, whereas the ADF is a measure of the average time the envelope remains below that level.

2.4.2.1 LCR

In accordance to Rice [Rice44], the LCR $N_{\xi}^{+}(r)$ of the envelope $\boldsymbol{\xi}(t)$ is to be computed for a given signal level $r \geq 0$ by evaluating

$$N_{\boldsymbol{\xi}}(r) \;=\; \int_0^{\infty} \xi' p_{\boldsymbol{\xi}\boldsymbol{\xi}'}(r,\xi') d\xi' \tag{2.29}$$

where $p_{\boldsymbol{\xi}\boldsymbol{\xi}'}(\xi,\xi')$ is the joint PDF of $\boldsymbol{\xi}(t)$ and its derivative $\boldsymbol{\xi}'(t) = d\boldsymbol{\xi}(t)dt$ (the notation $(\cdot)'$ indicates time derivate). The analytical solution of (2.29) was derived in [Pae02a, Sec. 6.1.1.2] for the envelope of a complex Gaussian process having essentially the same statistical properties as $\boldsymbol{\nu}(t)$. Based on the result there presented, we can write

$$\begin{aligned} N_{\boldsymbol{\xi}}(r) \;=\; & \frac{r(1+c_R)\sqrt{8b_0}}{\sigma_{\boldsymbol{\nu}}^2 \pi^{3/2}} \exp\Big\{ -c_R - \frac{r^2(c_R+1)}{\sigma_{\boldsymbol{\nu}}^2} \Big\} \\ & \times \int_0^{\pi/2} \cosh\left(\frac{2r}{\sigma_{\boldsymbol{\nu}}} \sqrt{c_R(c_R+1)} \cos(y) \right) \cdot \left\{ \exp\Big\{ -\frac{c_R[a_0 \sigma_{\boldsymbol{\nu}} \sin(y)]^2}{c_R+1} \Big\} \right. \\ & \left. + \sqrt{\frac{\pi c_R}{c_R+1}} a_0 \sigma_{\boldsymbol{\nu}} \sin(y) \cdot \operatorname{erf}\left(\sqrt{\frac{c_R}{c_R+1}} a_0 \sigma_{\boldsymbol{\nu}} \sin(y) \right) \right\} dy \end{aligned} \tag{2.30}$$

for $r \geq 0$, where

$$a_0 \;=\; \sqrt{\frac{2}{b_0}} \left(\pi f_{\rho} - \frac{\dot{r}_{\boldsymbol{\mu}_I \boldsymbol{\mu}_Q}(0)}{\sigma_{\boldsymbol{\mu}}^2} \right) \tag{2.31}$$

$$b_0 \;=\; -\ddot{r}_{\boldsymbol{\mu}_I \boldsymbol{\mu}_I}(0) - \frac{2}{\sigma_{\boldsymbol{\mu}}^2} \dot{r}_{\boldsymbol{\mu}_I \boldsymbol{\mu}_Q}^2(0) \tag{2.32}$$

and $\operatorname{erf}(x)$ is the error function, which is defined as

$$\operatorname{erf}(x) \;\triangleq\; \frac{2}{\sqrt{\pi}} \int_0^{x} \exp\left\{ -y^2 \right\} dy. \tag{2.33}$$

Equation (2.30) shows that $N_{\boldsymbol{\xi}}(r)$ do not depend on the exact shape of the ACF of $\boldsymbol{\nu}(t)$, but only on its value, slope, and curvature at the origin. For the NLOS case ($c_R = 0$), $N_{\boldsymbol{\xi}}(r)$ converges to the LCR $N_{\boldsymbol{\zeta}}$ of the envelope $\boldsymbol{\zeta}(t)$ of $\boldsymbol{\mu}(t)$. By taking $c_R = 0$ in (2.30), it can be shown that $N_{\boldsymbol{\zeta}}$ is equal to

$$N_{\boldsymbol{\zeta}} \;=\; \sqrt{\frac{b_0}{2\pi}} \cdot p_{\boldsymbol{\zeta}}(r), \quad r \geq 0 \tag{2.34}$$

where $p_{\boldsymbol{\zeta}}(r)$ is the Rayleigh PDF [see 2.23]. Interestingly, (2.34) shows that the LCR of the diffuse component is proportional to the Rayleigh PDF.

2.4.2.2 ADF

On the other hand, the ADF $T_{\boldsymbol{\xi}}(r)$ is to be computed by evaluating the quotient

$$T_{\boldsymbol{\xi}}(r) \;=\; \frac{P_{\boldsymbol{\xi}}(r)}{N_{\boldsymbol{\xi}}(r)} \tag{2.35}$$

where $P_{\boldsymbol{\xi}}(x) \triangleq \int_0^x p_{\boldsymbol{\xi}}(y)dy$ is the cumulative distribution function (CDF) of the Rice process $\boldsymbol{\xi}(t)$. Such a CDF is equal to [Proa01, Eq. (2.1–142)]

$$P_{\boldsymbol{\xi}}(x) \;=\; 1 - \int_{\sqrt{2}r/\sigma_{\boldsymbol{\mu}}}^{\infty} xe^{-\frac{x^2+(\sqrt{2}r/\sigma_{\boldsymbol{\mu}})^2}{2}} I_0\left(x\sqrt{2}\frac{\rho}{\sigma_{\boldsymbol{\mu}}}\right) dx. \tag{2.36}$$

For the particular case $c_R = 0$, we find that $T_{\boldsymbol{\xi}}(r)$ simplifies to the ADF $T_{\boldsymbol{\zeta}}(r)$ of the envelope $\boldsymbol{\zeta}(t)$ of the diffuse component $\boldsymbol{\mu}(t)$. For this latter function, we find the closed-form solution

$$T_{\boldsymbol{\zeta}}(r) = \frac{\sigma_{\boldsymbol{\mu}}^2}{2r}\sqrt{-\frac{2\pi}{\ddot{r}_{\boldsymbol{\mu}_I\boldsymbol{\mu}_I}(0)}} \cdot \left(e^{\frac{r^2}{\sigma_{\boldsymbol{\mu}}^2}} - 1\right), \quad r \geq 0. \tag{2.37}$$

2.4.3 ACF of the Channel's Squared Envelope

Regarding the ACF $r_{\boldsymbol{\xi}^2\boldsymbol{\xi}^2}(t_1,t_2) \triangleq E\{\boldsymbol{\xi}^2(t_1)\boldsymbol{\xi}^2(t_2)\}$ of the channel's squared envelope $\boldsymbol{\xi}^2(t)$, it is shown in Appendix A that

$$\begin{aligned} r_{\boldsymbol{\xi}^2\boldsymbol{\xi}^2}(t_1,t_2) \;&=\; r_{\boldsymbol{\xi}^2\boldsymbol{\xi}^2}(\tau) && (2.38)\\ &=\; r_{\boldsymbol{\zeta}^2\boldsymbol{\zeta}^2}(\tau) + \frac{4\sigma_{\boldsymbol{\nu}}^2 c_R}{c_R+1}\Big\{ r_{\boldsymbol{\mu}_I\boldsymbol{\mu}_I}(\tau)\cos(2\pi f_\rho \tau) \\ &\quad + r_{\boldsymbol{\mu}_I\boldsymbol{\mu}_Q}(\tau)\sin(2\pi f_\rho\tau)\Big\} + \frac{c_R\,\sigma_{\boldsymbol{\nu}}^4(c_R+2)}{(c_R+1)^2} && (2.39)\end{aligned}$$

where

$$r_{\boldsymbol{\zeta}^2\boldsymbol{\zeta}^2}(\tau) \;=\; \frac{\sigma_{\boldsymbol{\nu}}^4}{(c_R+1)^2} + \left|r_{\boldsymbol{\mu}\boldsymbol{\mu}}(\tau)\right|^2 \tag{2.40}$$

is the ACF of the squared envelope $\boldsymbol{\zeta}^2(t) \triangleq |\boldsymbol{\mu}(t)|^2$ of $\boldsymbol{\mu}(t)$; the correlation functions $r_{\boldsymbol{\mu}_I\boldsymbol{\mu}_I}(\tau)$ and $r_{\boldsymbol{\mu}_I\boldsymbol{\mu}_Q}(\tau)$ are defined in (2.11). It is worth mentioning that if the IQ components of $\boldsymbol{\mu}(t)$ are uncorrelated, so that $r_{\boldsymbol{\mu}_I\boldsymbol{\mu}_Q}(\tau) = 0$, then (2.39) and (2.40) reduce to the expressions presented in [Pars00, p. 129] and [Auli79] for the squared envelope's ACF of isotropic scattering channels.

We observe that the channel's squared envelope $\boldsymbol{\xi}^2(t)$ is a WSS process, since its ACF $\boldsymbol{\xi}^2(t)$ depends only on τ and its mean value $m_{\boldsymbol{\xi}^2}(t) \triangleq E\{\boldsymbol{\xi}^2(t)\}$ can easily be found to be time-invariant and equal to $\sigma_{\boldsymbol{\nu}}^2$, i.e., $m_{\boldsymbol{\xi}^2}(t) = \sigma_{\boldsymbol{\nu}}^2$.

2.5 Distributions of the AOA and Particular Cases

In order to test and evaluate the performance of the simulation models proposed in this thesis, it is necessary to specify a concrete distribution for the random AOAs $\boldsymbol{\alpha}_n$. In this dissertation, we will consider two widely accepted AOA distributions, namely, the von Mises distribution [VonM18], and the Laplacian distribution [Kotz01]. We will concisely describe the characteristics of these distributions in the remaining of this chapter, and we will analyze also the resulting correlation and spectral properties of $\boldsymbol{\mu}(t)$. We restrict our attention to the diffuse component because the ACF and DPSD of $\boldsymbol{\nu}(t)$ can easily be obtained once the ACF and DPSD of $\boldsymbol{\mu}(t)$ are known—see (2.5), (2.14), and (2.15). Besides, we observe that the average Doppler shift $A_{\boldsymbol{\nu\nu}}$ and Doppler spread $D_{\boldsymbol{\nu\nu}}$ of $\boldsymbol{\nu}(t)$ can be written in terms of the corresponding averaged Doppler shift $A_{\boldsymbol{\mu\mu}}$ and Doppler spread $D_{\boldsymbol{\mu\mu}}$ of $\boldsymbol{\mu}(t)$ as follows:

$$A_{\boldsymbol{\nu\nu}} = A_{\boldsymbol{\mu\mu}} + \rho^2 f_\rho \tag{2.41}$$

$$D_{\boldsymbol{\nu\nu}} = \sqrt{\rho^2 f_\rho^2 + (D_{\boldsymbol{\mu\mu}})^2 + (A_{\boldsymbol{\mu\mu}})^2 - (A_{\boldsymbol{\nu\nu}})^2}. \tag{2.42}$$

To prevent confusions with the notation, we will make use of the superscripts $(\cdot)^{\mathrm{VM}}$ and $(\cdot)^{\mathrm{LA}}$ to indicate whether the statistics of $\boldsymbol{\mu}(t)$ are to be associated with the von Mises or the Laplacian AOA distributions.

2.5.1 The von Mises PDF of the AOA and the Associated ACF and DPSD of the Channel's Diffuse Component

The von Mises PDF is a distribution for angular (circular) variates [Wats82] that was originally introduced by Richard E. von Mises to study deviations of atomic weights from integer values [VonM18]. This distribution has widely been in use in the field of directional statistics, and its applications span from geophysics to vital statistics [Gumb54, Upto73]. It is also known as the circular normal distribution—as it is analogous in many respects to the normal distribution for linear variates [Gumb53], and it includes other important distributions as special cases, such as the uniform, cardioid, and wrapped Gaussian [Mard99]. The use of the von Mises PDF to model the AOA statistics of mobile fading channels was proposed in [Abd02a]. In that paper, the authors provide evidence of the suitability of such a PDF to match measured data.

The von Mises PDF and its even part are given by

$$p_{\boldsymbol{\alpha}}^{\mathrm{VM}}(\alpha) \triangleq \frac{\exp\{\kappa\cos(\alpha - m_\alpha)\}}{2\pi I_0(\kappa)} \tag{2.43}$$

$$g_{\boldsymbol{\alpha}}^{\mathrm{VM}}(\alpha) = \frac{\exp\{\kappa\cos(\alpha)\cos(m_\alpha)\}}{2\pi I_0(\kappa)} \cdot \cosh\left(\kappa\sin(\alpha)\sin(m_\alpha)\right) \tag{2.44}$$

respectively, where $\alpha \in [-\pi, \pi)$, $m_\alpha \in [-\pi, \pi)$ denotes the mean AOA, and $\kappa \geq 0$ is a concetration parameter determining the channel's angular spread. Following (2.15), one can readily verify that

$$\begin{aligned} S_{\boldsymbol{\mu}\boldsymbol{\mu}}^{\mathrm{VM}}(f) &= \mathrm{rect}\,(f) \cdot \cosh\left(\kappa \sin(m_\alpha)\sqrt{1-(f/f_{\max})^2}\right) \\ &\quad \times \frac{\sigma_{\boldsymbol{\mu}}^2 \exp\left\{\kappa \cos(m_\alpha) f/f_{\max}\right\}}{\pi f_{\max} I_0(\kappa)\sqrt{1-(f/f_{\max})^2}} \end{aligned} \tag{2.45}$$

whereas, by using (2.7), one may demonstrate that

$$r_{\boldsymbol{\mu}\boldsymbol{\mu}}^{\mathrm{VM}}(\tau) = \frac{\sigma_{\boldsymbol{\mu}}^2 I_0\left(\sqrt{\kappa^2 - (2\pi f_{\max}\tau)^2 + j4\pi\kappa f_{\max}\cos(m_\alpha)\tau}\right)}{I_0(\kappa)}. \tag{2.46}$$

It is worth noticing that for $\kappa = 0$, the DPSD shown in (2.45) reduces to the well-known U-shaped DPSD

$$S_{\boldsymbol{\mu}\boldsymbol{\mu}}(f) = \mathrm{rect}\,(f) \cdot \frac{\sigma_{\boldsymbol{\mu}}^2}{\pi f_{\max}\sqrt{1-(f/f_{\max})^2}} \tag{2.47}$$

characterizing isotropic scattering channels [Clar68], whilst the ACF in (2.46) simplifies to

$$r_{\boldsymbol{\mu}\boldsymbol{\mu}}(\tau) = \sigma_{\boldsymbol{\mu}}^2 J_0(2\pi f_{\max}\tau) \tag{2.48}$$

where $J_0(\cdot)$ is the Bessel function of the first kind and order zero.

On the other hand, we find by following (2.18) and (2.19) that the diffuse component's average Doppler shift $A_{\boldsymbol{\mu}\boldsymbol{\mu}}^{\mathrm{VM}}$ and Doppler spread $D_{\boldsymbol{\mu}\boldsymbol{\mu}}^{\mathrm{VM}}$ are given by

$$A_{\boldsymbol{\mu}\boldsymbol{\mu}}^{\mathrm{VM}} = f_{\max}\cos(m_\alpha)\frac{I_1(\kappa)}{I_0(\kappa)} \tag{2.49}$$

$$\begin{aligned} D_{\boldsymbol{\mu}\boldsymbol{\mu}}^{\mathrm{VM}} &= \left\{\frac{f_{\max}^2}{\kappa I_0(\kappa)}\left[\frac{\kappa[I_0(\kappa)+I_2(\kappa)]\cos^2(m_\alpha)}{2}\right.\right. \\ &\quad \left.\left. + I_1(\kappa)\sin^2(m_\alpha)\right] - (A_{\boldsymbol{\mu}\boldsymbol{\mu}}^{\mathrm{VM}})^2\right\}^{-1/2} \end{aligned} \tag{2.50}$$

where $I_1(\cdot)$ and $I_2(\cdot)$ denote the first and second order modified Bessel functions, respectively. We observe that if $\kappa = 0$, then $A_{\boldsymbol{\mu}\boldsymbol{\mu}}^{\mathrm{VM}} = 0$ and $D_{\boldsymbol{\mu}\boldsymbol{\mu}}^{\mathrm{VM}} = f_{\max}/\sqrt{2}$.

Figures 2.3–2.5 show how the von Mises PDF and the resulting ACF and DPSD of $\boldsymbol{\mu}(t)$ look like for different combinations of the parameters m_α and κ. The graphs presented in those figures were computed by choosing $\sigma_{\boldsymbol{\mu}}^2 = 1$ and $f_{\max} = 91$ Hz. They are representative of scattering propagation conditions ranging from isotropic ($m_\alpha = 0$ and $\kappa = 0$) to extremely non-isotropic ($m_\alpha = 0$ and $\kappa = 20$). We can see in Fig. 2.5 and deduce from (2.45) that the diffuse

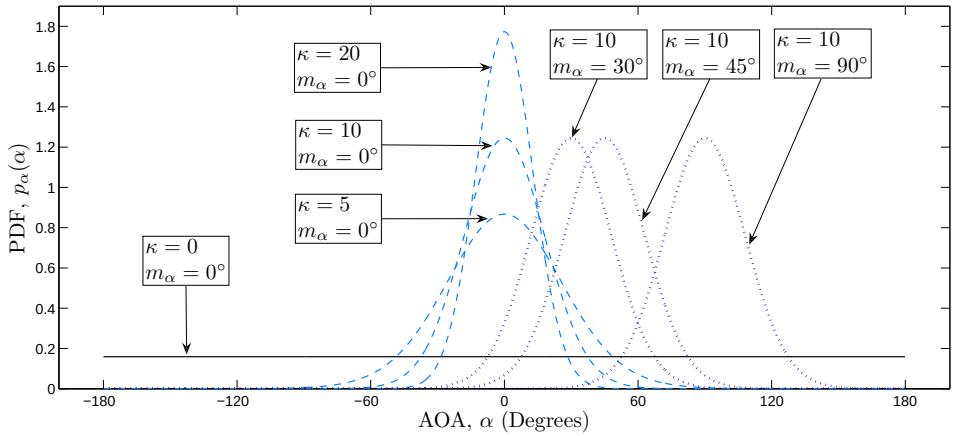

Figure 2.3: The von Mises PDF of the AOA.

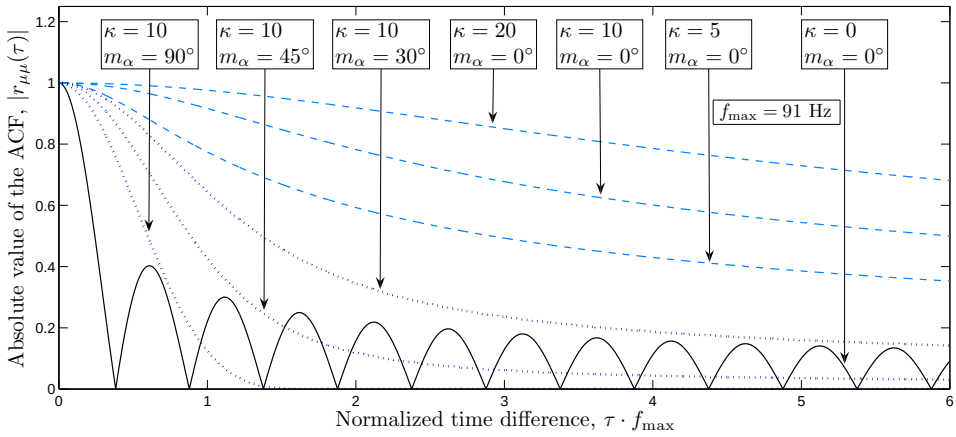

Figure 2.4: ACF of the channel's diffuse component, $r_{\boldsymbol{\mu\mu}}(\tau)$, by considering the von Mises PDF of the AOA with parameters m_α and κ.

component's DPSD is symmetrical only when $\kappa = 0$ and/or $m_\alpha = \pm 90°$, which happen to be the only values of m_α and κ for which the ACF of $\boldsymbol{\mu}(t)$ is real-valued. This is in line with the statements made in Section 2.3.1 about the properties of the DPSD of $\boldsymbol{\mu}(t)$. The corresponding average Doppler shift and Doppler spread of $\boldsymbol{\mu}(t)$ are presented in Table 2.1.

2.5.2 The Laplacian PDF of the AOA and the Associated ACF and DPSD of the Diffuse Component

Another relevant model for the AOA statistics of mobile fading channels is given by the (symmetrical) Laplacian distribution [Pede97, Spen00, Aspl06]. Such a PDF is used in the field of linear statistics to model data with long tails, and its applications range from astronomy to biological sciences [Kotz01]. The use

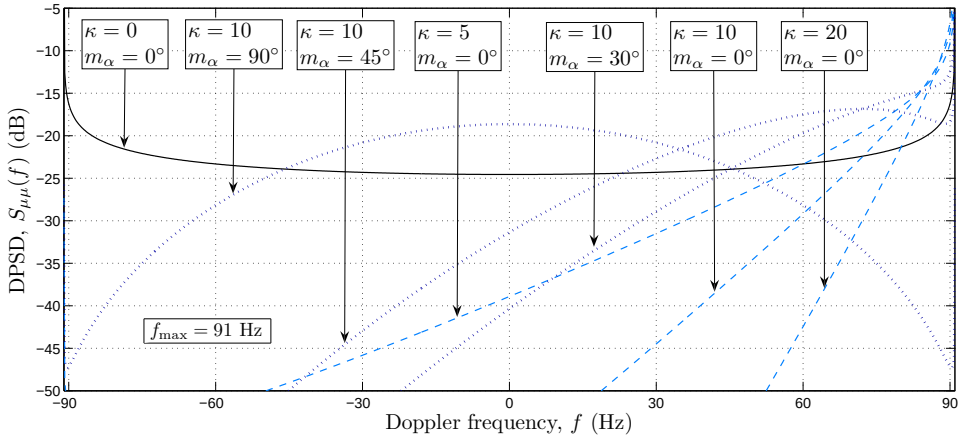

Figure 2.5: DPSD of the channel's diffuse component, $S_{\boldsymbol{\mu\mu}}(f)$, by considering the von Mises PDF of the AOA with parameters m_α and κ.

Table 2.1: Average Doppler shift $A^{\mathrm{VM}}_{\boldsymbol{\mu\mu}}$ and Doppler spread $D^{\mathrm{VM}}_{\boldsymbol{\mu\mu}}$ of the channel's diffuse component by considering the von Mises PDF of the AOA ($f_{\max} = 91$ Hz).

Parameters (m_α, κ):	$(0°, 0)$	$(0°, 5)$	$(0°, 20)$	$(0°, 10)$	$(30°, 10)$	$(90°, 10)$
$A^{\mathrm{VM}}_{\boldsymbol{\mu\mu}}$ (Hz):	0	81.297	88.695	86.322	74.757	0
$D^{\mathrm{VM}}_{\boldsymbol{\mu\mu}}$ (Hz):	64.346	13.857	3.2606	6.6239	15.142	28.027

of this distribution to characterize the AOA statistics of fading channels was first proposed in [Pede97]. There, the authors demonstrated the goodness of fit of such a distribution by direct comparison against measured data collected in outdoor environments. The validity of the Laplacian model has also been tested and corroborated by other researchers [Spen00].

The Laplacian PDF of the AOA has the form [Pede97, Spen00]

$$p^{\mathrm{LA}}_{\boldsymbol{\alpha}}(\alpha) \;=\; \frac{1}{c_s}\exp\left\{-\frac{|\alpha|\sqrt{2}}{\sigma_s}\right\}, \quad \alpha \in [-\pi, \pi) \tag{2.51}$$

where the parameter $\sigma_s > 0$ controls the angular spread, and

$$c_s = \sigma_s\sqrt{2}\left\{1 - \exp\left(-\tfrac{\sqrt{2}\pi}{\sigma_s}\right)\right\} \tag{2.52}$$

is a normalization quantity that guarantees $\int_{-\infty}^{\infty} p^{\mathrm{LA}}_{\boldsymbol{\alpha}}(\alpha)d\alpha = 1$. This PDF is depicted in Fig. 2.6 by considering $\sigma_s \in \{0.3, 0.5, 1, 5\}$. These values are representative of scattering propagation conditions that vary from moderated ($\sigma_s = 5$) to severe non-isotropic scattering ($\sigma_s = 0.3$).

The PDF defined in (2.51) is itself an even function (this is clear, since $p^{\mathrm{LA}}_{\boldsymbol{\alpha}}(-\alpha) = p^{\mathrm{LA}}_{\boldsymbol{\alpha}}(\alpha)$). Thus, one can show, by substituting $p^{\mathrm{LA}}_{\boldsymbol{\alpha}}(\alpha)$ from (2.51)

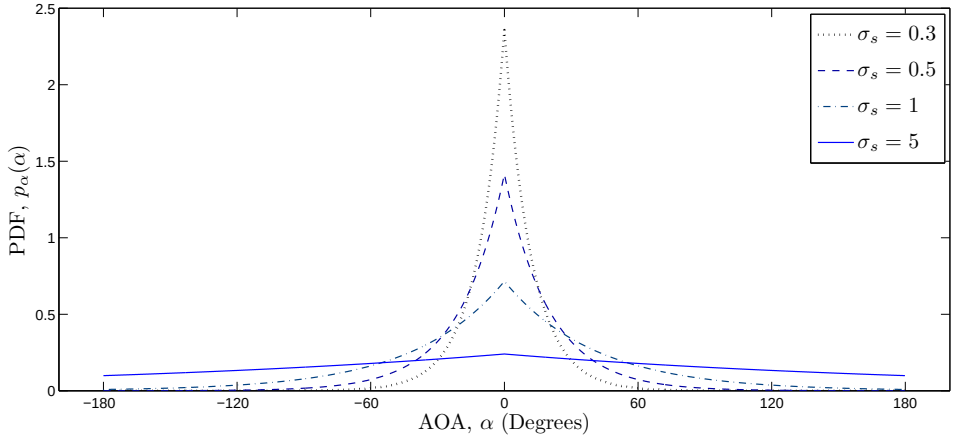

Figure 2.6: The Laplacian PDF of the AOA.

into (2.15), that

$$S_{\boldsymbol{\mu\mu}}^{\mathrm{LA}}(f) \;=\; \mathrm{rect}(f) \cdot \frac{2\sigma_{\boldsymbol{\mu}}^2 \exp\left\{-\sqrt{2}\arccos\left(f/f_{\max}\right)/\sigma_s\right\}}{c_s f_{\max}\sqrt{1-(f/f_{\max})^2}}. \tag{2.53}$$

In contrast to the case of the von Mises PDF, the ACF of $\boldsymbol{\mu}(t)$ cannot be evaluated analytically when the AOAs of the channel's multipath components follow the Laplacian distribution. Instead, one has to use numerical methods to solve

$$r_{\boldsymbol{\mu\mu}}^{\mathrm{LA}}(\tau) \;=\; \int_{-f_{\max}}^{f_{\max}} S_{\boldsymbol{\mu\mu}}^{\mathrm{LA}}(f)\exp\{j2\pi f\tau\}df. \tag{2.54}$$

Except by the additional work, the numerical evaluation of (2.54) does not pose any problems, since modern computers and programming languages—such as MATLAB®—can accomplish the task easily.

Regarding the average Doppler shift $A_{\boldsymbol{\mu\mu}}^{\mathrm{LA}}$ and Doppler spread $D_{\boldsymbol{\mu\mu}}^{\mathrm{LA}}$ of $\boldsymbol{\mu}(t)$, we find by following (2.18) and (2.19) that

$$A_{\boldsymbol{\mu\mu}}^{\mathrm{LA}} \;=\; \frac{f_{\max}\sqrt{8}\sigma_s}{c_s(2+\sigma_s^2)}\left\{1+e^{-\pi\sqrt{2}/\sigma_s}\right\} \tag{2.55}$$

$$D_{\boldsymbol{\mu\mu}}^{\mathrm{LA}} \;=\; \left\{\frac{f_{\max}^2}{2}\left[1+\frac{\sigma_s\sqrt{2}}{c_s(1+2\sigma_s^2)}(1-e^{-\pi\sqrt{2}/\sigma_s})\right]-(A_{\boldsymbol{\mu\mu}}^{\mathrm{LA}})^2\right\}^{-1/2}. \tag{2.56}$$

Figures 2.7 and 2.8 show graphs of $|r_{\boldsymbol{\mu\mu}}^{\mathrm{LA}}(\tau)|$ and $S_{\boldsymbol{\mu\mu}}^{\mathrm{LA}}(f)$ obtained for the same values of σ_s as considered for the curves of $p_{\boldsymbol{\alpha}}^{\mathrm{LA}}(\alpha)$ depicted in Fig. 2.6. The results obtained for the corresponding average Doppler shift and Doppler spread are presented in Table 2.2.

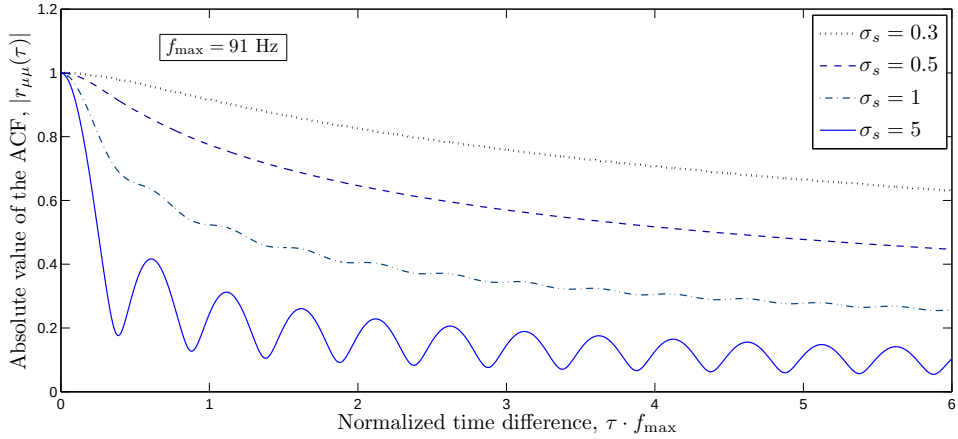

Figure 2.7: ACF of the channel's diffuse component, $r_{\boldsymbol{\mu\mu}}(\tau)$, by considering the Laplacian PDF of the AOA with parameter σ_s.

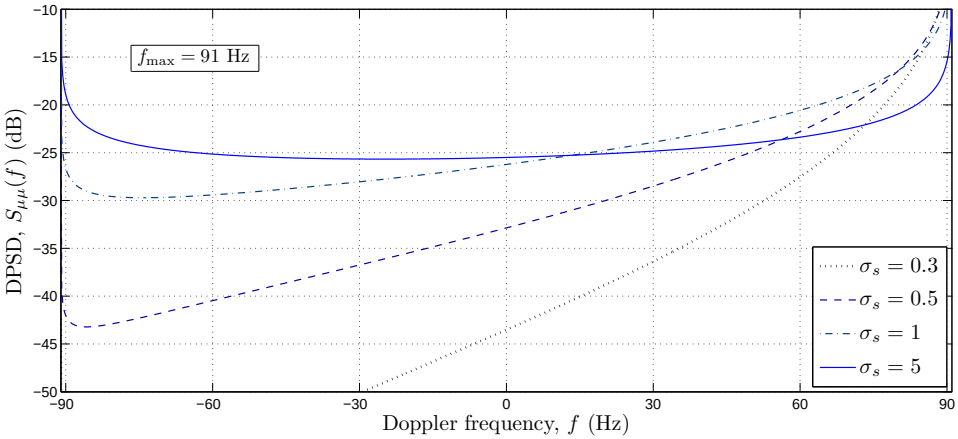

Figure 2.8: DPSD of the channel's diffuse component, $S_{\boldsymbol{\mu\mu}}(f)$, by considering the Laplacian PDF of the AOA with parameter σ_s.

2.6 Chapter Summary and Conclusions

In this chapter, we reviewed the characteristics and statistical properties of the narrowband Rician fading channel model that we will use as reference model to design the parameter computation methods proposed in this dissertation.

It was shown in Section 2.3 that the ACF of the complex Gaussian process $\boldsymbol{\nu}(t)$ characterizing our reference model does not depend on the choice of the time origin. In spite of this noteworthy characteristic, $\boldsymbol{\nu}(t)$ is in general a non-stationary process, since its mean value is a function of time. However, $\boldsymbol{\nu}(t)$ proves to be a SSS process under two conditions: (i) Either the LOS component is absent; (ii) or it is not Doppler shifted. The statistics of $\boldsymbol{\nu}(t)$ have been revised thoroughly under NLOS conditions.

Table 2.2: Average Doppler shift $A_{\boldsymbol{\mu\mu}}^{\mathrm{LA}}$ and Doppler spread $D_{\boldsymbol{\mu\mu}}^{\mathrm{LA}}$ of the channel's diffuse component by considering the Laplacian PDF of the AOA ($f_{\max} = 91$ Hz).

Parameter, σ_s:	0.3	0.5	1	5
$A_{\boldsymbol{\mu\mu}}^{\mathrm{LA}}$ (Hz):	87.0814	80.9113	62.1108	16.1574
$D_{\boldsymbol{\mu\mu}}^{\mathrm{LA}}$ (Hz):	8.138	18.8202	40.7789	62.9335

The relevant statistics of the signal fading, such as the distributions of the channel's envelope and phase, ADF, and LCR were studied in Section 2.4. In that section, it was shown that the envelope $\boldsymbol{\xi}(t)$ of $\boldsymbol{\nu}(t)$ is first-order stationary and Rician distributed, while its phase $\boldsymbol{\psi}(t)$ has a PDF that depends on time. In addition, we investigated the ACF of the squared envelope $\boldsymbol{\xi}^2(t)$ of $\boldsymbol{\nu}(t)$. In accordance to the results presented in Section 2.4.3, the channel's squared envelope is a WSS process. Finally, we described in Section 2.5 the distributions of the AOA that we will consider throughout this dissertation to assess the performance of the proposed channel simulation models.

Chapter 3

Narrowband SOC-Based Simulation Models

3.1 Introduction

We can observe from (2.3) that a hardware/software realization of the mobile fading channel described by $\boldsymbol{\nu}(t)$ is not possible, since it requires the implementation of a sum of an infinite number of cisoids. Fortunately, most of the statistical properties of $\boldsymbol{\nu}(t)$ relevant for system performance analysis—such as its correlation properties, spectral characteristics, and the first-order distributions of its envelope and phase—can satisfactorily be approximated via a simulation model based on a finite SOC. In this chapter, we present a narrowband stochastic SOC-based simulation model suitable for performing the above mentioned task. Such a stochastic SOC model constitutes in fact the core structure of the channel simulators proposed in this dissertation. In addition to analyzing the simulation model's correlation and spectral properties, the present chapter reviews the first-order PDFs of the envelope and phase processes. What is more, the correlation properties of the resulting squared envelope process are investigated here for the first time. The ergodicity of the simulation model (in terms of the mean value, power, and ACF) is also a topic addressed for the first time in this chapter.

We observe that some of the statistical properties of the stochastic SOC model herein described have previously been analyzed in [Paet07] and [Hogs08]. Specifically, the simulation model's ACF, average Doppler shift, and Doppler spread are studied in [Paet07] for the NLOS case (simulation of Rayleigh fading channels). The envelope and phase distributions of the simulator are investigated in the same paper by considering a LOS scenario with a time-invariant specular component (simulation of Rician fading channels), whereas the first-order stationarity of the envelope process is studied in [Hogs08] upon the NLOS assumption. The analysis presented throughout this chapter is broader in scope than the one made

in the above quoted papers in the sense that we consider a LOS scenario with a time-variant specular component.

3.2 SOC-Based Channel Simulators: General Structure and Classes

Figure 3.1 shows the general structure of an SOC-based simulation model for the mobile Rician fading channel model described by the complex Gaussian process $\boldsymbol{\nu}(t)$. Such a structure consists of two parts. One part is intended for the simulation of the channel's diffuse component $\boldsymbol{\mu}(t)$, whereas the other part is aimed at reproducing the specular component $m_\rho(t)$. The simulation of $\boldsymbol{\mu}(t)$ is carried out upon an SOC model comprising a finite number $N \in \mathbb{Z}^+$ ($N < \infty$) of homogeneous cisoids[1], the parameters of which—gains, frequencies, and phases—are defined either as random variables or deterministic quantities. The symbol $\mathbb{Z}^+$ stands for the set of positive integers. Such an SOC model can mathematically be described by a complex random process $\hat{\boldsymbol{\mu}}(t)$ if any of the cisoids' parameters is random, otherwise, it is to be represented by a complex deterministic (pseudo-random) process $\tilde{\mu}(t)$. The channel's specular part $m_\rho(t)$ is reproduced by means of a properly parameterized deterministic cisoid. It goes without saying that the superposition of $\hat{\boldsymbol{\mu}}(t)$ and $m_\rho(t)$ (or $\tilde{\mu}(t)$ and $m_\rho(t)$) is expected to result into a complex quasi-Gaussian random process $\hat{\boldsymbol{\nu}}(t)$ (or deterministic process $\tilde{\nu}(t)$) whose statistical properties resemble those of $\boldsymbol{\nu}(t)$.

Based on the nature (random or deterministic) of the N homogeneous cisoids underlying the process $\hat{\boldsymbol{\mu}}(t)$, we can identify eight fundamental classes of SOC-based simulation models for $\boldsymbol{\nu}(t)$: Seven classes of stochastic models, and one class of deterministic models—with the class of deterministic models being a superset of the other seven classes. The eight classes, which were originally defined in [Hogs08], are listed in Table 3.1. For the simulation of $\boldsymbol{\nu}(t)$, we will consider a stochastic simulation model of Class II, meaning that the homogeneous SOC model $\hat{\boldsymbol{\mu}}(t)$ comprises cisoids with random phases, constant gains, and constant Doppler frequencies. Our motivation to choose an SOC model of such a class is driven by the fact that only the Class II simulators are autocorrelation ergodic[2] (given the restriction $N < \infty$). This important property allows for the design of simulation models able to efficiently approximate the reference model's ACF without the need of averaging over multiple simulation runs. Besides, it will be shown throughout this chapter that the resulting random process $\hat{\boldsymbol{\nu}}(t)$ possesses stationarity characteristics similar as those of the reference model.

[1] By homogeneous cisoids we mean a group of cisoids characterized by the same type of parameters.

[2] We point out that the concept of ergodicity does not apply on the Class I simulators, since the nature of such a class of models is deterministic.

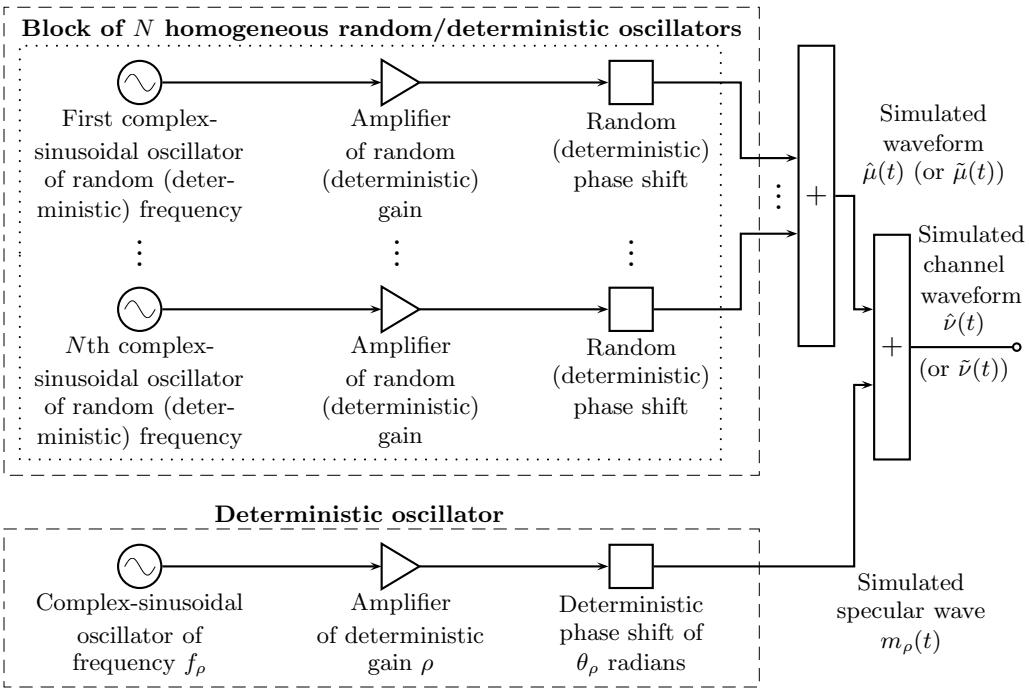

Figure 3.1: Block diagram of an SOC-based simulation model for Rician fading channels.

Table 3.1: Classification of SOC-based simulation models for Rician fading channels according to the nature of the cisoids' parameters.

Parameters[†]	Gains	Frequencies	Phases
Class I	Deterministic	Deterministic	Deterministic
Class II	Deterministic	Deterministic	Random
Class III	Deterministic	Random	Deterministic
Class IV	Deterministic	Random	Random
Class V	Random	Deterministic	Deterministic
Class VI	Random	Deterministic	Random
Class VII	Random	Random	Deterministic
Class VIII	Random	Random	Random

[†]This attribute refers to the parameters of the SOC model described by $\hat{\boldsymbol{\mu}}(t)$ (or $\tilde{\mu}(t)$).

3.3 The Stochastic SOC-Based Simulation Model

3.3.1 Structure and Considerations

The stochastic narrowband SOC-based simulation model of Class II considered in this dissertation is characterized by a random process of the form

$$\hat{\boldsymbol{\nu}}(t) = \underbrace{\sum_{n=1}^{N} \hat{c}_n \exp\left\{j\left(2\pi \hat{f}_n t + \hat{\boldsymbol{\theta}}_n\right)\right\}}_{\hat{\boldsymbol{\mu}}(t)} + \underbrace{\rho \exp\{j(2\pi f_\rho t + \theta_\rho)\}}_{m_\rho(t)}. \tag{3.1}$$

For the underlying homogeneous random SOC model

$$\hat{\boldsymbol{\mu}}(t) \;=\; \sum_{n=1}^{N} \hat{c}_n \exp\left\{j\left(2\pi \hat{f}_n t + \hat{\boldsymbol{\theta}}_n\right)\right\} \tag{3.2}$$

we assume the phases $\hat{\boldsymbol{\theta}}_n$ as being mutually independent random variables, each having a uniform distribution over $[-\pi, \pi)$. In addition, we impose the condition $\sum_{n=1}^{N} \hat{c}_n^2 = \sigma_{\boldsymbol{\mu}}^2$ on the set of gains $\{\hat{c}_n\}_{n=1}^{N}$ and define the deterministic Doppler frequencies $\hat{f}_n$ as

$$\hat{f}_n \;\triangleq\; f_{\max} \cos(\hat{\alpha}_n), \qquad \forall n = 1, \ldots, N \tag{3.3}$$

where $\hat{\alpha}_n \in [-\pi, \pi)$.

3.3.2 Mean Value, Variance, and Average Power

Under the aforementioned considerations, $\hat{\boldsymbol{\mu}}(t)$ proves to be a zero-mean stochastic process with constant variance $\mathrm{Var}\{\hat{\boldsymbol{\mu}}(t)\} = \sigma_{\boldsymbol{\mu}}^2$. In turn, the composite process $\hat{\boldsymbol{\nu}}(t) = \hat{\boldsymbol{\mu}}(t) + m_\rho(t)$ is found to have a time-variant mean value $m_{\hat{\boldsymbol{\nu}}}(t) \triangleq E\{\hat{\boldsymbol{\nu}}(t)\} = m_\rho(t)$ and a constant variance $\mathrm{Var}\{\hat{\boldsymbol{\nu}}(t)\} = \sigma_{\boldsymbol{\mu}}^2$. Furthermore, the average power $\mathcal{P}_{\hat{\boldsymbol{\nu}}}(t) \triangleq E\{|\hat{\boldsymbol{\nu}}(t)|^2\}$ of $\hat{\boldsymbol{\nu}}(t)$ turns out to be time-invariant and equal to $\sigma_{\boldsymbol{\nu}}^2 = \sigma_{\boldsymbol{\mu}}^2 + \rho^2$, i.e., $\mathcal{P}_{\hat{\boldsymbol{\nu}}}(t) = \mathcal{P}_{\hat{\boldsymbol{\nu}}} = \sigma_{\boldsymbol{\nu}}^2$. A comparison of these results with the ones presented in Section 2.2 for $\boldsymbol{\nu}(t)$ reveals that the simulation model defined in (3.1) is characterized by exactly the same mean value, variance, and average power as the reference model.

3.3.3 Correlation Properties and Spectral Characteristics

3.3.3.1 ACFs

Regarding the ACF $r_{\hat{\boldsymbol{\mu}}\hat{\boldsymbol{\mu}}}(t_1, t_2) \triangleq E\{\hat{\boldsymbol{\mu}}^*(t_1)\hat{\boldsymbol{\mu}}(t_2)\}$ of the zero-mean random process $\hat{\boldsymbol{\mu}}(t)$, one can show without difficulty that [Paet07]

$$r_{\hat{\boldsymbol{\mu}}\hat{\boldsymbol{\mu}}}(t_1, t_2) \;=\; r_{\hat{\boldsymbol{\mu}}\hat{\boldsymbol{\mu}}}(\tau) \tag{3.4}$$

$$\;=\; \sum_{n=1}^{N} \hat{c}_n^2 \exp\left\{j 2\pi \hat{f}_n \tau\right\}. \tag{3.5}$$

This result shows that the ACF of $\hat{\boldsymbol{\mu}}(t)$ depends only on the time difference $\tau = t_2 - t_1$. It can therefore be concluded that $\hat{\boldsymbol{\mu}}(t)$ is a WSS process, since its mean value is constant and its ACF is not influenced by the choice of the time origin. Other relevant characteristics of $r_{\hat{\boldsymbol{\mu}}\hat{\boldsymbol{\mu}}}(\tau)$ can readily be noticed by expressing such a function in terms of the ACFs and CCFs of the IQ components

$\hat{\boldsymbol{\mu}}_I(t) \triangleq \mathrm{Re}\{\hat{\boldsymbol{\mu}}(t)\}$ and $\hat{\boldsymbol{\mu}}_Q(t) \triangleq \mathrm{Im}\{\hat{\boldsymbol{\mu}}(t)\}$ of $\hat{\boldsymbol{\mu}}(t)$ as follows

$$\begin{aligned} r_{\hat{\boldsymbol{\mu}}\hat{\boldsymbol{\mu}}}(\tau) &= \big[r_{\hat{\boldsymbol{\mu}}_I\hat{\boldsymbol{\mu}}_I}(\tau) + r_{\hat{\boldsymbol{\mu}}_Q\hat{\boldsymbol{\mu}}_Q}(\tau)\big] + j\big[r_{\hat{\boldsymbol{\mu}}_I\hat{\boldsymbol{\mu}}_Q}(\tau) - r_{\hat{\boldsymbol{\mu}}_Q\hat{\boldsymbol{\mu}}_I}(\tau)\big] \\ &= 2\big[r_{\hat{\boldsymbol{\mu}}_I\hat{\boldsymbol{\mu}}_I}(\tau) + jr_{\hat{\boldsymbol{\mu}}_I\hat{\boldsymbol{\mu}}_Q}(\tau)\big] \end{aligned} \tag{3.6}$$

where

$$r_{\hat{\boldsymbol{\mu}}_I\hat{\boldsymbol{\mu}}_I}(\tau) = r_{\hat{\boldsymbol{\mu}}_Q\hat{\boldsymbol{\mu}}_Q}(\tau) = \sum_{n=1}^{N} \frac{\hat{c}_n^2}{2} \cos\big(2\pi\hat{f}_n\tau\big) \tag{3.7a}$$

$$r_{\hat{\boldsymbol{\mu}}_I\hat{\boldsymbol{\mu}}_Q}(\tau) = -r_{\hat{\boldsymbol{\mu}}_Q\hat{\boldsymbol{\mu}}_I}(\tau) = \sum_{n=1}^{N} \frac{\hat{c}_n^2}{2} \sin\big(2\pi\hat{f}_n\tau\big). \tag{3.7b}$$

One may observe from (3.6) and (3.7) that $r_{\hat{\boldsymbol{\mu}}\hat{\boldsymbol{\mu}}}(\tau)$ is a complex valued and hermitian symmetric function if $\hat{\boldsymbol{\mu}}_I(t)$ and $\hat{\boldsymbol{\mu}}_Q(t)$ are cross-correlated. On the contrary, if the IQ components of $\hat{\boldsymbol{\mu}}(t)$ are uncorrelated, then $r_{\hat{\boldsymbol{\mu}}\hat{\boldsymbol{\mu}}}(\tau)$ will be even and real valued. We recall that the uncorrelation between the processes $\hat{\boldsymbol{\mu}}_I(t)$ and $\hat{\boldsymbol{\mu}}_Q(t)$ is a requisite for the simulation of fading channels characterized by symmetrical DPSDs [Paet98]. Taking account of the expression presented in (3.7b) for $r_{\hat{\boldsymbol{\mu}}_I\hat{\boldsymbol{\mu}}_Q}(\tau)$ and $r_{\hat{\boldsymbol{\mu}}_Q\hat{\boldsymbol{\mu}}_I}(\tau)$, we can deduce that a sufficient condition for guaranteeing the uncorrelation between $\hat{\boldsymbol{\mu}}_I(t)$ and $\hat{\boldsymbol{\mu}}_Q(t)$ is the following:

Condition 3.1 *The number of cisoids N is even, i.e., $N = 2M$, where $M \in \mathbb{Z}^+$, and for each pair of parameters $(\hat{c}_n, \hat{f}_n)$, $n = 1, \ldots, N$, there exists one and only one pair $(\hat{c}_m, \hat{f}_m)$, $n \neq m$, such that $\hat{c}_n = \hat{c}_m$ and $\hat{f}_n = -\hat{f}_m$.*

Notice that if the above mentioned requirements are met, then

$$r_{\hat{\boldsymbol{\mu}}\hat{\boldsymbol{\mu}}}(\tau) = 2\sum_{n=1}^{N/2} \hat{c}_n^2 \cos(2\pi\hat{f}_n\tau). \tag{3.8}$$

It is worth mentioning that the Condition 3.1 becomes a necessary condition for the uncorrelation of the IQ components of $\hat{\boldsymbol{\mu}}(t)$ if the Doppler frequencies are chosen in such a way that $\hat{f}_n \neq 0\ \forall n$ and $\hat{f}_n \neq \hat{f}_m$, $n \neq m$. These two latter considerations are relevant indeed, as they are fundamental for the design of ergodic channel simulators [see Sec. 3.5].

With respect to the ACF $r_{\hat{\boldsymbol{\nu}}\hat{\boldsymbol{\nu}}}(t_1, t_2) \triangleq E\{\hat{\boldsymbol{\nu}}^*(t_1)\hat{\boldsymbol{\nu}}(t_2)\}$ of the simulation model, it is straightforward to show that

$$r_{\hat{\boldsymbol{\nu}}\hat{\boldsymbol{\nu}}}(t_1, t_2) = r_{\hat{\boldsymbol{\nu}}\hat{\boldsymbol{\nu}}}(\tau) \tag{3.9}$$

$$= r_{\hat{\boldsymbol{\mu}}\hat{\boldsymbol{\mu}}}(\tau) + \rho^2 \exp\{j2\pi f_\rho\tau\} \tag{3.10}$$

$$= \sum_{n=1}^{N} \hat{c}_n^2 \exp\big\{j2\pi\hat{f}_n\tau\big\} + \rho^2 \exp\{j2\pi f_\rho\tau\}. \tag{3.11}$$

The equations above indicate that the ACF of $\hat{\boldsymbol{\nu}}(t)$ possesses the noteworthy property of being time-shift insensitive. Nonetheless, in contrast to the zero-mean process $\hat{\boldsymbol{\mu}}(t)$, $\hat{\boldsymbol{\nu}}(t)$ cannot be claimed to be a WSS process, because its mean value is in general time-variant. However, this characteristic should not be considered as a drawback, since the simulation model and the reference model are similar in that respect. In fact, the wide-sense stationarity property of both processes $\hat{\boldsymbol{\nu}}(t)$ and $\boldsymbol{\nu}(t)$ holds under the same conditions: The specular wave $m_\rho(t)$ is absent or not Doppler shifted [cf. Sec. 2.3.1].

3.3.3.2 DPSDs

Concerning the DPSD $S_{\hat{\boldsymbol{\nu}}\hat{\boldsymbol{\nu}}}(f)$ of the simulation model, we obtain on the basis of [Mill04, pp. 373–375] the solution

$$\begin{aligned} S_{\hat{\boldsymbol{\nu}}\hat{\boldsymbol{\nu}}}(f) &= \int_{-\infty}^{\infty} r_{\hat{\boldsymbol{\nu}}\hat{\boldsymbol{\nu}}}(\tau)\exp\{j2\pi f\tau\}d\tau \\ &= \sum_{n=1}^{N} \hat{c}_n^2\delta\big(f-\hat{f}_n\big) + \rho^2\delta(f-f_\rho). \end{aligned} \tag{3.12}$$

The DPSD $S_{\hat{\boldsymbol{\mu}}\hat{\boldsymbol{\mu}}}(f)$ of $\hat{\boldsymbol{\mu}}(t)$ follows from $S_{\hat{\boldsymbol{\nu}}\hat{\boldsymbol{\nu}}}(f)$ by taking $\rho = 0$. Consequently, we can write

$$S_{\hat{\boldsymbol{\mu}}\hat{\boldsymbol{\mu}}}(f) = \sum_{n=1}^{N} \hat{c}_n^2\delta\big(f-\hat{f}_n\big). \tag{3.13}$$

This latter result can be confirmed by computing the Fourier transform of the ACF defined in (3.5) [Paet07]. Interestingly, if Condition 3.1 is fulfilled, meaning that $r_{\hat{\boldsymbol{\mu}}_I\hat{\boldsymbol{\mu}}_Q}(\tau) = r_{\hat{\boldsymbol{\mu}}_Q\hat{\boldsymbol{\mu}}_I}(\tau) = 0$, then

$$S_{\hat{\boldsymbol{\mu}}\hat{\boldsymbol{\mu}}}(f) = \sum_{n=1}^{N/2} \hat{c}_n^2\big[\delta\big(f-\hat{f}_n\big) + \delta\big(f+\hat{f}_n\big)\big]. \tag{3.14}$$

Thus, the DPSD of $\hat{\boldsymbol{\mu}}(t)$ happens to be an even (symmetrical) function upon fulfillment of Condition 3.1, as was to be expected.

3.3.3.3 Average Doppler Shift and Doppler Spread

From (3.12), and taking into account that $\sum_{n=1}^{N}\hat{c}_n^2 = \sigma_{\boldsymbol{\mu}}^2$, one can verify that the average Doppler shift $A_{\hat{\boldsymbol{\nu}}\hat{\boldsymbol{\nu}}}$ and Doppler spread $D_{\hat{\boldsymbol{\nu}}\hat{\boldsymbol{\nu}}}$ of $\hat{\boldsymbol{\nu}}(t)$ are given by:

$$A_{\hat{\boldsymbol{\nu}}\hat{\boldsymbol{\nu}}} \triangleq \frac{\int_{-\infty}^{\infty} f S_{\hat{\boldsymbol{\nu}}\hat{\boldsymbol{\nu}}}(f)df}{\int_{-\infty}^{\infty} S_{\hat{\boldsymbol{\nu}}\hat{\boldsymbol{\nu}}}(f)df}$$

$$= \frac{1}{\sigma_{\boldsymbol{\nu}}^2}\left[\rho^2 f_\rho + \sum_{n=1}^{N} \hat{c}_n^2 \hat{f}_n\right] \tag{3.15}$$

$$D_{\hat{\boldsymbol{\nu}}\hat{\boldsymbol{\nu}}} \triangleq \sqrt{\frac{\int_{-\infty}^{\infty} S_{\hat{\boldsymbol{\nu}}\hat{\boldsymbol{\nu}}}(f)\left[f - A_{\hat{\boldsymbol{\nu}}\hat{\boldsymbol{\nu}}}\right]^2 df}{\int_{-\infty}^{\infty} S_{\hat{\boldsymbol{\nu}}\hat{\boldsymbol{\nu}}}(f) df}}$$

$$= \sqrt{\frac{1}{\sigma_{\boldsymbol{\nu}}^2}\left[\rho^2 f_\rho^2 + \sum_{n=1}^{N} \hat{c}_n^2 \hat{f}_n^2\right] - \left(A_{\hat{\boldsymbol{\nu}}\hat{\boldsymbol{\nu}}}\right)^2}. \tag{3.16}$$

What is more, one can deduce by taking $\rho = 0$ in (3.15) and (3.16) that the average Doppler shift $A_{\hat{\boldsymbol{\mu}}\hat{\boldsymbol{\mu}}}$ and Doppler spread $D_{\hat{\boldsymbol{\mu}}\hat{\boldsymbol{\mu}}}$ of $\hat{\boldsymbol{\mu}}(t)$ are equal to:

$$A_{\hat{\boldsymbol{\mu}}\hat{\boldsymbol{\mu}}} = A_{\hat{\boldsymbol{\nu}}\hat{\boldsymbol{\nu}}}\Big|_{\rho=0}$$

$$= \frac{1}{\sigma_{\boldsymbol{\mu}}^2}\sum_{n=1}^{N} \hat{c}_n^2 \hat{f}_n \tag{3.17}$$

$$D_{\hat{\boldsymbol{\mu}}\hat{\boldsymbol{\mu}}} = D_{\hat{\boldsymbol{\nu}}\hat{\boldsymbol{\nu}}}\Big|_{\rho=0}$$

$$= \sqrt{\frac{1}{\sigma_{\boldsymbol{\mu}}^2}\sum_{n=1}^{N} \hat{c}_n^2 \hat{f}_n^2 - \left(A_{\hat{\boldsymbol{\mu}}\hat{\boldsymbol{\mu}}}\right)^2} \tag{3.18}$$

which are the results presented in [Paet07]. We observe from (3.17) that the average Doppler shift $A_{\hat{\boldsymbol{\mu}}\hat{\boldsymbol{\mu}}}$ of $\hat{\boldsymbol{\mu}}(t)$ is equal to zero if the Condition 3.1 is met. This result is in line with the statement made in Section 2.3.3 regarding the average Doppler shift of symmetrical DPSDs.

It is worth noticing that the simulation model's ACF, DPSD, average Doppler shift, and Doppler spread are fully specified by the sets of gains $\{\hat{c}_n, \rho\}$ and Doppler frequencies $\{\hat{f}_n, f_\rho\}$.

3.3.4 PDFs of the Stochastic SOC Model's Envelope and Phase

The first-order distributions of the envelope $\hat{\boldsymbol{\xi}}(t) \triangleq |\hat{\boldsymbol{\nu}}(t)|$ and phase $\hat{\boldsymbol{\psi}}(t) \triangleq \arg\{\hat{\boldsymbol{\nu}}(t)\}$ of $\hat{\boldsymbol{\nu}}(t)$ have recently been investigated in [Paet07]. There, analytical expressions were derived for such statistical functions by assuming the specular wave $m_\rho(t)$ to be not Doppler shifted. In this section, we provide generalized expressions of those formulas covering the more realistic case where $m_\rho(t)$ is Doppler shifted. The generalization of the results presented in [Paet07] is straightforward, and can systematically be done by following the procedure outlined in [Paet07, Sec. IV-*E*]. We will therefore omit details about the derivations and present only the obtained generalized expressions. The correctness of our results will be demonstrated by simulations in Chapter 4.

3.3.4.1 First-Order PDF of the Envelope

By proceeding as in [Paet07, Sec. IV-*E*], one can verify that the first-order PDF $p_{\hat{\boldsymbol{\xi}}}(z;t)$ of the envelope $\hat{\boldsymbol{\xi}}(t)$ of $\hat{\boldsymbol{\nu}}(t)$ is equal to

$$p_{\hat{\boldsymbol{\xi}}}(z;t) = p_{\hat{\boldsymbol{\xi}}}(z) \tag{3.19}$$

$$= z(2\pi)^2 \int_0^\infty \left[\prod_{n=1}^{N} J_0(2\pi|\hat{c}_n|x)\right] J_0(2\pi zx) J_0(2\pi|\rho|x)x\, dx, \quad z \geq 0. \tag{3.20}$$

It can be concluded from the previous equations that $\hat{\boldsymbol{\xi}}(t)$ is a first-order stationary process, because its PDF does not change over time. Interestingly, the expression presented in (3.20) proves to be the same as the one obtained in [Paet07, Eq. (26)]. This means that the time-variant behavior of the specular wave has no influence on the first-order distribution of $\hat{\boldsymbol{\xi}}(t)$. We notice that $p_{\hat{\boldsymbol{\xi}}}(z)$ is fully specified by the set of gains $\{\hat{c}_n, \rho\}$. For the special case $\rho = 0$, the PDF given in (3.20) reduces to the first-order distribution $p_{\hat{\boldsymbol{\zeta}}}(z)$ of the envelope $\hat{\boldsymbol{\zeta}}(t) \triangleq |\hat{\boldsymbol{\mu}}(t)|$ of $\hat{\boldsymbol{\mu}}(t)$. Thus, we can explicitly write the PDF of $\hat{\boldsymbol{\zeta}}(t)$ as follows

$$p_{\hat{\boldsymbol{\zeta}}}(z) = z(2\pi)^2 \int_0^\infty \left[\prod_{n=1}^{N} J_0(2\pi|\hat{c}_n|x)\right] J_0(2\pi zx)x\, dx, \quad z \geq 0. \tag{3.21}$$

Investigations in [Paet07] indicate that $p_{\hat{\boldsymbol{\xi}}}(z)$ is in good agreement with the Rice distribution for values of N as small as ten if $\hat{c}_n = \sigma_{\boldsymbol{\mu}}/\sqrt{N}\ \forall n$. In fact, it is shown in the above quoted paper that if $\hat{c}_n = \sigma_{\boldsymbol{\mu}}/\sqrt{N}$, then $p_{\hat{\boldsymbol{\xi}}}(z)$ converges to the Rice density in the limit $N \to \infty$. Figure 3.2 provides an exemplary demonstration of the veracity of these statements. In this figure, we present a comparison between the PDF defined in (3.20) and the Rice PDF introduced in (2.22) by considering $\hat{c}_n = \sigma_{\boldsymbol{\mu}}/\sqrt{N}\ \forall n$, $N \in \{10, 50\}$, $c_R \in \{0, 2, 4\}$, and $\sigma^2_{\boldsymbol{\nu}} = 1$. We remind that $c_R = \rho^2/\sigma^2_{\boldsymbol{\mu}}$ is the Rician factor.

3.3.4.2 First-Order PDF of the Phase

With respect to the first-order PDF $p_{\hat{\boldsymbol{\psi}}}(\theta;t)$ of the phase $\hat{\boldsymbol{\psi}}(t)$ of $\hat{\boldsymbol{\nu}}(t)$, it can be demonstrated that

$$p_{\hat{\boldsymbol{\psi}}}(\theta;t) = 2\pi \int_0^\infty \int_0^\infty \left[\prod_{n=1}^{N} J_0(2\pi|\hat{c}_n|x)\right] \times J_0\left(2\pi x\sqrt{z^2 + \rho^2 - 2z\rho\cos(\theta - 2\pi f_\rho t - \theta_\rho)}\right) xz\, dx\, dz \tag{3.22}$$

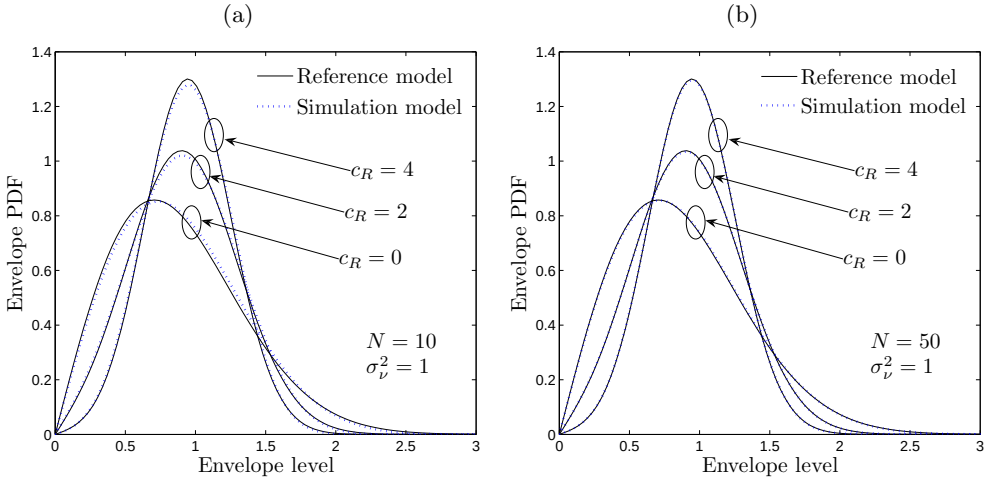

Figure 3.2: Comparison between the theoretical envelope PDF $p_{\hat{\boldsymbol{\xi}}}(z)$ of the stochastic SOC-based simulation model and the Rice PDF $p_{\boldsymbol{\xi}}(z)$ (reference model) by considering different values for both the Rician factor c_R and the number of cisoids N: (a) $N = 10$; (b) $N = 50$.

for $\theta \in [-\pi, \pi)$. The equation above shows that $\hat{\boldsymbol{\psi}}(t)$ is in general not first-order stationary, because its distribution $p_{\hat{\boldsymbol{\psi}}}(\theta; t)$ is not necessarily time-invariant. However, if $m_\rho(t)$ is not Doppler shifted, implying that $f_\rho = 0$, then

$$p_{\hat{\boldsymbol{\psi}}}(\theta; t) = p_{\hat{\boldsymbol{\psi}}}(\theta) \tag{3.23}$$

$$= 2\pi \int_0^\infty \int_0^\infty \left[\prod_{n=1}^{N} J_0(2\pi |\hat{c}_n| x) \right] \times J_0\left(2\pi x \sqrt{z^2 + \rho^2 - 2z\rho\cos(\theta - \theta_\rho)} \right) xz \, dx \, dz, \quad \theta \in [-\pi, \pi) \tag{3.24}$$

which is the result presented in [Paet07, Eq. (28)]. On other hand, if the specular wave is absent ($\rho = 0$), then $p_{\hat{\boldsymbol{\psi}}}(\theta; t)$ reduces to the first-order distribution $p_{\hat{\boldsymbol{\varphi}}}(\theta; t)$ of the phase $\hat{\boldsymbol{\varphi}}(t) \triangleq \arg\{\hat{\boldsymbol{\mu}}(t)\}$ of $\hat{\boldsymbol{\mu}}(t)$. It can be shown for the latter PDF that

$$p_{\hat{\boldsymbol{\varphi}}}(\theta; t) = p_{\hat{\boldsymbol{\varphi}}}(\theta) \tag{3.25}$$

$$= 2\pi \int_0^\infty \int_0^\infty \left[\prod_{n=1}^{N} J_0(2\pi |\hat{c}_n| x) \right] J_0(2\pi xz) xz \, dx dz \tag{3.26}$$

$$= \frac{1}{2\pi}, \qquad \theta \in [-\pi, \pi) \tag{3.27}$$

which implies that the first-order distribution of $\hat{\boldsymbol{\varphi}}(t)$ is time-invariant and uniform over $[-\pi, \pi)$. Interestingly, the PDF of $\hat{\boldsymbol{\varphi}}(t)$ is not influenced by any of the

parameters of $\hat{\boldsymbol{\mu}}(t)$ (not even by N). In view of (3.24) and (3.27), we can claim that the phase $\hat{\boldsymbol{\psi}}(t)$ of the simulation model is a first-order stationary process if either $f_\rho = 0$ or $\rho = 0$.

Figure 3.3 shows a comparison between the PDF given in (3.22) and the phase PDF of the reference model [see (2.26)]. The graphs presented in that figure correspond to the time instants $t = 0$ s and $t = 0.25$ s, and they were generated by choosing $\hat{c}_n = 1/\sqrt{N}\ \forall n$, $N \in \{10, 50\}$, $c_R \in \{0, 2, 4\}$, $f_\rho = 65$ Hz, and $\theta_\rho = 0°$. One may observe from Fig. 3.3 that the first-order distribution of the simulation model's phase, $p_{\hat{\boldsymbol{\psi}}}(\theta; t)$, is in excellent agreement with the phase PDF $p_{\boldsymbol{\psi}}(\theta; t)$ of reference model. Indeed, the graphs of $p_{\hat{\boldsymbol{\psi}}}(\theta; t)$ are quite close to the ones of $p_{\boldsymbol{\psi}}(\theta; t)$ even with as few as ten cisoids, as can be seen in Fig. 3.3(a).

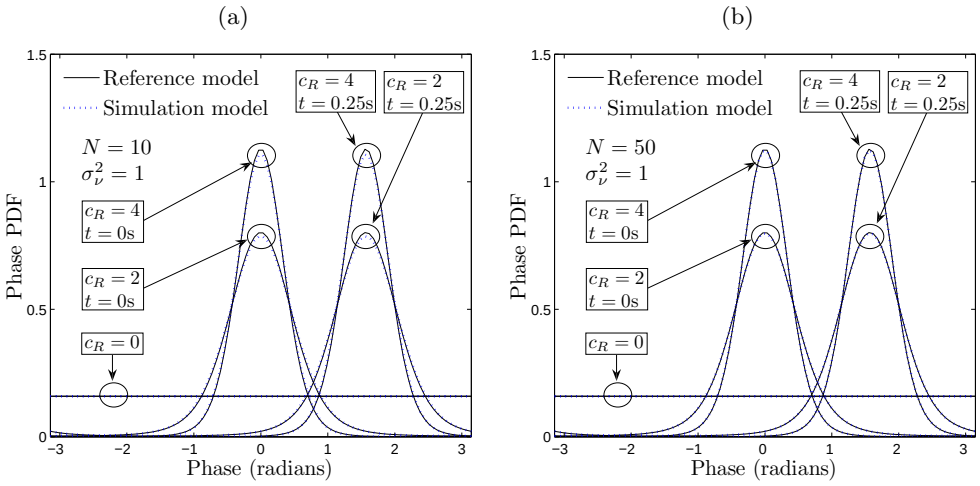

Figure 3.3: Comparison between the theoretical phase PDF $p_{\hat{\boldsymbol{\psi}}}(\theta; t)$ of the stochastic SOC-based simulation model and the phase PDF $p_{\boldsymbol{\psi}}(\theta; t)$ of reference model by considering different values for both the Rician factor c_R and the number of cisoids N: (a) $N = 10$; (b) $N = 50$ ($f_\rho = 65$ Hz and $\theta_\rho = 0°$).

Before we move on to the next topic, we would like to draw the reader's attention to the fact that $\hat{\boldsymbol{\xi}}(t)$ and $\hat{\boldsymbol{\psi}}(t)$ exhibit the same first-order stationarity characteristics as the envelope $\boldsymbol{\xi}(t)$ and phase $\boldsymbol{\psi}(t)$ of the reference model [cf. Sec. 2.4.1].

3.3.5 A Note on the LCR and ADF of the Stochastic SOC Model's Envelope

As of the time of witting of this thesis, exact solutions of the LCR $N_{\hat{\boldsymbol{\xi}}}(r)$ and ADF $T_{\hat{\boldsymbol{\xi}}}(r)$ of $\hat{\boldsymbol{\xi}}(t)$ are still lacking. A first attempt to close the gap was made in [Pae08b]. Closed-form expressions were presented in that paper for both $N_{\hat{\boldsymbol{\xi}}}(r)$

and $T_{\hat{\boldsymbol{\xi}}}(r)$ by considering $m_\rho(t) = \rho \exp\{j\theta_\rho\}$ and assuming that $\sum_{n=1}^{N} \hat{c}_n^2 \hat{f}_n = 0$, i.e., $A_{\hat{\boldsymbol{\mu}}\hat{\boldsymbol{\mu}}} = 0$. Early investigations showed a reasonably good resemblance between the analytical solutions provided there and the empirical data obtained from simulations. However, further analysis demonstrated that the expressions given in [Pae08b] underestimate the number of crossings at medium levels ($r \in [0.5, 2]$). Such an imprecision could be due to the fact that the cross-correlations at $\tau = 0$ among the IQ components of $\hat{\boldsymbol{\mu}}(t)$ and their time derivatives were neglected when deriving the formulas—it was assumed in [Pae08b] that $r_{\hat{\boldsymbol{\mu}}_I\hat{\boldsymbol{\mu}}'_I}(0) = r_{\hat{\boldsymbol{\mu}}_Q\hat{\boldsymbol{\mu}}'_Q}(0) = r_{\hat{\boldsymbol{\mu}}'_I\hat{\boldsymbol{\mu}}_Q}(0) = r_{\hat{\boldsymbol{\mu}}'_Q\hat{\boldsymbol{\mu}}_I}(0) = 0$. Those expressions are currently being revisited by the authors of [Paet07] by relaxing the aforementioned assumption.

3.3.6 ACF of the Stochastic SOC Model's Squared Envelope

Concerning the ACF $r_{\hat{\boldsymbol{\xi}}^2\hat{\boldsymbol{\xi}}^2}(t_1, t_2) \triangleq E\{\hat{\boldsymbol{\xi}}^2(t_1)\hat{\boldsymbol{\xi}}^2(t_2)\}$ of the squared envelope $\hat{\boldsymbol{\xi}}^2(t) \triangleq |\hat{\boldsymbol{\nu}}(t)|^2$ of $\hat{\boldsymbol{\nu}}(t)$, it is shown in Appendix B that

$$\begin{aligned} r_{\hat{\boldsymbol{\xi}}^2\hat{\boldsymbol{\xi}}^2}(t_1, t_2) &= r_{\hat{\boldsymbol{\xi}}^2\hat{\boldsymbol{\xi}}^2}(\tau) \qquad (3.28) \\ &= r_{\hat{\boldsymbol{\zeta}}^2\hat{\boldsymbol{\zeta}}^2}(\tau) + \frac{4\sigma_{\boldsymbol{\nu}}^2 c_R}{c_R + 1}\Big\{ r_{\hat{\boldsymbol{\mu}}_I\hat{\boldsymbol{\mu}}_I}(\tau)\cos(2\pi f_\rho \tau) \\ &\quad + r_{\hat{\boldsymbol{\mu}}_I\hat{\boldsymbol{\mu}}_Q}(\tau)\sin(2\pi f_\rho \tau)\Big\} + \frac{c_R\,\sigma_{\boldsymbol{\nu}}^4(c_R+2)}{(c_R+1)^2} \qquad (3.29) \end{aligned}$$

where $r_{\hat{\boldsymbol{\zeta}}^2\hat{\boldsymbol{\zeta}}^2}(\tau)$ is the ACF of the squared envelope $\hat{\boldsymbol{\zeta}}^2(t) \triangleq |\hat{\boldsymbol{\mu}}(t)|^2$ of $\hat{\boldsymbol{\mu}}(t)$. It is also shown in Appendix B that

$$r_{\hat{\boldsymbol{\zeta}}^2\hat{\boldsymbol{\zeta}}^2}(\tau) = \frac{\sigma_{\boldsymbol{\nu}}^4}{(c_R+1)^2} + |r_{\hat{\boldsymbol{\mu}}\hat{\boldsymbol{\mu}}}(\tau)|^2 - \sum_{n=1}^{N} \hat{c}_n^4. \qquad (3.30)$$

One can verify without difficulty that the mean value $m_{\hat{\boldsymbol{\xi}}^2}(t) \triangleq E\{\hat{\boldsymbol{\xi}}^2(t)\}$ of $\hat{\boldsymbol{\xi}}^2(t)$ is equal to $\sigma_{\boldsymbol{\nu}}^2$. Thus, we can conclude that $\hat{\boldsymbol{\xi}}^2(t)$ is a WSS process, since the ACF $r_{\hat{\boldsymbol{\xi}}^2\hat{\boldsymbol{\xi}}^2}(t_1, t_2)$ depends only on the time difference $\tau = t_2 - t_1$, i.e., $r_{\hat{\boldsymbol{\xi}}^2\hat{\boldsymbol{\xi}}^2}(t_1, t_2) = r_{\hat{\boldsymbol{\xi}}^2\hat{\boldsymbol{\xi}}^2}(\tau)$, and $m_{\hat{\boldsymbol{\xi}}^2}(t)$ is constant over time.

3.4 The Deterministic SOC-Based Simulation Model

3.4.1 Structure

In practice, the simulation of $\boldsymbol{\nu}(t)$ is performed by generating sample functions of $\hat{\boldsymbol{\mu}}(t)$ and combining the resulting process with the time-variant waveform $m_\rho(t)$ (as depicted in Fig. 3.1). Consequently, the simulator's output proves to be a

process of the form

$$\hat{\nu}^{(k)}(t) \;=\; \hat{\mu}^{(k)}(t) + \rho \exp\{j(2\pi f_\rho t + \theta_\rho)\}, \quad k \in \mathbb{Z}^+ \tag{3.31}$$

where $\hat{\nu}^{(k)}(t)$ and $\hat{\mu}^{(k)}(t)$ denote the kth sample functions of $\hat{\boldsymbol{\nu}}(t)$ and $\hat{\boldsymbol{\mu}}(t)$, respectively. The complex process $\hat{\mu}^{(k)}(t)$ is given by

$$\hat{\mu}^{(k)}(t) \;=\; \sum_{n=1}^{N} \hat{c}_n \exp\left\{j\left(2\pi \hat{f}_n t + \hat{\theta}_n^{(k)}\right)\right\}, \quad k \in \mathbb{Z}^+ \tag{3.32}$$

where $\hat{\theta}_n^{(k)}$ is the outcome of $\hat{\boldsymbol{\theta}}_n$ associated to the kth sample function of $\hat{\boldsymbol{\mu}}(t)$. We note that $\hat{\nu}^{(k)}(t)$ can unequivocally be predicted at any time instant t once the values of $\hat{\theta}_n^{(k)}$ are known (those values are to be resolved at random during the simulation set-up phase and they are kept constant during the simulation run). The simulator's output can therefore be regarded as being a deterministic process. In fact, $\hat{\nu}^{(k)}(t)$ and $\hat{\mu}^{(k)}(t)$ can be classified as deterministic SOC-based simulators (Class I simulators).

Information about the time averages[3] of the sample functions of $\hat{\boldsymbol{\nu}}(t)$ is also relevant for the characterization of the simulation model. Such an information is fundamental not only to analyze the properties of the generated waveforms $\hat{\nu}^{(k)}(t)$, but also to determine whether the simulation model is ergodic or not. In fact, to investigate the subject of ergodicity, it is necessary to find out under what conditions the time averages of $\hat{\boldsymbol{\nu}}(t)$ are equal to the ensemble averages. In that regard, we present in what follows an analysis of the time-averaged characteristics of the simulation model's sample functions.

3.4.2 Mean Value and Average Power

In the case of the random process $\hat{\boldsymbol{\mu}}(t)$, one can easily verify that the mean value $m_{\hat{\mu}^{(k)}} \triangleq \langle \hat{\mu}^{(k)}(t) \rangle$ of $\hat{\mu}^{(k)}(t)$ is equal to the ensemble mean, $m_{\hat{\boldsymbol{\mu}}}(t) \triangleq E\{\hat{\boldsymbol{\mu}}(t)\} = 0$, if the following condition is fulfilled:

Condition 3.2 *The N cisoids underlying $\hat{\boldsymbol{\mu}}(t)$ are all Doppler shifted, meaning that $\hat{f}_n \neq 0 \; \forall n$.*

Besides, one may demonstrate that the average power $\mathcal{P}_{\hat{\mu}^{(k)}} \triangleq \langle |\hat{\mu}^{(k)}(t)|^2 \rangle$ of $\hat{\mu}^{(k)}(t)$ equals that of the ensemble, $P_{\hat{\boldsymbol{\mu}}} = E\{|\hat{\boldsymbol{\mu}}(t)|^2\} = \sigma^2_{\hat{\boldsymbol{\nu}}}$, if the above mentioned condition is satisfied and:

Condition 3.3 *The N cisoids underlying $\hat{\boldsymbol{\mu}}(t)$ are specified in such a way that $\hat{f}_n \neq \hat{f}_m$ for $n \neq m$.*

[3]The time average of a function $x(t)$ is denoted by $\langle x(t) \rangle$ and defined as $\langle x(t) \rangle \triangleq \lim_{T\to\infty} \frac{1}{2T} \int_{-T}^{T} x(t)dt$.

On the other hand, we find that the mean value $m_{\hat{\nu}^{(k)}} \triangleq \langle \hat{\nu}^{(k)}(t) \rangle$ of the sample functions of $\hat{\boldsymbol{\nu}}(t)$ equals $m_{\hat{\nu}^{(k)}} = 0 \ \forall k$ if Condition 3.2 holds and $f_\rho \neq 0$. If the latter requirement is not satisfied, i.e., if $f_\rho = 0$, then $m_{\hat{\nu}^{(k)}} = \rho \exp\{j\theta_\rho\}$ $\forall k$. Since the mean value of the ensemble is in general a function of time $m_{\hat{\boldsymbol{\nu}}}(t) \triangleq E\{\hat{\boldsymbol{\nu}}(t)\} = \rho \exp\{j(2\pi f_\rho t + \theta_\rho)\}$, we have that $m_{\hat{\nu}^{(k)}}$ is equal to $m_{\hat{\boldsymbol{\nu}}}(t)$ only when $\rho = 0$ or $f_\rho = 0$. Regarding the average power $\mathcal{P}_{\hat{\nu}^{(k)}} \triangleq \langle |\hat{\nu}^{(k)}(t)|^2 \rangle$ of $\hat{\nu}^{(k)}(t)$, we have $\mathcal{P}_{\hat{\nu}^{(k)}} = \sigma^2_{\boldsymbol{\nu}} \ \forall k$ if in addition to Conditions 3.2 and 3.3, the following is observed:

Condition 3.4 *The specular wave $m_\rho(t)$ and the random cisoids underlying $\hat{\boldsymbol{\mu}}(t)$ are specified in such a way that $f_\rho \neq \hat{f}_n \ \forall n$.*

Notice that the average power of $\hat{\nu}^{(k)}(t)$ equals the mean power of the ensemble upon fulfillment of such conditions, since $\mathcal{P}_{\hat{\boldsymbol{\nu}}} = E\{|\hat{\boldsymbol{\nu}}(t)|^2\} = \sigma^2_{\boldsymbol{\nu}}$ [Sec. 3.3.2].

3.4.3 Correlation Properties and Spectral Characteristics

3.4.3.1 Time-averaged ACFs

In order to analyze the correlation properties of the simulation model's sample functions, let us assume that the zero-mean process $\hat{\boldsymbol{\mu}}(t)$ is defined in such a way that Conditions 3.2 and 3.3 are fulfilled, meaning that $\hat{f}_n \neq 0 \ \forall n$ and $\hat{f}_n \neq \hat{f}_m$ for $n \neq m$. Under these considerations, the time-averaged ACF $r_{\hat{\mu}^{(k)}\hat{\mu}^{(k)}}(\tau) \triangleq \langle \big(\hat{\mu}^{(k)}(t)\big)^* \hat{\mu}^{(k)}(t+\tau) \rangle$ of the kth sample function of $\hat{\boldsymbol{\mu}}(t)$ is found to be equal to

$$r_{\hat{\mu}^{(k)}\hat{\mu}^{(k)}}(\tau) \;=\; \sum_{n=1}^{N} \hat{c}_n^2 \exp\{j2\pi \hat{f}_n \tau\}, \quad \forall k. \tag{3.33}$$

It follows from (3.33) that the ACF of $\hat{\mu}^{(k)}(t)$ is equal to the one of the ensemble, $r_{\hat{\boldsymbol{\mu}}\hat{\boldsymbol{\mu}}}(\tau)$, since $r_{\hat{\boldsymbol{\mu}}\hat{\boldsymbol{\mu}}}(\tau) = \sum_{n=1}^{N} \hat{c}_n \exp\{j2\pi \hat{f}_n \tau\}$ [Eq. (3.5)]. We observe that the time-averaged ACF $r_{\hat{\mu}^{(k)}\hat{\mu}^{(k)}}(\tau)$ can be factorized in terms of the ACFs and CCFs of the IQ components $\hat{\mu}_I^{(k)}(t)$ and $\hat{\mu}_Q^{(k)}(t)$ of $\hat{\mu}^{(k)}(t)$ in a similar way as described in Section 3.3.3.1 for the ACF of the ensemble, that is,

$$\begin{aligned} r_{\hat{\mu}^{(k)}\hat{\mu}^{(k)}}(\tau) &= \big[r_{\hat{\mu}_I^{(k)}\hat{\mu}_I^{(k)}}(\tau) + r_{\hat{\mu}_Q^{(k)}\hat{\mu}_Q^{(k)}}(\tau)\big] + j\big[r_{\hat{\mu}_I^{(k)}\hat{\mu}_Q^{(k)}}(\tau) - r_{\hat{\mu}_Q^{(k)}\hat{\mu}_I^{(k)}}(\tau)\big] \\ &= 2\big[r_{\hat{\mu}_I^{(k)}\hat{\mu}_I^{(k)}}(\tau) + j r_{\hat{\mu}_I^{(k)}\hat{\mu}_Q^{(k)}}(\tau)\big] \end{aligned} \tag{3.34}$$

where

$$r_{\hat{\mu}_I^{(k)}\hat{\mu}_I^{(k)}}(\tau) \;=\; r_{\hat{\mu}_Q^{(k)}\hat{\mu}_Q^{(k)}}(\tau) \;=\; \sum_{n=1}^{N} \frac{\hat{c}_n^2}{2} \cos\big(j2\pi \hat{f}_n \tau\big), \quad \forall k \tag{3.35a}$$

$$r_{\hat{\mu}_I^{(k)}\hat{\mu}_Q^{(k)}}(\tau) \;=\; -r_{\hat{\mu}_Q^{(k)}\hat{\mu}_I^{(k)}}(\tau) \;=\; \sum_{n=1}^{N} \frac{\hat{c}_n^2}{2} \sin\big(j2\pi \hat{f}_n \tau\big), \quad \forall k. \tag{3.35b}$$

Let us assume also that the Doppler frequency f_ρ of the specular wave $m_\rho(t)$ is defined in such a way that the Condition 3.4 holds, so that $f_\rho \neq \hat{f}_n \ \forall n$. One can then show that the time-averaged ACF $r_{\hat{\nu}^{(k)}\hat{\nu}^{(k)}}(\tau) \triangleq \left\langle \left(\hat{\nu}^{(k)}(t)\right)^* \hat{\nu}^{(k)}(t+\tau)\right\rangle$ of the kth sample function of $\hat{\boldsymbol{\nu}}(t)$ meets

$$r_{\hat{\nu}^{(k)}\hat{\nu}^{(k)}}(\tau) = r_{\hat{\mu}^{(k)}\hat{\mu}^{(k)}}(\tau) + \rho^2 \exp\{j2\pi f_\rho \tau\} \tag{3.36}$$

$$= \sum_{n=1}^{N} \hat{c}_n^2 \exp\{j2\pi \hat{f}_n \tau\} + \rho^2 \exp\{j2\pi f_\rho \tau\}, \quad \forall k. \tag{3.37}$$

Interestingly, a comparison between (3.37) and the result presented in (3.11) for the ACF $r_{\hat{\boldsymbol{\nu}}\hat{\boldsymbol{\nu}}}(\tau)$ of the ensemble shows that $r_{\hat{\nu}^{(k)}\hat{\nu}^{(k)}}(\tau) = r_{\hat{\boldsymbol{\nu}}\hat{\boldsymbol{\nu}}}(\tau) \ \forall k$.

3.4.3.2 DPSDs

For completeness, we will also analyze the spectral characteristics of the simulation model's sample functions. To simplify our notation, we will henceforth omit the superscript $\{\cdot\}^{(k)}$ whenever there is no need to make a distinction among sample functions, or among their statistical properties.

It is straightforward to show, by computing the Fourier transform of (3.37), that the DPSD $S_{\hat{\nu}\hat{\nu}}(f)$ of the sample functions of $\hat{\boldsymbol{\nu}}(t)$ is given by

$$S_{\hat{\nu}\hat{\nu}}(f) = \sum_{n=1}^{N} \hat{c}_n^2 \delta\big(f - \hat{f}_n\big) + \rho^2 \delta(f - f_\rho). \tag{3.38}$$

Analogously, the DPSD $S_{\hat{\mu}\hat{\mu}}(f)$ of the sample functions of $\hat{\boldsymbol{\mu}}(t)$ is found to be equal to

$$S_{\hat{\mu}\hat{\mu}}(f) = \sum_{n=1}^{N} \hat{c}_n^2 \delta\big(f - \hat{f}_n\big). \tag{3.39}$$

3.4.3.3 Average Doppler Shift and Doppler Spread

By comparing the results presented in (3.38) and (3.12), we realize that the DPSDs of $\hat{\nu}(t)$ and $\hat{\boldsymbol{\nu}}(t)$ are exactly the same, i.e., $S_{\hat{\nu}\hat{\nu}}(f) = S_{\hat{\boldsymbol{\nu}}\hat{\boldsymbol{\nu}}}(f)$. Consequently, we can deduce that the average Doppler shift $A_{\hat{\nu}\hat{\nu}}$ and Doppler spread $D_{\hat{\nu}\hat{\nu}}$ of $\hat{\nu}(t)$ are equal to those of $\hat{\boldsymbol{\nu}}(t)$. In the spirit of this reasoning, we can write: $A_{\hat{\nu}\hat{\nu}} = \frac{1}{\sigma^2_{\hat{\boldsymbol{\nu}}}}\big[\rho^2 f_\rho + \sum_{n=1}^{N} \hat{c}_n^2 \hat{f}_n\big]$; and $D_{\hat{\nu}\hat{\nu}} = \big\{\frac{1}{\sigma^2_{\hat{\boldsymbol{\nu}}}}\big[\rho^2 f_\rho^2 + \sum_{n=1}^{N} \hat{c}_n^2 \hat{f}_n^2\big] - (A_{\hat{\nu}\hat{\nu}})^2\big\}^{1/2}$. Accordingly, the average Doppler shift $A_{\hat{\mu}\hat{\mu}}$ and Doppler spread $D_{\hat{\mu}\hat{\mu}}$ of $\hat{\mu}(t)$ can be presumed to be equal to those of $\hat{\boldsymbol{\mu}}(t)$, so that $A_{\hat{\mu}\hat{\mu}} = \frac{1}{\sigma^2_{\hat{\boldsymbol{\mu}}}} \sum_{n=1}^{N} \hat{c}_n^2 \hat{f}_n$ and $D_{\hat{\mu}\hat{\mu}} = \big\{\frac{1}{\sigma^2_{\hat{\boldsymbol{\mu}}}} \sum_{n=1}^{N} \hat{c}_n^2 \hat{f}_n^2 - (A_{\hat{\mu}\hat{\mu}})^2\big\}^{1/2}$. These results are remarkable indeed, as they imply that the relevant spectral moments of the simulation model can be measured from a single sample function $\hat{\nu}(t)$.

3.4.4 ACF of the Deterministic Squared Envelope

To close this section, we investigate the time-averaged ACF $r_{\hat{\xi}^2\hat{\xi}^2}(\tau) \triangleq \langle \hat{\xi}^2(t) \cdot \hat{\xi}^2(t+\tau) \rangle$ of the sample functions $\hat{\xi}^2(t)$ of $\hat{\boldsymbol{\xi}}^2(t)$. A closed-form solution for such an ACF is derived in Appendix C upon the assumption that the Conditions 3.2, 3.3, and the three conditions stated below are satisfied altogether:

Condition 3.5 *If $N \geq 4$, then the N Doppler frequencies $\hat{f}_n$ of $\hat{\boldsymbol{\mu}}(t)$ are specified in such a way that*

$$\hat{f}_l + \hat{f}_m = \hat{f}_n + \hat{f}_k, \quad \textit{iff} \begin{cases} l = m = n = k; \\ \textit{or } l = n, m = k, l \neq m; \\ \textit{or } l = k, m = n, l \neq m. \end{cases}$$

Condition 3.6 *The specular wave $m_\rho(t)$ and the random cisoids underlying $\hat{\boldsymbol{\mu}}(t)$ are defined in such a way that $|f_\rho| \neq |\hat{f}_n| \; \forall n$.*

Condition 3.7 *If $N \geq 2$, then the Doppler frequency f_ρ of the specular wave $m_\rho(t)$ and the N Doppler frequencies $\hat{f}_n$ of $\hat{\boldsymbol{\mu}}(t)$ are defined in such a way that $f_\rho + \hat{f}_l \neq \hat{f}_m + \hat{f}_n, \quad \forall l, m, n$.*

Under these considerations, it is shown there that

$$\begin{aligned} r_{\hat{\xi}^2\hat{\xi}^2}(\tau) &= r_{\hat{\zeta}^2\hat{\zeta}^2}(\tau) + \frac{4\sigma_{\boldsymbol{\nu}}^2 c_R}{c_R+1}\Big\{ r_{\hat{\mu}_I\hat{\mu}_I}(\tau)\cos(2\pi f_\rho \tau) \\ &\quad + r_{\hat{\mu}_I\hat{\mu}_Q}(\tau)\sin(2\pi f_\rho \tau) \Big\} + \frac{c_R\,\sigma_{\boldsymbol{\nu}}^4(c_R+2)}{(c_R+1)^2} \end{aligned} \tag{3.40}$$

where $r_{\hat{\zeta}^2\hat{\zeta}^2}(\tau) \triangleq \langle \hat{\zeta}^2(t)\hat{\zeta}^2(t+\tau) \rangle$ is the ACF of the squared envelope $\hat{\zeta}^2(t) \triangleq |\hat{\mu}(t)|^2$ of $\hat{\mu}(t)$. For this latter ACF, it is shown in Appendix C that

$$r_{\hat{\zeta}^2\hat{\zeta}^2}(\tau) = \frac{\sigma_{\boldsymbol{\mu}}^4}{(c_R+1)^2} + |r_{\hat{\mu}\hat{\mu}}(\tau)|^2 - \sum_{n=1}^{N} \hat{c}_n^4 \tag{3.41}$$

if the Condition 3.5 is met. Notice that the results presented in (3.40) and (3.29) are equivalent to each other, implying that the ACF of $\hat{\xi}^2(t)$ is equal to that of the ensemble, i.e., $r_{\hat{\boldsymbol{\xi}}^2\hat{\boldsymbol{\xi}}^2}(\tau) = r_{\hat{\xi}^2\hat{\xi}^2}(\tau)$. With respect to the mean value $m_{\hat{\xi}^2} \triangleq \langle \hat{\xi}^2(t) \rangle$ of the sample functions of $\hat{\boldsymbol{\xi}}^2(t)$, it can easily be shown that $m_{\hat{\xi}^2} = \sigma_{\boldsymbol{\nu}}^2$. This result holds provided that the Conditions 3.2 and 3.3 are fulfilled.

We pointed out in Section 3.3.3.1 that if the Doppler frequencies $\hat{f}_n$ of $\hat{\boldsymbol{\mu}}(t)$ satisfy the Conditions 3.2 and 3.3, i.e., if $\hat{f}_n \neq 0 \; \forall n$, and $\hat{f}_n \neq \hat{f}_m$, $n \neq m$, then the fulfillment of the Condition 3.1 becomes necessary in order for the IQ components of $\hat{\boldsymbol{\mu}}(t)$ to be uncorrelated. Under such circumstances, the solution given in (3.41) for $r_{\hat{\zeta}^2\hat{\zeta}^2}(\tau)$ is no longer valid, since the Condition 3.1 is not compatible with the

Condition 3.5. This is clear, as the former condition states that for each pair of parameters $(\hat{c}_n, \hat{f}_n)$, $n = 1, \ldots, N$, there exists one and only one pair $(\hat{c}_m, \hat{f}_m)$, $n \neq m$, such that $\hat{c}_n = \hat{c}_m$ and $\hat{f}_n = -\hat{f}_m$ (N is even), whereas the latter condition establishes that $\hat{f}_l + \hat{f}_m = \hat{f}_n + \hat{f}_k$ iff: $l = m = n = k$; or $l = n, m = k$, $l \neq m$; or $l = k, m = n$, $l \neq m$ ($N \geq 4$). Obviously, if the Condition 3.1 is met, then the equation $\hat{f}_l + \hat{f}_m = \hat{f}_n + \hat{f}_k$ will have more solutions than the ones specified by the Condition 3.5.

Since the simulation of fading channels having diffuse components with uncorrelated IQ components is relevant for many practical purposes, e.g., for analyzing the system performance under isotropic scattering conditions, we derive in Appendix D a solution for $r_{\hat{\zeta}^2\hat{\zeta}^2}(\tau)$ by assuming the fulfillment of the Conditions 3.1–3.3. For notational convenience, and without loss of generality, we suppose that the Doppler frequencies $\hat{f}_n$ are indexed in such a way that $\hat{f}_n < \hat{f}_m \; \forall n < m$. The expression we have obtained for such a particular case is the following

$$\begin{aligned} r_{\hat{\zeta}^2\hat{\zeta}^2}(\tau) &= \frac{\sigma_{\boldsymbol{\mu}}^4}{(c_R+1)^2} + |r_{\hat{\mu}\hat{\mu}}(\tau)|^2 - \sum_{n=1}^{N} \hat{c}_n^4 \\ &\quad + 4\Bigg\{ \Bigg| \sum_{m=1}^{N/2} \hat{c}_m^2 \cos\left(2\pi \hat{f}_m \tau\right) \exp\left\{ j(\hat{\theta}_m + \hat{\theta}_{N-m+1}) \right\} \Bigg|^2 \\ &\quad - \sum_{k=1}^{N/2} \hat{c}_k^4 \cos^2\left(2\pi \hat{f}_k \tau\right) \Bigg\} \end{aligned} \tag{3.42}$$

where N is even. Interestingly, the result present above depends on the cisoids phases $\hat{\theta}_n$. This is in contrast to the solution given in (3.41), which is not influenced by those parameters. We notice that the result presented in (3.40) for the time-averaged ACF $r_{\hat{\xi}^2\hat{\xi}^2}(\tau)$ of the sample functions $\hat{\xi}^2(t)$ of $\hat{\boldsymbol{\xi}}^2(t)$ does not change if we remove the Condition 3.5 from our assumptions. However, in this case the function $r_{\hat{\xi}^2\hat{\xi}^2}(\tau)$ proves to be different from the ACF of the ensemble $r_{\hat{\boldsymbol{\xi}}^2\hat{\boldsymbol{\xi}}^2}(\tau)$, since $r_{\hat{\zeta}^2\hat{\zeta}^2}(\tau) \neq r_{\hat{\boldsymbol{\zeta}}^2\hat{\boldsymbol{\zeta}}^2}(\tau)$ [cf. (3.30) and (3.42)].

3.5 On the Ergodicity of the Stochastic SOC-Based Simulation Model

On the basis of the statistical properties of $\hat{\boldsymbol{\mu}}(t)$ and $\hat{\boldsymbol{\nu}}(t)$ described so far, we can analyze the mean, power, and autocorrelation ergodicity of our stochastic SOC-based simulation model. Before we proceed to study the subject, we will define the concepts of mean ergodicity, power ergodicity, and autocorrelation ergodicity (cf. [Leon94, Sec. 6.6]).

Definition 3.1 *Let $\boldsymbol{x}(t)$ be a random process whose mean value $m_{\boldsymbol{x}}(t) \triangleq E\{\boldsymbol{x}(t)\}$ is constant over time, i.e., $m_{\boldsymbol{x}}(t) = m_{\boldsymbol{x}}$. Then, $\boldsymbol{x}(t)$ is said to be mean-ergodic if:*

- *The mean value $m_x^{(k)}(t) \triangleq \langle x^{(k)}(t) \rangle$ of every sample function $x^{(k)}(t)$ of $\boldsymbol{x}(t)$ is equal to $m_{\boldsymbol{x}}$, i.e., $m_x^{(k)}(t) = m_{\boldsymbol{x}}$ $\forall k$.*

Definition 3.2 *Let $\boldsymbol{x}(t)$ be a random process whose power $\mathcal{P}_{\boldsymbol{x}}(t) \triangleq E\{|\boldsymbol{x}(t)|^2\}$ is constant over time, i.e., $\mathcal{P}_{\boldsymbol{x}}(t) = \mathcal{P}_{\boldsymbol{x}}$. Then, $\boldsymbol{x}(t)$ is said to be power-ergodic if:*

- *The time-averaged power $\mathcal{P}_x^{(k)} \triangleq \langle |x^{(k)}(t)|^2 \rangle$ of every sample function $x^{(k)}(t)$ of $\boldsymbol{x}(t)$ is equal to $\mathcal{P}_{\boldsymbol{x}}$, meaning that $\mathcal{P}_x^{(k)} = \mathcal{P}_{\boldsymbol{x}}$ $\forall k$.*

Definition 3.3 *Let $\boldsymbol{x}(t)$ be a random process whose ACF $r_{\boldsymbol{xx}}(t_1, t_2) \triangleq E\{\boldsymbol{x}^*(t_1) \cdot \boldsymbol{x}(t_2)\}$ depends only on the time difference $\tau = t_2 - t_1$, so that $r_{\boldsymbol{xx}}(t_1, t_2) = r_{\boldsymbol{xx}}(\tau)$. Then, $\boldsymbol{x}(t)$ is said to be autocorrelation-ergodic if:*

- *The time-averaged ACF $r_{x^{(k)}x^{(k)}}(\tau) \triangleq \langle (x^{(k)}(t))^* x^{(k)}(t+\tau) \rangle$ of every sample function $x^{(k)}(t)$ of $\boldsymbol{x}(t)$ is equal to $r_{\boldsymbol{xx}}(\tau)$, that is, $r_{x^{(k)}x^{(k)}}(\tau) = r_{\boldsymbol{xx}}(\tau)$ $\forall k$.*

We observe that an autocorrelation-ergodic random process is always power-ergodic, but the converse is not necessarily true.

In accordance to the previous definitions, and from the results presented in Sections 3.3 and 3.4, we can conclude that the WSS zero-mean process $\hat{\boldsymbol{\mu}}(t)$ is mean-ergodic, power-ergodic, and autocorrelation-ergodic provided that the Conditions 3.2 and 3.3 are satisfied. This is clear, since $m_{\hat{\boldsymbol{\mu}}} = m_{\hat{\mu}^{(k)}} = 0$, $\mathcal{P}_{\hat{\boldsymbol{\mu}}} = \mathcal{P}_{\hat{\mu}^{(k)}} = \sigma^2_{\boldsymbol{\mu}}$, and $r_{\hat{\boldsymbol{\mu}}\hat{\boldsymbol{\mu}}}(\tau) = r_{\hat{\mu}^{(k)}\hat{\mu}^{(k)}}(\tau) = \sum_{n=1}^{N} \hat{c}_n^2 \exp\{j2\pi \hat{f}_n \tau\}$ for all k upon fulfillment of the above mentioned conditions.

On the other hand, if the Conditions 3.2–3.4 are met, then the simulation model described by $\hat{\boldsymbol{\nu}}(t)$ turns out to be power-ergodic and autocorrelation-ergodic too, as $\mathcal{P}_{\hat{\boldsymbol{\nu}}} = \mathcal{P}_{\hat{\nu}^{(k)}} = \sigma^2_{\boldsymbol{\nu}}$ and $r_{\hat{\boldsymbol{\nu}}\hat{\boldsymbol{\nu}}}(\tau) = r_{\hat{\nu}^{(k)}\hat{\nu}^{(k)}}(\tau) = r_{\hat{\boldsymbol{\mu}}\hat{\boldsymbol{\mu}}}(\tau) + \rho^2 \exp\{j2\pi \cdot f_\rho \tau\}$ $\forall k$. However, the simulation model is in general not mean-ergodic, because its mean value $m_{\hat{\boldsymbol{\nu}}}(t)$ may vary over time [Sec. 3.3.2]. Nevertheless, if the Conditions 3.2–3.4 are satisfied and the specular wave $m_\rho(t)$ is not Doppler shifted, so that $f_\rho = 0$, then $\hat{\boldsymbol{\nu}}(t)$ proves to be mean-ergodic. Notice that $m_{\hat{\boldsymbol{\nu}}}(t) = m_{\hat{\nu}^{(k)}} = \rho^2 \exp\{j2\pi\theta_\rho\}$ $\forall k$ under such circumstances. Needless to say, $\hat{\boldsymbol{\nu}}(t)$ is mean-ergodic if $\rho = 0$, since $\hat{\boldsymbol{\nu}}(t)$ reduces to $\hat{\boldsymbol{\mu}}(t)$ when $\rho = 0$.

In a similar spirit, we can conclude from the results presented in Sections 3.3.6 and 3.4.4, that the SOC model's squared envelope $\hat{\boldsymbol{\xi}}^2(t)$ is a mean-ergodic and an autocorrelation-ergodic process, since $m_{\hat{\boldsymbol{\xi}}^2} = m_{\hat{\xi}^{2(k)}} = \sigma^2_{\boldsymbol{\nu}}$ and $r_{\hat{\boldsymbol{\xi}}^2\hat{\boldsymbol{\xi}}^2}(\tau) = r_{\hat{\xi}^{2(k)}\hat{\xi}^{2(k)}}(\tau)$ $\forall k$. We point out, nonetheless, that these properties are subject to the fulfillment of the Conditions 3.2, 3.3, and 3.5–3.7. If any of these conditions is not met, then the time-averaged ACF $r_{\hat{\xi}^{2(k)}\hat{\xi}^{2(k)}}(t)$ of the kth sample function of $\hat{\boldsymbol{\xi}}^2(t)$ will depend on the set of phases $\{\hat{\theta}_n^{(k)}, \theta_\rho\}$, as mentioned in Appendix C. In

such a case, the requirements stated in Definition 3.3 will not be satisfied, since the ACF of the ensemble does not depend on the cisoids' phases [see (3.29)]. Moreover, we can conclude on the basis of (3.29), (3.30), (3.40), and (3.42) that the squared envelope processes $\hat{\boldsymbol{\zeta}}^2(t)$ and $\hat{\boldsymbol{\xi}}^2(t)$ are non-autocorrelation-ergodic if the simulation model is parameterized in such a way that the Doppler frequencies $\hat{f}_n$ of $\hat{\boldsymbol{\mu}}(t)$ satisfy the Conditions 3.1–3.3, i.e., if $\hat{\boldsymbol{\mu}}(t)$ is autocorrelation-ergodic and its IQ components are uncorrelated.

3.6 Chapter Summary and Conclusions

In this chapter, we described the characteristics of the stochastic SOC-based simulation model that we have adopted as core structure for the narrowband channel simulators proposed in this dissertation. Important statistics of the simulation model, such as its ACF $r_{\hat{\boldsymbol{\nu}}\hat{\boldsymbol{\nu}}}(\tau)$ and DPSD $S_{\hat{\boldsymbol{\nu}}\hat{\boldsymbol{\nu}}}(f)$, as well as the first-order distributions of its envelope $\hat{\boldsymbol{\xi}}(t)$ and phase $\hat{\boldsymbol{\phi}}(t)$, were revised throughout the chapter. It was shown in Section 3.3.3 that $r_{\hat{\boldsymbol{\nu}}\hat{\boldsymbol{\nu}}}(\tau)$ and $S_{\hat{\boldsymbol{\nu}}\hat{\boldsymbol{\nu}}}(f)$ are fully specified by the cisoids gains and Doppler frequencies. In addition, it was shown in the same section that the random process $\hat{\boldsymbol{\nu}}(t)$ characterizing our simulation model possesses similar stationarity characteristics as the complex Gaussian process $\boldsymbol{\nu}(t)$ describing our reference model. We demonstrated in Section 3.3.4 that the envelope $\hat{\boldsymbol{\xi}}(t)$ of $\hat{\boldsymbol{\nu}}(t)$ is a first-order stationary process, whereas its phase $\hat{\boldsymbol{\phi}}(t)$ is in general not (unless $\rho = 0$ or $f_\rho = 0$). Similar observations were made in Chapter 2 regarding the first-order stationarity of the envelope $\boldsymbol{\xi}(t)$ and phase $\boldsymbol{\phi}(t)$ of $\boldsymbol{\nu}(t)$. Interestingly, the numerical results presented in Figs. 3.2 and 3.3 [see Sec. 3.3.4] indicate that the simulation model is well suited for approximating the first-order distributions of $\boldsymbol{\xi}(t)$ and $\boldsymbol{\phi}(t)$.

The mean, power, and autocorrelation ergodicity of $\hat{\boldsymbol{\nu}}(t)$ was also investigated here. In this regard, it was found that $\hat{\boldsymbol{\nu}}(t)$ is both power and autocorrelation ergodic, but its mean ergodicity is restricted to the cases where $f_\rho = 0$ or $\rho = 0$. The mean and autocorrelation ergodicity of the SOC model's squared envelope $\hat{\boldsymbol{\xi}}^2(t)$ was analyzed in this chapter too. The results presented in Sections 3.3.6 and 3.4.4 show that $\hat{\boldsymbol{\xi}}^2(t)$ is mean ergodic and autocorrelation ergodic if the cisoids' parameters are computed in conformity with the Conditions 3.2, 3.3, and 3.5–3.7. We observe, nonetheless, that the squared envelope process $\hat{\boldsymbol{\xi}}^2(t)$ is not autocorrelation ergodic when the simulation model's random component $\hat{\boldsymbol{\mu}}(t)$ is autocorrelation ergodic and its IQ components are uncorrelated.

Chapter 4

Parameter Computation Methods

4.1 Introduction

Once the structure of the stochastic SOC-based simulation model has been defined, the problem consists in finding values for the cisoids' parameters that allow for a proper emulation of the reference model. Basically, the problem lies in specifying the gains and the Doppler frequencies of the simulation model's random component, $\hat{\boldsymbol{\mu}}(t)$, in such a way that the statistical properties of $\hat{\boldsymbol{\mu}}(t)$ resemble those of the zero-mean complex Gaussian process $\boldsymbol{\mu}(t)$ characterizing the channel's diffuse component. The computation of the phases of $\hat{\boldsymbol{\mu}}(t)$ does not require any special attention, since these parameters have been defined in Section 3.3.1 as i.i.d. random variables uniformly distributed in $[-\pi, \pi)$.

Currently, there exist only two methods suitable for the computation of the gains and Doppler frequencies of $\hat{\boldsymbol{\mu}}(t)$, namely, the extended method of exact Doppler spread (EMEDS) [Pae08a] and the L_p-norm method (LPNM) [Pae02a, Sec. 5.1.5]. The EMEDS was introduced in [Hogs05] as an extension of the method of exact Doppler spread (MEDS) [Paet98] for SOC-based channel simulators. The LPNM, on the other hand, was proposed in [Paet98] as a parameter computation method for SOS models, and the approach was later applied in [Paet01] to design SOC-based channel simulators.

The EMEDS and the LPNM have widely been in use to simulate SISO and MIMO mobile fading channels, e.g., [Rafi08], [Pae04a]. The performance of both methods is remarkable indeed, as one may conclude from the analysis presented in [Pae04a] and [Pae08a]. Unfortunately, the applicability of the EMEDS is restricted to the simulation of isotropic scattering channels, while the numerical optimization techniques, the LPNM relies upon, significantly increase the complexity of the SOC-based simulator.

Aiming at the simulation of both isotropic and non-isotropic scattering channels, and with the purpose of circumventing the computational burden of the LPNM, we introduce in this chapter two simple and effective methods to address the parameter computation problem at hand. One of such methods is built upon a Riemann sum approximation of the ACF of $\boldsymbol{\mu}(t)$, while the other is a generalization of the method of equal areas (MEA) described in [Pae02a, Sec. 5.1.3]. Even though the generalized MEA (GMEA) and the Riemann sum approximation method (RSAM) are presented here in the context of narrowband SISO systems, these two fundamental methods can easily be applied to the simulation of narrowband and wideband MIMO systems, as will be demonstrated in Chapters 5 and 6.

We herein analyze the performance of the proposed methods not only with respect to the emulation of the correlation and spectral characteristics of $\boldsymbol{\mu}(t)$, but also in terms of the approximation of the envelope and phase distributions of the Rician fading channel model characterized by the composite process $\boldsymbol{\nu}(t) = \boldsymbol{\mu}(t) + m_\rho(t)$. In addition, we evaluate the accuracy of the methods for approximating the ACF of the squared envelope of $\boldsymbol{\nu}(t)$. The results produced by the GMEA and RSAM are compared with results obtained by using the LPNM. For the special case of the design of simulation models for isotropic scattering channels, it will be shown that both the GMEA and RSAM simplify to the EMEDS.

4.2 Overview of the Existing Parameter Computation Methods for SOC-Based Channel Simulators

Before we proceed to introduce the GMEA and the RSAM, we will present in this section a brief review of the EMEDS and the LPNM.

4.2.1 The EMEDS

In the case on the EMEDS, the parameters $\hat{c}_n$ and $\hat{f}_n$ are defined as [Hogs05]:

$$\hat{c}_n = \frac{\sigma_{\boldsymbol{\mu}}}{\sqrt{N}} \tag{4.1}$$

$$\hat{f}_n = f_{\max} \cos\left(\frac{2\pi}{N}\left[n - \frac{1}{4}\right]\right) \tag{4.2}$$

for $n = 1, \ldots, N$. One can easily verify, by substituting (4.1) and (4.2) into (3.18), that the Doppler spread of $\hat{\boldsymbol{\mu}}(t)$ reduces to the one of isotropic scattering channels for any $N \in \mathbb{Z}^+$, meaning that $D_{\hat{\boldsymbol{\mu}}\hat{\boldsymbol{\mu}}} = D_{\boldsymbol{\mu}\boldsymbol{\mu}} = f_{\max}/\sqrt{2}$, $\forall N \geq 1$. We recall that $D_{\hat{\boldsymbol{\mu}}\hat{\boldsymbol{\mu}}}$ and $D_{\boldsymbol{\mu}\boldsymbol{\mu}}$ denote the Doppler spread of $\hat{\boldsymbol{\mu}}(t)$ and $\boldsymbol{\mu}(t)$, respectively. Thus, as the name suggests, the EMEDS exactly reproduces the Doppler spread of isotropic scattering channels.

4.2.2 The LPNM

The LPNM, as originally introduced in [Paet01] for the design of SOC channel simulators, also defines the gains of $\hat{\boldsymbol{\mu}}(t)$ as in (4.1), but it requires the Doppler frequencies $\hat{f}_n$ to be computed in a way that minimizes the L_p-norm

$$\epsilon^{(p)}_{r_{\boldsymbol{\mu}\boldsymbol{\mu}}} \triangleq \left\{ \frac{1}{\tau_{\max}} \int_0^{\tau_{\max}} \left| r_{\boldsymbol{\mu}\boldsymbol{\mu}}(\tau) - r_{\hat{\boldsymbol{\mu}}\hat{\boldsymbol{\mu}}}(\tau) \right|^p d\tau \right\}^{1/p}, \quad p \in \mathbb{Z}^+ \tag{4.3}$$

where $\tau_{\max} > 0$ determines the length of the interval $[0, \tau_{\max}]$ inside of which the approximation $r_{\boldsymbol{\mu}\boldsymbol{\mu}}(\tau) \approx r_{\hat{\boldsymbol{\mu}}\hat{\boldsymbol{\mu}}}(\tau)$ is of interest. We bring back to memory that $r_{\boldsymbol{\mu}\boldsymbol{\mu}}(\tau)$ and $r_{\hat{\boldsymbol{\mu}}\hat{\boldsymbol{\mu}}}(\tau)$ denote the ACFs of $\boldsymbol{\mu}(t)$ and $\hat{\boldsymbol{\mu}}(t)$, in that order.

There exist other versions of the LPNM, which are surveyed in [Pae02a, Sec. 5.1.5]. In this chapter, we will consider two of them for the performance comparison with the parameter computation methods herein proposed. For the first variant under consideration, the gains and the Doppler frequencies of $\hat{\boldsymbol{\mu}}(t)$ are to be computed in such a way that the cost function

$$\epsilon^{(p)}_{r_{\boldsymbol{\mu}\boldsymbol{\mu}}, p_{\boldsymbol{\zeta}}} \triangleq W_1 \cdot \epsilon^{(p)}_{r_{\boldsymbol{\mu}\boldsymbol{\mu}}} + W_2 \cdot \epsilon^{(p)}_{p_{\boldsymbol{\zeta}}} \tag{4.4}$$

is minimized, where W_1 and W_2 are weighting factors and

$$\epsilon^{(p)}_{p_{\boldsymbol{\zeta}}} \triangleq \left\{ \int_0^{\infty} \left| p_{\boldsymbol{\zeta}}(z) - p_{\hat{\boldsymbol{\zeta}}}(z) \right|^p dz \right\}^{1/p}, \quad p \in \mathbb{Z}^+. \tag{4.5}$$

We remember that $p_{\boldsymbol{\zeta}}(z)$ and $p_{\hat{\boldsymbol{\zeta}}}(z)$ stand for the first-order PDFs of the envelopes of $\boldsymbol{\mu}(t)$ and $\hat{\boldsymbol{\mu}}(t)$, respectively. The second variant aims to minimize $\epsilon^{(p)}_{r_{\boldsymbol{\mu}\boldsymbol{\mu}}, p_{\boldsymbol{\zeta}}}$ too, but it considers only $N-1$ pairs of parameters $(\hat{c}_n, \hat{f}_n)$ for that purpose. To guarantee that the boundary conditions $r_{\hat{\boldsymbol{\mu}}\hat{\boldsymbol{\mu}}}(0) = r_{\boldsymbol{\mu}\boldsymbol{\mu}}(0)$ and $\ddot{r}_{\hat{\boldsymbol{\mu}}\hat{\boldsymbol{\mu}}}(0) = \ddot{r}_{\boldsymbol{\mu}\boldsymbol{\mu}}(0)$ are fulfilled, the remaining parameters $\hat{c}_N$ and $\hat{f}_N$ are obtained by following:

$$\hat{c}_N = \sqrt{\sigma^2_{\boldsymbol{\mu}} - \sum_{n=1}^{N-1} \hat{c}_n^2} \tag{4.6}$$

$$\hat{f}_N = \frac{1}{\hat{c}_N} \sqrt{\frac{-\ddot{r}_{\boldsymbol{\mu}\boldsymbol{\mu}}(0)}{4\pi^2} - \sum_{n=1}^{N-1} \left(\hat{c}_n \hat{f}_n \right)^2}. \tag{4.7}$$

The minimums of the cost function in (4.4) can be found by applying the optimization algorithm proposed in [Laga98], the which is implemented as `fminsearch` function in MATLAB®. We will refer to the original version of the LPNM as the LPNM I, while we will call the first and second variants described above the

LPNM II and LPNM III, respectively. It is worth mentioning that, in accordance to [Pae02a, Sec. 5.1.5], the LPNM III is the most efficient variant of the LPNM.

4.3 The GMEA

4.3.1 Description

The numerical results presented in Section 3.3.4 indicate that the envelope distribution of the simulation model's random component is closely in line with the Rayleigh distribution [2.23] when the gains $\hat{c}_n$ are given as in (4.1) and $N \geq 10$ (see Fig. 3.1(a) for the case $c_R = 0$). In fact, it is shown in [Paet07] that the rms error function

$$\epsilon_{p_{\boldsymbol{\zeta}}}^{(2)} \quad = \quad \left\{ \int_0^\infty \left[p_{\boldsymbol{\zeta}}(z) - p_{\hat{\boldsymbol{\zeta}}}(z) \right]^2 dz \right\}^{1/2} \tag{4.8}$$

is around 0.02 if $N = 10$, and smaller than 0.01 if $N > 20$. Motivated by these results, we choose the same gains $\hat{c}_n$ as in (4.1) for the GMEA.

Concerning the computation of the Doppler frequencies $\hat{f}_n$, we recall that the ACF of $\boldsymbol{\mu}(t)$ is given in terms of the PDF $p_{\boldsymbol{\alpha}}(\alpha)$ of the random AOAs $\boldsymbol{\alpha}_n$, or more specifically, in terms of the even part $g_{\boldsymbol{\alpha}}(\alpha)$ of $p_{\boldsymbol{\alpha}}(\alpha)$ [see (2.7)–(2.9)]. On the other hand, the ACF of $\hat{\boldsymbol{\mu}}(t)$ is completely specified by the parameters $\hat{c}_n$, $\hat{f}_n$, and N [see (3.5)]. In view of this, it is reasonable to think that in order for $r_{\hat{\boldsymbol{\mu}}\hat{\boldsymbol{\mu}}}(\tau)$ to resemble the ACF of the channel's diffuse component for a given value of N, the gains and Doppler frequencies of $\hat{\boldsymbol{\mu}}(t)$ should provide information about the function $g_{\boldsymbol{\alpha}}(\alpha)$. In the spirit of this reasoning, and since the gains in (4.1) are blind to the AOA statistics, we will compute the Doppler frequencies of $\hat{\boldsymbol{\mu}}(t)$ such that the underlying deterministic AOAs $\hat{\alpha}_n$ satisfy the equation

$$\int_{\hat{\alpha}_{n-1}}^{\hat{\alpha}_n} g_{\boldsymbol{\alpha}}(\alpha) d\alpha \quad = \quad \frac{1}{2N}, \qquad n = 2, \ldots, N \tag{4.9}$$

with $\hat{\alpha}_n \in (0, \pi)$. We recall that the uncorrelation between the IQ components of $\hat{\boldsymbol{\mu}}(t)$ is a fundamental feature for the design of simulation models for fading channels having diffuse components characterized by symmetrical DPSDs [Sec. 3.3.3.1]. We show in Appendix E that if the DPSD of $\boldsymbol{\mu}(t)$ is symmetrical, and the deterministic AOAs $\hat{\alpha}_n$ satisfy (4.9), then the IQ components of $\hat{\boldsymbol{\mu}}(t)$ are mutually uncorrelated if and only if

$$\int_0^{\hat{\alpha}_1} g_{\boldsymbol{\alpha}}(\alpha) d\alpha \quad = \quad \frac{1}{4N}. \tag{4.10}$$

We will consider (4.10) as an initial condition for computing the AOAs $\hat{\alpha}_n$ to ensure that the parameter computation method presented in this section is well suited for the simulation of fading channels characterized by symmetrical DPSDs.

On the other hand, it was pointed out in Section 3.4.2 that the simulation model described by $\hat{\boldsymbol{\mu}}(t)$ is mean-ergodic and autocorrelation-ergodic if:

$$\text{Condition 3.2}: \quad \hat{f}_n \neq 0, \quad \forall n \tag{4.11}$$

$$\text{Condition 3.3}: \quad \hat{f}_n \neq \hat{f}_m, \quad n \neq m. \tag{4.12}$$

An important implication of the requirement stated in (4.9) is that the AOAs $\hat{\alpha}_n$ will satisfy $\hat{\alpha}_n \neq \hat{\alpha}_m$ for $n \neq m$, and $\hat{\alpha}_n > 0 \ \forall n$. Thus, by demanding the AOAs $\hat{\alpha}_n$ to meet (4.9), we implicitly guarantee the fulfillment of the Condition 3.3, as the equality $\hat{f}_n = \hat{f}_m$ holds for some $n \neq m$ if and only if $\hat{\alpha}_n = \pm\hat{\alpha}_m$. Furthermore, the Condition 3.2 is unsatisfied if and only if $\hat{\alpha}_n = \pi/2$ for some n. This situation is rather unlikely when the DPSD of $\boldsymbol{\mu}(t)$, $S_{\boldsymbol{\mu}\boldsymbol{\mu}}(f)$, is asymmetrical, and it is never the case when $S_{\boldsymbol{\mu}\boldsymbol{\mu}}(f)$ is symmetrical and the number of cisoids N is even.

On the basis of (4.9) and (4.10), we can compute the AOAs $\hat{\alpha}_n$ by employing numerical root-finding techniques to solve

$$\int_0^{\hat{\alpha}_n} g_{\boldsymbol{\alpha}}(\alpha)d\alpha \;=\; \frac{1}{2N}\left(n-\frac{1}{2}\right), \quad n = 1, \ldots, N. \tag{4.13}$$

The function $g_{\boldsymbol{\alpha}}(\alpha)$ may itself be regarded as being a PDF, the CDF of which is given by $G_{\boldsymbol{\alpha}}(\alpha) \triangleq \int_{-\infty}^{\alpha} g_{\boldsymbol{\alpha}}(x)dx$. The evaluation of $G_{\boldsymbol{\alpha}}(\alpha)$ for $\alpha \leq \hat{\alpha}_n$ results into $G_{\boldsymbol{\alpha}}(\hat{\alpha}_n) = \frac{1}{2N}\left(n + N - \frac{1}{2}\right)$. Hence, if a closed-form solution exist for the inverse function $G_{\boldsymbol{\alpha}}^{-1}$ of $G_{\boldsymbol{\alpha}}$, then the AOAs $\hat{\alpha}_n$ can be computed by evaluating

$$\hat{\alpha}_n \;=\; G_{\boldsymbol{\alpha}}^{-1}\left(\frac{1}{2N}\left[n+N-\frac{1}{2}\right]\right), \quad n = 1, \ldots, N. \tag{4.14}$$

Once the AOAs $\hat{\alpha}_n$ are known, the Doppler frequencies $\hat{f}_n$ can easily be obtained by using the transformation $\hat{f}_n = f_{\max}\cos(\hat{\alpha}_n)$ [Eq. (3.3)]. Often, however, the channel's ACF and/or DPSD are introduced without giving any explicit information about the distribution of the random AOAs $\boldsymbol{\alpha}_n$, such as in [Blau06]. For those cases, we observe that

$$\begin{aligned}\int_0^{\hat{\alpha}_n} g_{\boldsymbol{\alpha}}(\alpha)d\alpha \;&=\; \int_{\hat{f}_n}^{f_{\max}} \frac{g_{\boldsymbol{\alpha}}(\arccos(f/f_{\max}))}{f_{\max}\sqrt{1-(f/f_{\max})^2}}df \\ &=\; \frac{1}{2}\int_{\hat{f}_n}^{f_{\max}} p_{\boldsymbol{f}}(f)df.\end{aligned} \tag{4.15}$$

Taking into account the result presented in (4.13), and given that the DPSD of $\boldsymbol{\mu}(t)$ is equal to $S_{\boldsymbol{\mu}\boldsymbol{\mu}}(f) = \sigma^2_{\boldsymbol{\mu}}\, p_{\boldsymbol{f}}(f)$ [cf. Eqs. (2.9) and (2.15)], we have

$$\int_{-f_{\max}}^{\hat{f}_n} S_{\boldsymbol{\mu}\boldsymbol{\mu}}(f)df \;=\; \frac{\sigma^2_{\boldsymbol{\mu}}}{N}\left(N - n + \frac{1}{2}\right), \quad n = 1, \ldots, N \tag{4.16}$$

where $\hat{f}_n \in (-f_{\max}, f_{\max})$. The integral in (4.16) describes a sort of cumulative power function that is proportional to the CDF $P_{\boldsymbol{f}}(f) \triangleq \int_{-\infty}^{f} p_{\boldsymbol{f}}(x)\,dx$ of the random Doppler frequencies of $\boldsymbol{\mu}(t)$; notice that

$$P_{\boldsymbol{f}}(f) \;=\; \frac{1}{\sigma^2_{\boldsymbol{\mu}}}\int_{-\infty}^{f} S_{\boldsymbol{\mu}\boldsymbol{\mu}}(y)dy. \tag{4.17}$$

Thus, for the special case where the inverse $P_{\boldsymbol{f}}^{-1}$ of $P_{\boldsymbol{f}}$ exists, the Doppler frequencies of $\hat{\boldsymbol{\mu}}(t)$ can be computed by evaluating

$$\hat{f}_n \;=\; P_{\boldsymbol{f}}^{-1}\left(\frac{1}{N}\left[N - n + \frac{1}{2}\right]\right), \quad n = 1, \ldots, N. \tag{4.18}$$

Otherwise, the deterministic Doppler frequencies $\hat{f}_n$ are to be computed by solving (4.16) with the aid of numerical root-finding techniques.

4.3.2 Differences Between the GMEA and Other Versions of the MEA

The parameter computation method presented in this section establishes the so-called GMEA. This method is basically an extension of the MEA described in [Pae02a, Sec. 5.1.3] with respect to the simulation of Rayleigh fading channels characterized by asymmetrical DPSDs. Such an extension was necessary, since the original MEA is specific for the SOS-based simulation of fading channels with symmetrical DPSDs. In fact, the deterministic AOAs $\hat{\alpha}_n$ obtained by using the MEA are confined within $(0, \frac{\pi}{2})$, an interval that does not convey enough information about the distribution of the random AOAs $\boldsymbol{\alpha}_n$ as to allow for an adequate simulation of channels having asymmetrical DPSDs.

We notice that a previous attempt to generalize the MEA was made in [Pae02c, Sec. 4-B]. The generalization proposed in that paper was designed by assuming that $p_{\boldsymbol{\alpha}}(\alpha)$ is symmetrical, implying that $p_{\boldsymbol{\alpha}}(\alpha) = g_{\boldsymbol{\alpha}}(\alpha)$. Under this consideration, the parameters $\hat{\alpha}_n$ are computed there by solving

$$\int_{0}^{\hat{\alpha}_n} p_{\boldsymbol{\alpha}}(\alpha)d\alpha \;=\; \frac{1}{N}, \quad \hat{\alpha}_n \in (0, \pi) \tag{4.19}$$

for $n = 1, \ldots, N/2$. The remaining $N/2$ AOAs $\hat{\alpha}_n$ are specified as mirrored versions of the solutions of (4.19), i.e., $\hat{\alpha}_n = -\hat{\alpha}_{N/2+1-n}$, $n = 1, \ldots, N/2$. Such a parameter computation approach is obviously inadequate when $p_{\boldsymbol{\alpha}}(\alpha)$ is not an even function. What is more, taking $\hat{\alpha}_n = -\hat{\alpha}_{N/2+1-n}$, $n = 1, \ldots, N/2$ produces duplicated Doppler frequencies, since $\cos(\hat{\alpha}_n) = \cos(-\hat{\alpha}_{N/2+1-n})$, $n = 1, \ldots, N/2$. This characteristic not only results into a non-autocorrelation-ergodic simulator, but also reduces the efficiency of the simulation model. Another problem of the method in [Pae02c, Sec. 4-B] is that the solutions of (4.19) do not guarantee the uncorrelation between the IQ components of $\hat{\boldsymbol{\mu}}(t)$ when the DPSD of the channel's diffuse component is symmetrical. For this reason, the generalized MEA there presented proves to be unsuitable for the simulation of channels characterized by such a type of DPSDs.

To illustrate the above mentioned problems, we present in Fig. 4.1 a comparison between the ACFs of $\boldsymbol{\mu}(t)$ and $\hat{\boldsymbol{\mu}}(t)$ by considering the method proposed in [Pae02c, Sec. 4-B] with $N = 20$ and the von Mises distribution of the AOA with pairs of parameters: $m_\alpha = 30°$, $\kappa = 10$; and $m_\alpha = 90°$, $\kappa = 10$. The former pair of parameters is representative of the case $p_{\boldsymbol{\alpha}}(\alpha) \neq p_{\boldsymbol{\alpha}}(-\alpha)$, while the latter pair exemplifies the case where the IQ components of $\boldsymbol{\mu}(t)$ are uncorrelated. It can be observed from Fig. 4.1 that the generalization of the MEA described in [Pae02c] produces a poor approximation to the ACF of $\boldsymbol{\mu}(t)$. In contrast, it will be shown in Section 4.5.1.1 that the GMEA proposed in this chapter provides a good approximation to $r^{\mathrm{VM}}_{\boldsymbol{\mu}\boldsymbol{\mu}}(\tau)$ in both cases.

4.3.3 Implementation

In what follows, we will apply the GMEA to the von Mises and Laplacian AOA distributions with the purpose of demonstrating the method's implementation.

4.3.3.1 von Mises Distributed AOAs

In the case of the von Mises PDF, $p^{\mathrm{VM}}_{\boldsymbol{\alpha}}(\alpha)$ [Eq. 2.43], neither the CDF of the even part of such a distribution, nor the cumulative power function of the resulting DPSD of $\boldsymbol{\mu}(t)$ [Eq. (2.45)], can be evaluated analytically. The Doppler frequencies of $\hat{\boldsymbol{\mu}}(t)$ shall therefore be computed by numerically finding the values of $\hat{f}_n$ that solve

$$\frac{1}{\pi f_{\max} I_0(\kappa)} \int_{-f_{\max}}^{\hat{f}_n} \cosh\left(\kappa \sin(m_\alpha)\sqrt{1-(f/f_{\max})^2}\right) \frac{\exp\left\{\kappa \cos(m_\alpha) f/f_{\max}\right\}}{\sqrt{1-(f/f_{\max})^2}}\, df - \frac{1}{N}\left(N - n + \frac{1}{2}\right) = 0, \qquad |\hat{f}_n| < f_{\max} \tag{4.20}$$

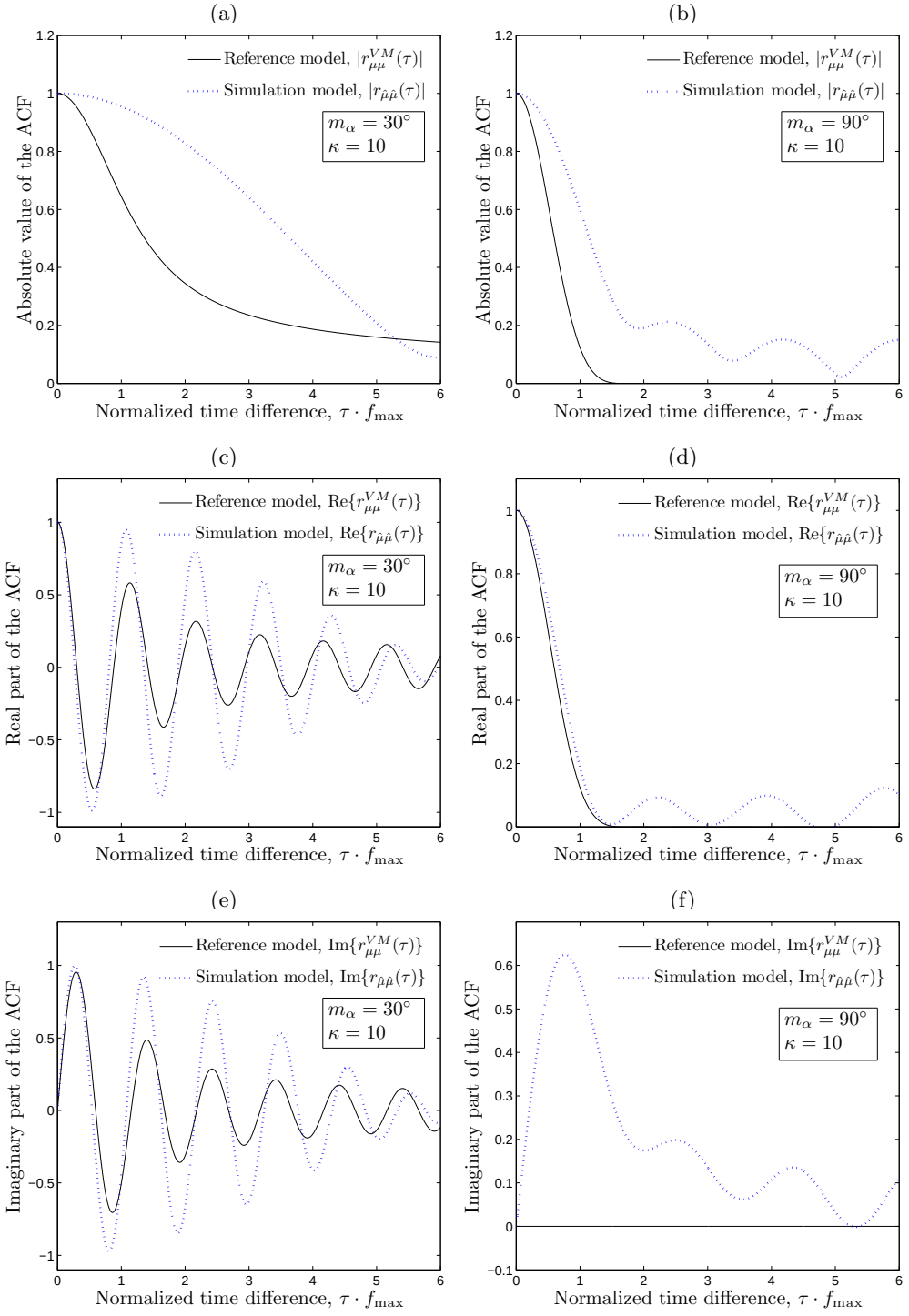

Figure 4.1: Comparison between the ACF of the channel's diffuse component and the ACF of the SOC-based simulation model's random component by considering the von Mises PDF of the AOA and the generalized version of the MEA proposed in [Pae02c] with $N = 20$.

for $n = 1, \ldots, N$. Alternatively, one may compute the underlying AOAs $\hat{\alpha}_n$ of $\hat{\boldsymbol{\mu}}(t)$ by solving

$$\frac{1}{2\pi I_0(\kappa)} \int_0^{\hat{\alpha}_n} \exp\{\kappa \cos(\alpha)\cos(m_\alpha)\} \cosh\left(\kappa \sin(\alpha)\sin(m_\alpha)\right) d\alpha - \frac{1}{2N}\left(n - \frac{1}{2}\right) = 0, \qquad \hat{\alpha}_n \in (0, \pi) \tag{4.21}$$

for $n = 1, \ldots, N$. This latter approach is indeed the one we will follow in this dissertation. We recall that the von Mises PDF reduces to the uniform distribution when $\kappa = 0$. In that case, both (4.20) and (4.21) have the analytical solution

$$\hat{f}_n = f_{\max} \cos\left(\frac{\pi}{N}\left[n - \frac{1}{2}\right]\right), \quad n = 1, \ldots, N. \tag{4.22}$$

Without going into details, we observe that (4.22) and (4.2) produce the same set of Doppler frequencies $\{\hat{f}_n\}_{n=1}^N$. Therefore, we can state that the GMEA contains the EMEDS as a special case for the simulation of isotropic scattering channels.

4.3.3.2 Laplacian Distributed AOAs

In the case of the Laplacian distribution, $p_{\boldsymbol{\alpha}}^{\mathrm{LA}}(\alpha)$ [see (2.51], the Doppler frequencies $\hat{f}_n$ are to be computed by finding the roots of

$$\frac{2}{c_s f_{\max}} \int_{f_{\max}}^{\hat{f}_n} \frac{\exp\left\{-\sqrt{2}\arccos\left(f/f_{\max}\right)/\sigma_s\right\}}{\sqrt{1-(f/f_{\max})^2}} df \; - \; \frac{1}{N}\left(N - n + \frac{1}{2}\right) = 0, \qquad |\hat{f}_n| < f_{\max} \tag{4.23}$$

for $n = 1, \ldots, N$. One could also proceed by solving

$$\frac{1}{c_s} \int_0^{\hat{\alpha}_n} \exp\left\{-\frac{1}{\sigma_s}\sqrt{2}|\alpha|\right\} d\alpha \; - \; \frac{1}{2N}\left(n - \frac{1}{2}\right) = 0, \qquad \hat{\alpha}_n \in (0, \pi) \tag{4.24}$$

for $n = 1, \ldots, N$. In either case, we obtain the closed-form solution

$$\hat{f}_n = f_{\max} \cos\left(\frac{\sigma_s}{\sqrt{2}} \ln\left\{1 - \frac{c_s}{\sqrt{2}N\sigma_s}\left(n - \frac{1}{2}\right)\right\}\right) \tag{4.25}$$

for $n = 1, \ldots, N$, where $\ln\{\cdot\}$ is the natural logarithm.

Figures 4.2 and 4.3 show a comparison between the DPSDs of the simulation model and the reference model by applying the GMEA to the von Mises (Fig. 4.2) and Laplacian (Fig. 4.3) AOA distributions. Such figures graphically demonstrate

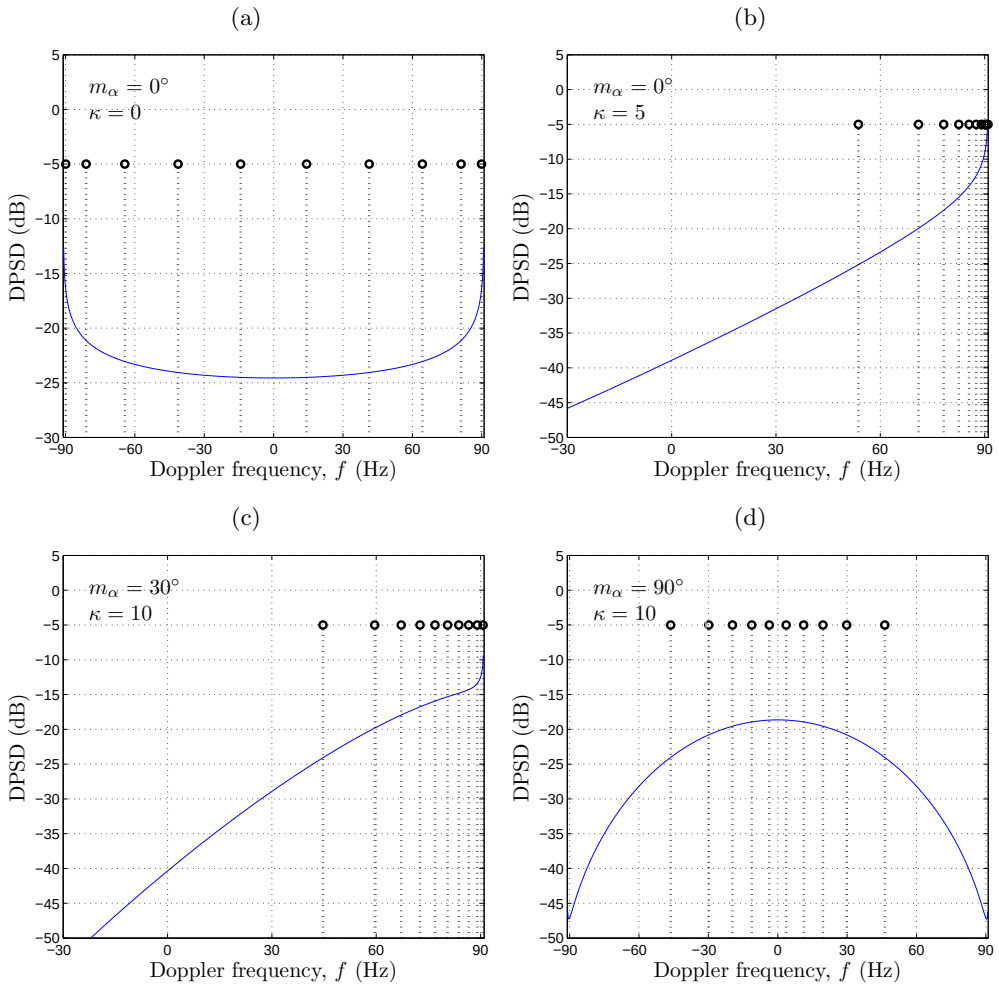

Figure 4.2: Comparison between the DPSD of the channel's diffuse component (blue-solid lines) and the DPSD of the random component of the SOC-based simulation model (black-dotted lines with '$\circ$' markers) by considering the von Mises PDF of the AOA and the GMEA ($f_{\max} = 91$ Hz, $\sigma^2_{\boldsymbol{\mu}} = 1$, and $N = 10$).

that despite the fact that the GMEA assigns the same amount of power to each of the cisoids in $\hat{\boldsymbol{\mu}}(t)$, the method specifies the Doppler frequencies $\hat{f}_n$ in such a way that the power of $\hat{\boldsymbol{\mu}}(t)$ is more densely concentrated within the zones where the DPSD of $\boldsymbol{\mu}(t)$ is higher. This characteristic enables the method to provide a good approximation to the correlation and spectral properties of $\boldsymbol{\mu}(t)$, as will be demonstrated in Section 4.5.

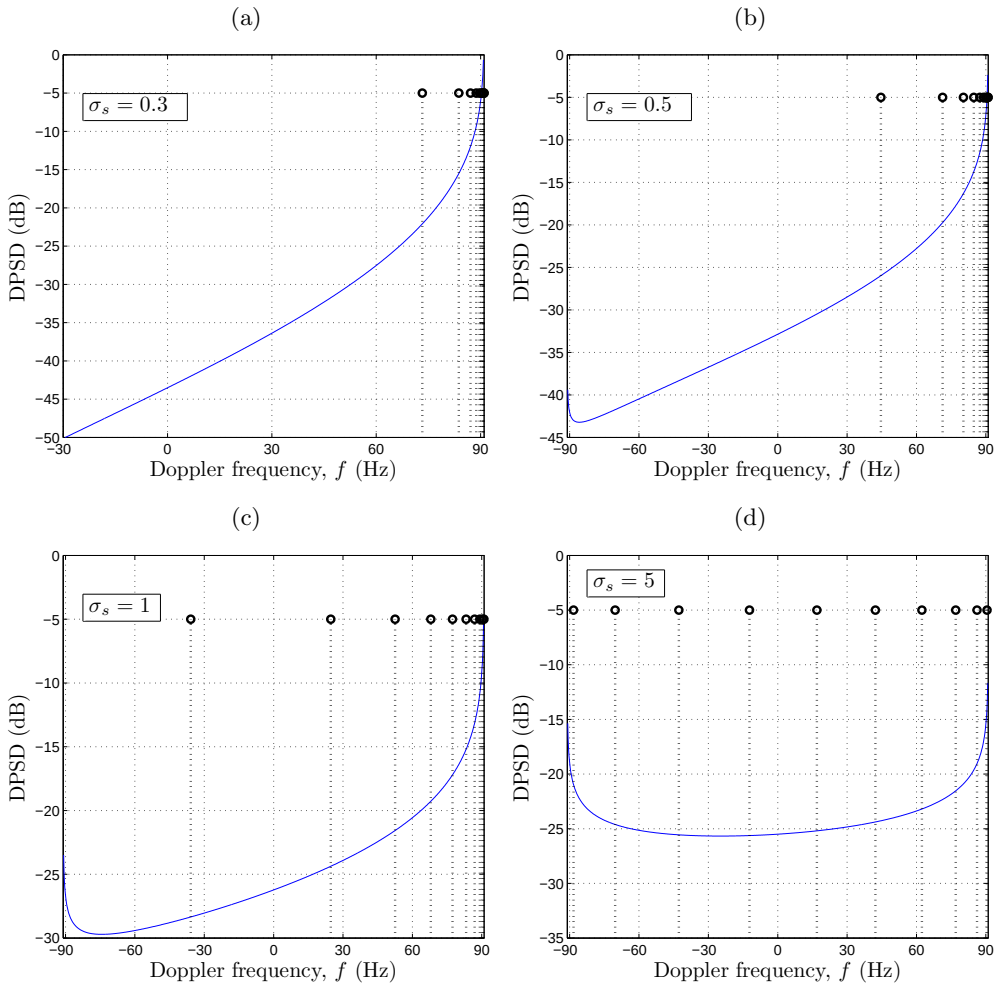

Figure 4.3: Comparison between the DPSD of the channel's diffuse component $\boldsymbol{\mu}(t)$ (blue-solid lines) and the DPSD of the random component $\hat{\boldsymbol{\mu}}(t)$ of the SOC-based simulation model (black-dotted lines with '$\circ$' markers) by considering the Laplacian PDF of the AOA and the GMEA ($f_{\max} = 91$ Hz, $\sigma^2_{\boldsymbol{\mu}} = 1$, and $N = 10$).

4.4 The RSAM

4.4.1 Description

4.4.1.1 Basic Approach

For the second parameter computation method, the RSAM, we will assume that the PDF of the random AOAs $\boldsymbol{\alpha}_n$ contains no singularities, so that one can regard the integral underlying the ACF of the channel's diffuse component [see (2.7)] as being a proper integral. Under such an assumption, the ACF of $\boldsymbol{\mu}(t)$ can be

written as a midpoint Riemann sum [Edwa98, Sec. 5.4] of the form

$$r_{\boldsymbol{\mu\mu}}(\tau) \;=\; \frac{2\pi\sigma_{\boldsymbol{\mu}}^2}{N} \lim_{N\to\infty} \sum_{n=1}^{N} g_{\boldsymbol{\alpha}}\Big(\frac{\pi}{N}\Big[n-\frac{1}{2}\Big]\Big) \exp\left\{ j2\pi f_{\max} \cos\Big(\frac{\pi}{N}\Big[n-\frac{1}{2}\Big]\Big)\tau \right\}.$$

If we drop the limit from the equation above, then we may presume that

$$r_{\boldsymbol{\mu\mu}}(\tau) \;\approx\; \frac{2\pi\sigma_{\boldsymbol{\mu}}^2}{N} \sum_{n=1}^{N} g_{\boldsymbol{\alpha}}\Big(\frac{\pi}{N}\Big[n-\frac{1}{2}\Big]\Big) \exp\left\{ j2\pi f_{\max} \cos\Big(\frac{\pi}{N}\Big[n-\frac{1}{2}\Big]\Big)\tau \right\}. \quad (4.26)$$

A comparison of (4.26) and the expression given in (3.5) for the ACF of $\hat{\boldsymbol{\mu}}(t)$ suggests that $r_{\hat{\boldsymbol{\mu}}\hat{\boldsymbol{\mu}}}(\tau)$ will render a good approximation to $r_{\boldsymbol{\mu\mu}}(\tau)$ if we choose:

$$\hat{\alpha}_n \;=\; \frac{\pi}{N}\Big(n-\frac{1}{2}\Big) \quad (4.27)$$

$$\hat{c}_n \;=\; \sigma_{\boldsymbol{\mu}} \sqrt{\frac{g_{\boldsymbol{\alpha}}(\hat{\alpha}_n)}{\sum_{m=1}^{N} g_{\boldsymbol{\alpha}}(\hat{\alpha}_m)}} \quad (4.28)$$

for $n = 1, \ldots, N$. The methodology given by (4.27) and (4.28) establishes a parameter computation method that we will refer to as the basic RSAM (BRSAM). It is worth mentioning that the idea behind the BRSAM has recently been applied in [Gut07a] to simulate mobile MIMO Rayleigh fading channels, yielding remarkable results concerning the emulation of the spatial CCF and temporal ACF of the channel. Interestingly, the Doppler frequencies $\hat{f}_n = f_{\max}\cos\big(\frac{\pi}{N}\big[n-\frac{1}{2}\big]\big)$ obtained by using this method always satisfy the Condition 3.3, and the fulfillment of the Condition 3.2 is guaranteed too provided that $[0, \pi)$ is partitioned into an even number of segments, implying that $N = 2M$, $M \in \mathbb{Z}^+$.

4.4.1.2 Problems of the Basic Approach

From experiments, we have observed that irrespective of the AOA statistics, the BRSAM produces an excellent approximation to the ACF of $\boldsymbol{\mu}(t)$ for values of τ close to the origin, say, $\tau \in \Big[-\frac{N}{4f_{\max}}, \frac{N}{4f_{\max}}\Big]$. However, our experiments have also revealed that this method performs poorly regarding the emulation of the envelope distribution of $\boldsymbol{\mu}(t)$ if the range of $g_{\boldsymbol{\alpha}}(\alpha)$ is huge. Under such circumstances, there is a large difference between the gains $\hat{c}_n$ of the cisoids. While this characteristic does not entail any problems for the emulation of $r_{\boldsymbol{\mu\mu}}(\tau)$, it does affect the ability of $\hat{\boldsymbol{\mu}}(t)$ for approximating the PDF of the envelope of $\boldsymbol{\mu}(t)$, as the envelope distribution of the simulation model's random component is heavily influenced by the gains $\hat{c}_n$ [see (3.21)]. Figures 4.4 and 4.5 illustrate the problem by considering the von Mises PDF $p_{\boldsymbol{\alpha}}^{\mathrm{VM}}(\alpha)$ with parameters $m_\alpha = 0^\circ$ and $\kappa \in \{10, 20\}$. Such parameters characterize the AOA statistics of propagation scenarios that exhibit

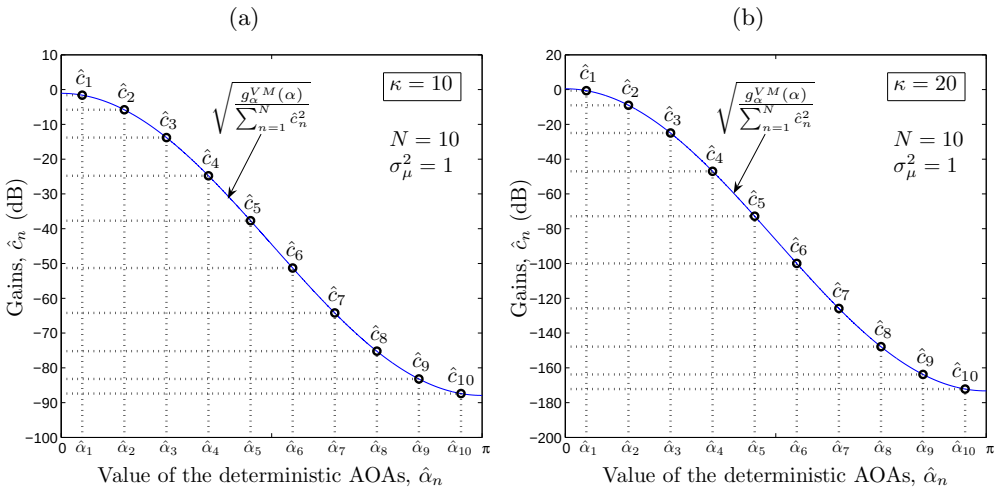

Figure 4.4: Relationship between the gains $\hat{c}_n$ and AOAs $\hat{\alpha}_n$ of the SOC-based simulation model's random component, $\hat{\boldsymbol{\mu}}(t)$, by applying the BRSAM to the von Mises PDF of the AOA with parameters $m_\alpha = 0°$ and $\kappa \in \{10, 20\}$.

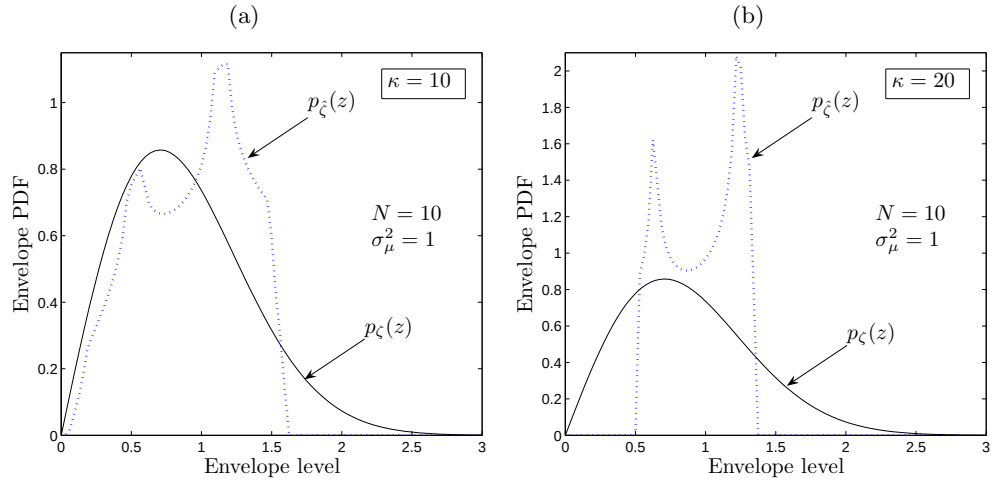

Figure 4.5: Comparison between the Rayleigh PDF ($p_{\boldsymbol{\zeta}}(z)$) and the first-order PDF of the envelope of the simulation model's random component ($p_{\hat{\boldsymbol{\zeta}}}(z)$) by applying the BRSAM to the von Mises PDF of the AOA with parameters $m_\alpha = 0°$ and $\kappa \in \{10, 20\}$.

severe non-isotropic scattering conditions. Figure 4.4 shows graphs of the relationship between the gains $\hat{c}_n$ and AOAs $\hat{\alpha}_n$ obtained by applying the BRSAM with $N = 10$. Plots of the Rayleigh distribution [Eq. (2.23)] and the PDF of the envelope of $\hat{\boldsymbol{\mu}}(t)$ [Eq. (3.21)] are presented in Fig. 4.5.

4.4.1.3 Improved Approach

To overcome the aforementioned problem, we will present in what follows an improved version of the BRSAM. To that end, we will assume that the PDF of the AOA is defined in such a way that its even part has at most one maximum in $[0, \pi)$. Thereby, for any given threshold $\gamma \in \big(0, \sup\{g_{\boldsymbol{\alpha}}(\alpha)\}_{\alpha\in[0,\pi)}\big)$, where $\sup\{\cdot\}$ denotes the supremum, we can identify one and only one subinterval $\mathcal{I}_U$ in $[0, \pi)$ satisfying

$$g_{\boldsymbol{\alpha}}(\alpha) \;\; > \;\; \gamma, \qquad \forall \alpha \in \mathcal{I}_U \tag{4.29}$$

implying that $g_{\boldsymbol{\alpha}}(\alpha)$ is above the threshold only along $\mathcal{I}_U$. If the value of γ is chosen small, so that $g_{\boldsymbol{\alpha}}(\alpha) \approx 0 \; \forall \alpha \notin \mathcal{I}_U$, then one can state that

$$r_{\boldsymbol{\mu}\boldsymbol{\mu}}(\tau) \;\; \approx \;\; \sigma^2_{\boldsymbol{\mu}} \int\limits_{\alpha\in\mathcal{I}_U} g_{\boldsymbol{\alpha}}(\alpha) \exp\{j2\pi f_{\max} \cos(\alpha)\tau\} d\alpha. \tag{4.30}$$

In such a case, it makes sense to compute the gains and AOAs of the stochastic SOC model described by $\hat{\boldsymbol{\mu}}(t)$ by taking into account only the subinterval $\mathcal{I}_U$. Following this reasoning, we will redefine the AOAs $\hat{\alpha}_n$ as follows

$$\hat{\alpha}_n \;\; = \;\; \alpha_\ell + \frac{\alpha_u - \alpha_\ell}{N} \left(n - \frac{1}{2} \right), \quad \alpha_u > \alpha_\ell \tag{4.31}$$

for $n = 1, \ldots, N$, where α_ℓ and α_u designate the lower and the upper boundaries of $\mathcal{I}_U$. The methodology given by (4.28) and (4.31) constitutes the RSAM. We observe that irrespective of the value of γ, the Doppler frequencies $\hat{f}_n = f_{\max} \cos\left(\alpha_\ell + \frac{\alpha_u - \alpha_\ell}{N} \left[n - \frac{1}{2}\right]\right)$ obtained by applying the RSAM always meet the Condition 3.3, such as in the case of the BRSAM. Nevertheless, in contrast to the BRSAM, the RSAM does not ensure the fulfillment of the Condition 3.2.

Choosing a proper value for the threshold γ is clearly the critical step in the RSAM. In fact, when setting the threshold, one has to be aware that the method will be affected by the same problems of the BRSAM if γ is too small. On the other hand, if γ is given a large value, then the RSAM will become more precise regarding the approximation of the envelope distribution of $\boldsymbol{\mu}(t)$, but it will loose accuracy with respect to the approximation of $r_{\boldsymbol{\mu}\boldsymbol{\mu}}(\tau)$. While determining an optimal value for γ is not a trivial issue, we have found from practice that setting $\gamma = 1 \times 10^{-3}$ results in case of the von Mises and Laplacian AOA distributions in a good approximation to $r_{\boldsymbol{\mu}\boldsymbol{\mu}}(\tau)$ and $p_{\boldsymbol{\zeta}}(z)$, as will be shown in Section 4.5.

The parameters $\hat{\alpha}_n$ and $\hat{c}_n$ can alternatively be computed by applying the RSAM directly on the DPSD of $\boldsymbol{\mu}(t)$. We can claim that if there exist only one subinterval $\mathcal{I}_U$ in $[0, \pi)$ for which (4.29) holds, then there exist only one

subinterval $\mathcal{V}_U = (f_\ell, f_u]$ in $(-f_{\max}, f_{\max}]$ satisfying

$$S_{\boldsymbol{\mu\mu}}(f) \;\geq\; \frac{\gamma \cdot 2\,\sigma_{\boldsymbol{\mu}}^2}{f_{\max}\sqrt{1-(f/f_{\max})^2}}, \qquad \forall f \in \mathcal{V}_U. \tag{4.32}$$

The transformation $\alpha = \arccos(f/f_{\max})$ establishes a one-to-one relation between the points in $\mathcal{V}_U$ and $\mathcal{I}_U$. Thus, by means of such a transformation, we can rewrite (4.28) and (4.31) as follows:

$$\hat{c}_n \;=\; \sigma_{\boldsymbol{\mu}} \sqrt{\frac{S_{\boldsymbol{\mu\mu}}\big(\arccos(\hat{f}_n/f_{\max})\big)\sqrt{f_{\max}^2-\hat{f}_n^2}}{\sum_{m=1}^{N} S_{\boldsymbol{\mu\mu}}\big(\arccos(\hat{f}_m/f_{\max})\big)\sqrt{f_{\max}^2-\hat{f}_m^2}}} \tag{4.33}$$

$$\begin{aligned}\hat{\alpha}_n \;=\;& \frac{1}{\pi}\arccos\left(\frac{f_u}{f_{\max}}\right) + \frac{1}{N}\left(n-\frac{1}{2}\right) \\ & \times \arccos\left(\frac{f_\ell f_u + \sqrt{\big(f_{\max}^2-f_\ell^2\big)\big(f_{\max}^2-f_u^2\big)}}{f_{\max}^2}\right)\end{aligned} \tag{4.34}$$

for $n = 1, \ldots, N$.

The RSAM has been presented here upon the implicit assumption that there exists only one cluster of scatterers in the proximities of the receiver. However, it has been reported from measurements [Spen00] that several clusters of scatterers may surround the mobile terminal. Consequently, the function $g_{\boldsymbol{\alpha}}(\alpha)$ could have two or more maximums in $[0, \pi)$, so that various disjoint subintervals $\mathcal{I}_{U,m}$ might be identified in $[0, \pi)$ satisfying $g_{\boldsymbol{\alpha}}(\alpha) > \gamma \; \forall \alpha \in \mathcal{I}_{U,m}$, $m = 1, \ldots, M$, $2 \leq M < \infty$. For the simulation of such a kind of channels, we refer the reader to [Gut09a], where the RSAM has been extended with respect to multiple clusters of scatters.

4.4.2 Implementation

In order to demonstrate the implementation of the RSAM, let us consider again the von Mises and the Laplacian AOAs distributions. The parameters $\hat{c}_n$ and $\hat{\alpha}_n$ can be computed by applying the method either on the PDF of the AOA or on the DPSD of $\hat{\boldsymbol{\mu}}(t)$. In this dissertation, we will focus our attention on the former approach.

4.4.2.1 von Mises Distributed AOAs

In the case of the von Mises PDF[1], $p_{\boldsymbol{\alpha}}^{\mathrm{VM}}(\alpha)$, the boundaries of the subinterval $\mathcal{I}_U = [\alpha_\ell, \alpha_u)$ are to be found by identifying the points in $[0, \pi)$ at which the function $g_{\boldsymbol{\alpha}}^{\mathrm{VM}}(\alpha)$ crosses the threshold γ from up to down (corresponding to α_u)

[1] We note that the von Mises PDF $p_{\boldsymbol{\alpha}}^{\mathrm{VM}}(\alpha)$ and its even part $g_{\boldsymbol{\alpha}}^{\mathrm{VM}}(\alpha)$ have only one maximum in $[0, \pi)$, so that at most one subinterval $\mathcal{I}_U$ can be identified in $[0, \pi)$ satisfying (4.29).

and/or from down to up (corresponding to α_ℓ). This has to be done in general by solving $g_{\boldsymbol{\alpha}}^{\mathrm{VM}}(\alpha) - \gamma = 0$ with the aid of numerical root-finding techniques. However, if $m_\alpha \in \{-\pi, 0, \pi\}$ and $\kappa > 0$, then the von Mises PDF proves to be an even function that decreases (for $m_\alpha = 0$) or increases (for $m_\alpha = \pm\pi$) monotonically in $[0, \pi)$. Thus, for such values of m_α and κ, there is at most one real solution to $g_{\boldsymbol{\alpha}}^{\mathrm{VM}}(\alpha) - \gamma = 0$, $\alpha \in (0, \pi)$, which if happens to exist is then given by

$$\alpha^+ = \arccos\left(\frac{\ln\left(2\pi\gamma I_o(\kappa)\right)}{\kappa\cos(m_\alpha)}\right). \tag{4.35}$$

Consequently, the boundaries of $\mathcal{I}_U$ can be found by following

$$\alpha_\ell = \begin{cases} \alpha^+, & \text{if } g_{\boldsymbol{\alpha}}^{\backprime\mathrm{VM}}(\alpha^+) > 0 \\ 0, & \begin{cases} \text{if } g_{\boldsymbol{\alpha}}^{\backprime\mathrm{VM}}(\alpha^+) \leq 0 \\ \text{or } g_{\boldsymbol{\alpha}}^{\mathrm{VM}}(\alpha) \neq \gamma, \quad \forall\alpha \in [0, \pi) \end{cases} \end{cases} \tag{4.36}$$

$$\alpha_u = \begin{cases} \alpha_k^+, & \text{if } g_{\boldsymbol{\alpha}}^{\backprime\mathrm{VM}}(\alpha^+) < 0 \\ \pi, & \begin{cases} \text{if } g_{\boldsymbol{\alpha}}^{\backprime\mathrm{VM}}(\alpha^+) \geq 0 \\ \text{or } g_{\boldsymbol{\alpha}}^{\mathrm{VM}}(\alpha) \neq \gamma, \quad \forall\alpha \in [0, \pi) \end{cases} \end{cases} \tag{4.37}$$

for $\kappa > 0$, where α^+ is given by (4.35) and

$$g_{\boldsymbol{\alpha}}^{\backprime\mathrm{VM}}(\alpha) = \frac{dg_{\boldsymbol{\alpha}}^{\mathrm{VM}}(\alpha)}{d\alpha} \tag{4.38}$$

$$= \frac{-\kappa}{2\pi I_0(\kappa)}\Big\{\sin(\alpha - m_\alpha)\exp\{\kappa\cos(\alpha - m_\alpha)\} + \sin(\alpha + m_\alpha)\exp\{\kappa\cos(\alpha + m_\alpha)\}\Big\}. \tag{4.39}$$

On the other hand, if $\kappa = 0$, then the boundaries of $\mathcal{I}_U$ are equal to $\alpha_\ell = 0$ and $\alpha_u = \pi$, and it can be shown that $\hat{f}_n = f_{\max}\cos\left(\frac{\pi}{N}\left[n - \frac{1}{2}\right]\right)$ and $\hat{c}_n = \sigma_{\boldsymbol{\mu}}\sqrt{1/N}$, $n = 1, \ldots, N$. Under such circumstances, the RSAM and the GMEA are equivalent to each other, and the EMEDS happens to be a special case also of the RSAM for the design of simulation models for isotropic scattering channels. In fact, the RSAM and the EMEDS are developed upon similar approaches. This is evident, as the latter method has essentially been derived from a Riemann sum approximation of the ACF $r_{\boldsymbol{\mu}\boldsymbol{\mu}}(\tau) = J_0(2\pi f_{\max}\tau)$ characterizing isotropic scattering channels [Pae02a, Sec. 5.1.6].

4.4.2.2 Laplacian Distributed AOAs

In the case of the Laplacian distribution, $p_{\boldsymbol{\alpha}}^{\mathrm{LA}}(\alpha)$, the lower boundary of $\mathcal{I}_U$ is in all cases equal to $\alpha_\ell = 0$, since the even part of $p_{\boldsymbol{\alpha}}^{\mathrm{LA}}(\alpha)$ is a monotonically decreasing

function in $[0, \pi)$ and therefore no up-crossings occur within that interval. In turn, the upper boundary of $\mathcal{I}_U$ is found to be given as

$$\alpha_u = -\frac{\sigma_s}{\sqrt{2}} \ln(\gamma c_s) \tag{4.40}$$

which is the solution of $g_{\boldsymbol{\alpha}}^{\mathrm{LA}}(\alpha) - \gamma = 0$. If the equation above has no solution in $[0, \pi)$, then α_u is set equal to π.

A comparison between the DPSDs of $\hat{\boldsymbol{\mu}}(t)$ and $\boldsymbol{\mu}(t)$ by applying the RSAM to the von Mises and Laplacian PDFs is given in Figs. 4.6 and 4.7, respectively. One may notice from these figures that the DPSD of $\hat{\boldsymbol{\mu}}(t)$ exhibits a trend similar as the one described by the DPSD of $\boldsymbol{\mu}(t)$. Such a characteristic is reflected by the power of the cisoids of $\hat{\boldsymbol{\mu}}(t)$.

4.5 Performance Analysis

In this section, we will analyze the performance of the proposed parameter computation methods with respect to the emulation of the correlation and spectral characteristics of $\boldsymbol{\mu}(t)$, as well as in terms of the approximation of the fading statistics of the reference model described by the composite process $\boldsymbol{\nu}(t) = \boldsymbol{\mu}(t) + m_\rho(t)$. In addition, the performance of such methods will be compared with that of the LPNM I, LPNM II, and LPNM III. For the aforementioned purposes, we will assume that the channel's AOA statistics follow the von Mises distribution. We focus our attention on this distribution since a wide variety of propagation scenarios can be studied from it, spanning from isotropic to non-isotropic scattering scenarios. However, results obtained by considering the Laplacian PDF can be found in[2] [Gut09b]. The conclusions drawn in that paper about the methods' performance are the same as the ones presented in this chapter.

We carry out our simulations by choosing $f_{\max} = 91$ Hz, $\sigma_{\boldsymbol{\mu}}^2 = 1$, and taking into account six different propagation scenarios characterized by the von Mises PDF with pairs of parameters: $(m_\alpha = 0^\circ, \kappa = 0)$; $(m_\alpha = 0^\circ, \kappa = 5)$; $(m_\alpha = 0^\circ, \kappa = 20)$; $(m_\alpha = 0^\circ, \kappa = 10)$; $(m_\alpha = 30^\circ, \kappa = 10)$; $(m_\alpha = 90^\circ, \kappa = 10)$. The first and the last of such pairs of parameters are related to channels having diffuse components characterized by symmetrical DPSDs, whereas the other four pairs are associated to channels with asymmetrical DPSDs, as illustrated in Fig. 2.5.

Regarding the methods' configuration, we set $\gamma = 1 \times 10^{-3}$ for the RSAM, whilst we consider $p = 2$ and $\tau_{\max} = N/(4f_{\max})$ for the three versions of the LPNM. In the case of the LPNM I, we use the Doppler frequencies produced by the GMEA as initial values to minimize the L_p-norm $\epsilon_{r_{\boldsymbol{\mu}\boldsymbol{\mu}}}^{(p)}$ defined in (4.3). On the other hand, for the LPNM II and LPNM III, we employ the gains and

[2]We point out, nonetheless, that due to the space limitation, the results obtained for the LPNM II and LPNM III are not presented in [Gut09b].

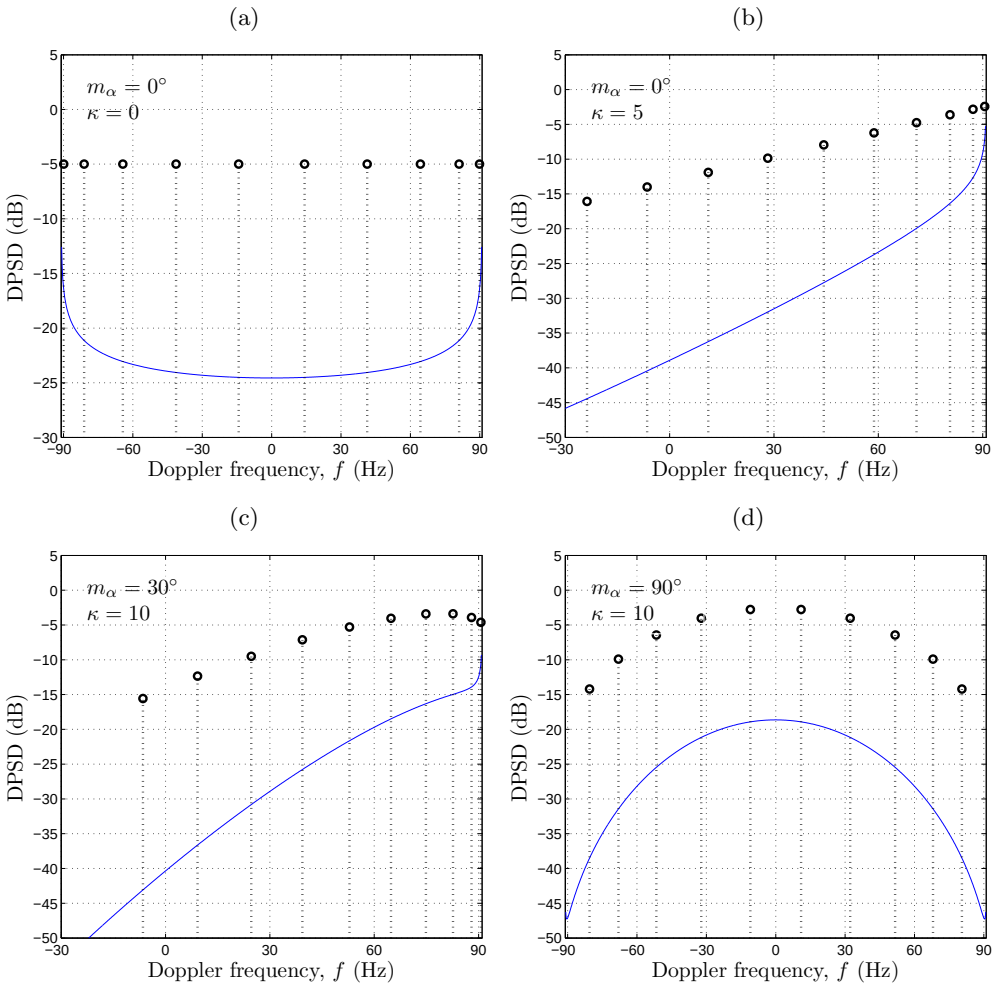

Figure 4.6: Comparison between the DPSD of the channel's diffuse component (blue-solid lines) and the DPSD of the random component of the SOC-based simulation model (black-dotted lines with '$\circ$' markers) by considering the von Mises PDF of the AOA and the RSAM ($f_{\max} = 91$ Hz, $\sigma^2_{\boldsymbol{\mu}} = 1$, $\gamma = 1 \times 10^{-3}$, and $N = 10$).

Doppler frequencies produced by the RSAM as initial conditions to minimize the cost function $\epsilon^{(p)}_{r_{\boldsymbol{\mu\mu}}, p_{\boldsymbol{\zeta}}}$ introduced in (4.4). Following the experiments performed in [Pae02a, Sec. 5.1.5], we set the underlying weighting factors W_1 and W_2 of $\epsilon^{(p)}_{r_{\boldsymbol{\mu\mu}}, p_{\boldsymbol{\zeta}}}$ to $W_1 = 1/4$ and $W_2 = 3/4$.

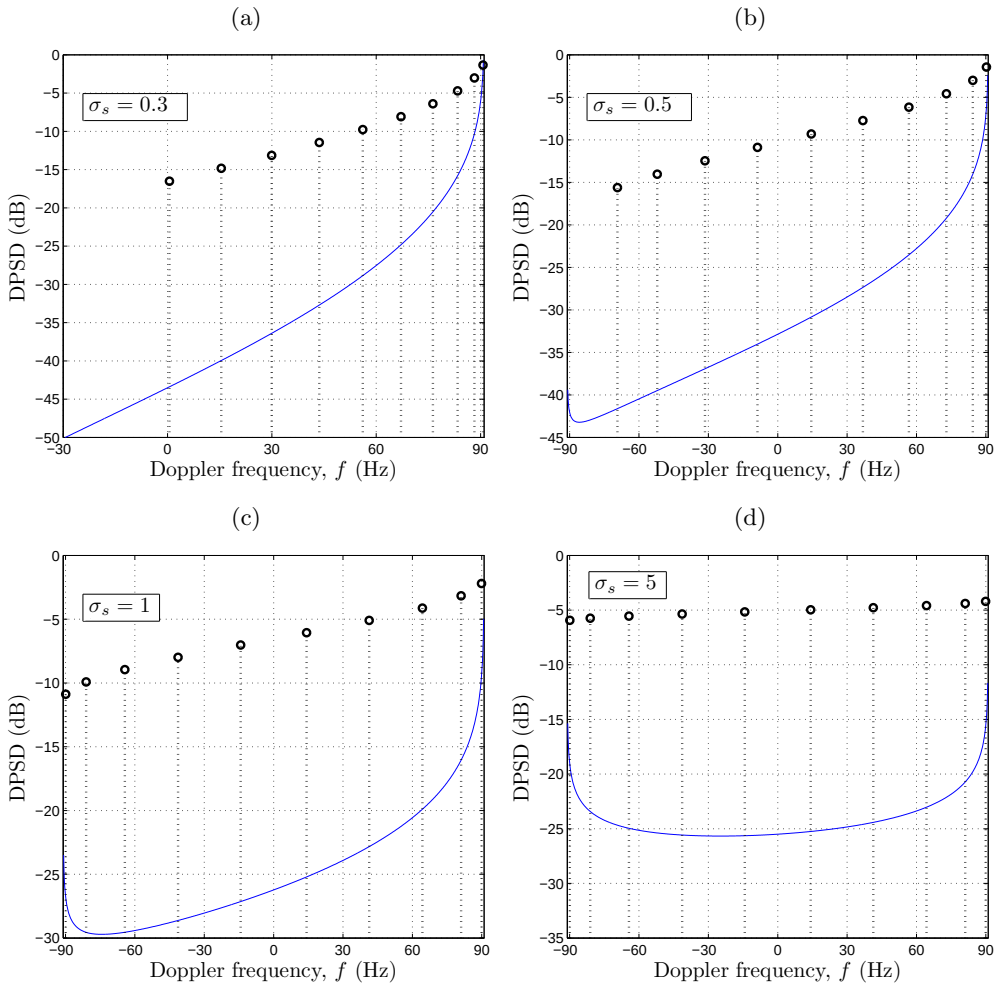

Figure 4.7: Comparison between the DPSD of the channel's diffuse component (blue-solid lines) and the DPSD of the random component of the SOC-based simulation model (black-dotted lines with '$\circ$' markers) by considering the Laplacian PDF of the AOA and the RSAM ($f_{\max} = 91$ Hz, $\sigma^2_{\boldsymbol{\mu}} = 1$, $\gamma = 1 \times 10^{-3}$, and $N = 10$).

4.5.1 Emulation of the Correlation and Spectral Characteristics of the Reference Model's Random Component

4.5.1.1 ACF

Figures 4.8–4.10 show a comparison between the absolute value of the ACF of the channel's diffuse component [see (2.46)] and the absolute value of the ACF of $\hat{\boldsymbol{\mu}}(t)$ by applying the parameter computation methods under consideration with $N = 20$. For the sake of clarity, we present the results obtained for the three version of the LPNM in different figures. In addition to theoretical curves of

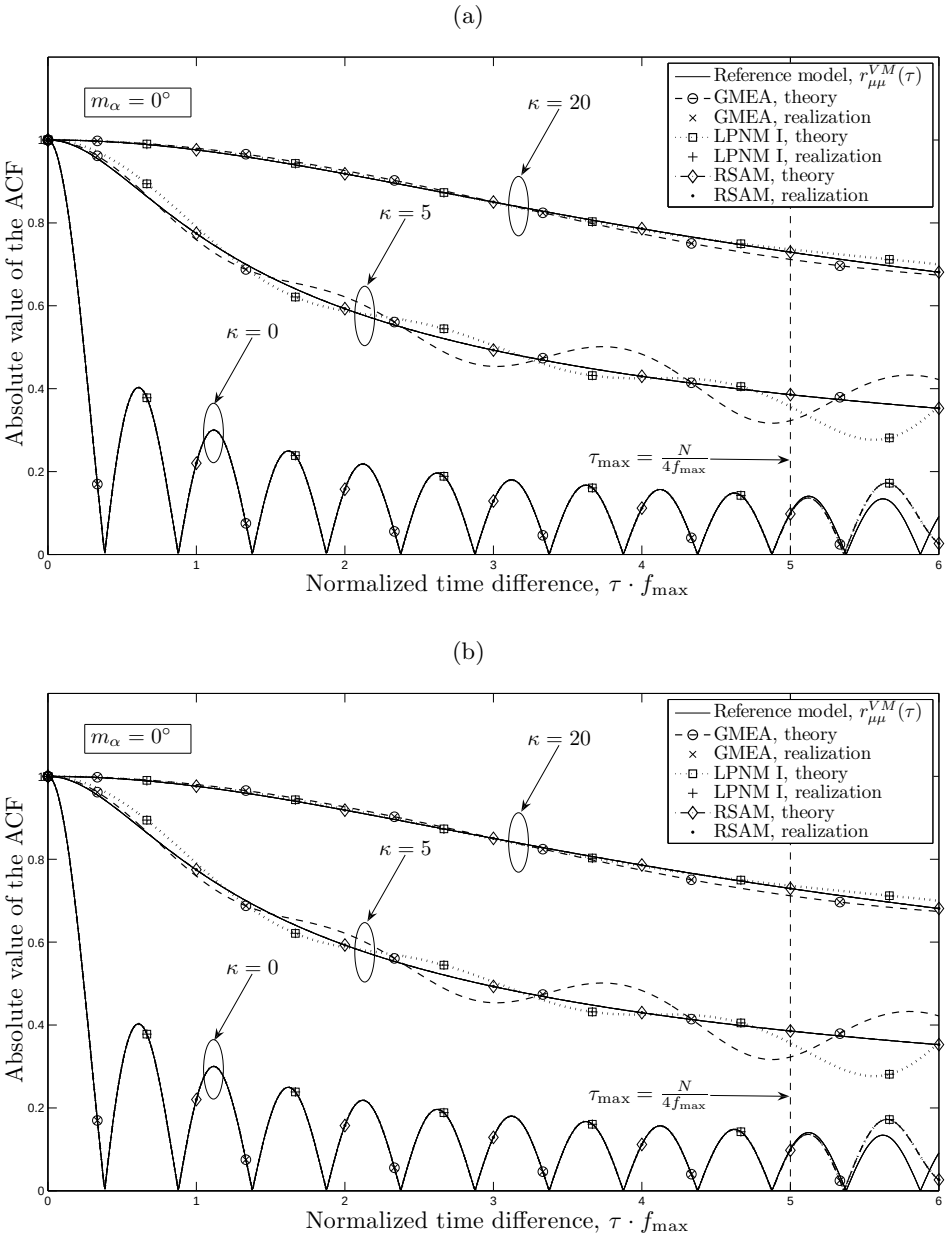

Figure 4.8: Comparison among the GMEA, RSAM, and LPNM I in terms of the emulation of the ACF of channel's diffuse component (reference model) by considering the von Mises PDF of the AOA with different pairs of parameters m_α and κ ($f_{\max} = 91$ Hz, $\sigma_{\boldsymbol{\mu}}^2 = 1$, $N = 20$, $\gamma = 1 \times 10^{-3}$, $p = 2$, and $\tau_{\max} = N/(4f_{\max})$).

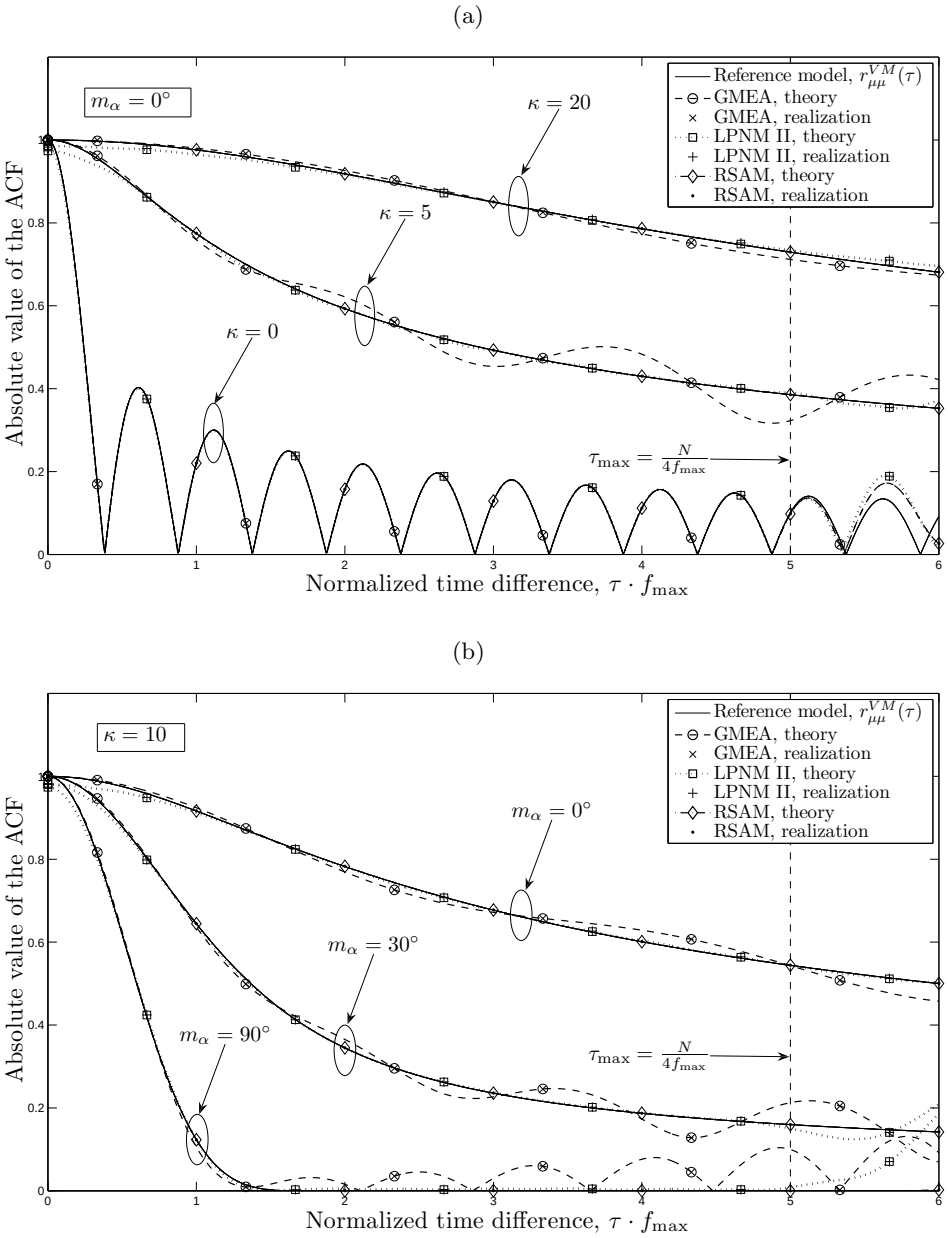

Figure 4.9: Comparison among the GMEA, RSAM, and LPNM II in terms of the emulation of the ACF of channel's diffuse component (reference model) by considering the von Mises PDF of the AOA with different pairs of parameters m_α and κ ($f_{\max} = 91$ Hz, $\sigma_{\boldsymbol{\mu}}^2 = 1$, $N = 20$, $\gamma = 1 \times 10^{-3}$, $p = 2$, and $\tau_{\max} = N/(4f_{\max})$).

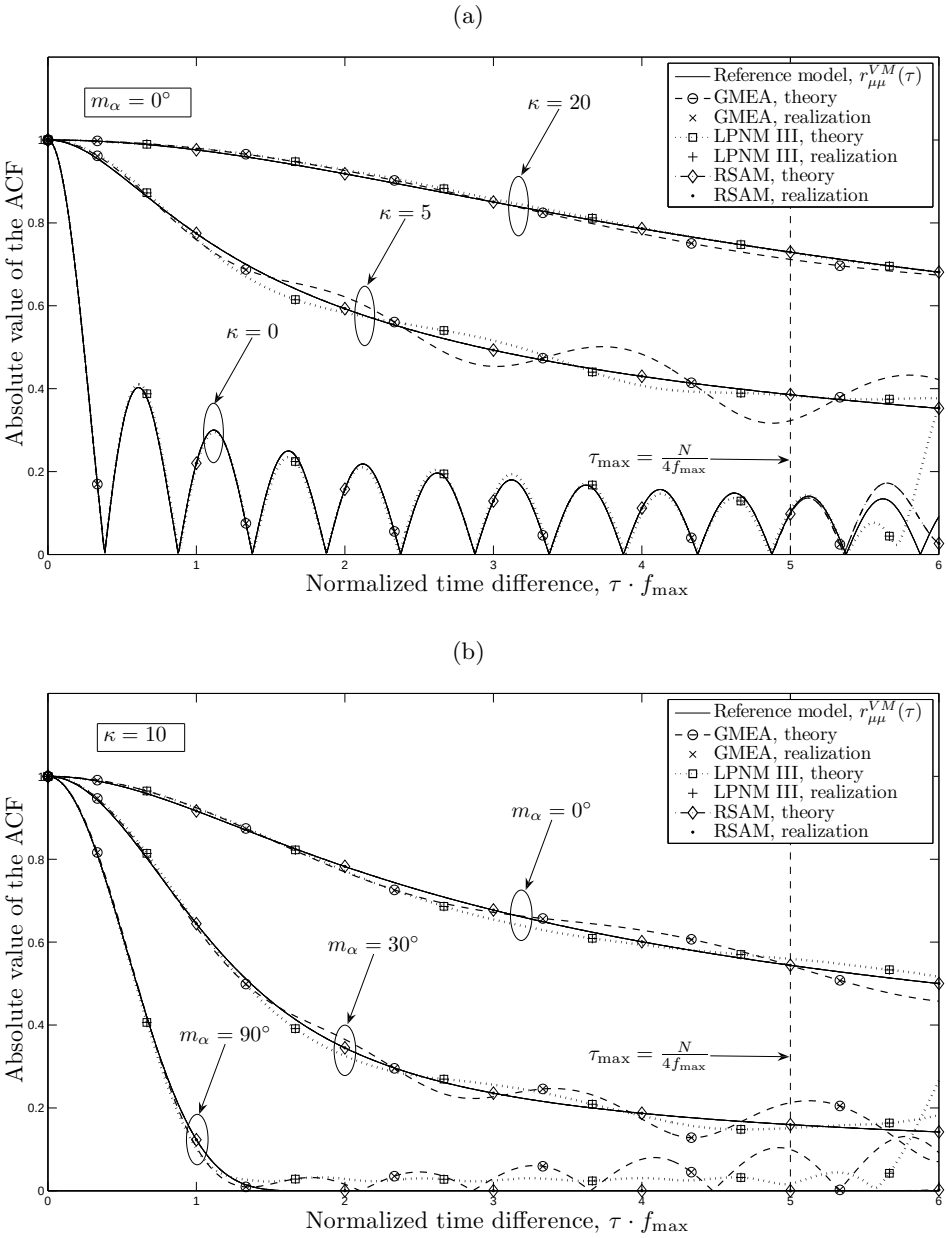

Figure 4.10: Comparison among the GMEA, RSAM, and LPNM III in terms of the emulation of the ACF of channel's diffuse component (reference model) by considering the von Mises PDF of the AOA with different pairs of parameters m_α and κ ($f_{\max} = 91$ Hz, $\sigma_{\boldsymbol{\mu}}^2 = 1$, $N = 20$, $\gamma = 1 \times 10^{-3}$, $p = 2$, and $\tau_{\max} = N/(4f_{\max})$).

$|r_{\hat{\boldsymbol{\mu}}\hat{\boldsymbol{\mu}}}(\tau)|$ [see (3.5)], Figs. 4.8–4.10 present empirical graphs of the absolute value of the time-averaged ACF $r_{\hat{\mu}\hat{\mu}}(\tau)$ of the sample functions of $\hat{\boldsymbol{\mu}}(t)$. Such graphs were generated by considering a single realization of $\hat{\boldsymbol{\mu}}(t)$. It can be seen in the figures that the graphs of $|r_{\hat{\mu}\hat{\mu}}(\tau)|$ match perfectly the ones of $|r_{\hat{\boldsymbol{\mu}}\hat{\boldsymbol{\mu}}}(\tau)|$, meaning that the autocorrelation-ergodicity of $\hat{\boldsymbol{\mu}}(t)$ is preserved by all methods.

Concerning the methods' performance, one may observe from the results presented in the three figures that the RSAM outperforms by far the LPNM and the GMEA. In fact, in the case of the RSAM, no differences between $|r^{\mathrm{VM}}_{\boldsymbol{\mu}\boldsymbol{\mu}}(\tau)|$ and $|r_{\hat{\boldsymbol{\mu}}\hat{\boldsymbol{\mu}}}(\tau)|$ are visible within the interval $[0, 5/f_{\max}]$. The six curves of $|r_{\hat{\boldsymbol{\mu}}\hat{\boldsymbol{\mu}}}(\tau)|$ corresponding to such a method can be distinguished from those of $|r^{\mathrm{VM}}_{\boldsymbol{\mu}\boldsymbol{\mu}}(\tau)|$ only with the aid of the markers '$\diamond$' and '$\cdot$'. Even though the performance of the LPNM and GMEA is not as impressive as that of the RSAM, these two methods produced a quite good approximation to $r^{\mathrm{VM}}_{\boldsymbol{\mu}\boldsymbol{\mu}}(\tau)$. Interestingly, the LPNM II provided very good results for $\tau \in [1/f_{\max}, 5/f_{\max}]$, although the quality of the relationship $|r_{\hat{\boldsymbol{\mu}}\hat{\boldsymbol{\mu}}}(\tau)| \approx |r^{\mathrm{VM}}_{\boldsymbol{\mu}\boldsymbol{\mu}}(\tau)|$ is rather poor around the origin. Indeed, Fig. 4.8 clearly shows that the LPNM II does not satisfy the boundary condition $r_{\hat{\boldsymbol{\mu}}\hat{\boldsymbol{\mu}}}(0) = r_{\boldsymbol{\mu}\boldsymbol{\mu}}(0)$, meaning that $\sum_{n=1}^{N} \hat{c}_n^2 \neq \sigma^2_{\boldsymbol{\mu}}$.

Without surprise, we can see in Figs. 4.8–4.10 that the LPNM performs better than the GMEA. Nonetheless, the graphs of $|r_{\hat{\boldsymbol{\mu}}\hat{\boldsymbol{\mu}}}(\tau)|$ associated to the GMEA are in general closer to those of $|r^{\mathrm{VM}}_{\boldsymbol{\mu}\boldsymbol{\mu}}(\tau)|$ at the vicinities of the origin than the graphs obtained by using the LPNM I and the LPNM II. This remarkable characteristic suggests that the GMEA is better suited than those versions of the LPNM to approximate the statistics of $\boldsymbol{\mu}(t)$ that depend only on the value, slope, and curvature of $r_{\boldsymbol{\mu}\boldsymbol{\mu}}(\tau)$ at $\tau = 0$ (e.g., the average Doppler shift, Doppler spread, LCR, and ADF).

The resulting rms error, $\epsilon^{(2)}_{r_{\boldsymbol{\mu}\boldsymbol{\mu}}}$, between $r_{\hat{\boldsymbol{\mu}}\hat{\boldsymbol{\mu}}}(\tau)$ and $r^{\mathrm{VM}}_{\boldsymbol{\mu}\boldsymbol{\mu}}(\tau)$ [see (4.3)] is shown in Fig. 4.11. The error $\epsilon^{(2)}_{r_{\boldsymbol{\mu}\boldsymbol{\mu}}}$ is plotted there by considering $N \in \{10, 20, 30, 40, 50\}$. To enable a fair comparison with the LPNM, we set $\tau_{\max}$ to $N/(4f_{\max})$. The obtained results confirm that the RSAM is better suited than the other methods to approximate $r^{\mathrm{VM}}_{\boldsymbol{\mu}\boldsymbol{\mu}}(\tau)$. The results also show that the LPNM produces a smaller error than the GMEA, as was to be expected. Among the three versions under analysis, the LPNM II performed the best, although in some cases it registered a larger error than the LPNM I. Interestingly, the LPNM III produced in general worse results than the other two versions of the LPNM, specially when the number of cisoids was small ($N \leq 30$). This is due to the fact that the LPNM III has to sacrifice some accuracy in the approximation of $r_{\boldsymbol{\mu}\boldsymbol{\mu}}(\tau)$ to ensure that the boundary conditions $r_{\hat{\boldsymbol{\mu}}\hat{\boldsymbol{\mu}}}(\tau) = r_{\boldsymbol{\mu}\boldsymbol{\mu}}(\tau)$ and $\ddot{r}_{\hat{\boldsymbol{\mu}}\hat{\boldsymbol{\mu}}}(\tau) = \ddot{r}_{\boldsymbol{\mu}\boldsymbol{\mu}}(\tau)$ are fulfilled. However, such a sacrifice pays off when it comes to the emulation of the average Doppler shift and Doppler spread of $\boldsymbol{\mu}(t)$, as will be shown next.

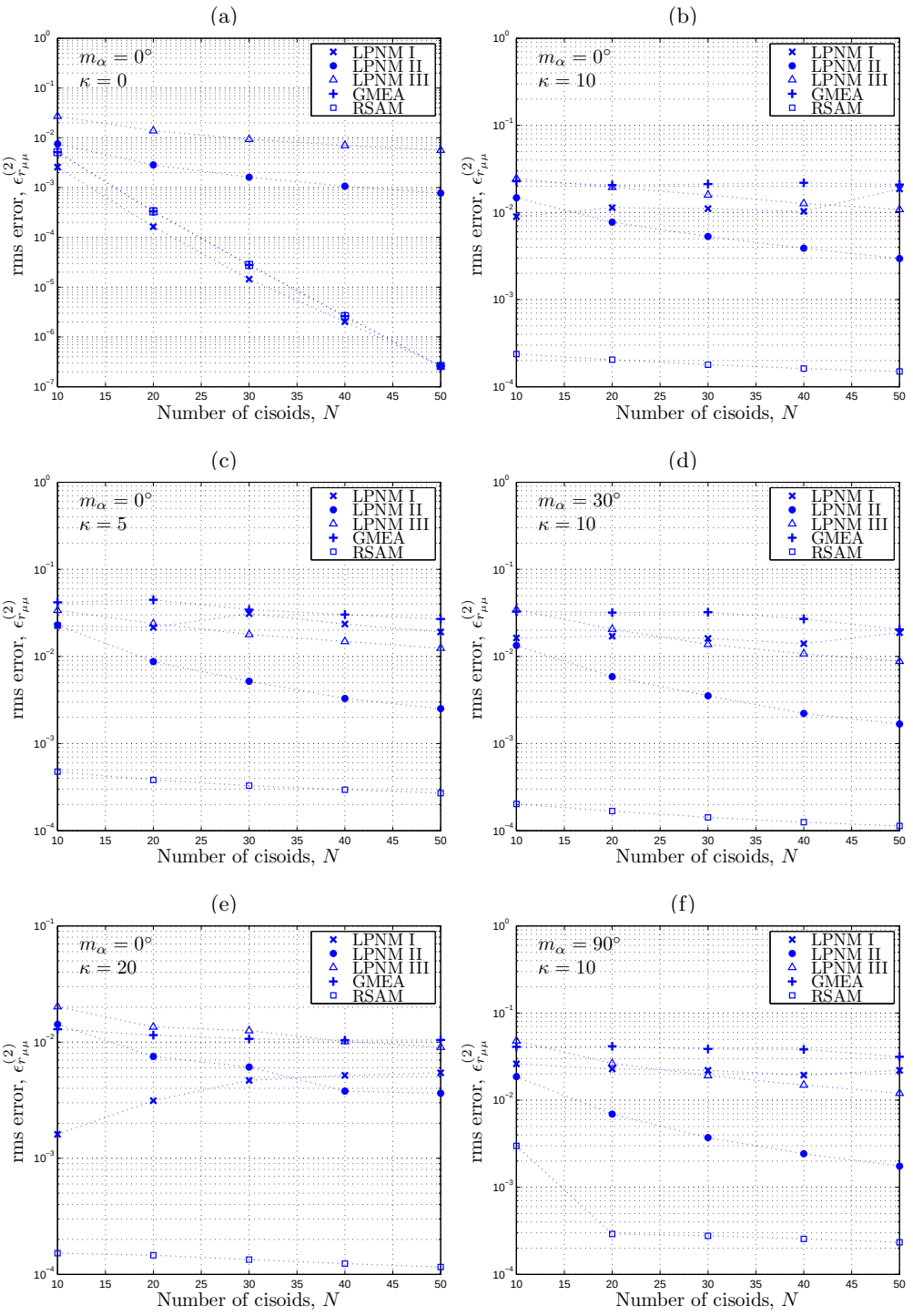

Figure 4.11: Root mean square error function between the ACF of the channel's diffuse component and the ACF of the SOC-based simulation model's random component by considering the von Mises PDF of the AOA and the GMEA, RSAM, and LPNM ($\tau_{\max} = N/(4f_{\max})$).

4.5.1.2 Average Doppler Shift and Doppler Spread

With respect to the emulation of the spectral characteristics of $\boldsymbol{\mu}(t)$, we plot in Fig. 4.12 the absolute error

$$\epsilon_{A_{\boldsymbol{\mu}\boldsymbol{\mu}}} = |A_{\boldsymbol{\mu}\boldsymbol{\mu}} - A_{\hat{\boldsymbol{\mu}}\hat{\boldsymbol{\mu}}}| \tag{4.41}$$

between the average Doppler shift of $\boldsymbol{\mu}(t)$ [Eq. (2.49)] and the average Doppler shift of $\hat{\boldsymbol{\mu}}(t)$ [Eq. 3.17]. In addition, results obtained for the relative error

$$\epsilon_{D_{\boldsymbol{\mu}\boldsymbol{\mu}}} = \frac{|D_{\boldsymbol{\mu}\boldsymbol{\mu}} - D_{\hat{\boldsymbol{\mu}}\hat{\boldsymbol{\mu}}}|}{D_{\boldsymbol{\mu}\boldsymbol{\mu}}} \tag{4.42}$$

between the Doppler spreads of $\boldsymbol{\mu}(t)$ [Eq. 2.50] and $\hat{\boldsymbol{\mu}}(t)$ [Eq. 3.18] are shown in Fig. 4.13. Again, we have considered $N \in \{10, 20, 30, 40, 50\}$ to evaluate these error functions.

The results presented in Figs. 4.12 and 4.13 indicate that the RSAM performs better than the LPNM and GMEA regarding the emulation of $A_{\boldsymbol{\mu}\boldsymbol{\mu}}$ and $D_{\boldsymbol{\mu}\boldsymbol{\mu}}$. Furthermore, the obtained results confirm that GMEA is in general better suited than the LPNM I and LPNM II to approximate the average Doppler shift and the Doppler spread of $\boldsymbol{\mu}(t)$. Interestingly, the performance of the RSAM is essentially the same irrespective of the value of N, meaning that the number of cisoids exerts little influence on the slope and curvature of $r_{\hat{\boldsymbol{\mu}}\hat{\boldsymbol{\mu}}}(0)$ when the parameters of $\hat{\boldsymbol{\mu}}(t)$ are computed by applying such a method. On the contrary, the results produced by the LPNM and GMEA reveal that the slope and curvature of $r_{\hat{\boldsymbol{\mu}}\hat{\boldsymbol{\mu}}}(0)$ are highly sensitive to the value of N when applying these methods.

We mentioned in Section 2.3.3 that the average Doppler shift of $\boldsymbol{\mu}(t)$ is equal to zero when the DPSD characterizing such a process is symmetrical with respect to the origin. In this respect, it can be shown that the average Doppler shift of the simulation model's random component is equal to zero for both the RSAM and the GMEA if $S_{\boldsymbol{\mu}\boldsymbol{\mu}}(f)$ is symmetrical—the proof of this statement is a consequence of the theorems presented in Appendix E. The results presented in Fig. 4.12 for the two propagation scenarios associated with symmetrical DPSDs (cases: $m_\alpha = 0°$, $\kappa = 0$; and $m_\alpha = 90°$, $\kappa = 10$) provide evidence of the veracity of such a claim. Since the observation of $A_{\hat{\boldsymbol{\mu}}\hat{\boldsymbol{\mu}}} = 0$ indicates that the IQ components of $\hat{\boldsymbol{\mu}}(t)$ are uncorrelated [see Sec. 3.3.3.1 and 3.3.3.3], we can conclude that the GMEA and RSAM are suitable methods for the design of SOC-based simulation models for fading channel having diffuse components with uncorrelated IQ components. Such a conclusion cannot be extrapolated to the case of the LPNM, because this method produces in general an average Doppler shift that is different from zero, as one can observe in Figs. 4.12(a) and 4.12(f). Not even the LPNM III, which satisfies the boundary conditions $r_{\hat{\boldsymbol{\mu}}\hat{\boldsymbol{\mu}}}(0) = r_{\boldsymbol{\mu}\boldsymbol{\mu}}(0)$ and $\ddot{r}_{\hat{\boldsymbol{\mu}}\hat{\boldsymbol{\mu}}}(0) = \ddot{r}_{\boldsymbol{\mu}\boldsymbol{\mu}}(0)$, is

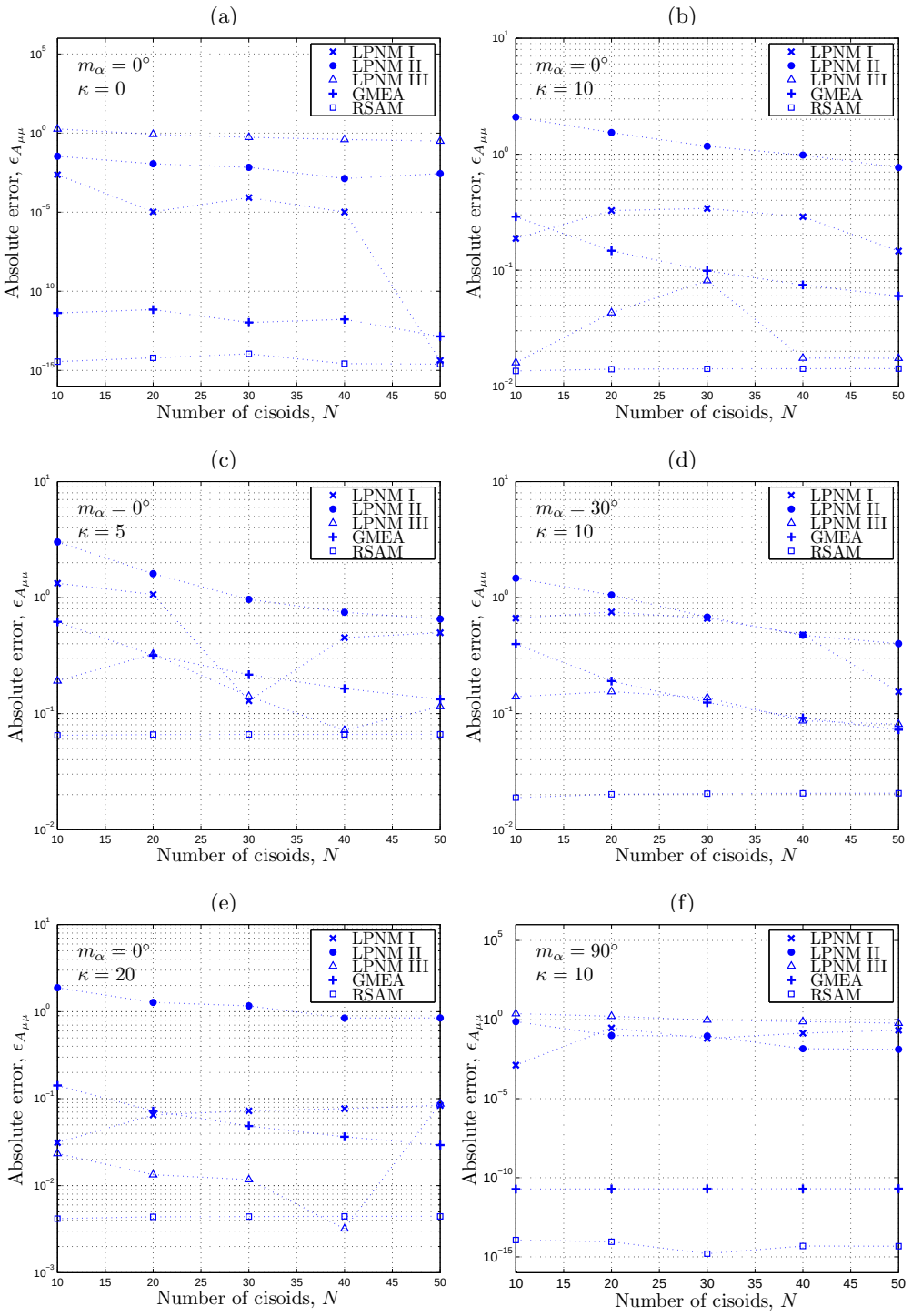

Figure 4.12: Absolute error $\epsilon_{A_{\mu\mu}}$ between the average Doppler shift of the channel's diffuse component and the average Doppler shift of the SOC-based simulation model's random component by considering the von Mises PDF of the AOA and the GMEA, RSAM, and LPNM.

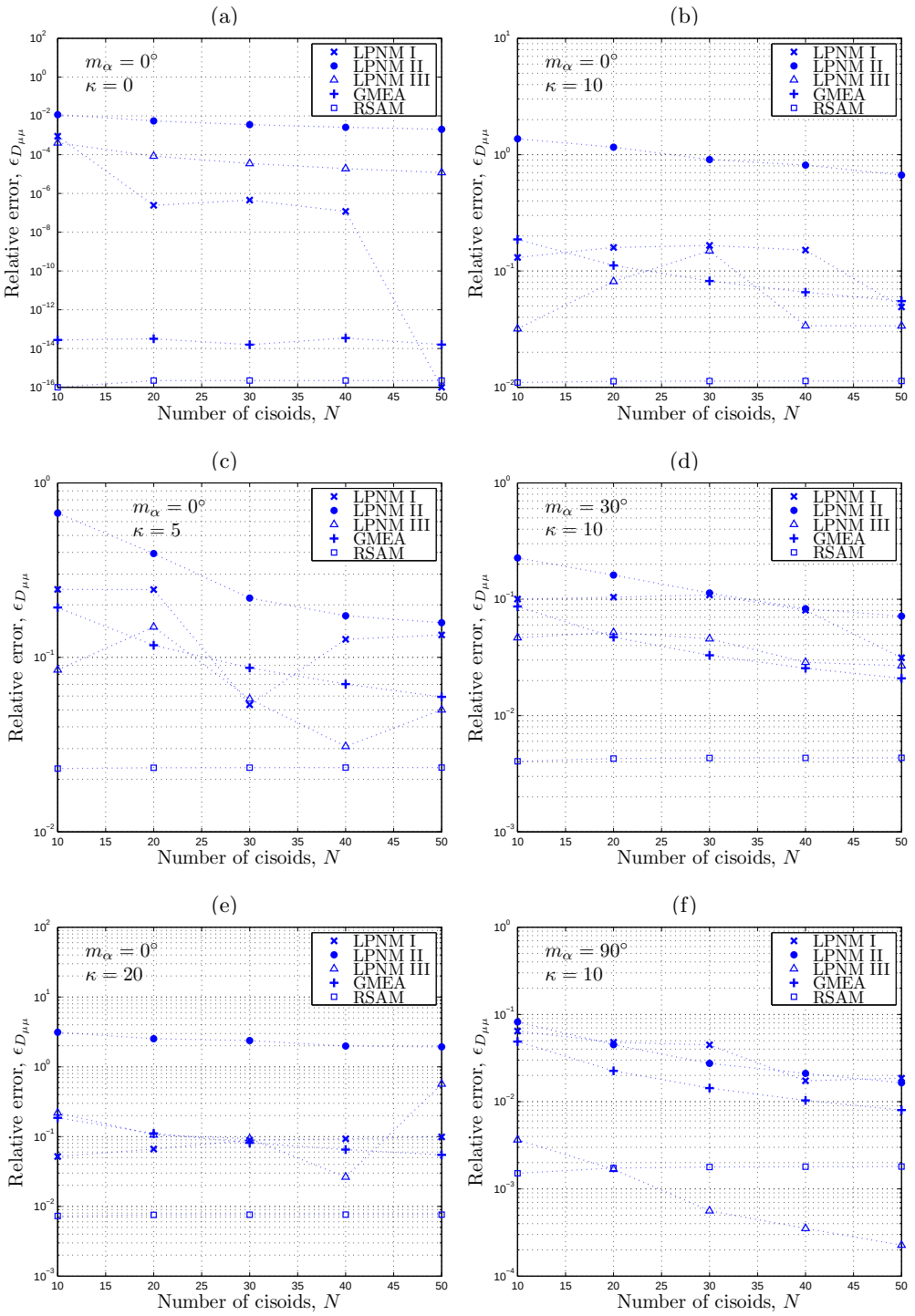

Figure 4.13: Relative error $\epsilon_{D_{\boldsymbol{\mu\mu}}}$ between the Doppler spread of the channel's diffuse component and the Doppler spread of the SOC-based simulation model's random component by considering the von Mises PDF of the AOA and the GMEA, RSAM, and LPNM.

able to guarantee the uncorrelation of the IQ components of $\boldsymbol{\mu}(t)$ when $S_{\boldsymbol{\mu}\boldsymbol{\mu}}(f)$ is symmetrical. Actually, the LPNM III is the method that registered the highest error $\epsilon_{A_{\boldsymbol{\mu}\boldsymbol{\mu}}}$ in the propagation scenarios that are related to fading channels having uncorrelated IQ components.

4.5.2 Emulation of the Fading Statistics of the Reference Model

In the remaining of this section, we will evaluate the methods' performance in terms of the emulation of the fading statistics of the mobile Rician fading channel model characterized by the random process $\boldsymbol{\nu}(t) = \boldsymbol{\mu}(t) + m_\rho(t)$. To that end, we will assume that the specular wave $m_\rho(t)$ is parameterized in such a way that the channel's power equals $\sigma^2_{\boldsymbol{\nu}} = 1$, and $c_R \in \{0, 2, 4\}$, where $c_R = \sigma^2_{\boldsymbol{\mu}}/\rho^2$ is the Rician factor. Besides, we will suppose that the Doppler frequency and the phase of $m_\rho(t)$ are equal to $f_\rho = 65$ Hz and $\theta_\rho = 0°$, respectively.

4.5.2.1 PDF of the Envelope

Figures 4.14–4.18 show a comparison between the first-order PDF $p_{\boldsymbol{\xi}}(z)$ of the envelope of $\boldsymbol{\nu}(t)$ and the first-order PDF $p_{\hat{\boldsymbol{\xi}}}(z)$ of the envelope of the SOC-based simulation model. Curves of $p_{\hat{\boldsymbol{\xi}}}(z)$ corresponding to the GMEA and LPNM I are presented in Figs. 4.14 and 4.15, respectively, whilst those corresponding to the LPNM II, LPNM III, and RSAM are shown in Figs. 4.16–4.18, in that order. Such curves were generated by considering $N = 10$.

The above mentioned figures present both analytical and empirical graphs of $p_{\hat{\boldsymbol{\xi}}}(z)$. The analytical graphs were generated by numerically evaluating (3.20) with the aid of the MATLAB® `trapz` function. For the particular case of the LPNM I and the GMEA, we notice that (3.20) results always in the same theoretical PDF $p_{\hat{\boldsymbol{\xi}}}(z)$ regardless of the simulated propagation scenario. This is due to the fact that (3.20) is solely influenced by the set of gains $\{\hat{c}_n, \rho\}$, and these two methods define a unique set of gains $\hat{c}_n$ for each value of N irrespective of the channel statistics [cf. (4.1)]. In contrast, the solution of (3.20) varies in the case of the LPNM II, LPNM III, and RSAM from one propagation scenario to another, as these methods specify the gains $\hat{c}_n$ by taking into account the distribution of the AOA or the ACF of $\boldsymbol{\mu}(t)$.

On the other hand, the empirical graphs of $p_{\hat{\boldsymbol{\xi}}}(z)$ were obtained by measuring the distribution of 50×10^6 samples of $\hat{\boldsymbol{\xi}}(t) = |\hat{\boldsymbol{\nu}}(t)|^2$. Such samples were collected at the same time instant $t = t_i$, where the value of t_i was chosen at random over a time interval of two hours. We can see in the figures that the analytical graphs of $p_{\hat{\boldsymbol{\xi}}}(z)$ are in excellent agreement with the empirical ones, so that one can presume the correctness of (3.20). In fact, the thesis implied by (3.20) about $p_{\hat{\boldsymbol{\xi}}}(z)$ being a function that depends only on the set of gains $\{\hat{c}_n, \rho\}$ is supported by the empirical data obtained for the LPNM I and GMEA. Despite the fact

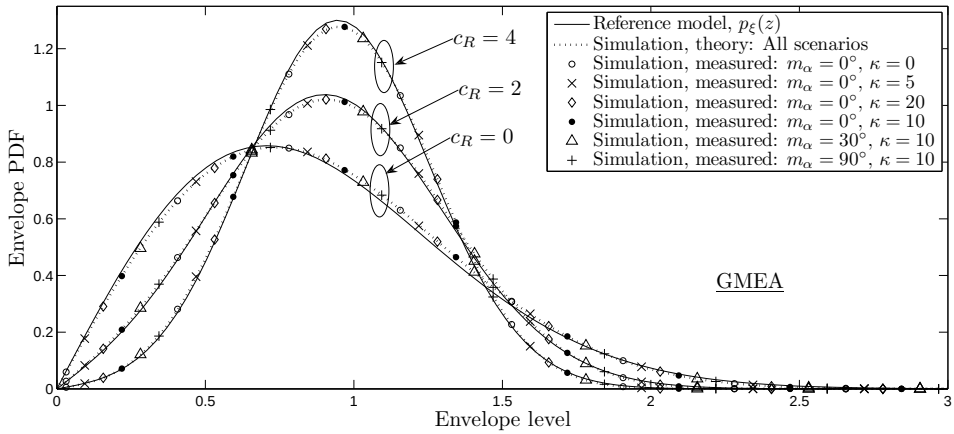

Figure 4.14: Comparison between the first-order PDF of the reference model's envelope and the first-order PDF of the envelope of the SOC-based simulation model by applying the GMEA to the von Mises PDF of the AOA with different pairs of parameters m_α and κ ($f_{\max} = 91$ Hz, $\sigma^2_{\boldsymbol{\nu}} = 1$, $f_p = 65$ Hz, $\theta_\rho = 0°$, and $N = 10$.

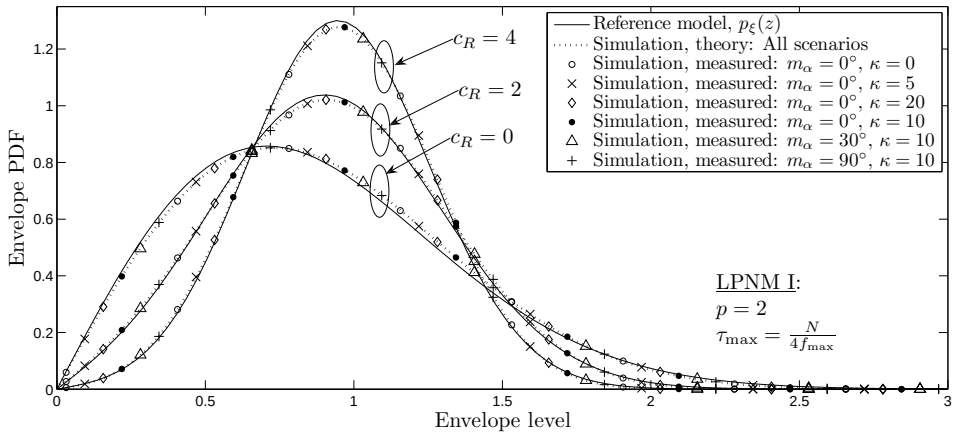

Figure 4.15: Comparison between the first-order PDF of the reference model's envelope and the first-order PDF of the envelope of the SOC-based simulation model by applying the LPNM I to the von Mises PDF of the AOA with different pairs of parameters m_α and κ ($f_{\max} = 91$ Hz, $\sigma^2_{\boldsymbol{\nu}} = 1$, $f_p = 65$ Hz, $\theta_\rho = 0°$, and $N = 10$).

that these methods produce different sets of Doppler frequencies $\{\hat{f}_n\}_{n=1}^N$ for each scenario, the resulting empirical PDFs of $\hat{\boldsymbol{\xi}}(t)$ converged in all cases to the same curve of $p_{\hat{\boldsymbol{\xi}}}(z)$. What is more, the empirical graphs of $p_{\hat{\boldsymbol{\xi}}}(z)$ obtained by using the LPNM I and GMEA are identical to each other, as one can observe by comparing Figs. 4.15 and 4.14. This was to be expected, since these two methods

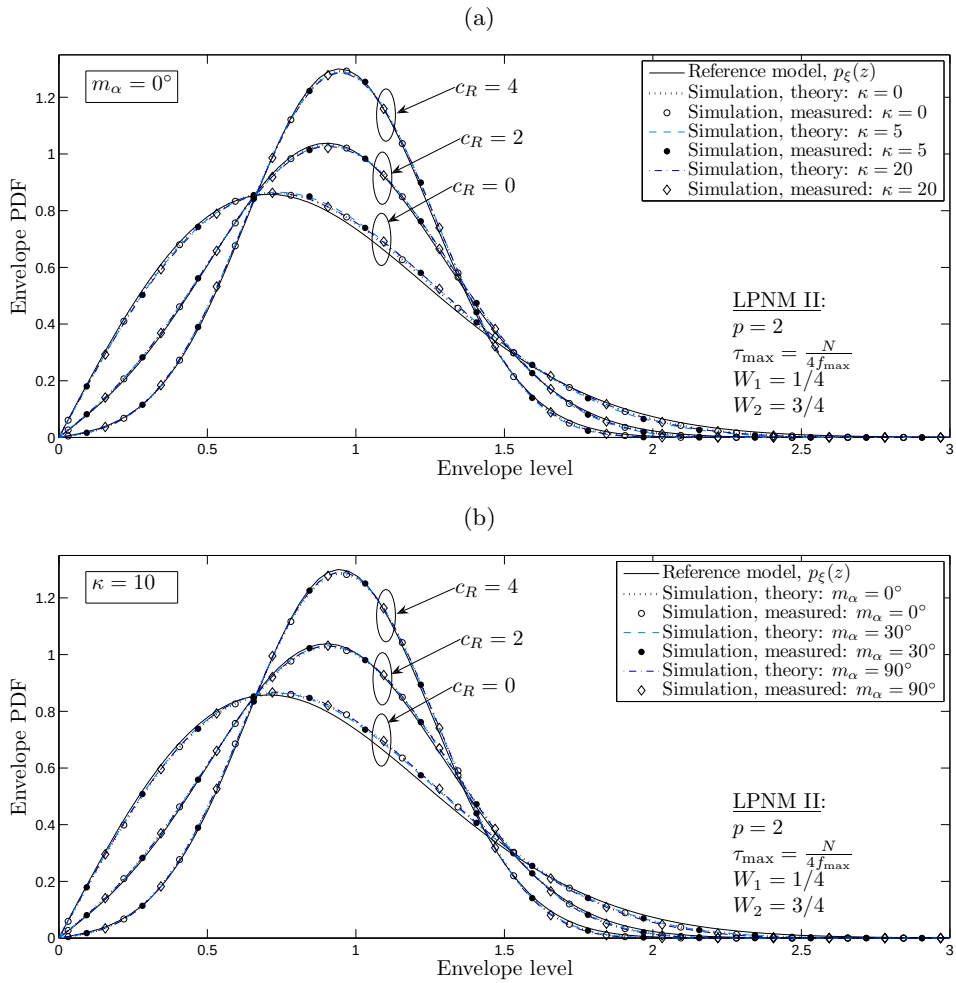

Figure 4.16: Comparison between the first-order PDF of the reference model's envelope and the first-order PDF of the envelope of the SOC-based simulation model by applying the LPNM II to the von Mises PDF of the AOA with different pairs of parameters m_α and κ ($f_{\max} = 91$ Hz, $\sigma^2_{\boldsymbol{\nu}} = 1$, $f_p = 65$ Hz, $\theta_\rho = 0°$, and $N = 10$).

specify the gains $\hat{c}_n$ in the same way.

The graphs depicted in Figs. 4.14–4.18 show a good concordance between the envelope distributions of the reference model and simulation model. It is worth mentioning that the curves of $p_{\hat{\boldsymbol{\zeta}}}(z)$ plotted in Fig. 4.18 for the RSAM, specifically those corresponding to the case $c_R = 0$, $m_\alpha = 0°$, and $\kappa \in \{10, 20\}$, are significantly better than the graphs shown in Fig. 4.5 for the BRSAM. However, despite of such an improvement, a close inspection of Figs. 4.14–4.18 reveals that the RSAM is less accurate than the LPNM and the GMEA regarding the emulation of $p_{\boldsymbol{\zeta}}(z)$.

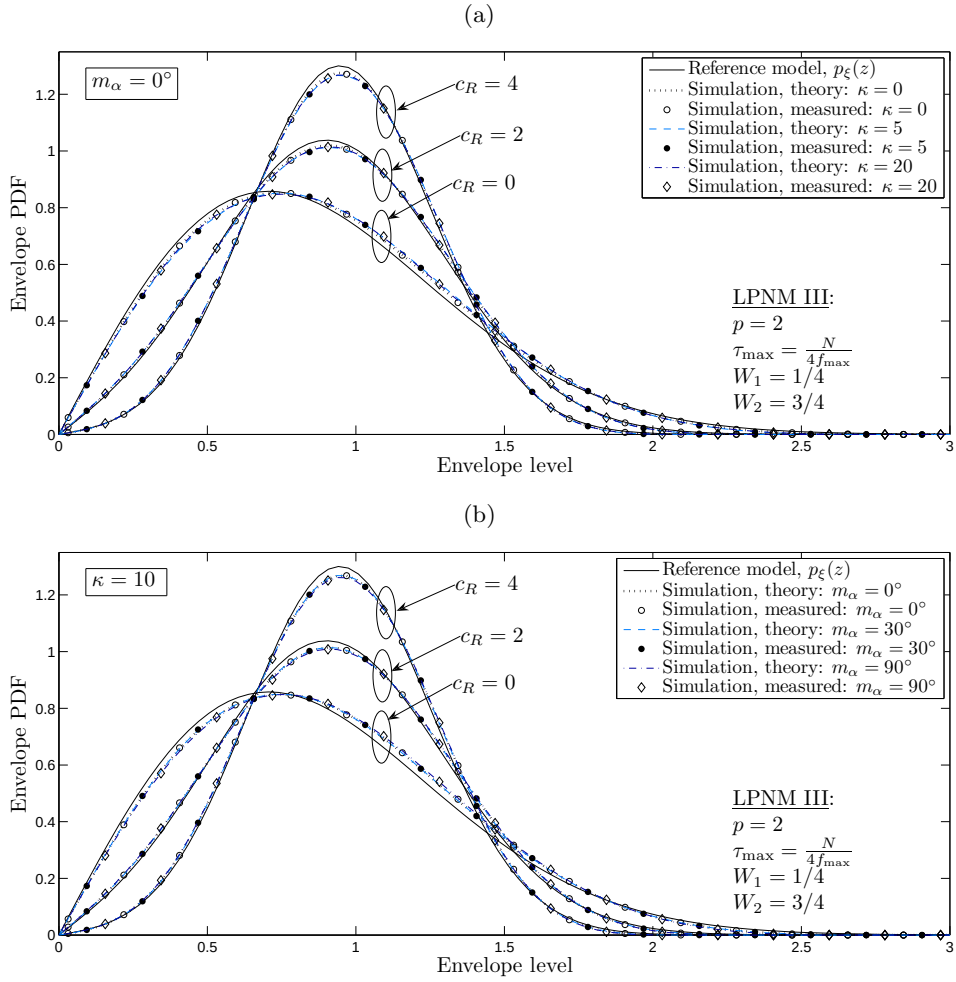

Figure 4.17: Comparison between the first-order PDF of the reference model's envelope and the first-order PDF of the envelope of the SOC-based simulation model by applying the LPNM III to the von Mises PDF of the AOA with different pairs of parameters m_α and κ ($f_{\max} = 91$ Hz, $\sigma^2_{\boldsymbol{\nu}} = 1$, $f_p = 65$ Hz, $\theta_\rho = 0°$, and $N = 10$).

In order to quantitatively measure the methods' performance, we present in Fig. 4.19 the resulting rms error $\epsilon_{p_{\boldsymbol{\xi}}}$ between $p_{\boldsymbol{\xi}}(z)$ and $p_{\hat{\boldsymbol{\xi}}}(z)$ [see (4.8)], computed for each method by considering $c_R = 0$ and $N = \{10, 20, 30, 40, 50\}$. The results presented in Fig. 4.19 leave no doubt that the LPNM I and GMEA are better suited than the other methods to approximate the envelope distribution of the reference model when the scattering conditions are non-isotropic. In turn, the results show that the LPNM II performs better than the rest of the methods under isotropic scattering conditions. On the other hand, the figure shows that the highest error was produced by the RSAM. Even though the rms error $\epsilon_{p_{\boldsymbol{\xi}}}$

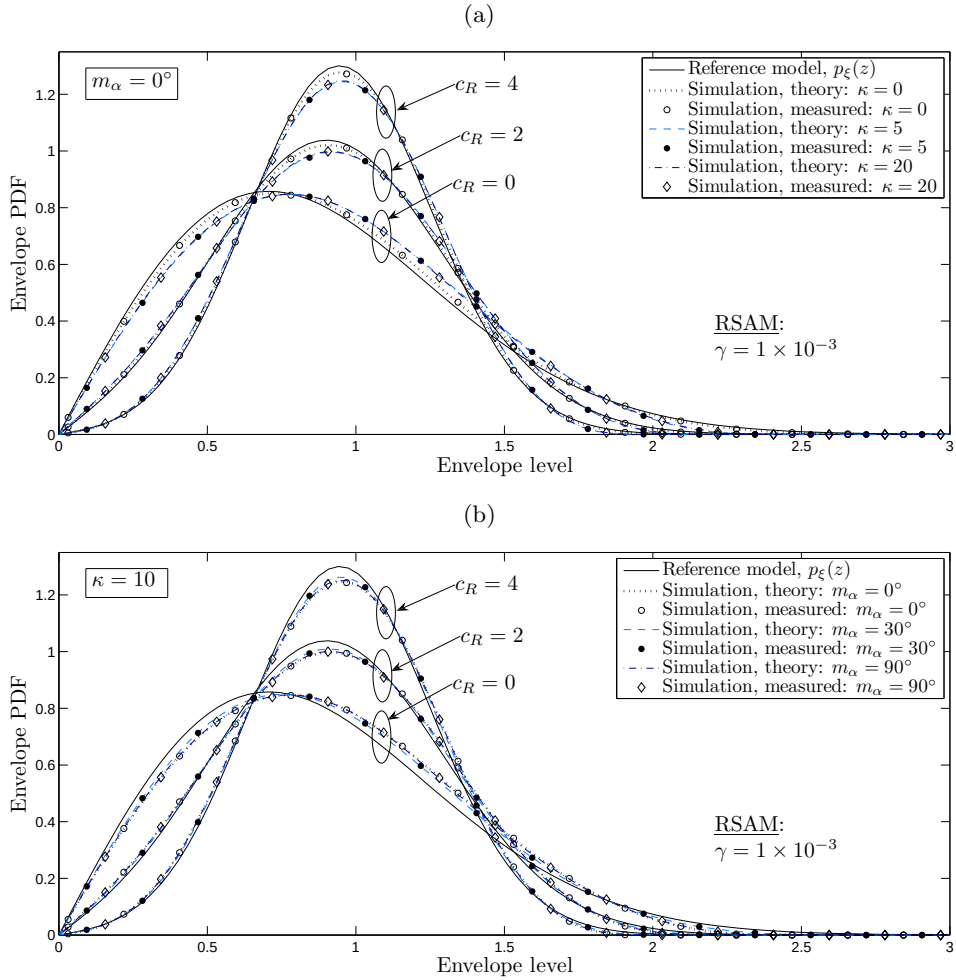

Figure 4.18: Comparison between the first-order PDF of the reference model's envelope and the first-order PDF of the envelope of the SOC-based simulation model by applying the RSAM to the von Mises PDF of the AOA with different pairs of parameters m_α and κ ($f_{\max} = 91$ Hz, $\sigma_{\boldsymbol{\nu}}^2 = 1$, $f_p = 65$ Hz, $\theta_\rho = 0°$, and $N = 10$.

registered by such a method is rather small, it is around two to three times higher than the one produced by the GMEA/LPNM I. With respect to the LPNM II and LPNM III, it can be observed that only the former method provides a real advantage over the RSAM, since the LPNM III and the RSAM perform basically the same when the number of cisoids is higher than thirty.

4.5.2.2 PDF of the Phase

Concerning the emulation of the first-order PDF of the reference model's phase, $p_{\boldsymbol{\psi}}(\theta; t)$, we present in Figs. 4.20–4.24 a comparison between $p_{\boldsymbol{\psi}}(\theta; t)$ and the

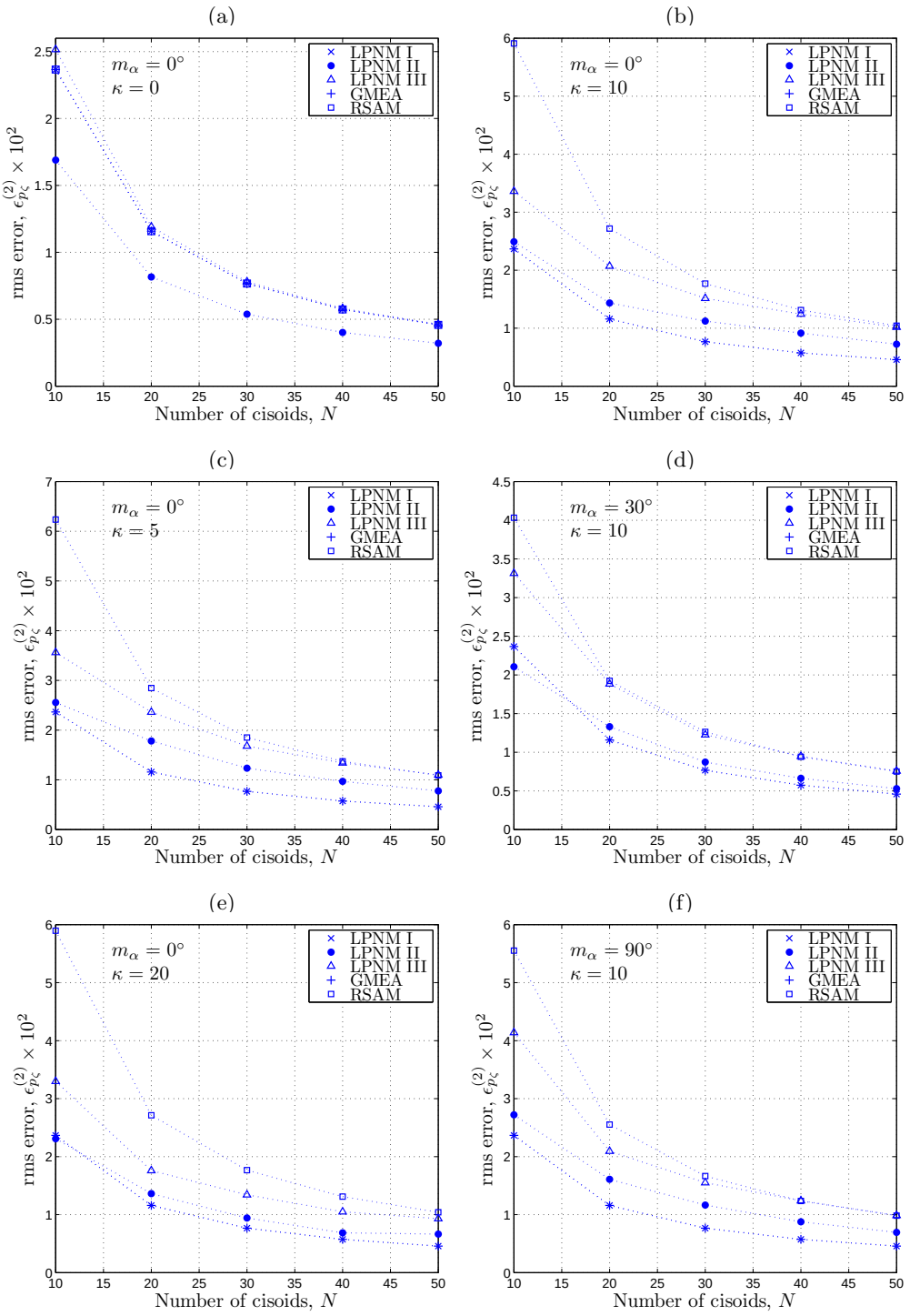

Figure 4.19: Root mean square error between the envelope distributions of the channel's diffuse component and SOC-based simulation model's random component by considering the von Mises PDF of the AOA and the GMEA, RSAM, and LPNM ($\tau_{\max} = N/(4f_{\max})$).

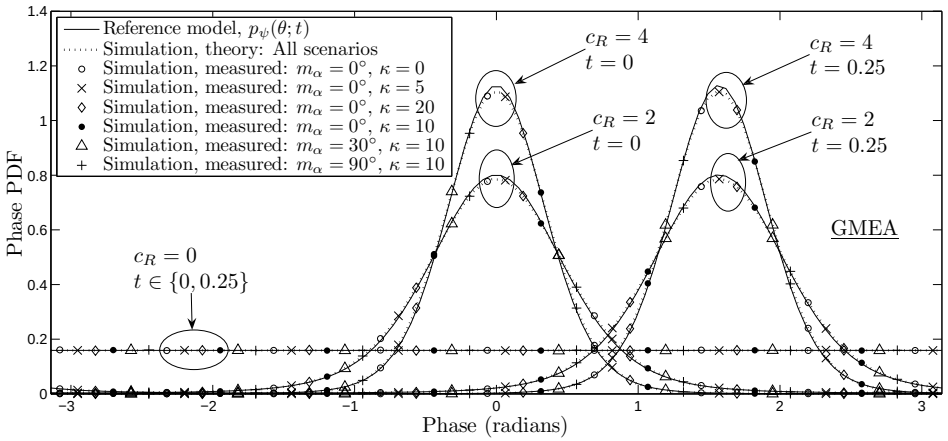

Figure 4.20: Comparison between the first-order PDF of the reference model's phase and the first-order PDF of the phase of the SOC-based simulation model by applying the GMEA to the von Mises PDF of the AOA ($f_{\max} = 91$ Hz, $\sigma^2_{\boldsymbol{\nu}} = 1$, $f_p = 65$ Hz, $\theta_\rho = 0°$, $t \in \{0, 0.25\}$, and $N = 10$).

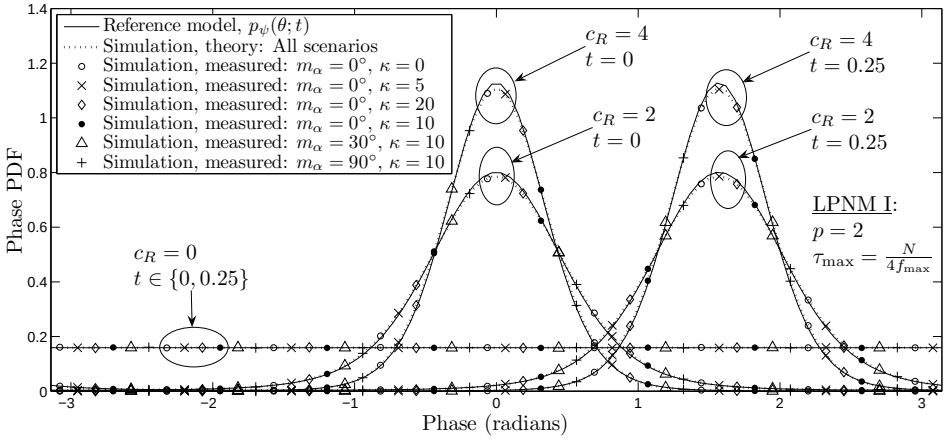

Figure 4.21: Comparison between the first-order PDF of the reference model's phase and the first-order PDF of the phase of the SOC-based simulation model by applying the LPNM I to the von Mises PDF of the AOA ($f_{\max} = 91$ Hz, $\sigma^2_{\boldsymbol{\nu}} = 1$, $f_p = 65$ Hz, $\theta_\rho = 0°$, $t \in \{0, 0.25\}$, and $N = 10$).

first-order PDF of the simulation model's phase, $p_{\hat{\boldsymbol{\psi}}}(\theta;t)$. The graphs of $p_{\hat{\boldsymbol{\psi}}}(\theta;t)$ presented in those figures were computed both analytically and empirically for the methods under investigation by considering $N = 10$ and $t \in \{0, 0.25\}$. Figures 4.20 and 4.21 show results obtained for the GMEA and LPNM I, in that order, while results obtained for the LPNM II, LPNM III, and RSAM are pre-

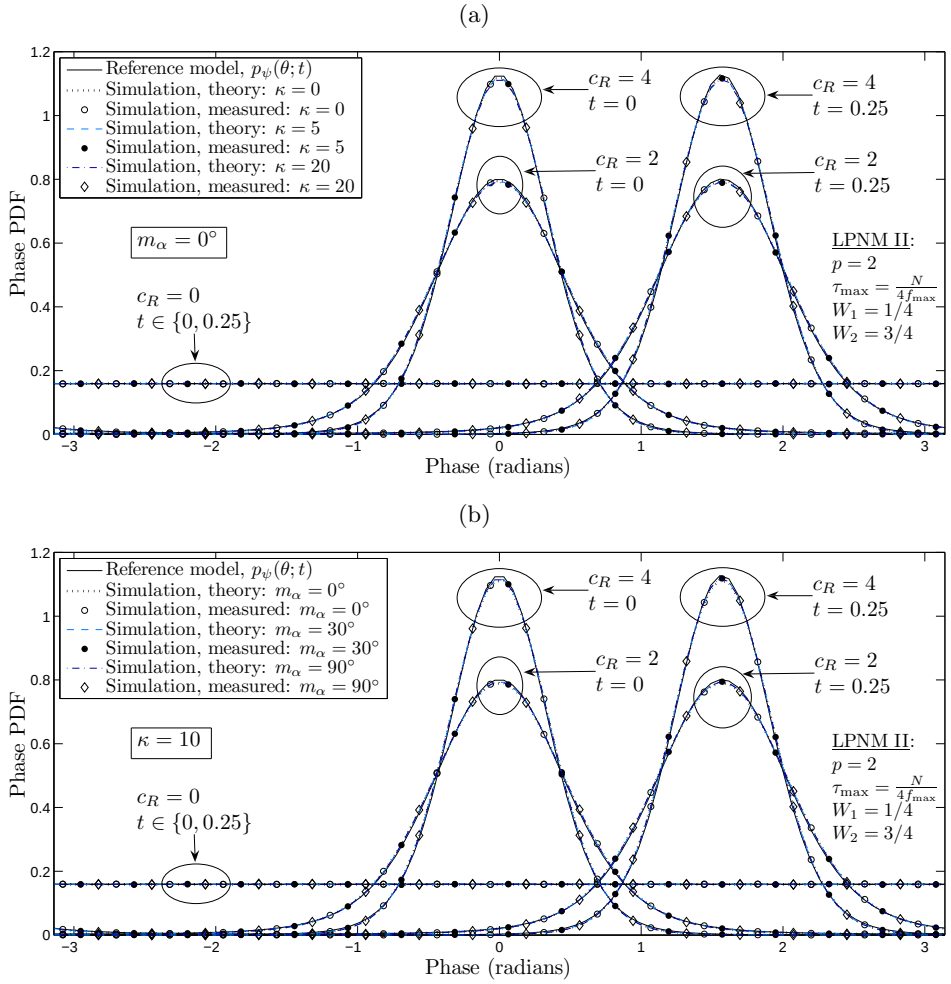

Figure 4.22: Comparison between the first-order PDF of the reference model's phase and the first-order PDF of the phase of the SOC-based simulation model by applying the LPNM II to the von Mises PDF of the AOA ($f_{\max} = 91$ Hz, $\sigma^2_{\boldsymbol{\nu}} = 1$, $f_p = 65$ Hz, $\theta_\rho = 0°$, $t \in \{0, 0.25\}$, and $N = 10$).

sented in Figs. 4.22–4.24, respectively. For the analytical graphs, we evaluated (3.22) with the aid of the MATLAB's `trapz` function. For the empirical graphs, we made the same considerations and followed the same procedure as described in Section 4.5.2.1 concerning the computation of the empirical envelope distribution. The figures graphically demonstrate the correctness of the analytical solution given in (3.22) for the PDF of the simulation model's phase.

The results presented in Figs. 4.20–4.24 show that the phase of the simulation model is in general not a first-order stationary process, since $p_{\hat{\boldsymbol{\psi}}}(\theta;0) \neq p_{\hat{\boldsymbol{\psi}}}(\theta;0.25)$ for $c_R \in \{2, 4\}$. However, $p_{\hat{\boldsymbol{\psi}}}(\theta;t)$ proves to be time-invariant and equal to $p_{\hat{\boldsymbol{\psi}}}(\theta) =$

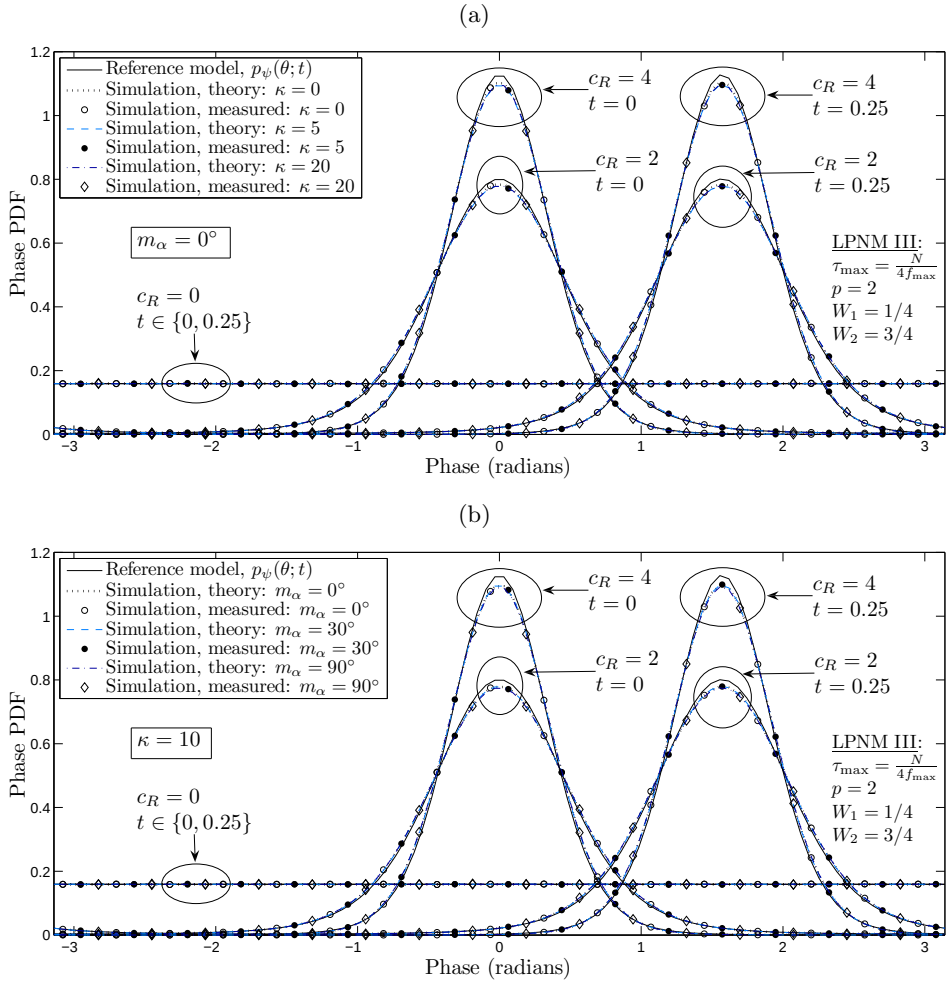

Figure 4.23: Comparison between the first-order PDF of the reference model's phase and the first-order PDF of the phase of the SOC-based simulation model by applying the LPNM III to the von Mises PDF of the AOA ($f_{\max} = 91$ Hz, $\sigma_{\boldsymbol{\nu}}^2 = 1$, $f_p = 65$ Hz, $\theta_\rho = 0°$, $t \in \{0, 0.25\}$, and $N = 10$).

$1/(2\pi)$ irrespective of the parameter computation method when $c_R = 0$. These remarks are in line with the statements made in that respect in Section 3.3.4.2.

With regard to the methods' performance, one may observe from Figs. 4.21–4.24 that the five methods provide a close approximation to the phase PDF of the reference model. Indeed, all methods render an exact match of $p_{\boldsymbol{\psi}}(\theta;t)$ for the Rayleigh fading scenario ($c_R = 0$). However, for the Rician fading case ($c_R > 0$), the obtained results show clearly that the RSAM and LPNM III are less effective than the other methods.

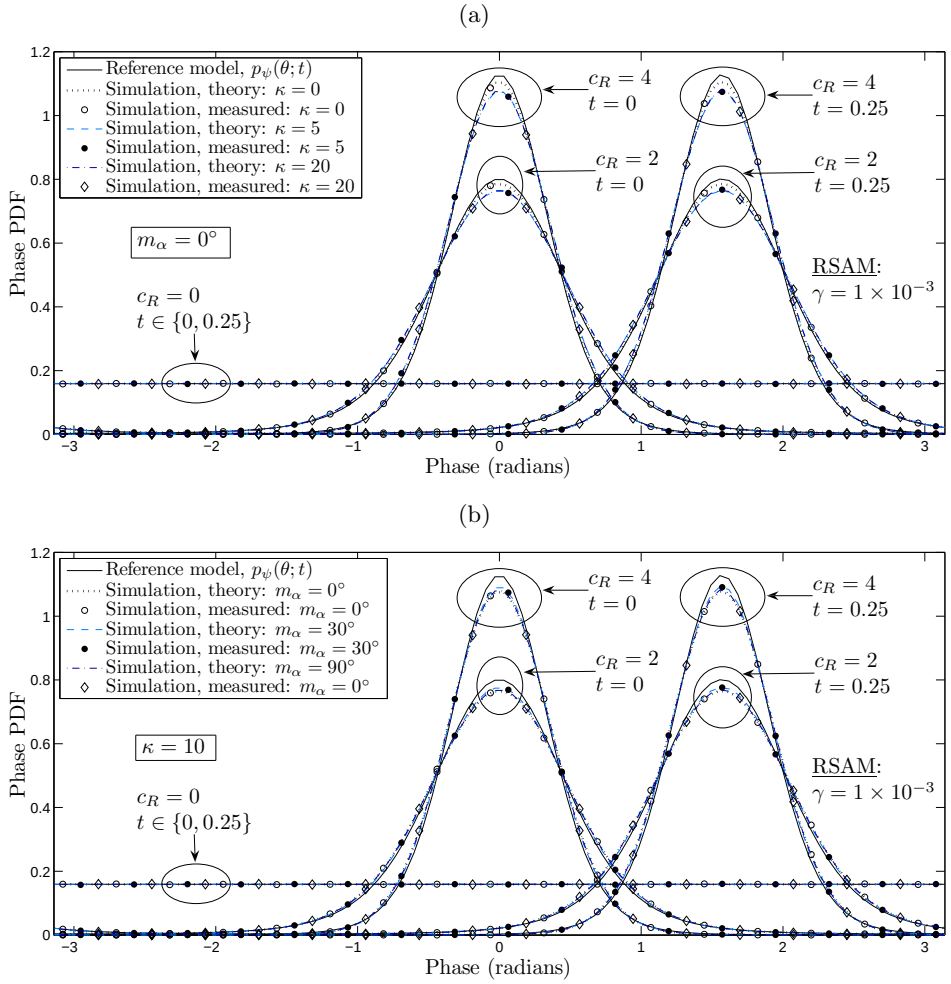

Figure 4.24: Comparison between the first-order PDF of the reference model's phase and the first-order PDF of the phase of the SOC-based simulation model by applying the RSAM to the von Mises PDF of the AOA with different pairs of parameters m_α and κ ($f_{\max} = 91$ Hz, $\sigma^2_{\boldsymbol{\nu}} = 1$, $f_p = 65$ Hz, $\theta_\rho = 0°$, $t \in \{0, 0.25\}$, and $N = 10$).

4.5.2.3 ACF of the Squared Envelope

To close this section, we present in Figs. 4.25–4.33 a comparison between the ACF of the reference model's squared envelope, $r_{\boldsymbol{\xi}^2\boldsymbol{\xi}^2}(\tau)$, and the ACF of the squared envelope of the simulation model, $r_{\hat{\boldsymbol{\xi}}^2\hat{\boldsymbol{\xi}}^2}(\tau)$, by considering $N = 20$ and $c_R \in \{0, 2, 4\}$. To keep the figures readable, we have plotted the results produced by each versions of the LPNM against results obtained for the GMEA and RSAM in different figures. The figures show both theoretical and empirical curves of the ACF of $\hat{\boldsymbol{\xi}}^2(t) = |\hat{\boldsymbol{\nu}}(t)|^2$. The theoretical graphs of $r_{\hat{\boldsymbol{\xi}}^2\hat{\boldsymbol{\xi}}^2}(\tau)$ were produced by

evaluating (3.29), while the empirical curves were generated by averaging over the measured ACFs of 60 samples functions of $\hat{\boldsymbol{\xi}}^2(t)$. Such an averaging was necessary, since the process $\hat{\boldsymbol{\xi}}^2(t)$ is not always autocorrelation ergodic[3]. However, with the purpose of demonstrating the correctness of the analytical solutions provided in Section 3.4.4 for the time-averaged ACF $r_{\hat{\xi}^2\hat{\xi}^2}(\tau)$ of the sample functions of $\hat{\boldsymbol{\xi}}^2(t)$, we present results obtained for $r_{\hat{\xi}^2\hat{\xi}^2}(\tau)$ in Appendix F. We pointed out in Section 4.5.1.1 that the LPNM II does not satisfy the condition $\sum_{n=1}^{N}\hat{c}_n^2 = \sigma_{\boldsymbol{\mu}}^2$. For this reason, the theoretical ACF of $\hat{\boldsymbol{\xi}}^2(t)$ was computed for that particular method by evaluating

$$\begin{aligned} r_{\hat{\boldsymbol{\xi}}^2\hat{\boldsymbol{\xi}}^2}(\tau) &= r_{\hat{\zeta}^2\hat{\zeta}^2}(\tau) + \frac{c_R^2\,\sigma_{\boldsymbol{\nu}}^4}{(c_R+1)^2} + \frac{4\sigma_{\boldsymbol{\nu}}^2 c_R}{c_R+1}\Bigg\{ r_{\hat{\boldsymbol{\mu}}_I\hat{\boldsymbol{\mu}}_I}(\tau)\cos(2\pi f_\rho\tau) \\ &\quad + r_{\hat{\boldsymbol{\mu}}_I\hat{\boldsymbol{\mu}}_Q}(\tau)\sin(2\pi f_\rho\tau) - \frac{1}{2}\sum_{n=1}^{N}\hat{c}_n^2\Bigg\} \end{aligned} \tag{4.43}$$

where

$$r_{\hat{\zeta}^2\hat{\zeta}^2}(\tau) = |r_{\hat{\boldsymbol{\mu}}\hat{\boldsymbol{\mu}}}(\tau)|^2 + \left[\sum_{n=1}^{N}\hat{c}_n^2\right]^2 - \sum_{n=1}^{N}\hat{c}_n^4. \tag{4.44}$$

One can observe from Figs. 4.25–4.33 that the results predicted by the theory are in excellent agreement with the ones obtained in practice. This can be taken as an indicator of the correctness of the analytical expressions introduced in Section 3.3.6 for $r_{\hat{\boldsymbol{\xi}}^2\hat{\boldsymbol{\xi}}^2}(\tau)$.

Figures 4.28–4.33 show that the three methods under consideration yield a very good approximation to the graphs of $r_{\boldsymbol{\xi}^2\boldsymbol{\xi}^2}(\tau)$ when $c_R > 0$. This is not surprising, since under such circumstances the correlation properties of $\hat{\boldsymbol{\xi}}^2(t)$ (and also of $\boldsymbol{\xi}^2(t)$) are mainly determined by the time-variant specular wave $m_\rho(t)$. The characteristics of the parameter computation methods exert in consequence little influence on the quality of the relationship $r_{\hat{\boldsymbol{\xi}}^2\hat{\boldsymbol{\xi}}^2}(\tau) \approx r_{\boldsymbol{\xi}^2\boldsymbol{\xi}^2}(\tau)$. However, for the NLOS scenario ($c_R = 0$), it is clear that the methods' characteristics determine the capability of the simulation model for emulating the function $r_{\boldsymbol{\xi}^2\boldsymbol{\xi}^2}(\tau)$. In this respect, we can see in Figs. 4.25–4.27 that the best fitting of the ACF of $\hat{\boldsymbol{\xi}}^2(t)$ is produced by the GMEA and the LPNM I, while the LPNM II yields the worst. The LPNM III and the RSAM perform similarly, although the LPNM III is slightly more accurate.

An inspection of the results presented in Figs. 4.25–4.33 reveals that, irrespective of the parameter computation method, there exists an offset between

[3]We pointed out in Section 3.5 that $\hat{\boldsymbol{\xi}}^2(t)$ is non-autocorrelation-ergodic when the IQ components of $\hat{\boldsymbol{\mu}}(t)$ are uncorrelated and the Doppler frequencies $\hat{f}_n$ satisfy the Conditions 3.2 and 3.3. Such a situation ensues in the case of the GMEA and RSAM when the DPSD of the channel's diffuse component is symmetrical [Appx. E] (cases: $m_\alpha = 0°, \kappa = 0$; and $m_\alpha = 90°, \kappa = 10$).

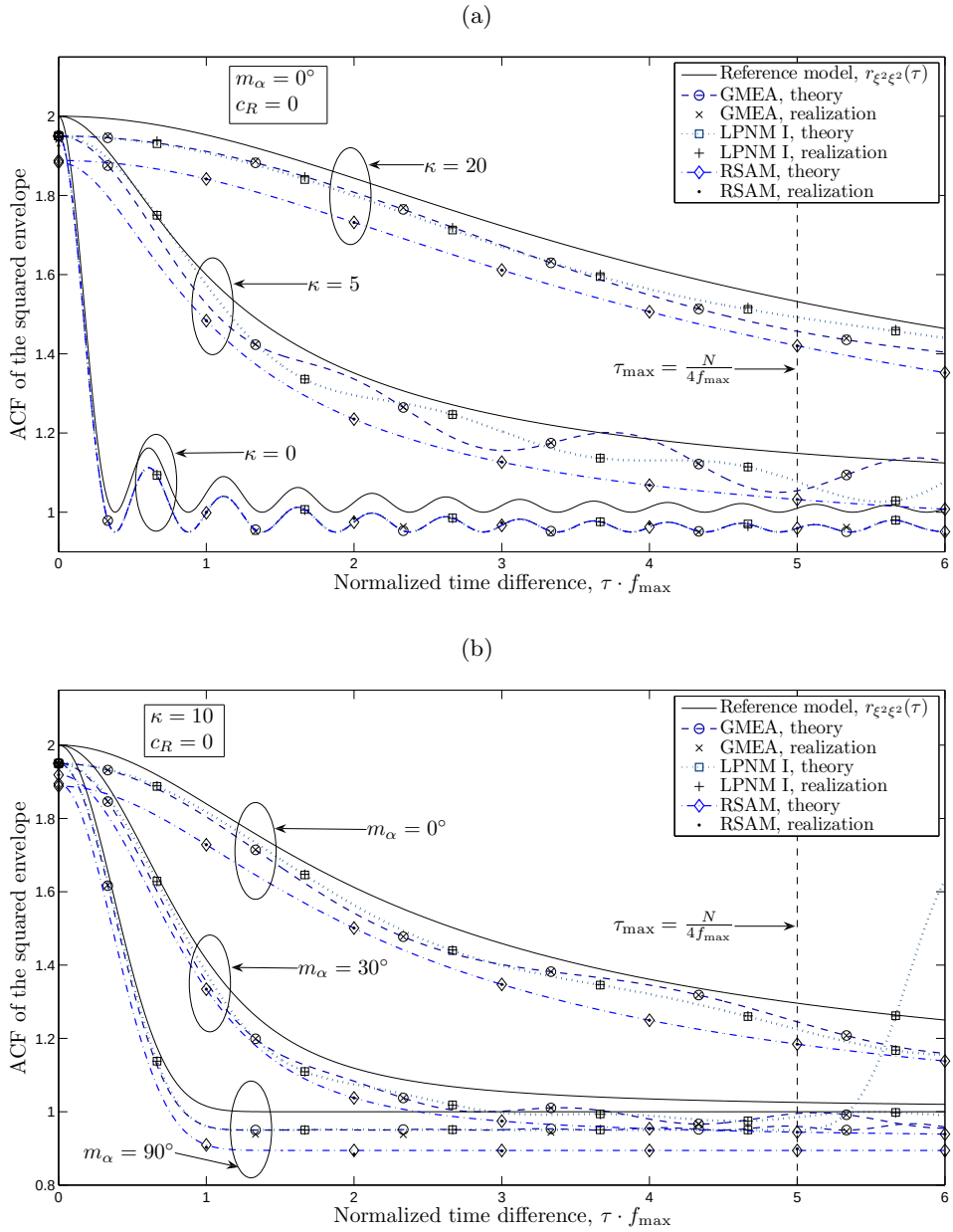

Figure 4.25: Comparison among the GMEA, RSAM, and LPNM I in terms of the emulation of the ACF of the reference model's squared envelope by considering a Rician factor $c_R = 0$ and the von Mises PDF of the AOA with different pairs of parameters m_α and κ ($N = 20$, $\sigma^2_{\boldsymbol{\nu}} = 1$, $p = 2$, $\tau_{\max} = 5/f_{\max}$, $\gamma = 1 \times 10^{-3}$).

(a)

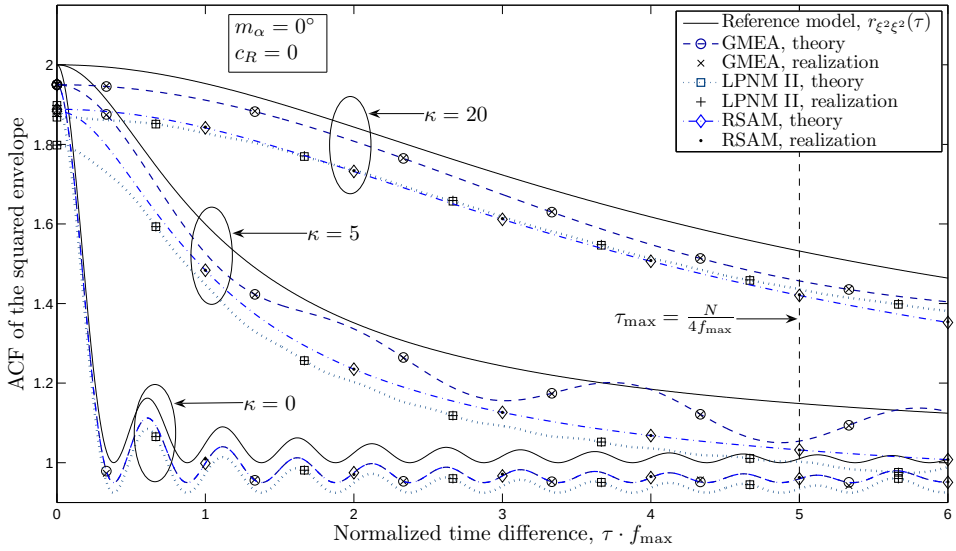

(b)

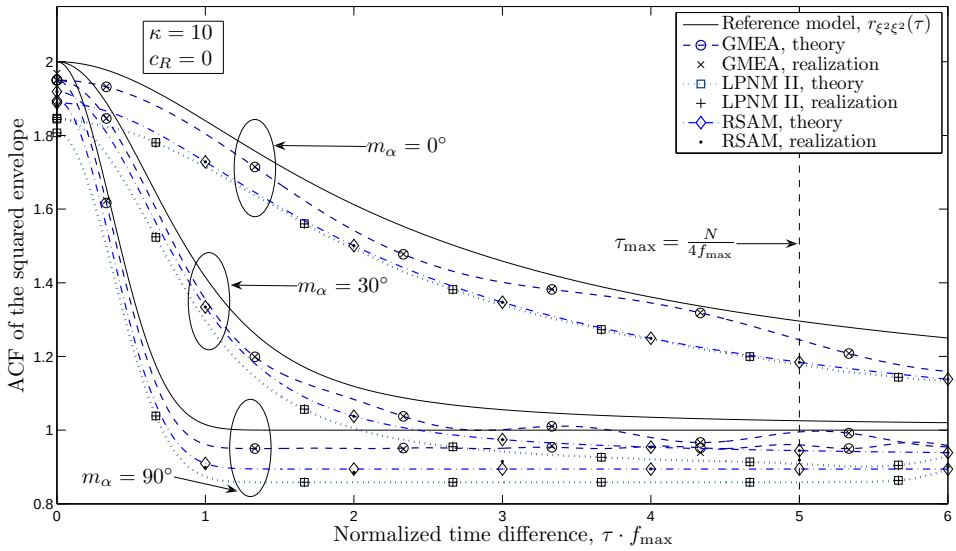

Figure 4.26: Comparison among the GMEA, RSAM, and LPNM II in terms of the emulation of the ACF of the reference model's squared envelope by considering a Rician factor $c_R = 0$ and the von Mises PDF of the AOA with different pairs of parameters m_α and κ ($N = 20$, $\sigma_{\boldsymbol{\nu}}^2 = 1$, $p = 2$, $\tau_{\max} = 5/f_{\max}$, $\gamma = 1 \times 10^{-3}$).

(a)

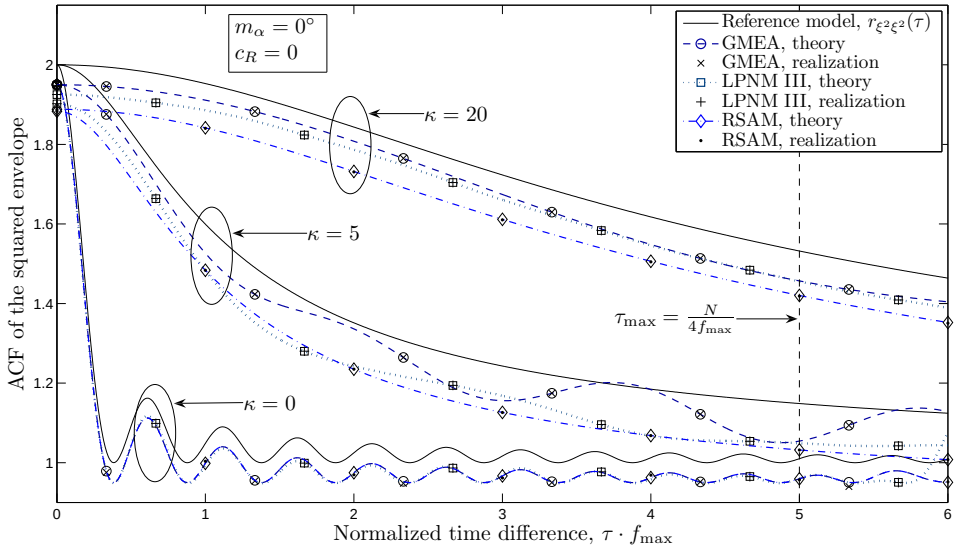

(b)

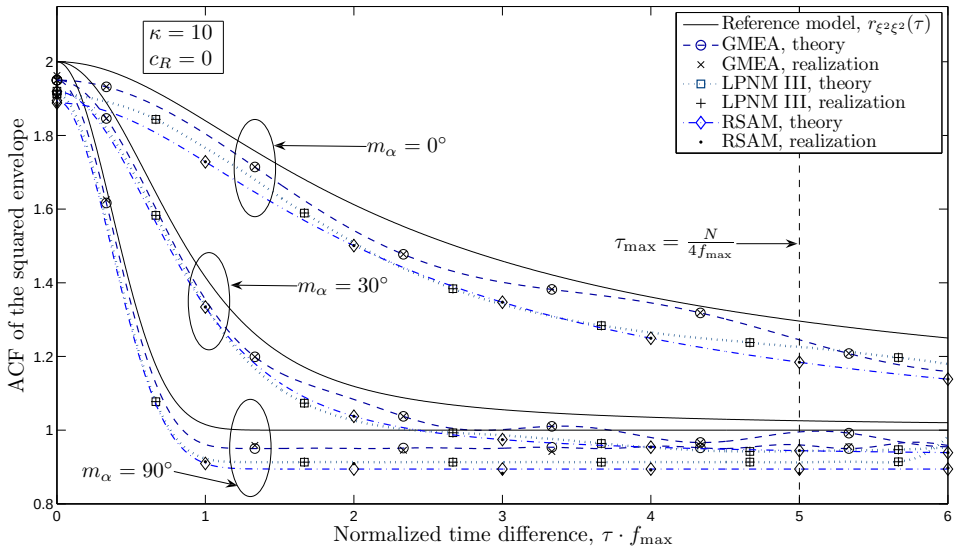

Figure 4.27: Comparison among the GMEA, RSAM, and LPNM III in terms of the emulation of the ACF of the reference model's squared envelope by considering a Rician factor $c_R = 0$ and the von Mises PDF of the AOA with different pairs of parameters m_α and κ ($N = 20$, $\sigma^2_{\boldsymbol{\nu}} = 1$, $p = 2$, $\tau_{\max} = 5/f_{\max}$, $\gamma = 1 \times 10^{-3}$).

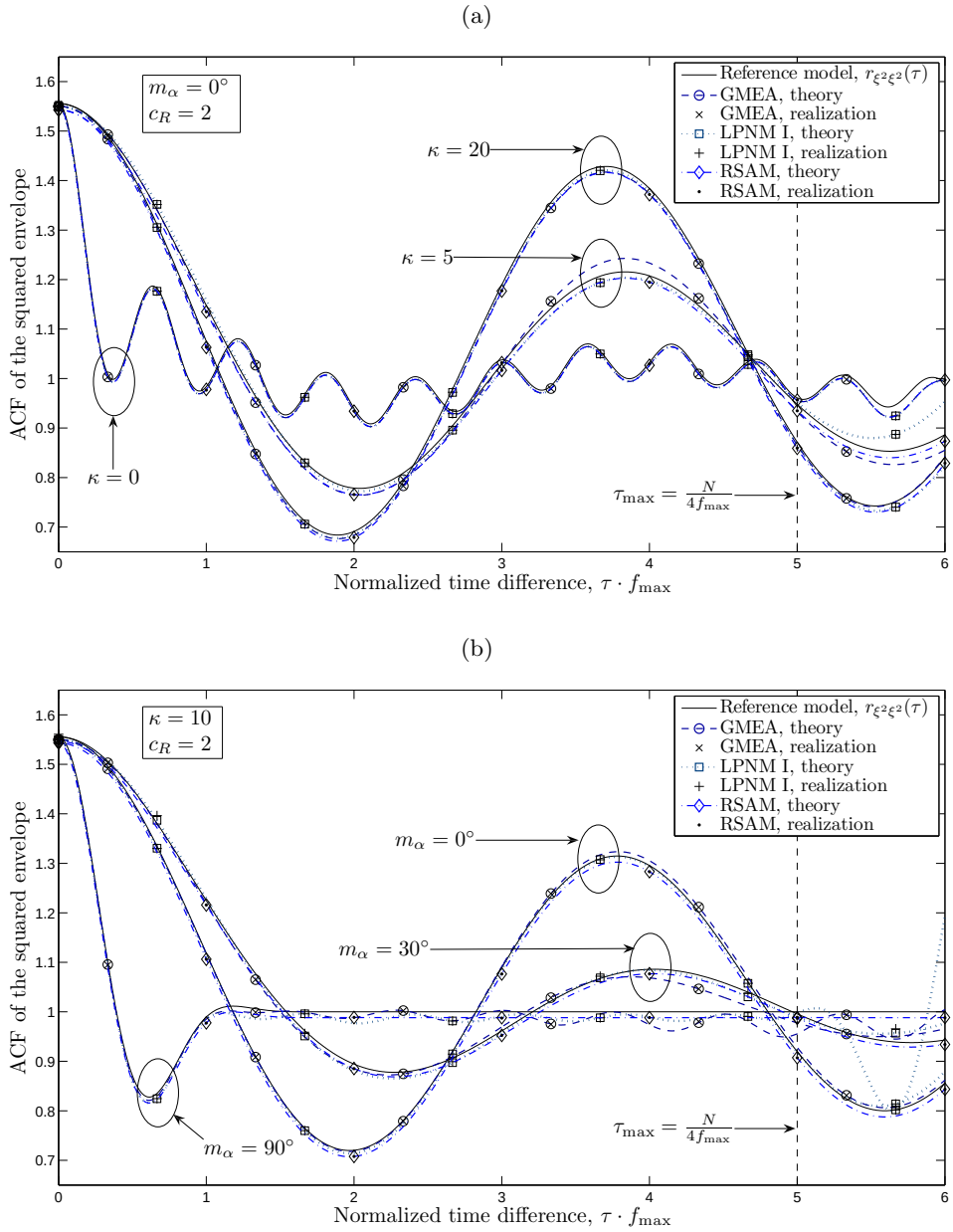

Figure 4.28: Comparison among the GMEA, RSAM, and LPNM I in terms of the emulation of the ACF of the reference model's squared envelope by considering a Rician factor $c_R = 2$ and the von Mises PDF of the AOA with different pairs of parameters m_α and κ ($N = 20$, $\sigma^2_{\boldsymbol{\nu}} = 1$, $p = 2$, $\tau_{\max} = 5/f_{\max}$, $\gamma = 1 \times 10^{-3}$).

(a)

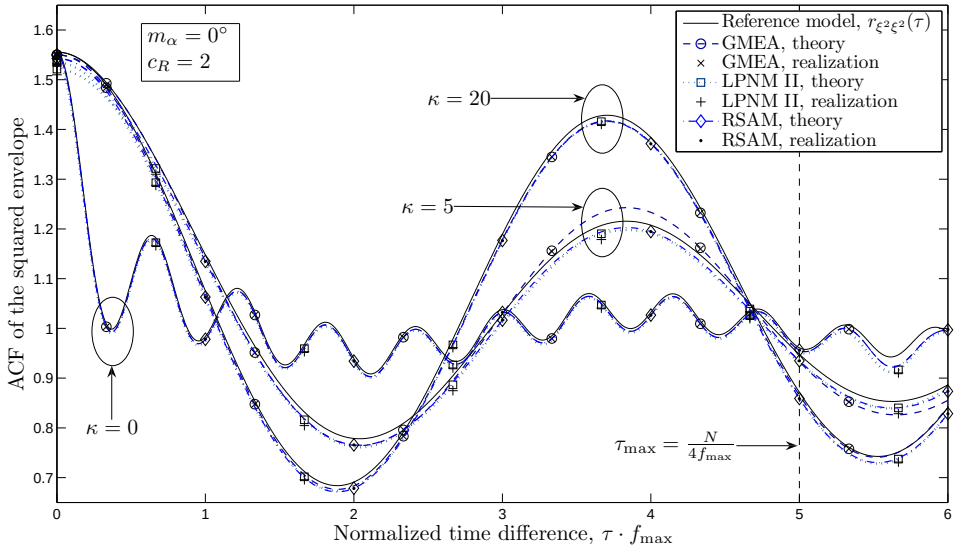

(b)

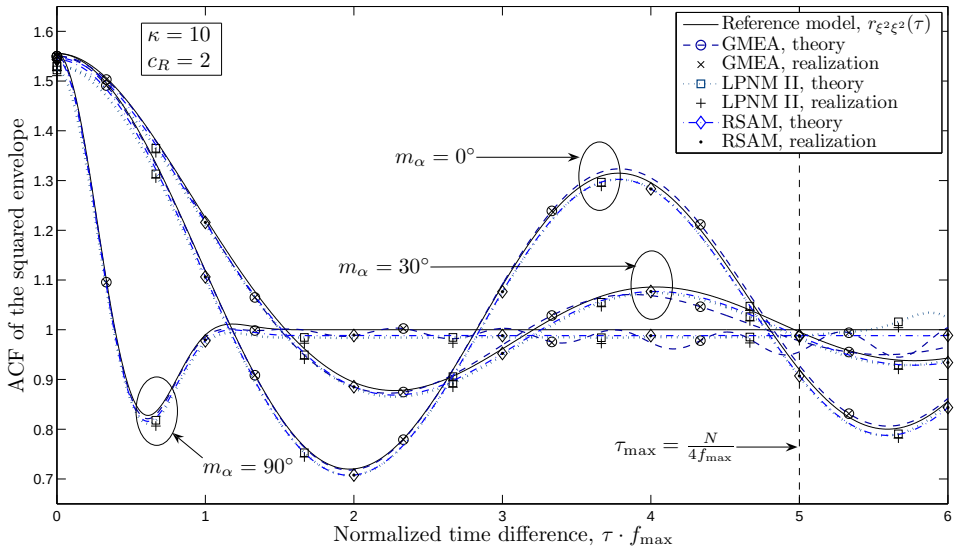

Figure 4.29: Comparison among the GMEA, RSAM, and LPNM II in terms of the emulation of the ACF of the reference model's squared envelope by considering a Rician factor $c_R = 2$ and the von Mises PDF of the AOA with different pairs of parameters m_α and κ ($N = 20$, $\sigma^2_{\boldsymbol{\nu}} = 1$, $p = 2$, $\tau_{\max} = 5/f_{\max}$, $\gamma = 1 \times 10^{-3}$).

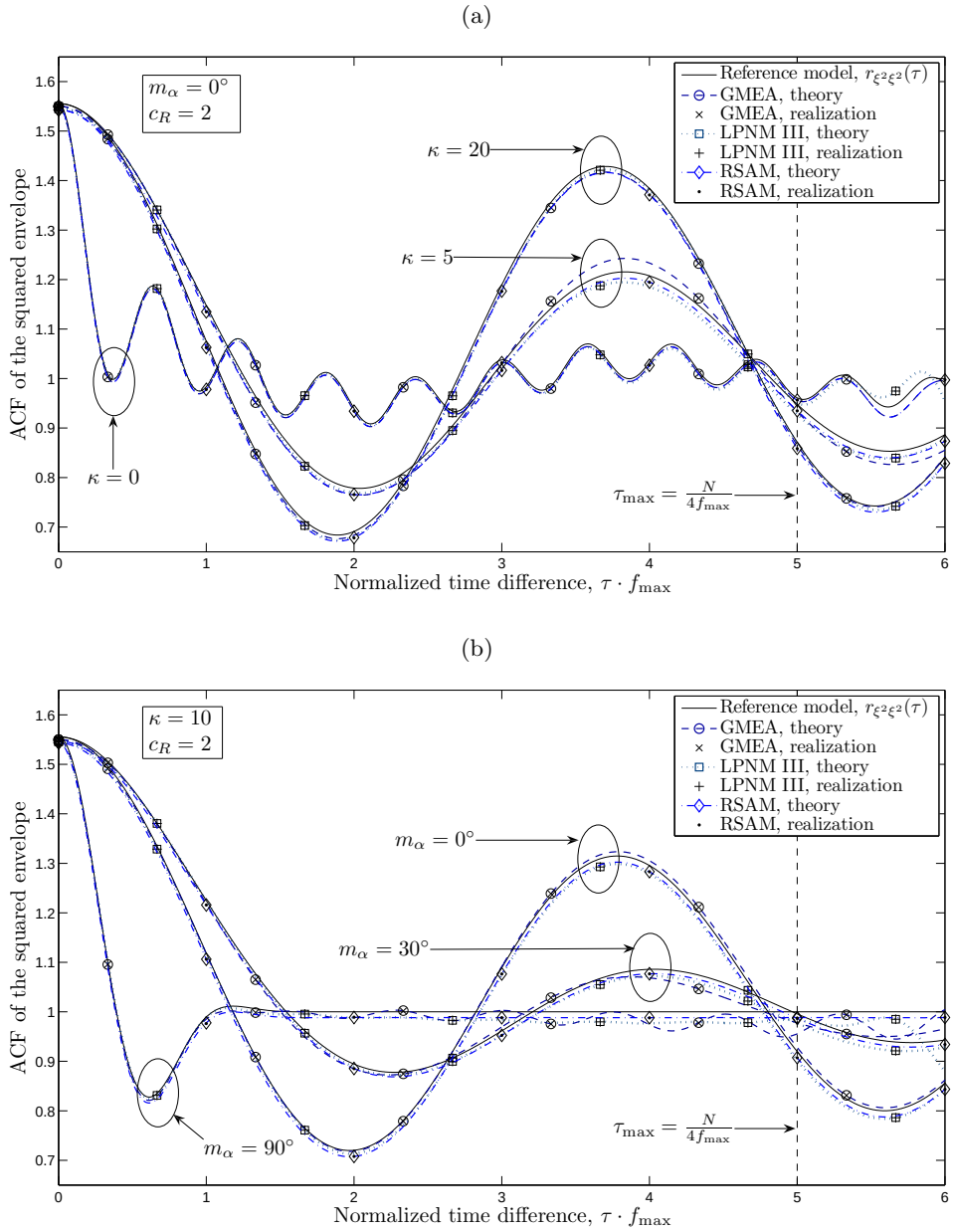

Figure 4.30: Comparison among the GMEA, RSAM, and LPNM III in terms of the emulation of the ACF of the reference model's squared envelope by considering a Rician factor $c_R = 2$ and the von Mises PDF of the AOA with different pairs of parameters m_α and κ ($N = 20$, $\sigma_{\boldsymbol{\nu}}^2 = 1$, $p = 2$, $\tau_{\max} = 5/f_{\max}$, $\gamma = 1 \times 10^{-3}$).

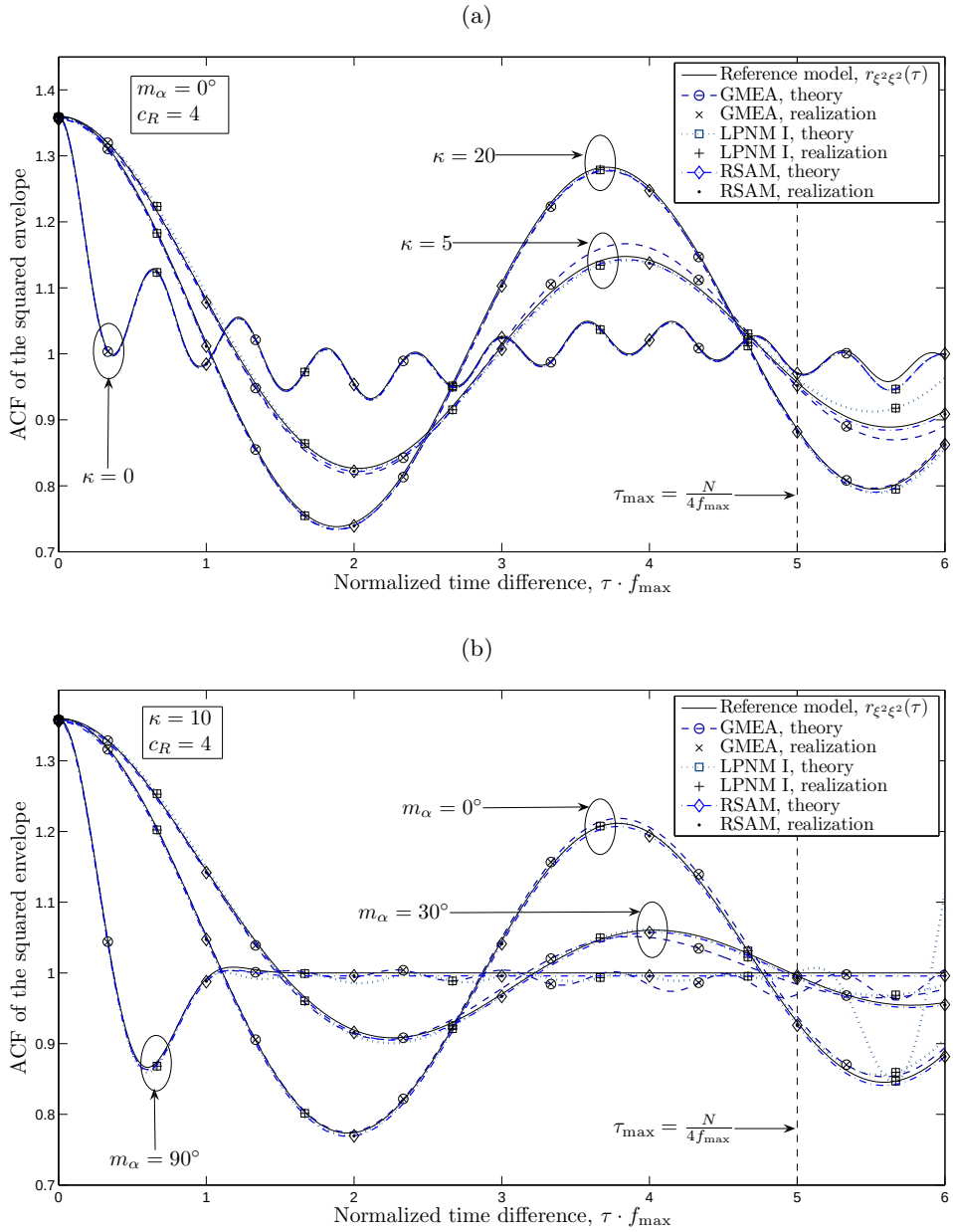

Figure 4.31: Comparison among the GMEA, RSAM, and LPNM I in terms of the emulation of the ACF of the reference model's squared envelope by considering a Rician factor $c_R = 4$ and the von Mises PDF of the AOA with different pairs of parameters m_α and κ ($N = 20$, $\sigma^2_{\boldsymbol{\nu}} = 1$, $p = 2$, $\tau_{\max} = 5/f_{\max}$, $\gamma = 1 \times 10^{-3}$).

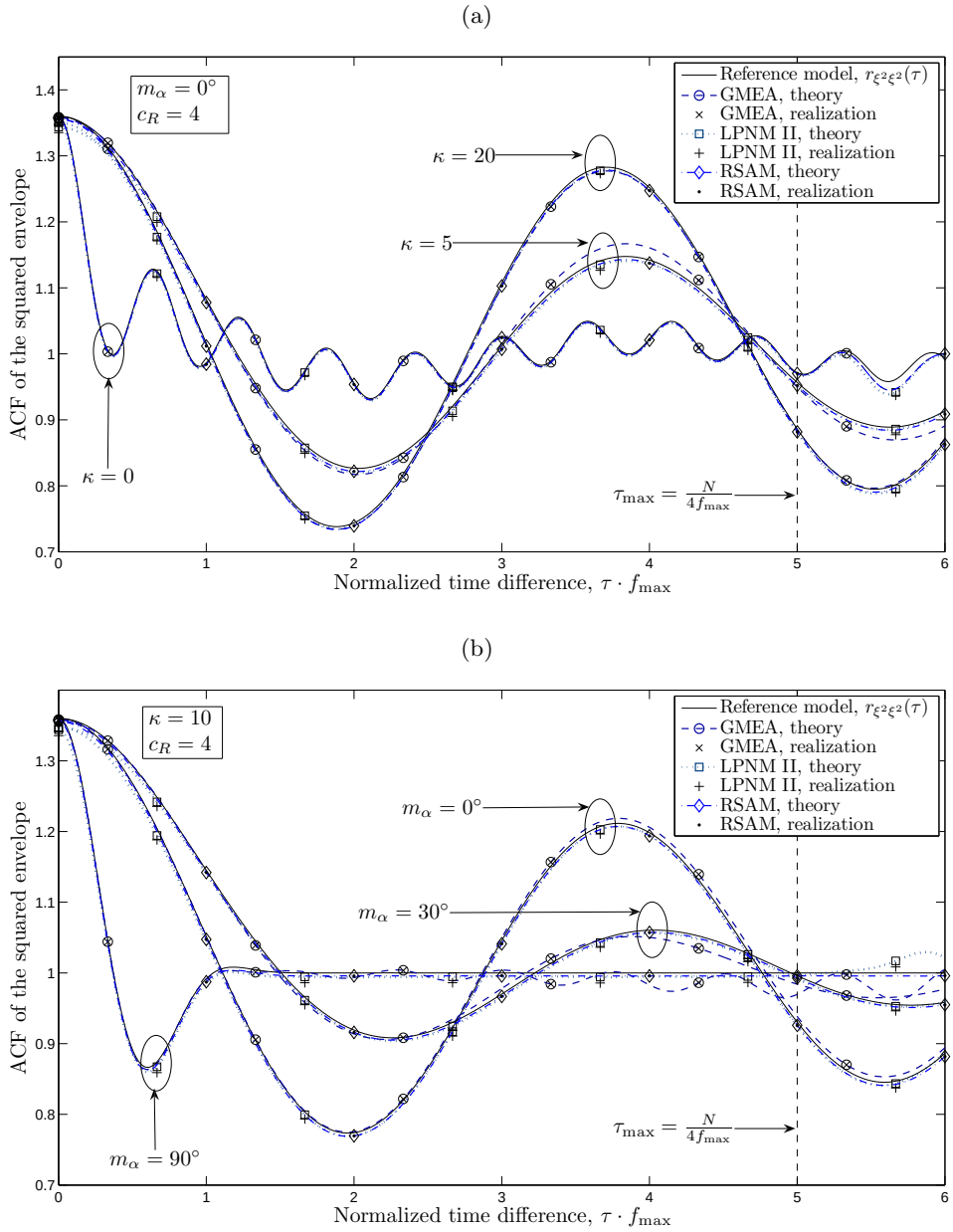

Figure 4.32: Comparison among the GMEA, RSAM, and LPNM II in terms of the emulation of the ACF of the reference model's squared envelope by considering a Rician factor $c_R = 4$ and the von Mises PDF of the AOA with different pairs of parameters m_α and κ ($N = 20$, $\sigma^2_{\boldsymbol{\nu}} = 1$, $p = 2$, $\tau_{\max} = 5/f_{\max}$, $\gamma = 1 \times 10^{-3}$).

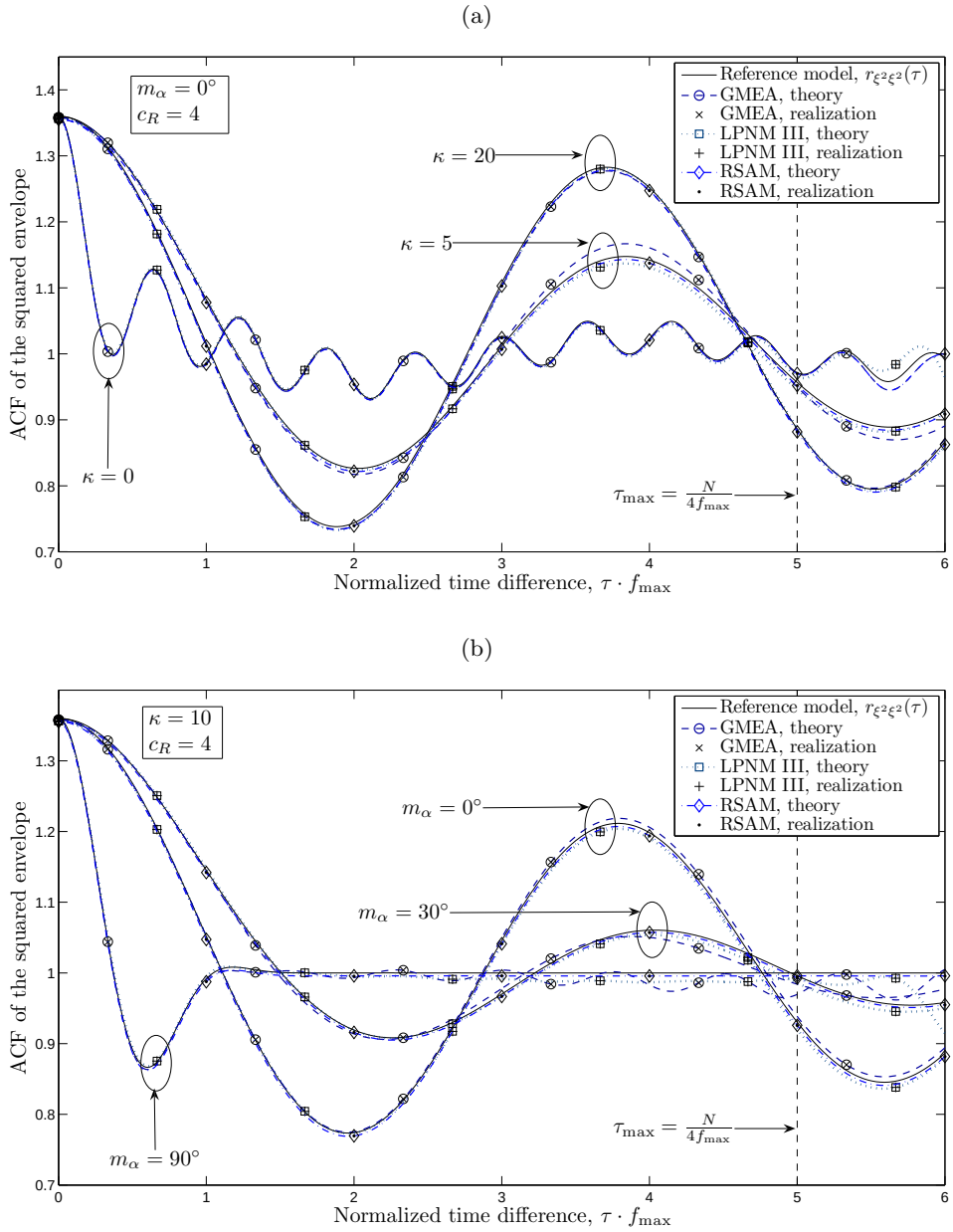

Figure 4.33: Comparison among the GMEA, RSAM, and LPNM III in terms of the emulation of the ACF of the reference model's squared envelope by considering a Rician factor $c_R = 4$ and the von Mises PDF of the AOA with different pairs of parameters m_α and κ ($N = 20$, $\sigma_{\boldsymbol{\nu}}^2 = 1$, $p = 2$, $\tau_{\max} = 5/f_{\max}$, $\gamma = 1 \times 10^{-3}$).

the ACFs of $\hat{\boldsymbol{\xi}}^2(t)$ and $\boldsymbol{\xi}^2(t)$. Such an offset, which can clearly be distinguished at $\tau = 0$, is caused by the term $\sum_{n=1}^{N} \hat{c}_n^4$ affecting the ACF $r_{\hat{\boldsymbol{\zeta}}^2\hat{\boldsymbol{\zeta}}^2}(\tau)$ of the squared envelope $\boldsymbol{\zeta}^2(t) = |\boldsymbol{\mu}(t)|^2$ of the simulation model's random component [see (3.30)]. It is evident from Figs. 4.25–4.27 that the smallest offset is produced by the GMEA and LPNM I, and the largest by the LPNM II.

4.6 Chapter Summary and Conclusions

In this chapter, we presented two simple and effective parameter computation method for the design of SOC-based channel simulation models. The proposed methods, which we have named the GMEA and the RSAM, are intended to allow for an accurate emulation of the channel's correlation properties and fading statistics. We evaluated the performance of the proposed methods in terms of the approximation of the ACF, average Doppler shift, and Doppler spread of the channel's diffuse component. In addition, we evaluated the methods' performance with respect to the emulation of the envelope and phase distributions of a Rician fading channel model, as well as in terms of the approximation of the squared envelope ACF. Results obtained by applying three different versions of the LPNM were also reported in this section and compared with those produced by the GMEA and RSAM.

All in all, the results presented in Section 4.5 show that the GMEA and the RSAM are suitable methods for the simulation of mobile fading channels characterized by symmetrical and asymmetrical DPSDs. However, our investigations indicate that the RSAM is better suited than the GMEA, and also than the LPNM, to emulate the channel's correlation and spectral characteristics. In turn, the GMEA and the LPNM perform better than the RSAM in terms of the emulation of the channel's fading statistics. The three version of the LPNM produce a better approximation to the channel ACF than the GMEA, but the GMEA proves to be more accurate than the LPNM I and LPNM II in reproducing the channel's average Doppler shift and Doppler spread.

Owing to their flexibility and good performance, the methods herein proposed can easily be used to design efficient simulation platforms for the software-assisted analysis of MBWCS, as we will demonstrate in Chapters 5 and 6.

Chapter 5

Simulation of Mobile MIMO Fading Channels Under Single-Bounce Non-Isotropic Scattering Conditions

5.1 Introduction

Simulation models having the ability to reproduce the statistical properties of mobile MIMO fading channels in non-isotropic scattering environments are highly desirable for the laboratory analysis of modern wireless communication systems. They are important, for example, to study the channel capacity [Abd02a] and the system bit error rate performance [Miti04] under directional propagation conditions.

It has been shown in a number of papers, e.g., [Gut07a, Han02, Pae04a, Paet05], that the simulation of MIMO fading channels can efficiently be performed by means of a SOC model. In fact, investigation carried out in [Mayy07] and [Pae04a] demonstrate, respectively, that a SOC channel simulator is a very useful tool for the performance assessment of multi-element antenna OFDM systems and for the analysis of the second order statistics of the channel capacity. However, as mentioned in the preceding chapter, the LPNM is currently the only method available for the design of SOC simulators for fading channels under non-isotropic scattering conditions. The development of new methods is therefore necessary to bypass the computational burden of the LPNM and facilitate the analysis of MIMO communication systems operating in non-isotropic scattering environments.

In this chapter, we show that the GMEA and the RSAM introduced in Chapter 4 can be applied, after some simple modifications, to the simulation of MIMO

channels with specified space-time correlation properties. Specifically, we address here the design of SOC simulation models for narrowband mobile MIMO Rayleigh fading channels in single-bounce scattering environments. It is important to notice that the GMEA and the RSAM cannot directly be applied as they were presented in Chapter 4 to the case of MIMO channels, since an accurate approximation of the channel spatial CCF (SCCF) requires special considerations.

The outline to the rest of the chapter is as follows. In Section 5.2, we describe the characteristics of a geometrical narrowband single-bounce scattering mobile MIMO channel model that will act as a reference model throughout this chapter. We also provide in that section a brief review of the autocorrelation, spectral, and spatial cross-correlation properties of such a channel model. In Section 5.3, we give a concise description of the stochastic SOC model that we will employ as a basis for the simulation of the reference model. The extension of the GMEA and the RSAM to the case of MIMO channels is presented in Section 5.4. The methods' performance is evaluated in Section 5.5 with respect to the emulation of the ACF and the SCCF of the reference model. An application of the GMEA and the RSAM to the simulation of wideband MIMO channels is discussed in Section 5.6. Finally, Section 5.7 summarizes the main points of the chapter.

5.2 Reference Model

5.2.1 The Geometrical One-Ring Scattering Model

The frequency-non-selective mobile MIMO channel model considered in this chapter is an extension of the SISO channel model described in Chapter 2 with respect to an elementary 2×2 multi-element antenna system and a two-dimensional single-bounce scattering environment. We assume that the transmitter (BS) is fixed and unobstructed by local scatterers, whereas the receiver (MT) moves at a speed v and is surrounded by a ring of local scatterers. The geometrical configuration of such a propagation scenario is depicted in Fig. 5.1. The symbols introduced in that figure stand for:

T_m: the mth transmitter antenna;

R_k: the kth receiver antenna;

S_n: the nth scatterer;

O_T: the center of the transmitter antenna array;

O_R: the center of the receiver antenna array;

D: the distance from O_T to O_R.

R: the radius of the ring of scatterers;

Δ_T: the distance between the transmitter antennas;

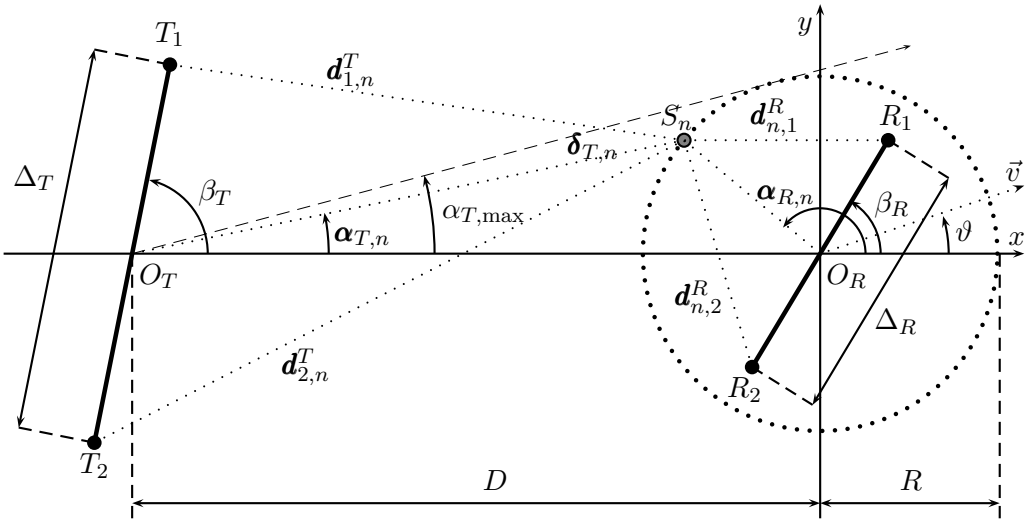

Figure 5.1: The geometrical one-ring scattering propagation model

Δ_R: the distance between the receiver antennas;

$\boldsymbol{d}^T_{m,n}$: the distance from the mth transmitter antenna to the nth scatter;

$\boldsymbol{d}^R_{n,k}$: the distance from the nth scatter to the kth receiver antenna;

$\boldsymbol{\delta}_{T,n}$: the distance from O_T to the nth scatter;

$\boldsymbol{\alpha}_{R,n}$: the AOA of the nth scattered wave;

$\boldsymbol{\alpha}_{T,n}$: the angle of departure (AOD) of the transmitted wave impinging the nth scatterer;

$\alpha_{T,\max}$: one half of the maximum angle of spread seen at the BS;

β_T: the orientation angle of the transmitter antenna array;

β_R: the orientation angle of the receiver antenna array;

ϑ: the angle of the vector $\vec{v}$ pointing at the direction of motion of the receiver.

The geometrical one-ring scattering model shown in 5.1 was originally proposed in [Jake74, Sec. 1.6.1] to study the channel spatial correlation at the base station, and it was extended in [Shiu00] to the case of MIMO channels. The model has widely been in use as a basis for assessing the performance of multi-element antenna systems, e.g., [Chen00, Mayy07].

We will assume that the AOAs $\boldsymbol{\alpha}_{R,n}$ are i.i.d. random variables characterized by a circular PDF $p_{\boldsymbol{\alpha}_R}(\alpha)$, whereas $\boldsymbol{\alpha}_{T,n}$, $\boldsymbol{d}^R_{n,k}$, $\boldsymbol{d}^T_{m,n}$, and $\boldsymbol{\delta}_{T,n}$ can be defined as functions of $\boldsymbol{\alpha}_{R,n}$. Specifically, $\boldsymbol{\delta}_{T,n}$ and $\boldsymbol{\alpha}_{T,n}$ can be determined by solving the following equations in the triangle $O_T S_n O_R$ [Abd02a, Chen00]

$$\frac{D}{\sin(\boldsymbol{\alpha}_{R,n} - \boldsymbol{\alpha}_{T,n})} = \frac{R}{\sin(\boldsymbol{\alpha}_{T,n})} = \frac{\boldsymbol{\delta}_{T,n}}{\sin(\boldsymbol{\alpha}_{R,n})} \tag{5.1}$$

while the distances $\boldsymbol{d}_{n,k}^{R}$ and $\boldsymbol{d}_{m,n}^{T}$ are defined as

$$\boldsymbol{d}_{m,n}^{T} = \frac{\Delta_T}{4} + \boldsymbol{\delta}_{T,n}^2 + (-1)^m \Delta_T \, \boldsymbol{\delta}_{T,n} \cos(\beta_T - \boldsymbol{\alpha}_{T,n}) \tag{5.2}$$

$$\boldsymbol{d}_{n,k}^{R} = \frac{\Delta_R}{4} + R^2 + (-1)^m \Delta_R \, R \cos(\boldsymbol{\alpha}_{R,n} - \beta_R). \tag{5.3}$$

Notice that the dependence of $\boldsymbol{d}_{m,n}^{T}$ on $\boldsymbol{\alpha}_{R,n}$ is implicit in the random parameters $\boldsymbol{\delta}_{T,n}$ and $\boldsymbol{\alpha}_{T,n}$. We will suppose that the far-field assumption holds, meaning that $D \gg R \gg \sup\{\Delta_T, \Delta_R\}$ and $\alpha_{\max,T}$ is small. Thereby, $\boldsymbol{d}_{m,n}^{T}$ and $\boldsymbol{d}_{n,k}^{R}$ can be rewritten as [Abd02a, Chen00]

$$\boldsymbol{d}_{m,n}^{T} = \boldsymbol{\delta}_{T,n} + \frac{(-1)^m \Delta_T}{2} [\cos(\beta_T) + \alpha_{T,\max} \sin(\beta_T) \sin(\boldsymbol{\alpha}_{R,n}) \tag{5.4}$$

$$\boldsymbol{d}_{n,k}^{R} = R + \frac{(-1)^m \Delta_R}{2} \cos(\boldsymbol{\alpha}_{R,n} - \beta_R). \tag{5.5}$$

5.2.2 Narrowband MIMO Rayleigh Fading Channel Model

Following the modeling approach described in Section 2.2, we characterize the channel gain associated to the link between the mth transmitter antenna and the kth receiver antenna in the equivalent complex baseband by a stationary complex Gaussian process $\boldsymbol{\mu}_{km}(t)$ with mean zero and variance $\sigma^2_{\boldsymbol{\mu}_{km}}$. For simplicity, we assume that $\sigma^2_{\boldsymbol{\mu}_{km}} = \sigma^2_{\boldsymbol{\mu}} \ \forall m, k$, where $0 < \sigma^2_{\boldsymbol{\mu}} < \infty$. The random process $\boldsymbol{\mu}_{km}(t)$ can be represented, in the context of the single-bounce scattering model in Fig. 5.1, by means of a sum of an infinite number of azimuthal plane waves as follows [Abd02a, Pae04a]

$$\boldsymbol{\mu}_{km}(t) = \lim_{N\to\infty} \sum_{n=1}^{N} \boldsymbol{a}_{m,n} \, \boldsymbol{b}_{k,n} \, \boldsymbol{c}_n \exp\{j\,(2\pi \boldsymbol{f}_n \, t + \boldsymbol{\theta}_n)\} \tag{5.6}$$

where $\boldsymbol{a}_{m,n} \triangleq a_m(\boldsymbol{\alpha}_{R,n})$ and $\boldsymbol{b}_{k,n} \triangleq b_k(\boldsymbol{\alpha}_{R,n})$, with

$$a_m(\boldsymbol{\alpha}_{R,n}) = \exp\left\{ \frac{j\pi(-1)^{m+1}\Delta_T}{\lambda} [\cos(\beta_T) + \alpha_{T,\max} \sin(\beta_T) \sin(\boldsymbol{\alpha}_{R,n}) \right\} \tag{5.7}$$

$$b_k(\boldsymbol{\alpha}_{R,n}) = \exp\left\{ \frac{j\pi(-1)^{k+1}\Delta_R}{\lambda} \cos(\boldsymbol{\alpha}_{R,n} - \beta_R) \right\}. \tag{5.8}$$

In (5.7) and (5.8), λ designates the wavelength of the transmitted signal. In conformity with the considerations made in Section 2.2, we assume that the random gains $\boldsymbol{c}_n$, the random Doppler frequencies $\boldsymbol{f}_n$, and the random phases $\boldsymbol{\theta}_n$ are statistically independent. The phases $\boldsymbol{\theta}_n$ are i.i.d. random variables uniformly distributed in $[-\pi, \pi)$, and the gains $\boldsymbol{c}_n$ satisfy $E\{|\boldsymbol{c}_n|^2\} = \sigma^2_{\boldsymbol{\mu}}/N$. On the other

hand, the Doppler frequencies $\boldsymbol{f}_n$ are defined as

$$\boldsymbol{f}_n \triangleq f_{\max}\cos\big(\boldsymbol{\alpha}_{R,n} - \vartheta\big), \qquad \forall n. \tag{5.9}$$

The equation above is a consequence of the fact that the MT (receiver) can move in any arbitrary direction over the reference Cartesian plane. This is in contrast to the case of the mobile SISO channel model described in Chapter 2, where it is assumed that the MT is moving along the x-axis of the Cartesian plane, and thus $\vartheta \in \{0, \pi\}$ [Clar68]. The angle ϑ is an important parameter of the MIMO channel model. Indeed, ϑ exerts a strong influence on the autocorrelation and spectral properties of $\boldsymbol{\mu}_{km}(t)$, as will be shown next.

5.2.3 Correlation Properties of the Reference Model

5.2.3.1 ACF and DPSD of the MIMO Channel Gains

Under the above considerations, one can easily verify that the ACF $r_{\boldsymbol{\mu}_{km}\boldsymbol{\mu}_{km}}(\tau) \triangleq E\{\boldsymbol{\mu}^*_{km}(t)\boldsymbol{\mu}_{km}(t+\tau)\}$ of the Gaussian process $\boldsymbol{\mu}_{km}(t)$ describing the complex channel gain between T_m and R_k is given by

$$r_{\boldsymbol{\mu}_{km}\boldsymbol{\mu}_{km}}(\tau) = \sigma^2_{\boldsymbol{\mu}} \int_{-\pi}^{\pi} p_{\boldsymbol{\alpha}_R}(\alpha)\, \exp\big\{j2\pi f_{\max}\cos(\alpha - \vartheta)\tau\big\} d\alpha. \tag{5.10}$$

For the analysis of the spectral characteristics of $\boldsymbol{\mu}_{km}(t)$, it is convenient to perform the change of variable $x = \alpha - \vartheta$ in (5.10). By doing so, and taking into account that $p_{\boldsymbol{\alpha}_R}$ is a circular PDF, we obtain the expression

$$r_{\boldsymbol{\mu}_{km}\boldsymbol{\mu}_{km}}(\tau) = \sigma^2_{\boldsymbol{\mu}} \int_{-\pi}^{\pi} p_{\boldsymbol{\alpha}_R}(x + \vartheta)\, \exp\big\{j2\pi f_{\max}\cos(x)\tau\big\} dx \tag{5.11}$$

which can be rewritten as follows

$$r_{\boldsymbol{\mu}_{km}\boldsymbol{\mu}_{km}}(\tau) = 2\sigma^2_{\boldsymbol{\mu}} \int_{0}^{\pi} g_{\boldsymbol{\alpha}_R}(\alpha + \vartheta)\, \exp\big\{j2\pi f_{\max}\cos(\alpha)\tau\big\} d\alpha \tag{5.12}$$

where $g_{\boldsymbol{\alpha}_R}(\alpha) = [p_{\boldsymbol{\alpha}_R}(\alpha) + p_{\boldsymbol{\alpha}_R}(-\alpha)]/2$ is the even part of $p_{\boldsymbol{\alpha}_R}(\alpha)$. From (5.12), it is straightforward to show that the DPSD $S_{\boldsymbol{\mu}_{km}\boldsymbol{\mu}_{km}}(f) \triangleq \int_{-\infty}^{\infty} r_{\boldsymbol{\mu}_{km}\boldsymbol{\mu}_{km}}(\tau) \exp\big\{-j2\pi f\tau\big\} d\tau$ of $\boldsymbol{\mu}_{km}(t)$ is equal to

$$S_{\boldsymbol{\mu}_{km}\boldsymbol{\mu}_{km}}(f) = 2\sigma^2_{\boldsymbol{\mu}}\, \mathrm{rect}(f) \cdot \frac{g_{\boldsymbol{\alpha}_R}(\arccos(f/f_{\max}) + \vartheta)}{f_{\max}\sqrt{1 - (f/f_{\max})^2}}. \tag{5.13}$$

It follows from (5.12) and (5.13) that the ACF and DPSD of $\boldsymbol{\mu}_{km}(t)$ are completely specified by the even part of $p_{\boldsymbol{\alpha}_R}(\alpha)$ and the parameters ϑ, $f_{\max}$, and $\sigma^2_{\boldsymbol{\mu}}$. We observe that $S_{\boldsymbol{\mu}_{km}\boldsymbol{\mu}_{km}}(f)$ is symmetrical if the IQ components $\boldsymbol{\mu}_{I,km}(t)$ and $\boldsymbol{\mu}_{Q,km}(t)$ of $\boldsymbol{\mu}_{km}(t)$ are uncorrelated. On the contrary, $S_{\boldsymbol{\mu}_{km}\boldsymbol{\mu}_{km}}(f)$ is asymmetrical if $\boldsymbol{\mu}_{I,km}(t)$ and $\boldsymbol{\mu}_{Q,km}(t)$ are cross-correlated. In this respect, it is worth mentioning that the shape of $S_{\boldsymbol{\mu}_{km}\boldsymbol{\mu}_{km}}(f)$ depends not only on $g_{\boldsymbol{\alpha}_R}(\alpha)$, but also on the angle ϑ. In fact, $S_{\boldsymbol{\mu}_{km}\boldsymbol{\mu}_{km}}(f)$ is symmetrical if and only if $g_{\boldsymbol{\alpha}_R}(\alpha+\vartheta) = g_{\boldsymbol{\alpha}_R}(\pi-\alpha+\vartheta)$ for $\alpha \in [0,\pi)$. This condition is more general than the one that applies on the DPSD $S_{\boldsymbol{\mu}\boldsymbol{\mu}}(f)$ of the SISO channel model described in Chapter 2, where $S_{\boldsymbol{\mu}\boldsymbol{\mu}}(f) = S_{\boldsymbol{\mu}\boldsymbol{\mu}}(-f)$ if and only if $g_{\boldsymbol{\alpha}}(\alpha) = g_{\boldsymbol{\alpha}}(\pi-\alpha)$ for $\alpha \in [0,\pi)$.

5.2.3.2 Space-Time CCF of the MIMO Channel Gains

Information about the cross-correlation properties of the complex channel gains is also relevant for the characterization of the MIMO channel model. Such an information is important for the analysis of space-time block coding schemes and space diversity systems [Gold05, Ch. 10], just to give a few examples. The correlation between $\boldsymbol{\mu}_{km}(t)$ and $\boldsymbol{\mu}_{ql}(t)$ can be studied on the basis of the space-time CCF function (STCCF) $r_{\boldsymbol{\mu}_{km}\boldsymbol{\mu}_{ql}}(\Delta_T,\Delta_R,\tau) \triangleq E\{\boldsymbol{\mu}^*_{km}(t)\,\boldsymbol{\mu}_{ql}(t+\tau)\}$. This function gives a measure of the correlation between $\boldsymbol{\mu}_{km}(t)$ and $\boldsymbol{\mu}_{ql}(t)$ in terms of the time difference τ and the size of the transmitter and the receiver antenna arrays. From the expression given in (5.6) for $\boldsymbol{\mu}_{km}(t)$, one can show that

$$\begin{aligned} r_{\boldsymbol{\mu}_{km}\boldsymbol{\mu}_{ql}}(\Delta_T,\Delta_R,\tau) &= \sigma^2_{\boldsymbol{\mu}} \int_{-\pi}^{\pi} p_{\boldsymbol{\alpha}_R}(\alpha)\, \exp\{j2\pi f_{\max}\cos(\alpha-\vartheta)\tau\} \\ &\quad \times a^*_m(\alpha,\Delta_T)\, a_l(\alpha,\Delta_T)\, b^*_k(\alpha,\Delta_R)\, b_q(\alpha,\Delta_R) d\alpha. \end{aligned} \quad (5.14)$$

The SCCF $\rho_{\boldsymbol{\mu}_{km}\boldsymbol{\mu}_{ql}}(\Delta_T,\Delta_R) \triangleq E\{\boldsymbol{\mu}^*_{km}(t)\boldsymbol{\mu}_{ql}(t)\}$ between $\boldsymbol{\mu}_{km}(t)$ and $\boldsymbol{\mu}_{ql}(t)$ is important too. This function is relevant for the capacity analysis of MIMO fading channels [Shiu00, Abd02a]. By taking $\tau = 0$ in (5.14), we obtain the result

$$\begin{aligned} \rho_{\boldsymbol{\mu}_{km}\boldsymbol{\mu}_{ql}}(\Delta_T,\Delta_R) &= \sigma^2_{\boldsymbol{\mu}} \int_{-\pi}^{\pi} p_{\boldsymbol{\alpha}_R}(\alpha)\, a^*_m(\alpha,\Delta_T)\, a_l(\alpha,\Delta_T) \\ &\quad \times b^*_k(\alpha,\Delta_R)\, b_q(\alpha,\Delta_R) d\alpha. \end{aligned} \quad (5.15)$$

5.3 The Simulation Model

5.3.1 The Stochastic SOC Simulation Model

Following the simulation approach presented in Chapter 3, we can approximate the statistical properties of the complex Gaussian processes $\boldsymbol{\mu}_{km}(t)$ by means of

a stochastic SOC simulation model of the form

$$\hat{\boldsymbol{\mu}}_{km}(t) \;=\; \sum_{n=1}^{N} a_m(\hat{\alpha}_n)\, b_k(\hat{\alpha}_n)\, \hat{c}_n\, \exp\left\{j\big(2\pi \hat{f}_n\, t + \hat{\boldsymbol{\theta}}_n\big)\right\} \tag{5.16}$$

where

$$\hat{f}_n \;=\; f_{\max} \cos(\hat{\alpha}_n - \vartheta) \tag{5.17}$$

and $\hat{\alpha}_n \in [-\pi, \pi)$. We assume that the phases $\hat{\boldsymbol{\theta}}_n$ are i.i.d. random variables uniformly distributed in $[-\pi, \pi)$ and the gains $\hat{c}_n$ satisfy $\sum_{n=1}^{N} |\hat{c}_n|^2 = \sigma^2_{\boldsymbol{\mu}}$. The functions $a_m(\alpha)$ and $b_k(\alpha)$ are defined in (5.7) and (5.8), respectively.

5.3.2 Correlation Properties of the SOC Simulation Model

It is easy to show that $\hat{\boldsymbol{\mu}}_{km}(t)$ is a zero mean WSS random process with variance equal to $\sigma^2_{\boldsymbol{\mu}}$ and ACF $r_{\hat{\boldsymbol{\mu}}_{km}\hat{\boldsymbol{\mu}}_{km}}(\tau) \triangleq E\{\hat{\boldsymbol{\mu}}^*_{km}(t) \cdot \hat{\boldsymbol{\mu}}_{km}(t+\tau)\}$ given by

$$r_{\hat{\boldsymbol{\mu}}_{km}\hat{\boldsymbol{\mu}}_{km}}(\tau) \;=\; \sum_{n=1}^{N} \hat{c}_n^2 \exp\{j2\pi f_{\max} \cos(\hat{\alpha}_n - \vartheta)\tau\}. \tag{5.18}$$

In addition, one can show that the STCCF $r_{\hat{\boldsymbol{\mu}}_{km}\hat{\boldsymbol{\mu}}_{ql}}(\Delta_T, \Delta_R, \tau) \triangleq E\{\hat{\boldsymbol{\mu}}^*_{km}(t) \cdot \hat{\boldsymbol{\mu}}_{ql}(t+\tau)\}$ between $\hat{\boldsymbol{\mu}}_{km}(t)$ and $\hat{\boldsymbol{\mu}}_{ql}(t)$ is equal to

$$\begin{aligned} r_{\hat{\boldsymbol{\mu}}_{km}\hat{\boldsymbol{\mu}}_{ql}}(\Delta_T, \Delta_R, \tau) \;=\; & \sum_{n=1}^{N} \hat{c}_n^2 \exp\{j2\pi f_{\max} \cos(\hat{\alpha}_n - \vartheta)\tau\} \\ & \times a^*_m(\hat{\alpha}_n, \Delta_T)\, a_l(\hat{\alpha}_n, \Delta_T)\, b^*_k(\hat{\alpha}_n, \Delta_R)\, b_q(\hat{\alpha}_n, \Delta_R). \end{aligned} \tag{5.19}$$

With respect to the SCCF $\rho_{\hat{\boldsymbol{\mu}}_{km}\hat{\boldsymbol{\mu}}_{ql}}(\Delta_T, \Delta_R) \triangleq E\{\hat{\boldsymbol{\mu}}^*_{km}(t)\hat{\boldsymbol{\mu}}_{ql}(t)\}$ between $\hat{\boldsymbol{\mu}}_{km}(t)$ and $\hat{\boldsymbol{\mu}}_{ql}(t)$, we have

$$\rho_{\hat{\boldsymbol{\mu}}_{km}\hat{\boldsymbol{\mu}}_{ql}}(\Delta_T, \Delta_R) = \sum_{n=1}^{N} \hat{c}_n^2\, a^*_m(\hat{\alpha}_n, \Delta_T)\, a_l(\hat{\alpha}_n, \Delta_T)\, b^*_k(\hat{\alpha}_n, \Delta_R)\, b_q(\hat{\alpha}_n, \Delta_R). \tag{5.20}$$

We observe that if $\hat{f}_n \neq 0\ \forall n$ and $\hat{f}_n \neq \hat{f}_m\ \forall n \neq m$, then the processes $\hat{\boldsymbol{\mu}}_{km}(t)$ are ergodic with respect to the mean value, the ACF, and the STCCF.

5.4 Parameter Computation Methods

For the simulation of the MIMO channel model, the problem consists in finding proper values for the gains $\hat{c}_n$ and the AOAs $\hat{\alpha}_n$ such that the autocorrelation and cross-correlation properties of the random processes $\hat{\boldsymbol{\mu}}_{km}(t)$ resemble those

of the Gaussian processes $\boldsymbol{\mu}_{km}(t)$. In particular, we are interested in emulating the ACF $r_{\boldsymbol{\mu}_{km}\boldsymbol{\mu}_{ql}}(\tau)$ and the SCCF $\rho_{\boldsymbol{\mu}_{km}\boldsymbol{\mu}_{ql}}(\Delta_T, \Delta_R)$ of the reference model. In what follows, we will explain how to apply the GMEA and the RSAM to solve this parameter computation problem.

5.4.1 The GMEA

The results presented in Chapter 4 indicate that the ACF of $\boldsymbol{\mu}_{km}(t)$ can satisfactorily be approximated by defining the gains $\hat{c}_n$ as in (4.1), i.e., $\hat{c}_n = \sigma^2_{\boldsymbol{\mu}}/\sqrt{N}$, and computing the Doppler frequencies $\hat{f}_n$ by solving the equation

$$\int_{-f_{\max}}^{\hat{f}_n} S_{\boldsymbol{\mu}_{km}\boldsymbol{\mu}_{km}}(f)df \;=\; \frac{\sigma^2_{\boldsymbol{\mu}}}{N}\left(N - n + \frac{1}{2}\right) \tag{5.21}$$

for $n = 1, \ldots, N$. Since $\hat{f}_n = f_{\max}\cos(\hat{\alpha}_n - \vartheta)$ [see (5.17)], one can alternatively compute the Doppler frequencies $\hat{f}_n$ by finding the AOAs $\hat{\alpha}_n$ that solve

$$\int_{0}^{\hat{\alpha}_n - \vartheta} g_{\boldsymbol{\alpha}_R}(\alpha + \vartheta)d\alpha \;=\; \frac{1}{2N}\left(n - \frac{1}{2}\right). \tag{5.22}$$

We notice, nonetheless, that the solutions of (5.21) and (5.22) provide information only about the even part of $p_{\boldsymbol{\alpha}_R}(\alpha)$. This is sufficient to emulate the autocorrelation and spectral characteristics of $\boldsymbol{\mu}_{km}(t)$, but the emulation of the SCCF between $\boldsymbol{\mu}_{km}(t)$ and $\boldsymbol{\mu}_{ql}(t)$ requires information also about the odd part of $p_{\boldsymbol{\alpha}_R}(\alpha)$ [see (5.15)]. In order to take the odd part of $p_{\boldsymbol{\alpha}_R}(\alpha)$ into account, we propose to compute the AOAs $\hat{\alpha}_n$ by solving

$$\int_{-\pi}^{\hat{\alpha}_n - \vartheta} p_{\boldsymbol{\alpha}_R}(\alpha + \vartheta)d\alpha \;=\; \frac{1}{N}\left(n - \frac{1}{4}\right). \tag{5.23}$$

In the equation above, the factor of $1/(4N)$ has been introduced to guarantee the uncorrelation between the IQ components of $\hat{\boldsymbol{\mu}}_{km}(t)$ and to ensure that $\hat{f}_n \neq \hat{f}_m$ $\forall n \neq m$ when the DPSD $S_{\boldsymbol{\mu}_{km}\boldsymbol{\mu}_{km}}(f)$ of the reference model is symmetrical. Such a factor also ensures that $\hat{f}_n \neq 0$ $\forall n$ when $S_{\boldsymbol{\mu}_{km}\boldsymbol{\mu}_{km}}(f) = S_{\boldsymbol{\mu}_{km}\boldsymbol{\mu}_{km}}(-f)$ and the number of cisoids is even, i.e., when $N = 2M$, where $M \in \mathbb{Z}^+$. We emphasize that the number of cisoids shall be even in order for this latter characteristic to hold. Otherwise, if N is odd and $S_{\boldsymbol{\mu}_{km}\boldsymbol{\mu}_{km}}(f)$ is symmetrical, then the solutions of (5.23) will produce a Doppler frequency $\hat{f}_n$ equal to zero. The inequalities $\hat{f}_n \neq \hat{f}_m$ $\forall n \neq m$ and $\hat{f}_n \neq 0$ $\forall n$ are in general fulfilled when $S_{\boldsymbol{\mu}_{km}\boldsymbol{\mu}_{km}}(f)$ is asymmetrical, irrespective of the value of N.

5.4.2 The RSAM

In the case of the RSAM, we observe that the STCCF between $\boldsymbol{\mu}_{km}(t)$ and $\boldsymbol{\mu}_{ql}(t)$ can be expressed as

$$\begin{aligned} r_{\boldsymbol{\mu}_{km}\boldsymbol{\mu}_{ql}}(\Delta_T,\Delta_R,\tau) &= \frac{2\pi\sigma_{\boldsymbol{\mu}}^2}{N}\lim_{N\to\infty}\sum_{n=1}^{N} p_{\boldsymbol{\alpha}_R}(\alpha_n)\,\exp\{j2\pi f_{\max}\cos(\alpha_n-\vartheta)\tau\} \\ &\quad\times a_m^*(\alpha_n,\Delta_T)\,a_l(\alpha_n,\Delta_T)\,b_k^*(\alpha_n,\Delta_R)\,b_q(\alpha_n,\Delta_R) \quad (5.24) \end{aligned}$$

where $\alpha_n = n2\pi/N - \alpha_0$, and α_0 is a real number in $[0, 2\pi/N]$. By removing the limit in the previous equation, we can write

$$\begin{aligned} r_{\boldsymbol{\mu}_{km}\boldsymbol{\mu}_{ql}}(\Delta_T,\Delta_R,\tau) &\approx \frac{2\pi\sigma_{\boldsymbol{\mu}}^2}{N}\sum_{n=1}^{N} p_{\boldsymbol{\alpha}_R}(\alpha_n)\,\exp\{j2\pi f_{\max}\cos(\alpha_n-\vartheta)\tau\} \\ &\quad\times a_m^*(\alpha_n,\Delta_T)\,a_l(\alpha_n,\Delta_T)\,b_k^*(\alpha_n,\Delta_R)\,b_q(\alpha_n,\Delta_R). \quad (5.25) \end{aligned}$$

Based on the above result, and taking account of the expression given in (5.19) for the STCCF $r_{\hat{\boldsymbol{\mu}}_{km}\hat{\boldsymbol{\mu}}_{ql}}(\Delta_T,\Delta_R,\tau)$ of the simulation model, we can state that $r_{\hat{\boldsymbol{\mu}}_{km}\hat{\boldsymbol{\mu}}_{ql}}(\Delta_T,\Delta_R,\tau) \approx r_{\boldsymbol{\mu}_{km}\boldsymbol{\mu}_{ql}}(\Delta_T,\Delta_R,\tau)$ if

$$\hat{\alpha}_n = \frac{n2\pi}{N} - \alpha_0 \quad (5.26)$$

$$\hat{c}_n = \sigma_{\boldsymbol{\mu}}\sqrt{\frac{p_{\boldsymbol{\alpha}}(\hat{\alpha}_n)}{\sum_{m=1}^{N} p_{\boldsymbol{\alpha}}(\hat{\alpha}_m)}}. \quad (5.27)$$

Even though the value of α_0 can arbitrarily be chosen within $[0, 2\pi/N]$, we recommend to set $\alpha_0 = \pi/(2N)$ to ensure that $\hat{f}_n \neq \hat{f}_m\ \forall n \neq m$ and to guarantee the uncorrelation between the IQ components of $\hat{\boldsymbol{\mu}}_{km}(t)$ when the DPSD $S_{\boldsymbol{\mu}_{km}\boldsymbol{\mu}_{km}}(f)$ of the reference model is symmetrical. Furthermore, choosing $\alpha_0 = \pi/(2N)$ also assures that $\hat{f}_n \neq 0\ \forall n$ when $S_{\boldsymbol{\mu}_{km}\boldsymbol{\mu}_{km}}(f) = S_{\boldsymbol{\mu}_{km}\boldsymbol{\mu}_{km}}(-f)$ and $N = 2M$, $M \in \mathbb{Z}^+$. This latter condition does not hold if N is odd, as in the case of the GMEA.

We have demonstrated in [Gut07a] that the methodology in (5.26) and (5.27) provides excellent results concerning the emulation of the ACF $r_{\boldsymbol{\mu}_{km}\boldsymbol{\mu}_{km}}(\tau)$ and the SCCF $\rho_{\boldsymbol{\mu}_{km}\boldsymbol{\mu}_{ql}}(\Delta_T,\Delta_R)$. However, to properly approximate the envelope distribution of the complex Gaussian processes $\boldsymbol{\mu}_{km}(t)$, it is important to impose a constraint in the range of values that the gains $\hat{c}_n$ may take. With this in mind, we will assume that $p_{\boldsymbol{\alpha}_R}(\alpha)$ has only one maximum in $[-\pi, \pi)$. Then, following the idea behind the RSAM described in Section 4.4.1.3, we redefine

$$\hat{\alpha}_n = \alpha_\ell + \frac{\alpha_u - \alpha_\ell}{N}\left(n - \frac{1}{4}\right), \qquad \alpha_u > \alpha_\ell. \quad (5.28)$$

In (5.28), α_u and α_ℓ designate, in that order, the lower and the upper boundaries

of the subinterval $\mathcal{I}_U = [\alpha_\ell, \alpha_u]$ within the which the PDF $p_{\boldsymbol{\alpha}_R}(\alpha)$ is above a given threshold $\gamma \in \big(0, \sup\{p_{\boldsymbol{\alpha}_R}(\alpha)\}_{\alpha\in[-\pi,\pi)}\big)$.

5.5 Performance Analysis

5.5.1 Considerations

In this section, we will present some simulation examples demonstrating the good performance of the GMEA and the RSAM concerning the emulation of the ACF $r_{\boldsymbol{\mu}_{km}\boldsymbol{\mu}_{km}}(\tau)$ and the SCCF $\rho_{\boldsymbol{\mu}_{km}\boldsymbol{\mu}_{ql}}(\Delta_T, \Delta_R)$ of the reference model. To that end, we will assume that the random AOAs $\boldsymbol{\alpha}_R$ are von Mises distributed, so that:

$$p_{\boldsymbol{\alpha}_R}(\alpha+\vartheta) = \frac{\exp\{\kappa\cos(\alpha - m_\alpha + \vartheta)\}}{2\pi I_0(\kappa)} \tag{5.29}$$

$$g_{\boldsymbol{\alpha}_R}(\alpha+\vartheta) = \frac{\exp\big\{\kappa\cos(\alpha)\cos(m_\alpha-\vartheta)\big\}}{2\pi I_0(\kappa)} \cdot \cosh\big(\kappa\sin(\alpha)\sin(m_\alpha-\vartheta)\big) \tag{5.30}$$

where $\alpha \in [-\pi, \pi)$. It is easy to show, by substituting (5.30) into (5.13), that the DPSD of the complex Gaussian processes $\boldsymbol{\mu}_{km}(t)$ is given by

$$\begin{aligned} S^{\mathrm{VM}}_{\boldsymbol{\mu}_{km}\boldsymbol{\mu}_{km}}(f) &= \mathrm{rect}(f)\cdot\cosh\Big(\kappa\,\sin(m_\alpha-\vartheta)\sqrt{1-(f/f_{\max})^2}\Big) \\ &\quad\times\frac{\sigma^2_{\boldsymbol{\mu}}\,\exp\big\{\kappa\cos(m_\alpha-\vartheta)\,f/f_{\max}\big\}}{\pi f_{\max} I_0(\kappa)\sqrt{1-(f/f_{\max})^2}}. \end{aligned} \tag{5.31}$$

In turn, by following (5.12), one can show that the ACF of $\boldsymbol{\mu}_{km}(t)$ is equal to

$$r^{\mathrm{VM}}_{\boldsymbol{\mu}_{km}\boldsymbol{\mu}_{km}}(\tau) = \frac{\sigma^2_{\boldsymbol{\mu}}\, I_0\Big(\sqrt{\kappa^2-(2\pi f_{\max}\tau)^2 + j4\pi\kappa f_{\max}\tau\cos(m_\alpha-\vartheta)}\Big)}{I_0(\kappa)}. \tag{5.32}$$

The STCCF $r^{\mathrm{VM}}_{\boldsymbol{\mu}_{km}\boldsymbol{\mu}_{ql}}(\Delta_T, \Delta_R, \tau)$ between $\boldsymbol{\mu}_{km}(t)$ and $\boldsymbol{\mu}_{ql}(t)$ can also be expressed in closed form by substituting (5.29) into (5.14). Particularly, for the MIMO channel gains $\boldsymbol{\mu}_{11}(t)$ and $\boldsymbol{\mu}_{22}(t)$, we have [Abd02a]

$$\begin{aligned} r^{\mathrm{VM}}_{\boldsymbol{\mu}_{11}\boldsymbol{\mu}_{22}}(\Delta_T, \Delta_R, \tau) &= \frac{\sigma^2_{\boldsymbol{\mu}}\exp\{-j2\pi\bar{\Delta}_T\cos(\beta_T)\}}{I_0(\kappa)} \\ &\quad\times I_0\Big(\Big\{\kappa^2 - 4\pi^2\Big[\bar{\tau}^2 + \bar{\Delta}_R^2 + \big(\bar{\Delta}_T\,\alpha_{\max,T}\,\sin(\beta_T)\big)^2 \\ &\qquad -2\bar{\tau}\bar{\Delta}_R\cos(\beta_R-\vartheta) - 2\bar{\Delta}_T\,\alpha_{\max,T}\,\sin(\beta_T) \\ &\qquad \times\big(\bar{\tau}\sin(\vartheta) - \bar{\Delta}_R\sin(\beta_R)\big)\Big] \\ &\qquad +j4\pi\kappa\Big[\bar{\tau}\cos(m_\alpha-\vartheta) - \bar{\Delta}_R\cos(m_\alpha-\beta_R) \\ &\qquad -\bar{\Delta}_T\,\alpha_{\max,T}\,\sin(\beta_T)\sin(\vartheta)\Big]\Big\}^{-1/2}\Big). \end{aligned} \tag{5.33}$$

where $\bar{\tau} = \tau \cdot f_{\max}$, $\bar{\Delta}_T = \Delta_T/\lambda$, and $\bar{\Delta}_R = \Delta_R/\lambda$. One can deduce from (5.33) that the SCCF $\rho^{\mathrm{VM}}_{\boldsymbol{\mu}_{km}\boldsymbol{\mu}_{ql}}(\Delta_T, \Delta_R) = r^{\mathrm{VM}}_{\boldsymbol{\mu}_{km}\boldsymbol{\mu}_{ql}}(\Delta_T, \Delta_R, 0)$ is equal to

$$\begin{aligned}\rho^{\mathrm{VM}}_{\boldsymbol{\mu}_{11}\boldsymbol{\mu}_{22}}(\Delta_T, \Delta_R) \;=\; & \frac{\sigma^2_{\boldsymbol{\mu}} \exp\{-j2\pi\bar{\Delta}_T \cos(\beta_T)\}}{I_0(\kappa)} \\ & \times I_0\Big(\Big\{\kappa^2 - 4\pi^2\Big[\bar{\Delta}_R^2 + \big(\bar{\Delta}_T\, \alpha_{\max,T}\, \sin(\beta_T)\big)^2 + 2\bar{\Delta}_T\, \bar{\Delta}_R \\ & \times \alpha_{\max,T}\, \sin(\beta_T)\sin(\beta_R)\Big] - j4\pi\kappa\Big[\bar{\Delta}_R \cos(m_\alpha - \beta_R) \\ & + \bar{\Delta}_T\, \alpha_{\max,T}\, \sin(\beta_T)\sin(\vartheta)\Big]\Big\}^{-1/2}\Big). \end{aligned} \tag{5.34}$$

For the simulations, we will consider the following triplets of parameters for the von Mises PDF in (5.29): $(\kappa = 0, m_\alpha = 0^\circ, \gamma = 0^\circ)$; $(\kappa = 5, m_\alpha = 0^\circ, \gamma = 0^\circ)$; $(\kappa = 20, m_\alpha = 0^\circ, \gamma = 0^\circ)$; $(\kappa = 10, m_\alpha = 0^\circ, \gamma = 0^\circ)$; $(\kappa = 10, m_\alpha = 20^\circ, \gamma = -10^\circ)$; $(\kappa = 10, m_\alpha = 40^\circ, \gamma = -50^\circ)$. We notice that the first and the last of such triplets produce a symmetrical DPSD $S^{\mathrm{VM}}_{\boldsymbol{\mu}_{km}\boldsymbol{\mu}_{km}}(f)$, while the other four triplets result in an asymmetrical DPSD. We choose $\beta_T = \beta_R = 90^\circ$, $\alpha_{\max,T} = 2^\circ$, $f_{\max} = 91$ Hz, $\sigma^2_{\boldsymbol{\mu}} = 1$, and $N = 24$. Except by the number of cisoids, these parameters are the same as the ones considered in [Pae04a] for evaluating the performance of SOC simulators designed by applying the LPNM. In that paper, the number of cisoids was equal to $N = 25$. Here, we have chosen $N = 24$ to ensure that the GMEA and the RSAM satisfy the inequality $\hat{f}_n \neq 0\ \forall n$. Regarding the threshold γ of the RSAM, we set $\gamma = 1 \times 10^{-3}$.

5.5.2 Emulation of the ACF

Figure 5.2 shows a comparison between the ACF $r^{\mathrm{VM}}_{\boldsymbol{\mu}_{km}\boldsymbol{\mu}_{km}}(\tau)$ of the reference model [see (5.32)] and the ACF $r_{\hat{\boldsymbol{\mu}}_{km}\hat{\boldsymbol{\mu}}_{km}}(\tau)$ of the simulation model [see (5.18)] by applying the GMEA and the RSAM. We can observe from Fig. 5.2 that both methods produce a very good approximation to the ACF of the reference model. This indicates that the modifications introduced in this Chapter to the GMEA and the RSAM do not affect the capability of these methods to emulate the autocorrelation properties of the complex Gaussian processes $\boldsymbol{\mu}_{km}(t)$.

5.5.3 Emulation of the SCCF

To evaluate the accuracy of the GMEA and the RSAM for approximating the SCCF $\rho_{\boldsymbol{\mu}_{km}\boldsymbol{\mu}_{ql}}(\Delta_T, \Delta_R)$ of the reference model, we define the following absolute error function

$$\epsilon_{\rho_{\boldsymbol{\mu}_{11}\boldsymbol{\mu}_{22}}}(\Delta_T, \Delta_R) \;\triangleq\; |\rho_{\boldsymbol{\mu}_{11}\boldsymbol{\mu}_{22}}(\Delta_T, \Delta_R) - \rho_{\hat{\boldsymbol{\mu}}_{11}\hat{\boldsymbol{\mu}}_{22}}(\Delta_T, \Delta_R)|. \tag{5.35}$$

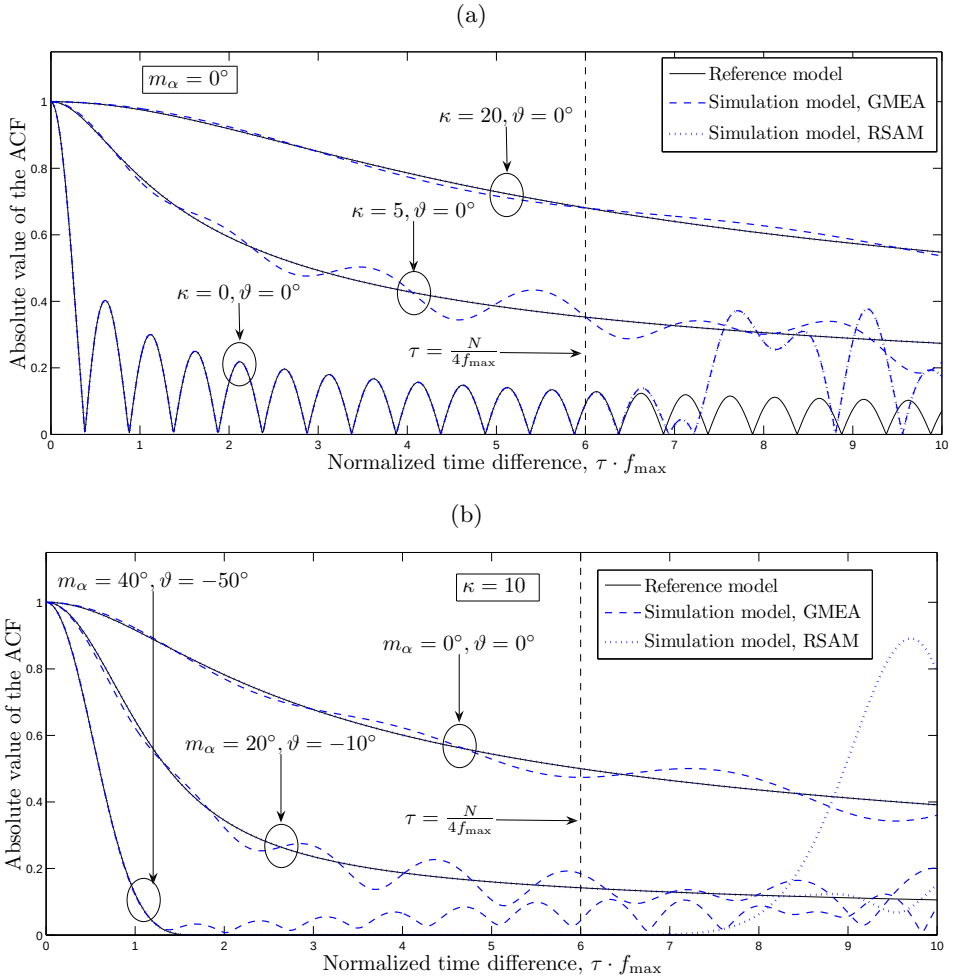

Figure 5.2: Comparison between the ACF $r_{\boldsymbol{\mu}_{km}\boldsymbol{\mu}_{km}}(\tau)$ of the MIMO channel gains (reference model) and the ACF $r_{\hat{\boldsymbol{\mu}}_{km}\hat{\boldsymbol{\mu}}_{km}}(\tau)$ of the simulation model by applying the GMEA and the RSAM with $N = 24$ to the von Mises PDF of the AOA with different triplets of parameters κ, m_α, and ϑ, ($f_{\max} = 91$ Hz and $\sigma^2_{\boldsymbol{\mu}} = 1$).

The absolute value of $\rho_{\boldsymbol{\mu}_{11}\boldsymbol{\mu}_{22}}(\Delta_T, \Delta_R)$ is depicted in Fig. 5.3 for $\Delta_T \in [0, 20/\lambda]$ and $\Delta_R \in [0, 3/\lambda]$. The resulting error function $\epsilon_{\rho_{\boldsymbol{\mu}_{11}\boldsymbol{\mu}_{22}}}(\Delta_T, \Delta_R)$ is plotted in Figs. 5.4 and 5.5 for the GMEA and RSAM, respectively.

The results presented in Figs. 5.4 and 5.5 demonstrate that the GMEA and the RSAM provide a close approximation to the SCCF $\rho_{\boldsymbol{\mu}_{11}\boldsymbol{\mu}_{22}}(\Delta_T, \Delta_R)$. This is clear, since the error produced by the GMEA under non-isotropic scattering conditions is smaller than 8×10^{-2}, while the one produced by the RSAM is lower than 6×10^{-4}. In turn, the error registered by both methods in the isotropic scattering scenario is smaller than 1×10^{-11}.

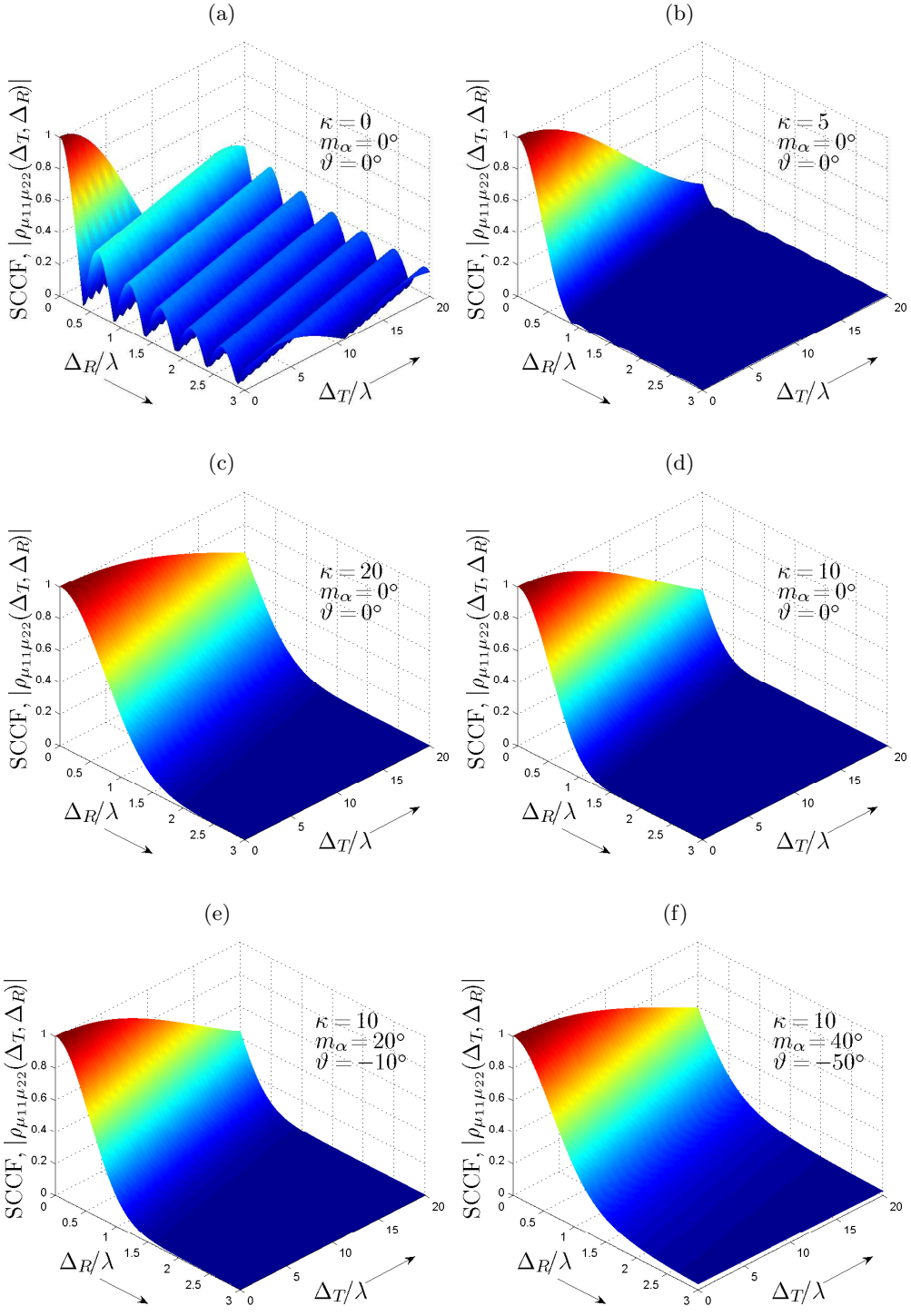

Figure 5.3: Absolute value of the SCCF $\rho_{\boldsymbol{\mu}_{11}\boldsymbol{\mu}_{22}}(\Delta_T, \Delta_R)$ of the MIMO channel model by considering the von Mises PDF of the AOA with different triplets of parameters κ, m_α, and ϑ ($\sigma^2_{\boldsymbol{\mu}} = 1$).

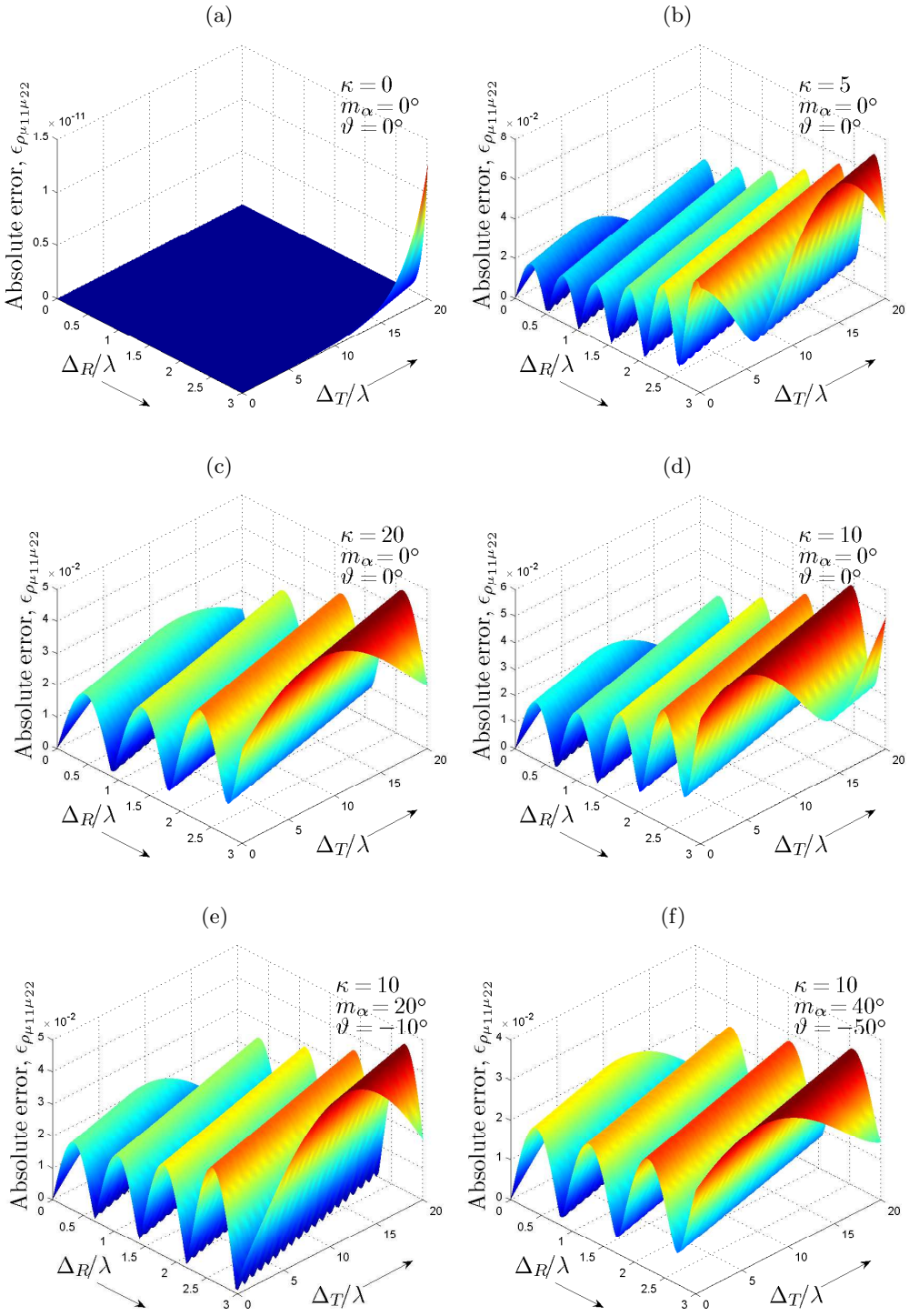

Figure 5.4: Error function $\epsilon_{r_{\boldsymbol{\mu}_{11}\boldsymbol{\mu}_{22}}}(\Delta_T, \Delta_R)$ between the SCCF $\rho_{\boldsymbol{\mu}_{11}\boldsymbol{\mu}_{22}}(\tau)$ of the MIMO channel gains (reference model) and the SCCF $\rho_{\hat{\boldsymbol{\mu}}_{11}\hat{\boldsymbol{\mu}}_{22}}(\Delta_T, \Delta_R)$ of the simulation model by applying the GMEA with $N = 24$ to the von Mises PDF of the AOA.

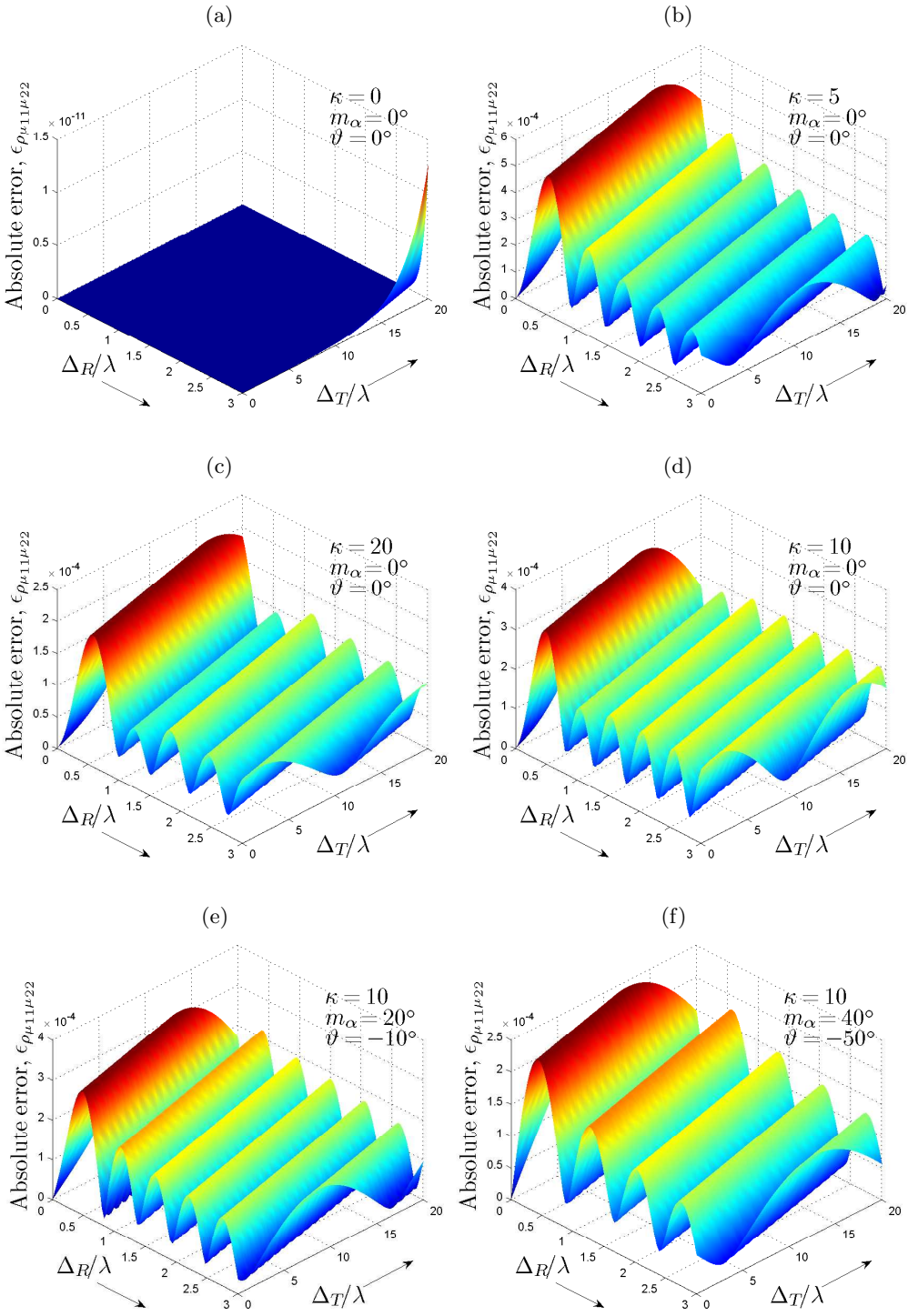

Figure 5.5: Error function $\epsilon_{r_{\boldsymbol{\mu}_{11}\boldsymbol{\mu}_{22}}}(\Delta_T, \Delta_R)$ between the SCCF $\rho_{\boldsymbol{\mu}_{11}\boldsymbol{\mu}_{22}}(\tau)$ of the MIMO channel gains (reference model) and the SCCF $\rho_{\hat{\boldsymbol{\mu}}_{11}\hat{\boldsymbol{\mu}}_{22}}(\Delta_T, \Delta_R)$ of the simulation model by applying the RSAM with $N = 24$ to the von Mises PDF of the AOA.

5.6 Simulation of Wideband MIMO Fading Channels

So far, we have focused our attention on the simulation of narrowband mobile MIMO fading channels. However, the design of simulation models for wideband MIMO channels is also an important research topic. It is relevant, for example, for the analysis of multi-element antenna systems that require a large bandwidth to operate, e.g., those based on spread-spectrum [Moli05, Ch. 18] and ultra-wideband [Roys04] technology. In this section, we will discuss an application of the GMEA and the RSAM to the design of simulation models for wideband MIMO fading channels in single-bounce scattering environments.

5.6.1 Modeling and Statistical Characterization of Wideband Mobile MIMO Fading Channels

From a system-theoretic point of view, the mobile fading channel can be described as a randomly time-variant linear filter (TVLF) [Bell63, Pars00, Pae02a, Proa01]. In this line of thought, we model the wideband subchannel connecting the mth transmitter antenna T_m with the kth receiver antenna R_k as a randomly TVLF with an equivalent complex baseband impulse response

$$\boldsymbol{h}_{km}(t,\eta) \;=\; \sum_{\ell=0}^{\mathcal{L}-1} \boldsymbol{\mu}_{km,\ell}(t)\,\delta(\eta-\eta_\ell). \tag{5.36}$$

In the equation above, $\boldsymbol{\mu}_{km,\ell}(t)$ denotes the complex attenuation factor due to the superposition of the transmitted signal's replicas that reached the kth receiver antenna through different paths but with the same propagation delay $\eta=\eta_\ell$. In line with the narrowband MIMO channel model described in Section 5.2.2, we will assume that the attenuation factors $\boldsymbol{\mu}_{km,\ell}(t)$ are stationary zero-mean complex Gaussian processes with corresponding variances equal to $\sigma^2_{\boldsymbol{\mu}_\ell}$, $\ell=0,\ldots,\mathcal{L}-1$. In addition, we will assume that the channel exhibits uncorrelated scattering (US) [Bell63], meaning that $E\{\boldsymbol{h}^*_{km}(t,\eta_1)\,\boldsymbol{h}_{km}(t+\tau,\eta_2)\}\neq 0$ iff $\eta_1=\eta_2$. This implies that the Gaussian processes $\boldsymbol{\mu}_{km,\ell}(t)$ are mutually uncorrelated. Considering a two-dimensional single-bounce scattering scenario, we can write

$$\boldsymbol{\mu}_{km,\ell}(t) \;=\; \lim_{N\to\infty}\sum_{n=1}^{N} a_m(\boldsymbol{\alpha}_{R,n,\ell})\,b_k(\boldsymbol{\alpha}_{R,n,\ell})\,\boldsymbol{c}_{n,\ell}\exp\{j\,(2\pi\boldsymbol{f}_{n,\ell}\,t+\boldsymbol{\theta}_{n,\ell})\} \tag{5.37}$$

for $\ell=0,\ldots,\mathcal{L}-1$. The parameters of $\boldsymbol{\mu}_{km,\ell}(t)$ can be defined in a similar manner as we defined their counterparts introduced in Section 5.2.2. Particularly, we will suppose that the gains $\boldsymbol{c}_{n,\ell}$ are given such that $\sum_{n=1}^{N}\boldsymbol{c}^2_{n,\ell}=\sigma^2_{\boldsymbol{\mu}_\ell}$, $\ell=0,\ldots,\mathcal{L}-1$, and the AOAs $\boldsymbol{\alpha}_{R,n,\ell}$ are i.i.d. random variables, $n=1,\ldots,N$ and $\ell=1,\ldots,\mathcal{L}$. It should be noticed that if the received signal is composed of a continuum of

multipath components, then the summation in (5.36) becomes an integration. This results in a diffuse impulse response given as [Proa01, p. 802]

$$\boldsymbol{h}_{km}(t,\eta) \;=\; \boldsymbol{\mu}_{km}(t,\eta). \tag{5.38}$$

The attenuation factor $\boldsymbol{\mu}_{km}(t,\eta)$ in (5.38) is a stationary zero-mean complex Gaussian processes with variance $\sigma^2_{\boldsymbol{\mu}_{km}}$. In this case, the US assumption implies that $E\{\boldsymbol{\mu}^*_{km}(t,\eta_1)\,\boldsymbol{\mu}_{km}(t+\tau,\eta_2)\} \neq 0$ iff $\eta_1 = \eta_2$. The subchannel between T_m and R_k can alternatively be described by means of the transfer function

$$\boldsymbol{H}_{km}(t,\upsilon) \;\triangleq\; \int_{-\infty}^{\infty} \boldsymbol{h}_{km}(t,\eta)\exp\{-2\pi\eta\,\upsilon\}d\eta. \tag{5.39}$$

For narrowband systems, $\boldsymbol{H}_{km}(t,\upsilon)$ can be seen as a function that fluctuates in the time domain and remains constant in the frequency domain, at least along the frequency range of the system bandwidth. For wideband systems, $\boldsymbol{H}_{km}(t,\upsilon)$ is to be treated as a function that fluctuates within the system bandwidth.

An exact statistical characterization of the random impulse response in (5.36) is a formidable task that requires knowledge of the multidimensional joint PDFs of $\boldsymbol{h}_{km}(t,\eta)$ (or $\boldsymbol{H}_{km}(t,\upsilon)$). However, since the attenuation factors $\boldsymbol{\mu}_{km,\ell}(t)$ are assumed to be complex Gaussian processes, the statistical properties of the MIMO channel model are completely specified by the ACFs, PSDs, CCFs, and cross-PSDs of the random processes $\boldsymbol{h}_{km}(t,\eta)$. The characterization of MIMO channels in terms of correlation functions and PSDs is surveyed somewhere else, e.g., [Fleu00] and [Moli05, Secs. 6.7 and 7.4]. For the purposes of this section, it is sufficient to know that the selectivity of the channel in space, time, and frequency domains can be studied with respect to the following correlation functions:

$$r_{\boldsymbol{h}_{km}\boldsymbol{h}_{ql}}(\Delta_T,\Delta_R) \;\triangleq\; E\left\{\boldsymbol{h}^*_{km}(t,\eta)\,\boldsymbol{h}_{ql}(t,\eta)\right\} \tag{5.40}$$

$$r_{\boldsymbol{h}_{km}\boldsymbol{h}_{km}}(\tau) \;\triangleq\; E\left\{\boldsymbol{h}^*_{km}(t,\eta)\,\boldsymbol{h}_{ql}(t+\tau,\eta)\right\} \tag{5.41}$$

$$r_{\boldsymbol{H}_{km}\boldsymbol{H}_{km}}(\varrho) \;\triangleq\; E\left\{\boldsymbol{H}^*_{km}(t,\upsilon)\,\boldsymbol{H}_{km}(t,\upsilon+\varrho)\right\}. \tag{5.42}$$

The functions defined in (5.40)–(5.42) are known as the temporal ACF (TACF), the SCCF, and the frequency correlation function (FCF), respectively.

5.6.2 Simulation Approach

The simulation of $\boldsymbol{h}_{km}(t,\eta)$ can be carried out upon a time-variant tapped-delay line (TDL) model of the form

$$\hat{\boldsymbol{h}}_{km}(t,\eta) \;=\; \sum_{\ell=0}^{\mathcal{L}-1} \hat{\boldsymbol{\mu}}_{km,\ell}(t)\,\delta(\eta-\eta_\ell). \tag{5.43}$$

For the simulation of wideband MIMO channels in single-bounce scattering environments, we define the complex gains $\hat{\boldsymbol{\mu}}_{km,\ell}(t)$ as follows

$$\hat{\boldsymbol{\mu}}_{km,\ell}(t) \;=\; \sum_{n=1}^{N} a_m(\hat{\alpha}_{n,\ell})\, b_k(\hat{\alpha}_{n,\ell})\, \hat{c}_{n,\ell}\, \exp\left\{j\big(2\pi \hat{f}_{n,\ell}\, t + \hat{\boldsymbol{\theta}}_{n,\ell}\big)\right\}. \quad (5.44)$$

The parameters of $\hat{\boldsymbol{\mu}}_{km,\ell}(t)$ are analogous to those of the narrowband SOC simulation model presented in Section 5.3.1, and they can be defined accordingly. In particular, we suppose that the phases $\hat{\boldsymbol{\theta}}_{n,\ell}$ are i.i.d. random variables uniformly distributed in $[-\pi, \pi)$, for $n = 1, \ldots, N$ and $\ell = 0, \ldots, \mathcal{L} - 1$. This consideration guarantees the wide-sense stationarity and the mutual uncorrelation of the processes $\hat{\boldsymbol{h}}_{km}(t, \eta)$.

The problem at hand lies in computing the gains $\hat{c}_{n,\ell}$ and the AOAs $\alpha_{n,\ell}$ of $\hat{\boldsymbol{\mu}}_{km,\ell}(t)$ such that:

$$r_{\hat{\boldsymbol{h}}_{km}\hat{\boldsymbol{h}}_{ql}}(\Delta_T, \Delta_R) \;\approx\; r_{\boldsymbol{h}_{km}\boldsymbol{h}_{ql}}(\Delta_T, \Delta_R) \quad (5.45)$$

$$r_{\hat{\boldsymbol{h}}_{km}\hat{\boldsymbol{h}}_{km}}(\tau) \;\approx\; r_{\boldsymbol{h}_{km}\boldsymbol{h}_{km}}(\tau) \quad (5.46)$$

$$r_{\hat{\boldsymbol{H}}_{km}\hat{\boldsymbol{H}}_{km}}(\varrho) \;\approx\; r_{\boldsymbol{H}_{km}\boldsymbol{H}_{km}}(\varrho) \quad (5.47)$$

where $r_{\hat{\boldsymbol{h}}_{km}\hat{\boldsymbol{h}}_{ql}}(\Delta_T, \Delta_R)$, $r_{\hat{\boldsymbol{h}}_{km}\hat{\boldsymbol{h}}_{km}}(\tau)$, and $r_{\hat{\boldsymbol{H}}_{km}\hat{\boldsymbol{H}}_{km}}(\varrho)$ designate, in that order, the TACF, the SCCF, and the FCF of $\hat{\boldsymbol{h}}_{km}(t, \eta)$. These functions are given as

$$r_{\hat{\boldsymbol{h}}_{km}\hat{\boldsymbol{h}}_{ql}}(\Delta_T, \Delta_R) \;\triangleq\; E\left\{\hat{\boldsymbol{h}}^{*}_{km}(t, \eta)\, \hat{\boldsymbol{h}}_{ql}(t, \eta)\right\} \quad (5.48)$$

$$r_{\hat{\boldsymbol{h}}_{km}\hat{\boldsymbol{h}}_{km}}(\tau) \;\triangleq\; E\left\{\hat{\boldsymbol{h}}^{*}_{km}(t, \eta)\, \hat{\boldsymbol{h}}_{ql}(t + \tau, \eta)\right\} \quad (5.49)$$

$$r_{\hat{\boldsymbol{H}}_{km}\hat{\boldsymbol{H}}_{km}}(\varrho) \;\triangleq\; E\left\{\hat{\boldsymbol{H}}^{*}_{km}(t, \upsilon)\, \hat{\boldsymbol{H}}_{km}(t, \upsilon + \varrho)\right\}. \quad (5.50)$$

A solution to this problem has recently been provided in [Paet06]. In that paper, the authors approximate the TACF and the SCCF of a wideband MIMO channel model derived from the geometrical one-ring scattering model by applying the EMEDS and the LPNM. Regarding the emulation of the FCF $r_{\boldsymbol{H}_{km}\boldsymbol{H}_{km}}(\varrho)$ of the MIMO channel, it was demonstrated in that paper that the TDL model in (5.43) exactly reproduces such an statistical function if the impulse response $\boldsymbol{h}_{km}(t, \eta)$ is a discrete function in the delay domain and the gains $\hat{c}_{n,\ell}$ satisfy $\sum_{n=1}^{N} \hat{c}^2_{n,\ell} = \sigma^2_{\boldsymbol{\mu}_\ell}$.

We will refrain ourselves from providing details about the simulation approach presented in [Paet06], since it was developed independently by other researchers. However, we observe that the idea can be implemented in a more efficient manner by employing either the GMEA or the RSAM. In fact, a third party demonstrated in [Mayy08] that the simulation of wideband MIMO channels can effectively be performed by applying the idea described in [Paet06] in connection with the GMEA. We notice that the authors of [Mayy08] made use of an alternative version

of the GMEA that we proposed in [Gut07b].

The simulation approach described in [Paet06] is based on the assumption that the impulse responses of the MIMO subchannels are discrete functions in the delay-domain, meaning that the processes $\boldsymbol{h}_{km}(t,\eta)$ are given as in (5.36). Under this consideration, it is evident that the TDL model defined in (5.43) is a natural structure for the simulation/representation of $\boldsymbol{h}_{km}(t,\eta)$. However, the characterization of $\boldsymbol{h}_{km}(t,\eta)$ by means of a TDL model is not straightforward when the impulse responses of the MIMO subchannels are given as in (5.38), i.e., when $\boldsymbol{h}_{km}(t,\eta)$ is a continuous (diffuse) function in η. In the following chapter, we will revisit a well-known procedure for the design of TDL for WSS complex Gaussian channels characterized by diffuse impulse responses that satisfy the US condition. The concepts studied in that chapter can be applied together with the idea proposed in [Paet06] to design simulation models for wideband mobile MIMO fading channels with continuous-delay impulse responses.

5.7 Chapter Summary and Conclusions

In this chapter, we demonstrated that the GMEA and the RSAM introduced in Chapter 4 can be applied to the simulation of narrowband mobile MIMO fading channels with specified correlation properties. We explained here that a proper emulation of the SCCF of the MIMO channel requires information about both the even and the odd parts of the PDF of the AOA. For this reason, some minor modifications were made in Section 5.4 to the GMEA and the RSAM in order to incorporate information about the odd part of the AOA distribution.

We evaluated the performance of the proposed parameter computation methods with respect to the approximation of the ACF and SCCF of the MIMO subchannels. The obtained results indicate that the modifications made to the GMEA and the RSAM do not affect the methods' capability for emulating the ACF of the MIMO subchannels. Concerning the emulation of the SCCF, the obtained results show that both methods provide a very good approximation to such a correlation function. Particularly, our investigations indicate that the RSAM is better suited than the GMEA to emulate the correlation properties of the MIMO channel. Finally, we discussed in Section 5.6 an application of the methods proposed in this dissertation to the design of simulation models for wideband mobile MIMO fading channels.

Chapter 6

Design of TDL Models for WSSUS Channels with Diffuse Impulse Responses

6.1 Introduction

The wide-sense stationary uncorrelated scattering (WSSUS) model proposed by Bello [Bell63] is a widely accepted model for small-scale mobile fading channels [Stei87, Skla88, Jeru00, Proa01, Pae02a, Pae02b]. A variety of standardized channel models for wireless and mobile communication systems has been developed on the basis of this stochastic model [Cos207, EtsGSM, Etsi99, Med98a, Med98b, Erce04]. In order to obtain realizable and well specified representations of WSSUS channels, one often has to resort in practice to the use of simulation models. Different types of models can be used for the simulation of WSSUS channels, e.g., those presented in [Yip95], [Chri02]. However, a fundamental requirement for any of such simulators is the proper emulation of the essential characteristics of the WSSUS model. This is necessary to allow for a reliable and reproducible system performance investigation.

Several simulation models basing on the time-variant TDL filter concept have been proposed for the simulation of WSSUS channels with continuous-delay impulse responses, such as those in [Pae02b] and [Yip95]. Among them, the simplest and perhaps most popular one is a so-called symbol-spaced TDL (SSTDL) model. Briefly speaking, a SSTDL model can be considered as a sampled version of the time-variant channel impulse response (CIR) obtained by using a sampling rate equal to the reciprocal of the symbol duration. Such a kind of TDL models was originally introduced by Kailath [Kail59] and Bello [Bell63] as canonical channel models—which are essentially simulation models—for band-limited time-variant linear systems. SSTDL models are nowadays widely in use

for the performance analysis of modern wireless communication systems, e.g., [Choi01, Yang02, Hou04].

It might seem that the applicability of SSTDL models is unquestionable, since they were developed in the framework of the sampling theorem [Bell63]. Nevertheless, the results reported in [Guti05] suggest that the validity of such TDL models is rather doubtful when the concept is applied to WSSUS channels. In fact, the answer to the question whether SSTDL models are suitable for modeling WSSUS channels is still lacking in the literature. What is more, despite the fact that this modeling approach dates back more than forty years [Bell63], [Kail59], the statistical properties of the resulting SSTDL are not well known. Most of the literature on this topic concentrates only on describing the structure of the SSTDL model [Stei87], [Proa01], and even though a statistical analysis can be found in [Bell63], [Jeru00] and [Syko00], no information concerning the channel FCF is provided there. The information about the FCF is very important because this function influences the performance of many wideband and frequency diversity wireless communication systems, such as multicarrier code division multiple access (MC-CDMA) systems [Choi01, Yang02, Hou04, Hara97, Schu05].

Closing the above mentioned gaps is necessary not only for a better understanding of channel modeling aspects, but also for carrying out a reliable system performance investigation. In this chapter, we aim at closing them by analyzing the validity and statistical behavior of SSTDL models for WSSUS channels. It is also our objective to discuss the problems associated with these TDL models, as well as to present a simple and effective strategy to avoid them.

The rest of the chapter is organized as follows. Section 6.2 is devoted to analyzing the suitability of SSTDL models to simulate WSSUS channels. It is shown in that section that using SSTDL models to model the CIR of WSSUS channels results in a violation of the US condition from the perspective of band-limited systems. In Section 6.3, we provide a concise description of the statistical behavior of these type of simulation models. We show in that section that SSTDL models suffer from strong limitations in emulating the FCF of WSSUS channels. In Section 6.4, we show that SSTDL models lead to an imprecise performance analysis of wireless communication systems sensitive to the FCF. To cope with this problem, we discuss a solution in Section 6.5 by doubling the sampling rate of the channel, resulting in a half-symbol-spaced TDL (HSSTDL) model. The usefulness of this solution is exemplary demonstrated by analyzing the bit error probability of a down-link MC-CDMA system. Finally, we present our conclusions in Section 6.6.

6.2 About the Validity of SSTDL Models

6.2.1 The SSTDL Modeling Approach

Before we proceed to analyze the suitability of SSTDL models for modeling WSSUS channels, it is convenient to review the approach followed in [Bell63] to develop such a type of simulation models. Toward that end, consider a wireless communication system characterized by the input-output relationship

$$y(t) = x(t) * h(t,\eta) = \int x(t)h(t,\eta)d\eta \tag{6.1}$$

where $*$ denotes convolution, $x(t)$ is the transmitted signal, $y(t)$ is the received signal, and $h(t,\eta)$ is the time-variant CIR, which is continuous in both t and η variables. The CIR $h(t,\eta)$, called the input delay-spread function by Bello, may be regarded as being the system response at time t to a unit impulse applied η seconds in the past.

For practical purposes, it is possible to derive a discrete-delay[1] representation of the CIR $h(t,\eta)$ on the basis of the sampling theorem by assuming that either the transmitted signal or the channel itself is bandwidth restricted. For the latter case, it was shown in [Bell63, pp. 378-379] that if the corresponding channel transfer function $H(t,\upsilon) = \int_{-\infty}^{\infty} h(t,\eta)\exp\{-j2\pi\upsilon\eta\}d\eta$ is confined to a bandwidth $\mathcal{W}$ (meaning that $H(t,\upsilon) = 0$ for $|\upsilon| > \mathcal{W}$), then, according to the sampling theorem, the CIR $h(t,\eta)$ may equivalently be expressed as [Bell63, eq. (123)]

$$h(t,\eta) \equiv \sum_{n=-\infty}^{\infty} h\left(t, \frac{n}{W}\right) \operatorname{sinc}\left(W\left[\eta - \frac{n}{W}\right]\right) \tag{6.2}$$

where $\operatorname{sinc}(\eta) \triangleq \sin(\pi\eta)/(\pi\eta)$ and $W \geq \mathcal{W}$ is an arbitrary sampling rate.

In conformity with the thesis in [Bell63], it turns out that the CIR $h(t,\eta)$ is well modeled by a TDL linear filter having a time-variant impulse response

$$\hat{h}(t,\eta) = \Delta_\eta \cdot \sum_{n=-\infty}^{\infty} h(t,n\Delta_\eta)\delta(\eta - n\Delta_\eta) \tag{6.3}$$

where the tap spacing $\Delta_\eta \triangleq 1/W$ is given such that $\Delta_\eta \leq 1/\mathcal{W}$. The equivalent discrete-delay CIR described by $\hat{h}(t,\eta)$ establishes the so-called SSTDL model when $W = \mathcal{W} = W_s$, where $W_s = 1/T$ is the nominal bandwidth of the transmit-

[1] In this chapter, we will be concerned only with the discrete-delay modeling of the CIR $h(t,\eta)$. The reader is referred to [Pae02a] for a detailed study on the modeling of $h(t,\eta)$ in discrete-time domain

ted symbols[2], and T is usually equal to the symbol duration[3]. Throughout the chapter, we will refer to $\hat{h}(t,\eta)$ either as the SSTDL model or as the T-spaced TDL model to stress the fact that $\Delta_\eta = T$ ($W_s = \mathcal{W} = W$), while we will use the term Δ_η-spaced TDL model for the more general case where $\Delta_\eta \leq T$ ($W_s \leq \mathcal{W} \leq W$).

The equivalence between the CIR $h(t,\eta)$ and its discrete-delay version defined by $\hat{h}(t,\eta)$ in (6.3) holds in the sense that the former impulse response can be reconstructed from the interpolation of the latter one, as indicated by (6.2).

6.2.2 The Validity of SSTDL Models

The SSTDL modeling approach may at first seem to be sound and thorough. Nevertheless, important problems arise when the random nature of the mobile fading channel is brought into consideration. The main source of conflict comes from the fact that the SSTDL model was derived on the basis of the sampling theorem for deterministic signals. If the CIR $h(t,\eta)$ is deemed to be a random process, as it is done usually for wireless communication system, then its discrete-delay representation should be obtained by invoking the sampling theorem for stochastic processes instead [Proa01, p. 71]. Thus, the bandwidth restriction is not to be associated with the (random) channel transfer function $\boldsymbol{H}(t,\upsilon)$, but with the power density spectrum of $\boldsymbol{h}(t,\eta)$. Fortunately, the amendment of such an imprecision results in an equivalent discrete-delay CIR $\hat{\boldsymbol{h}}(t,\eta)$ similar as the one defined in (6.3), and the results and conclusions drawn in [Bell63] remain basically unchanged. In this case, however, the equivalence defined in (6.2) holds only in the zero-mean-square-error sense [Proa01, p. 71]

$$E\left\{\left|\boldsymbol{h}(t,\eta) - \sum_{n=-\infty}^{\infty} \boldsymbol{h}\left(t,\frac{n}{W}\right)\operatorname{sinc}\left(W\left[\eta - \frac{n}{W}\right]\right)\right|^2\right\} = 0. \tag{6.4}$$

We point out that the sampling theorem for stochastic processes applies only on stationary processes.

A further problem arises if the random CIR $\boldsymbol{h}(t,\eta)$ meets per definition the WSSUS condition. If $\boldsymbol{h}(t,\eta)$ is a WSSUS random process, then the simulation approach described in Section 6.2.1 is not applicable, because the US condition is incompatible with the bandwidth constraint required to obtain $\hat{\boldsymbol{h}}(t,\eta)$ [Schu05].

[2]The nominal bandwidth may be defined as the width of the main lobe of the power spectral density of a digitally modulated signal.

[3]For instance, T equals the duration of the quadrature-amplitude-modulation (QAM) symbols in a conventional single carrier system, whereas T equals the chip duration in direct-sequence spread spectrum (DS-SS) systems [Schu05]. Multicarrier systems [Schu05], [VanN04] are a special case, where T is equal to the (non-cyclic-extended) symbol duration divided by the total number of subcarriers. In all cases, $W_s = 1/T$ holds. We note that the term "symbol" is used in this chapter for those digital signals that carry the information through the channel.

Such an incompatibility often passes unnoticed in the literature. Take as an example the conclusions drawn in [Proa01] at the end of Section 14.5.1. There, it is stated that the uncorrelation of the tap gains of $\hat{\boldsymbol{h}}(t,\eta)$ is a consequence of the US condition of $\boldsymbol{h}(t,\eta)$. This statement is not adequate in the way it was postulated in [Proa01], because it is based on the implicit assumption that the CIR $\boldsymbol{h}(t,\eta)$ satisfies both the WSSUS condition and the bandwitdh constraint. Notice that the equation (14.5–4) given in [Proa01, Sec. 14.5.1] holds only if the channel transfer function is band-limited.

Bello proposed a second TDL model which circumvents the incompatibility between the bandwidth limitation of $\boldsymbol{H}(t,\upsilon)$ and the US condition of $\boldsymbol{h}(t,\eta)$ [Bell63, pp. 379, second column]. In deriving that model, Bello shifted the bandwidth constraint onto the input signal $x(t)$. Thereby, since the bandwidth restriction is external to the CIR $\boldsymbol{h}(t,\eta)$, one can assume without problems that $\boldsymbol{h}(t,\eta)$ is a WSSUS process. In that case, it can be shown that the equivalent discrete-delay CIR is given by [Syko00]

$$\tilde{\boldsymbol{h}}(t,\eta) = \sum_{n=-\infty}^{\infty} \left[\int \boldsymbol{h}(t,\xi)\mathrm{sinc}(W[\xi - n\Delta_\eta])d\xi \right] \delta(\eta - n\Delta_\eta). \tag{6.5}$$

The impulse response $\tilde{\boldsymbol{h}}(t,\eta)$ is not equivalent to $\boldsymbol{h}(t,\eta)$ in the sense of (6.2), but in what

$$\boldsymbol{y}(t) \equiv \sum_{n=-\infty}^{\infty} x(t - n\Delta_\eta) \int \boldsymbol{h}(t,\xi)\mathrm{sinc}([\xi - n\Delta_\eta])d\xi. \tag{6.6}$$

The previous equation implies that the output of the system remains the same if the CIR $\boldsymbol{h}(t,\eta)$ is replaced by its discrete-delay version $\tilde{\boldsymbol{h}}(t,\eta)$; as $\boldsymbol{y}(t) = \tilde{\boldsymbol{y}}(t)$, where $\tilde{\boldsymbol{y}}(t) = x(t) * \tilde{\boldsymbol{h}}(t,\eta)$. Similar observations can be made for the SSTDL model, or more generally, for the Δ_η-spaced TDL model, since $\boldsymbol{y}(t) \equiv \hat{\boldsymbol{y}}(t) * \mathrm{sinc}\,(Wt)$, where $\hat{\boldsymbol{y}} = x(t) * \hat{\boldsymbol{h}}(t,\eta)$.

Even though the TDL model described in (6.5) is compatible with WSSUS channels, it is strictly speaking not a valid simulation model for them, since the tap gains of the equivalent discrete-delay CIR $\tilde{\boldsymbol{h}}(t,\eta)$ are mutually correlated. The cross-correlation among the taps can be neglected, nonetheless, if the autocorrelation function of $\boldsymbol{h}(t,\eta)$ varies slowly in the delay domain, as pointed out in [Bell63] and [Syko00]. However, since the US condition of the CIR $\boldsymbol{h}(t,\eta)$ is in general not reflected by $\tilde{\boldsymbol{h}}(t,\eta)$, it can be conclude that this simulation model is not adequate for WSSUS channels. In fact, the random process $\tilde{\boldsymbol{h}}(t,\eta)$ belongs to the class of non-WSSUS processes [Matz05].

6.3 Statistical Behavior of SSTDL Models

Despite the SSTDL model proves to be incompatible with WSSUS channels from the perspective of band-limited systems, simulation models of this kind are widely being in use in connection with the WSSUS model to evaluate the performance of wireless communication systems, e.g., [Choi01, Yang05, Hou04]. In defense of such a system performance investigation approach, we can argue that the SSTDL model might coexist with WSSUS channels if the bandwidth constraint imposed on the CIR $\boldsymbol{h}(t,\eta)$ is neglected[4]. To find out if this is the case, it is necessary to know whether $\hat{\boldsymbol{h}}(t,\eta)$ satisfactorily emulates the statistical properties of WSSUS channels. It should also be determined whether the resulting SSTDL model lends itself to system performance investigations. To accomplish the above-mentioned tasks, we need a complete description of the statistical behavior of the (nonequivalent) discrete-delay CIR $\hat{\boldsymbol{h}}(t,\eta)$. In this section, we provide such a description by assuming that $\boldsymbol{h}(t,\eta)$ is a zero-mean WSSUS complex Gaussian process. We will also assume that the CIR $\boldsymbol{h}(t,\eta)$ is causal and has finite duration. Consequently, we can write

$$\hat{\boldsymbol{h}}(t,\eta) = \Delta_\eta \cdot \sum_{n=0}^{N} \boldsymbol{h}(t, n\Delta_\eta)\delta(\eta - n\Delta_\eta) \tag{6.7}$$

where the number of taps $N \triangleq \lfloor W \cdot \eta_{\max} \rfloor + 1$ is defined with respect to the sampling rate W and the channel's maximum excess delay $\eta_{\max}$ [Skla88]. The operator $\lfloor \cdot \rfloor$ denotes the nearest integer toward minus infinity.

6.3.1 Statistical Description of the Reference Channel Model

Before we proceed, we will summarize the statistical properties of the WSSUS complex Gaussian CIR $\boldsymbol{h}(t,\eta)$ that are relevant for the purposes of this chapter. For a detailed discussion on the statistical properties of WSSUS channels, we refer the reader to [Bell63, Proa01, Pae02a, Schu05].

In line with the WSSUS Gaussian model, $\boldsymbol{h}(t,\eta)$ is characterized by its ACF

$$\begin{aligned} r_{\boldsymbol{hh}}(t_1,t_2;\eta_1,\eta_2) &\triangleq E\left\{\boldsymbol{h}(t_1,\eta_1)\boldsymbol{h}^*(t_2,\eta_2)\right\} \\ &= r_{\boldsymbol{hh}}(\tau;\eta_1)\,\delta(\eta_1-\eta_2) \end{aligned} \tag{6.8}$$

where $r_{\boldsymbol{hh}}(\tau;\eta) \triangleq E\{\boldsymbol{h}(t,\eta)\boldsymbol{h}^*(t+\tau,\eta)\}$ and $\tau = t_1 - t_2$. Similarly, $\boldsymbol{h}(t,\eta)$ can be

[4]Note, however, that the equivalences described in Section 6.2 for each of the pairs $\boldsymbol{H}(t,\eta)$, $\boldsymbol{h}(t,\eta)$ and $\hat{y}(t)$, $y(t)$ will no longer be valid. In any case, the corresponding relationships between those functions should be established as mere approximations in terms of their statistical properties.

characterized by means of its time-frequency ACF (TF-ACF)

$$\begin{aligned} R_{\boldsymbol{HH}}(t_1,t_2;\upsilon_1,\upsilon_2) &\triangleq E\left\{\boldsymbol{H}(t_1,\upsilon_1)\boldsymbol{H}^*(t_2,\upsilon_2)\right\} \\ &= \int\int r_{\boldsymbol{hh}}(t_1,t_2;\eta_1,\eta_2) \\ &\quad \times \exp\{j2\pi(\upsilon_1\eta_1-\upsilon_2\eta_2)\}\,d\eta_1\,d\eta_2 \qquad (6.9) \\ &= R_{\boldsymbol{HH}}(\tau;\varrho) \qquad (6.10) \end{aligned}$$

where $R_{\boldsymbol{HH}}(\tau;\varrho) \triangleq E\{\boldsymbol{H}(t,\eta)\,\boldsymbol{H}^*(t+\tau,\eta+\varrho)\}$ and $\varrho=\upsilon_1-\upsilon_2$. Equation (6.10) results from the substitution of $r_{\boldsymbol{hh}}(t_1,t_2;\eta_1,\eta_2)$ from (6.8) into (6.9), and states that the channel is WSS in both the time and the frequency variables[5].

The multipath behavior of $\boldsymbol{h}(t,\eta)$ is characterized in the frequency domain by the FCF $R_{\boldsymbol{HH}}(\varrho) \triangleq R_{\boldsymbol{HH}}(0;\varrho)$ and in the delay domain by the power delay profile (PDP)

$$\begin{aligned} S_\eta(\eta) &\triangleq E\{|\boldsymbol{h}(t,\eta)|^2\} \\ &= \int_{-\infty}^{\infty} R_{\boldsymbol{HH}}(\varrho)\exp\{j2\pi\eta\varrho\}\,d\varrho. \qquad (6.11) \end{aligned}$$

We will focus our attention on these two statistical quantities (especially on the FCF), since a TDL channel model is mostly intended to emulate them.

6.3.2 Statistical Description of Δ_η-Spaced TDL Models

Since $\hat{\boldsymbol{h}}(t,\eta)$ is a sampled version of a Gaussian process, it is in turn a Gaussian process, which is therefore completely characterized by its ACF

$$\begin{aligned} r_{\hat{\boldsymbol{h}}\hat{\boldsymbol{h}}}(t_1,t_2;\eta_1,\eta_2) &= E\{\hat{\boldsymbol{h}}(t_1,\eta_1)\hat{\boldsymbol{h}}^*(t_2,\eta_2)\} \\ &= \frac{1}{W^2} r_{\boldsymbol{hh}}(\tau;\eta_1)\,\delta(\eta_1-\eta_2)\sum_{n=-\infty}^{\infty}\delta(\eta_1-nT) \qquad (6.12) \end{aligned}$$

where $W \triangleq 1/\Delta_\eta$. We recall that $W=W_s$ for the T-spaced TDL model. Equation (6.12) shows that $\hat{\boldsymbol{h}}(t,\eta)$ is a WSSUS process, which was to be expected since the tap gains of $\hat{\boldsymbol{h}}(t,\eta)$ are samples of a WSS random process that fulfills the US condition. We can therefore conclude that $\hat{\boldsymbol{h}}(t,\eta)$ is an adequate simulation model for WSSUS channels. This is in line with the conclusion drawn in [Proa01]. In order to determine how accurate is this simulation model in emulating the statistical behavior of the reference model described by the CIR $\boldsymbol{h}(t,\eta)$, it is convenient to turn our attention to the FCF of $\hat{\boldsymbol{h}}(t,\eta)$.

We can express the TF-ACF $R_{\hat{\boldsymbol{H}}\hat{\boldsymbol{H}}}(t_1,t_2;\upsilon_1,\upsilon_2) \triangleq E\{\hat{\boldsymbol{H}}(t_1,\upsilon_1)\,\hat{\boldsymbol{H}}^*(t_2,\upsilon_2)\}$ of

[5] Actually, the channel is SSS in both domains, since the underlying process is a Gaussian process.

$\hat{\boldsymbol{h}}(t,\eta)$, where $\hat{\boldsymbol{H}}(t;\upsilon) = \int_{-\infty}^{\infty} \hat{\boldsymbol{h}}(t,\eta)\exp\{-j2\pi\upsilon\eta\}d\eta$, as the convolution of the channel TF-ACF $R_{\boldsymbol{HH}}(t_1,t_2;\upsilon_1,\upsilon_2) = R_{\boldsymbol{HH}}(\tau;\varrho)$ and the train of delta functions $\sum_{n=-\infty}^{\infty}\delta(\upsilon_1 - nW)/W$. In this way, we obtain

$$R_{\hat{\boldsymbol{H}}\hat{\boldsymbol{H}}}(t_1,t_2;\upsilon_1,\upsilon_2) = \frac{1}{W}\sum_{n=-\infty}^{\infty} R_{\boldsymbol{HH}}(\tau;\varrho - nW) \tag{6.13}$$

$$= R_{\hat{\boldsymbol{H}}\hat{\boldsymbol{H}}}(\tau;\varrho) \tag{6.14}$$

where $R_{\hat{\boldsymbol{H}}\hat{\boldsymbol{H}}}(\tau;\varrho) \triangleq E\{\hat{\boldsymbol{H}}(t,\eta)\,\hat{\boldsymbol{H}}^*(t+\tau,\eta+\varrho)\}$. In turn, we can define the FCF of $\hat{\boldsymbol{h}}(t,\eta)$ as $R_{\hat{\boldsymbol{H}}\hat{\boldsymbol{H}}}(\varrho) \triangleq R_{\hat{\boldsymbol{H}}\hat{\boldsymbol{H}}}(0;\varrho)$. Thereby, we can write

$$R_{\hat{\boldsymbol{H}}\hat{\boldsymbol{H}}}(\varrho) = \frac{1}{W}\sum_{n=-\infty}^{\infty} R_{\boldsymbol{HH}}(0;\varrho - nW). \tag{6.15}$$

An equivalent expression that allows for the analytical evaluation of the FCF $R_{\hat{\boldsymbol{H}}\hat{\boldsymbol{H}}}(\varrho)$ may be written as follows:

$$R_{\hat{\boldsymbol{H}}\hat{\boldsymbol{H}}}(\varrho) = \frac{1}{W^2}\sum_{n=0}^{N} S_\eta(n/W)\exp\{-j2\pi n\varrho/W\}. \tag{6.16}$$

We observe that $\hat{\boldsymbol{H}}(t;\upsilon)$ is WSS in the time domain and wide-sense periodic in the frequency domain with period W. In mathematical terms, this means that $R_{\hat{\boldsymbol{H}}\hat{\boldsymbol{H}}}(t_1,t_2;\upsilon_1,\upsilon_2) = R_{\hat{\boldsymbol{H}}\hat{\boldsymbol{H}}}(\tau;\varrho + kW)$, where k is an integer. Notice that $R_{\hat{\boldsymbol{H}}\hat{\boldsymbol{H}}}(\varrho) = R_{\hat{\boldsymbol{H}}\hat{\boldsymbol{H}}}(\varrho + kW)$. The FCF $R_{\hat{\boldsymbol{H}}\hat{\boldsymbol{H}}}(\Delta\eta)$ is also an Hermitian symmetric function, meaning that $R_{\hat{\boldsymbol{H}}\hat{\boldsymbol{H}}}(\varrho) = R^*_{\hat{\boldsymbol{H}}\hat{\boldsymbol{H}}}(-\varrho)$.

For an exact emulation of the FCF $R_{\boldsymbol{HH}}(\varrho)$ of the reference model, it is required that $R_{\hat{\boldsymbol{H}}\hat{\boldsymbol{H}}}(\varrho) = R_{\boldsymbol{HH}}(\varrho)$. However, this equality can be fulfilled only within the frequency interval $\varrho \in [-W/2, W/2]$, because $R_{\hat{\boldsymbol{H}}\hat{\boldsymbol{H}}}(\varrho) \neq R_{\boldsymbol{HH}}(\varrho)$ for $|\varrho| > W/2$ due to the periodicity of $R_{\hat{\boldsymbol{H}}\hat{\boldsymbol{H}}}(\varrho)$. What is more, the FCF $R_{\hat{\boldsymbol{H}}\hat{\boldsymbol{H}}}(\varrho)$ of the simulation model $\hat{\boldsymbol{h}}(t,\eta)$ is a weighted sum of shifted replicas of $R_{\boldsymbol{HH}}(\varrho)$, as one can observe from (6.15). Hence, to ensure that the relation $R_{\hat{\boldsymbol{H}}\hat{\boldsymbol{H}}}(\varrho) = R_{\boldsymbol{HH}}(\varrho)$ holds for $\varrho \in [-W/2, W/2]$, it is necessary that $R_{\boldsymbol{HH}}(\varrho) = 0$ for $|\varrho| > W/2$, otherwise the replicas of $R_{\boldsymbol{HH}}(\varrho)$ will overlap and $R_{\hat{\boldsymbol{H}}\hat{\boldsymbol{H}}}(\varrho)$ will be affected by aliasing. Unfortunately, the fulfillment of this condition cannot be guaranteed because the FCF of WSSUS channels is not band-limited, and $\hat{\boldsymbol{h}}(t,\eta)$ does not include any external bandwidth restriction for $R_{\boldsymbol{HH}}(\varrho)$—which is actually the main difference between $\hat{\boldsymbol{h}}(t,\eta)$ and the TDL model $\tilde{\boldsymbol{h}}(t,\eta)$ described in Section 6.2. The FCF of $\hat{\boldsymbol{h}}(t,\eta)$ will therefore be affected by a certain degree of aliasing, which will reduce its accuracy for emulating the FCF of $\boldsymbol{h}(t,\eta)$. This is in fact the main drawback of the Δ_η-spaced TDL model. Owing to the aliasing effects, the FCF $R_{\hat{\boldsymbol{H}}\hat{\boldsymbol{H}}}(\varrho)$ of $\hat{\boldsymbol{h}}(t,\eta)$ provides just an approximation to the FCF

$R_{\boldsymbol{HH}}(\varrho)$ of $\boldsymbol{h}(t,\eta)$ valid for $-W/2 \leq \varrho \leq W/2$. Aliasing is a well-known effect, but it is generally not recognized in the literature that this effect influences the statistical properties of the TDL simulation model in (6.3).

On the other hand, a reliable system performance analysis requires an accurate emulation of $R_{\boldsymbol{HH}}(\varrho)$ along the frequency range of the system bandwidth. Hence, satisfying the relation $R_{\hat{\boldsymbol{H}}\hat{\boldsymbol{H}}}(\varrho) \approx R_{\boldsymbol{HH}}(\varrho)$ within the interval $\varrho \in [-W_s, W_s]$ is highly desirable for system evaluation purposes. Unfortunately, this is not possible when we employ a T-spaced TDL model, because the period W of the FCF of this simulation model is equal to W_s, i.e., $W = W_s$, implying that the approximation $R_{\hat{\boldsymbol{H}}\hat{\boldsymbol{H}}}(\varrho) \approx R_{\boldsymbol{HH}}(\varrho)$ cannot be satisfied for $W_s/2 \leq |\varrho| \leq W_s$. As will be shown next, this characteristic of T-spaced TDL models affects the performance evaluation of wireless communication systems sensitive to the FCF.

6.4 Numerical Examples

6.4.1 The Truncated-Exponential-Decay PDP

In what follows, we will provide some examples illustrating the issues discussed in Section 6.3.2. To this end, let us assume that the CIR $\boldsymbol{h}(t,\eta)$ of the reference model has a truncated-exponential-decay PDP (TED-PDP)

$$S_\eta(\eta) = \begin{cases} \frac{1}{c} \cdot \exp\{-\eta/\sigma\}, & 0 \leq \eta \leq \eta_{\max} \\ 0, & \text{else} \end{cases} \tag{6.17}$$

where $\sigma > 0$ is the falling factor of the PDP, and $c = [1 - \exp\{-\eta_{\max}/\sigma\}]/\sigma$. The TED-PDP has been shown to be an adequate model for characterizing the PDP of outdoor and indoor wideband channels [Erce99]. Indeed, this type of PDP has been adopted as a reference by several bodies of standardization for wireless communication systems [Cos207, EtsGSM, Med98b, Med98a, Corr06, Erce04].

In the case of the TED-PDP in (6.17), the FCF $R_{\boldsymbol{HH}}(\varrho)$ of the reference model is given by

$$R_{\boldsymbol{HH}}(\varrho) = \frac{1 - \exp\left\{-\frac{\eta_{\max}}{\sigma}(1 - j2\pi\varrho\sigma)\right\}}{(1 - j2\pi\varrho\sigma) \cdot \left(1 - \exp\left\{-\frac{\eta_{\max}}{\sigma}\right\}\right)}. \tag{6.18}$$

From (6.16) and (6.17), we can express the FCF $R_{\hat{\boldsymbol{H}}\hat{\boldsymbol{H}}}(\varrho)$ of the Δ_η-spaced TDL model $\hat{\boldsymbol{h}}(t,\eta)$ as

$$R_{\hat{\boldsymbol{H}}\hat{\boldsymbol{H}}}(\varrho) = \frac{\left(1 - \exp\left\{-\frac{1}{\sigma W}\right\}\right)\left(1 - \exp\left\{-\frac{N}{\sigma W}(1 + j2\pi\varrho\sigma)\right\}\right)}{\left(1 - \exp\left\{-\frac{N}{\sigma W}\right\}\right)\left(1 - \exp\left\{-\frac{1}{\sigma W}(1 + j2\pi\varrho\sigma)\right\}\right)}. \tag{6.19}$$

We normalized (6.16) to obtain the above expression, so that $R_{\hat{\boldsymbol{H}}\hat{\boldsymbol{H}}}(0) = 1$.

6.4.2 Effects of Aliasing on the FCF

In Fig. 6.1, we present a comparison between the absolute values of $R_{\boldsymbol{HH}}(\varrho)$ and $R_{\hat{\boldsymbol{H}}\hat{\boldsymbol{H}}}(\varrho)$ by considering $\eta_{\max} = 800$ ns, $W = W_s = 20$ MHz, and $\sigma \in \{30 \text{ ns}, 60 \text{ ns}, 105 \text{ ns}\}$. These parameters are representative of the propagation conditions encountered inside office buildings ($\sigma = 30$ ns), at large open space environments ($\sigma = 60$ ns), and at outdoor environments under non-line of sight conditions ($\sigma = 105$ ns) [Med98a] for applications in wireless local area networks (WLANs), such as HIPERLAN/2, where the system bandwidth W_s is equal to 20 MHz [Etsi99].

From the graphs depicted in Fig. 6.1, it is evident that the SSTDL model does not provide a good approximation to the FCF of the reference model within the relevant interval $[-W_s/2, W_s/2]$. Actually, by taking the graphs of $|R_{\boldsymbol{HH}}(\varrho)|$ as a reference, we can observe that $|R_{\hat{\boldsymbol{H}}\hat{\boldsymbol{H}}}(\varrho)|$ exhibits a correlation offset that increases monotonically as ϱ moves from zero to $\pm W/2$. The above mentioned offset is indeed an effect caused by aliasing. We can also observe in Fig. 6.1 that $R_{\boldsymbol{HH}}(\varrho)$ and $R_{\hat{\boldsymbol{H}}\hat{\boldsymbol{H}}}(\varrho)$ follow different trends for frequencies in excess of $W/2$. From the graphs depicted in that figure, it is evident that $|R_{\hat{\boldsymbol{H}}\hat{\boldsymbol{H}}}(\varrho)| \neq |R_{\boldsymbol{HH}}(\varrho)|$ for $|\varrho| > W/2$.

6.4.3 The Influence of the FCF on the System Performance

Consider a frequency diversity system described by the following baseband equivalent signal model (it is assumed that the system is free from inter-symbol interference (ISI))

$$\vec{\boldsymbol{y}} = \vec{\boldsymbol{C}}\vec{x} + \vec{\boldsymbol{n}} \tag{6.20}$$

where $\vec{x}$, $\vec{\boldsymbol{y}}, \vec{\boldsymbol{n}} \in \mathbb{C}^{M\times 1}$ represent a vector of M transmitted signals, a random vector of M received signals, and a random vector with M complex additive white Gaussian noise (AWGN) components, respectively. The random channel matrix $\vec{\boldsymbol{C}}$ is defined as $\vec{\boldsymbol{C}} = \text{diag}\{\vec{\boldsymbol{H}}\}$, where $\vec{\boldsymbol{H}} \in \mathbb{C}^{M\times 1}$ and $\langle\vec{\boldsymbol{H}}\rangle_n = \boldsymbol{H}(t; n\,\upsilon_0)$ for all t. The symbol υ_0 stands for the fundamental frequency of the system. The notation $\mathbb{C}^{m\times n}$ designates the set of all $m \times n$ complex matrices, and $\langle\cdot\rangle_{n,m}$ denotes the entry of a matrix at its mth column and nth row (subindex m is omitted for vectors). The diag$\{\cdot\}$ operator produces a diagonal matrix from a vector, where the diagonal elements of the matrix are equal to the elements of the vector between curly braces. The channel correlation matrix is given as follows $\vec{R}_{\boldsymbol{C}} = E\{\vec{\boldsymbol{C}}\vec{\boldsymbol{C}}^*\}$. We define the (n,m)th entry of $\vec{R}_{\boldsymbol{C}}$ as

$$\langle\vec{R}_{\boldsymbol{C}}\rangle_{n,m} = R_{\boldsymbol{HH}}(W \cdot \Delta_{m-n}/M) \tag{6.21}$$

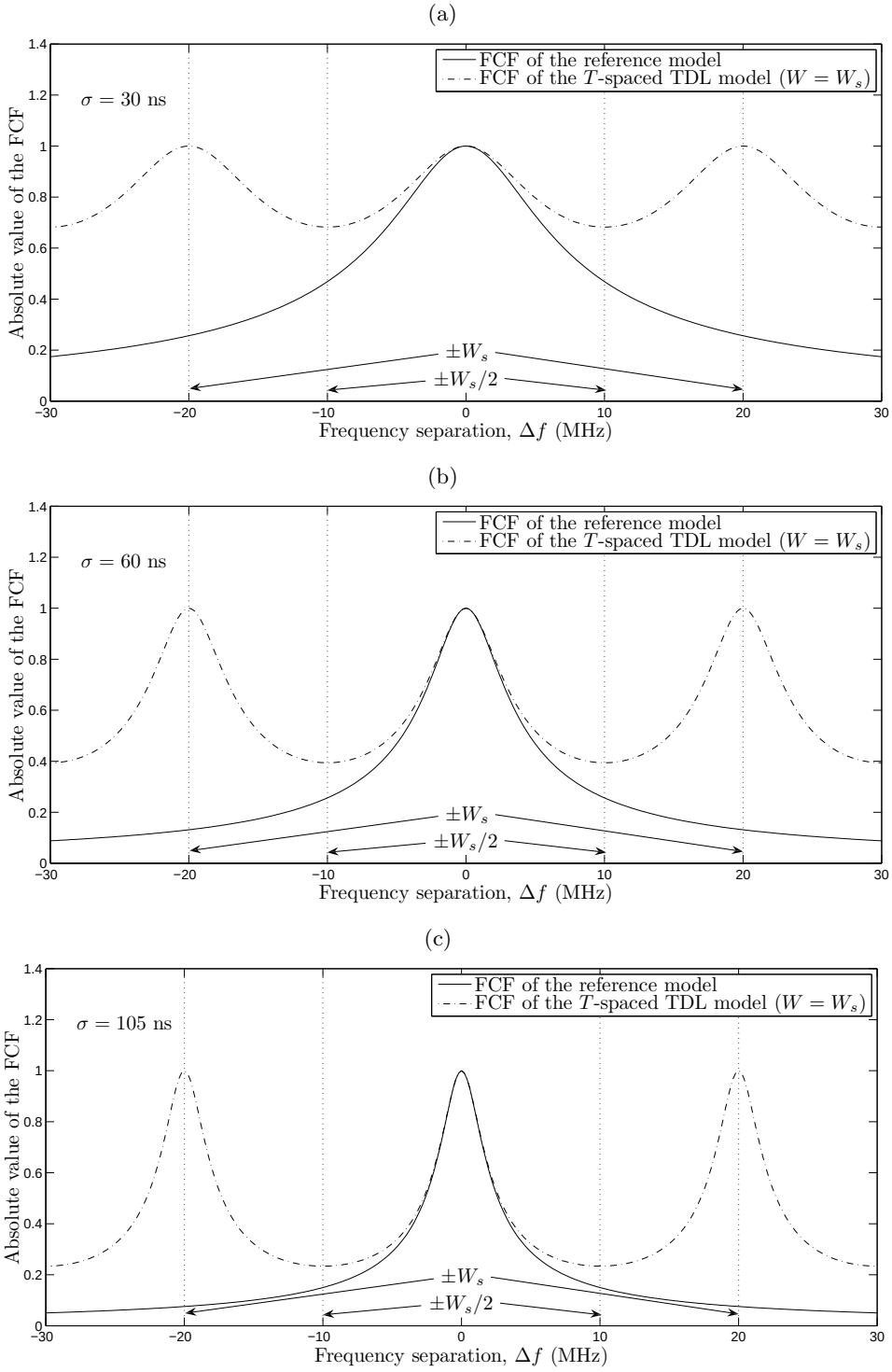

Figure 6.1: Comparison between the absolute value of the FCF of the reference model and the absolute value of the FCF of the SSTDL by considering the TED-PDP with $\tau_{\max} = 800$ ns, $W_s = 20$ MHz, and different values for the decay factor σ of the PDF.

where $\Delta_{m-n} = m - n$ denotes the $(m-n)$th lag of $\vec{R}_{\boldsymbol{C}}$. By assuming binary phase shift keying (BPSK) modulation, and maximal ratio combining (MRC), we obtain the following expression for the BEP of this system [Schu05, Sec. 2.4.6]

$$P_{BEP} = \frac{1}{\pi} \int_0^{\pi/2} \prod_{i=1}^{M} \left(1 + \frac{E_b}{N_0} \cdot \frac{\lambda_i}{M \cdot \sin^2\theta} \right)^{-1} d\theta \tag{6.22}$$

where E_b is the bit energy, N_0 is the noise density, and λ_i is the ith eigenvalue of the correlation matrix $\vec{R}_{\boldsymbol{C}}$.

When using a T-spaced TDL model for the laboratory analysis of such a frequency diversity system (or any other Δ_η-spaced TDL model), the channel matrix $\vec{\boldsymbol{C}}$ in (6.20) is substituted by a random matrix $\hat{\vec{\boldsymbol{C}}} = \mathrm{diag}\{\hat{\vec{\boldsymbol{H}}}\}$, where $\hat{\vec{\boldsymbol{H}}} \in \mathbb{C}^{M\times 1}$, and $\langle \hat{\vec{\boldsymbol{H}}} \rangle_n = \hat{\boldsymbol{H}}(t; n\,\upsilon_0)$ for all t. The correlation matrix of $\hat{\vec{\boldsymbol{C}}}$ is then given by $\vec{R}_{\hat{\boldsymbol{C}}} = E\{\hat{\vec{\boldsymbol{C}}}\hat{\vec{\boldsymbol{C}}}^*\}$, where

$$\langle \vec{R}_{\hat{\boldsymbol{C}}} \rangle_{n,m} \;=\; R_{\hat{\boldsymbol{H}}\hat{\boldsymbol{H}}}(W \cdot \Delta_{m-n}/M). \tag{6.23}$$

For an accurate system performance analysis, it is desirable that $\vec{R}_{\hat{\boldsymbol{C}}} = \vec{R}_{\boldsymbol{C}}$. However, due to the problems discussed in the preceding section, we have

$$\langle \vec{R}_{\hat{\boldsymbol{C}}} \rangle_{n,m} \;\approx\; \langle \vec{R}_{\boldsymbol{C}} \rangle_{n,m}, \quad \text{for } |\Delta_{m-n}| \le \lfloor M/2 \rfloor \tag{6.24}$$

$$\langle \vec{R}_{\hat{\boldsymbol{C}}} \rangle_{n,m} \;\neq\; \langle \vec{R}_{\boldsymbol{C}} \rangle_{n,m}, \quad \text{for } |\Delta_{m-n}| > \lfloor M/2 \rfloor\,. \tag{6.25}$$

From (6.24) and (6.25), it follows that the eigenvalues $\hat{\lambda}_i$ of $\vec{R}_{\hat{\boldsymbol{C}}}$ are not the same as those of $\vec{R}_{\boldsymbol{C}}$. Consequently, the simulated system

$$\hat{\vec{\boldsymbol{y}}} = \hat{\vec{\boldsymbol{C}}}\vec{x} + \vec{\boldsymbol{n}} \tag{6.26}$$

will provide an imprecise picture of the BEP of the actual system defined in (6.20). To demonstrate the veracity of this remark, let us analyze the BEP of a downlink MC-CDMA system [Guti06] comprising $M = 64$ orthogonal subcarriers with $\upsilon_0 = 312.5$ kHz, all of them used as data subcarriers. The nominal bandwidth of this system is $W_s = 20$ MHz ($W_s = 64 \times 312.5$ kHz). The sampling rate T is therefore equal to $T = 1/W_s = 50$ ns. We assume a multiple-user-interference-(MUI)-free network scenario and BPSK modulation with MRC at the receiver. With respect to the spreading factor M_{SF} of the system, we consider $M_{\mathrm{SF}} \in \{1, 2, 4, 8, 16, 32, 64\}$. To compute the BEP for different spreading factors, we use a slightly modified version of (6.22), which is given by

$$P_{BEP-SF} \;=\; \frac{1}{\pi} \int_0^{\pi/2} \prod_{i=1}^{M_{\mathrm{SF}}} \left(1 + \frac{E_b}{N_0} \cdot \frac{\ell_i^{(M_{\mathrm{SF}})}}{M_{\mathrm{SF}} \cdot \sin^2\theta} \right)^{-1} d\theta \tag{6.27}$$

where $\ell_i^{(M_{\mathrm{SF}})}$ is the ith eigenvalue of an arbitrary correlation matrix $\vec{R}^{(M_{\mathrm{SF}})} \in \mathbb{C}^{M_{\mathrm{SF}} \times M_{\mathrm{SF}}}$. To measure the BEP of the reference system for a spreading factor M_{SF}, we define the (n,m)th entry of $\vec{R}^{(M_{\mathrm{SF}})}$ as $\langle \vec{R}^{(M_{\mathrm{SF}})} \rangle_{n,m} = \langle \vec{R}_{\boldsymbol{C}} \rangle_{n,m}$. Analogously, to compute the BEP of the simulated system, we set $\langle \vec{R}^{(M_{\mathrm{SF}})} \rangle_{n,m} = \langle \vec{R}_{\hat{\boldsymbol{C}}} \rangle_{n,m}$. We have evaluated (6.27) by considering the TED-PDP [see (6.17)] with $\eta_{max} = 800$ ns and the same values of the falling factor σ as considered for drawing the graphs presented in Fig. 6.1. The obtained results are plotted in Fig. 6.2.

It can be seen in Figs. 6.2(a), 6.2(b), and 6.2(c) that the BEP of the reference system is not exactly the same as that of the simulated system when $M_{\mathrm{SF}} > 1$. In fact, the difference between the BEP of both systems increases with increasing the value of the spreading factor. This is because the aliasing effects affecting the FCF of the SSTDL model are more severe as the spreading factor increases. Interestingly, the results presented in Fig. 6.2(c) show that the aliasing effects can be neglected if σ is large. This is not surprising, since the FCF $R_{\boldsymbol{HH}}(\varrho)$ of $\boldsymbol{h}(t,\eta)$ decays fast for large values of σ [cf. Fig. 6.1]. However, the BEP of $\hat{\vec{\boldsymbol{y}}}$ is clearly different from that of $\vec{\boldsymbol{y}}$ when $M_{\mathrm{SF}} = 64$, even for a large value of σ. The reason for such a sharp difference is that half of the elements in $\vec{R}_{\hat{\boldsymbol{C}}}^{(64)}$ do not meet the relation $\langle \vec{R}_{\hat{\boldsymbol{C}}}^{(64)} \rangle_{m,n} \approx \langle \vec{R}_{\boldsymbol{C}}^{(64)} \rangle_{m,n}$ [see (6.25)].

6.5 Avoiding the Problems Caused by SSTDL Models

SSTDL models lead to an imprecise system performance evaluation because of two reasons. On the one hand, the quality of the relation $R_{\hat{\boldsymbol{H}}\hat{\boldsymbol{H}}}(\varrho) \approx R_{\boldsymbol{HH}}(\varrho)$ is affected by aliasing effects within $[-W_s/2, W_s/2]$. On the other hand, $R_{\hat{\boldsymbol{H}}\hat{\boldsymbol{H}}}(\varrho) \neq R_{\boldsymbol{HH}}(\varrho)$ for $|\varrho| > W_s/2$ since $R_{\hat{\boldsymbol{H}}\hat{\boldsymbol{H}}}(\varrho)$ behaves different from $R_{\boldsymbol{HH}}(\varrho)$ when $|\varrho| > W_s/2$. Fortunately, these problems can be solved, or at least sufficiently reduced, simply by increasing the sampling rate of the channel, i.e., by reducing the tap spacing Δ_η of $\boldsymbol{h}(t,\eta)$.

Reducing Δ_η will result in less severe aliasing effects provided that $R_{\boldsymbol{HH}}(\varrho) \to 0$ as $\varrho \to \pm\infty$ (most PDPs, including the TED-PDP in (6.17), meet this condition). In addition, it is obvious from (6.15) that a higher sampling rate will result in a larger period for $R_{\hat{\boldsymbol{H}}\hat{\boldsymbol{H}}}(\varrho)$ and, consequently, in a larger approximation interval. Indeed, it can be shown that $R_{\hat{\boldsymbol{H}}\hat{\boldsymbol{H}}}(\varrho) \to R_{\boldsymbol{HH}}(\varrho)$ as $\Delta_\eta \to 0$. Particularly, if we choose $\Delta_\eta = T/2$, then the period W of $R_{\hat{\boldsymbol{H}}\hat{\boldsymbol{H}}}(\varrho)$ will be conveniently equal to twice W_s, i.e., $W = 2W_s$. In this way, the approximation $R_{\hat{\boldsymbol{H}}\hat{\boldsymbol{H}}}(\varrho) \approx R_{\boldsymbol{HH}}(\varrho)$ will hold for the relevant interval $\varrho \in [-W_s, W_s]$. As a result, we will obtain a more reliable picture of the system's performance while keeping the complexity of the TDL model low. For the above mentioned reasons, we suggest to sample the CIR at a rate equal to twice W_s to avoid the problems caused by T-spaced

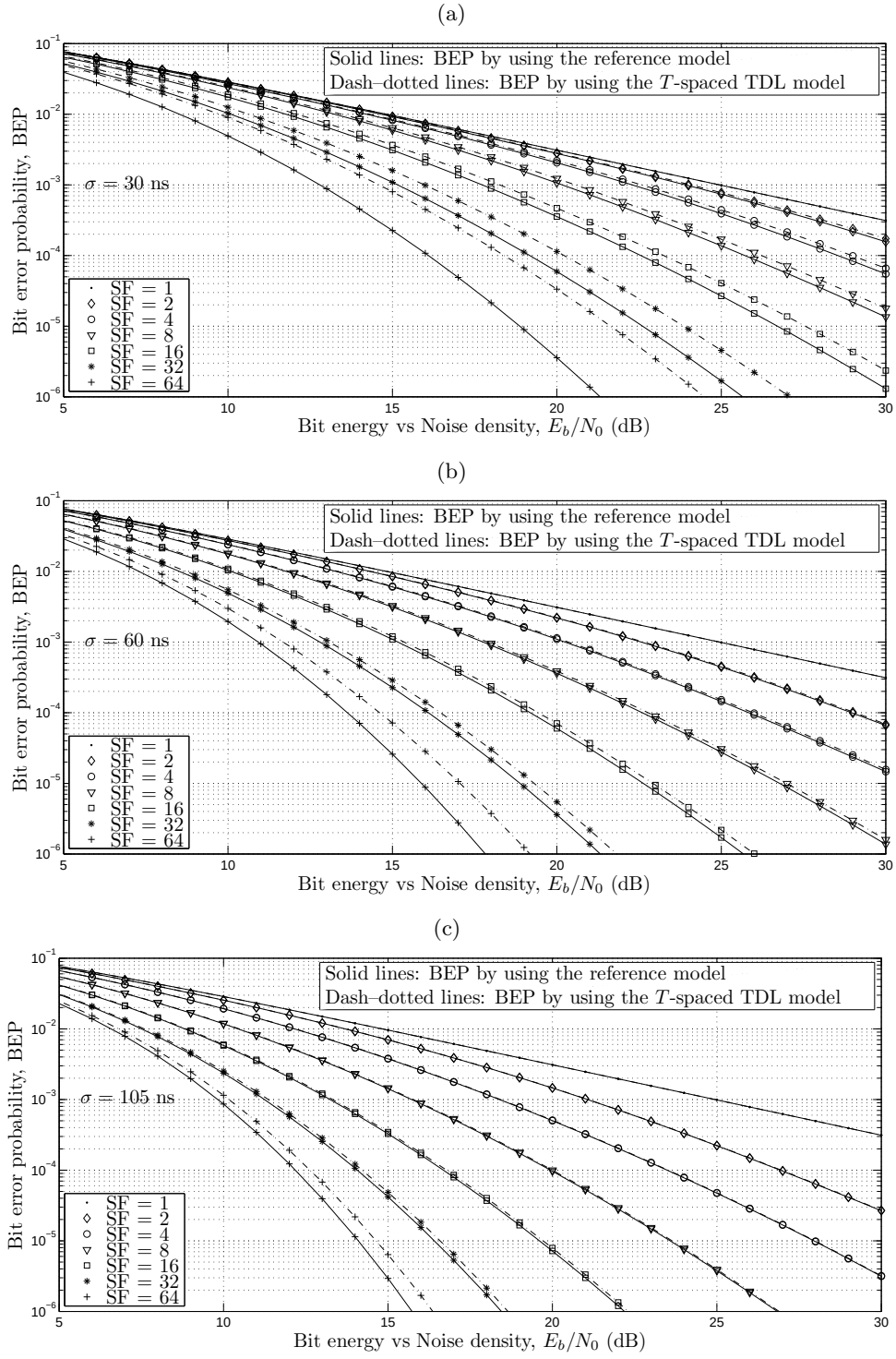

Figure 6.2: Comparison between the theoretical and the empirical BEPs of a MUI-free downlink MC-CDMA system with MRC by considering the T-spaced TDL model and the TED-PDP with different values of the decay factor σ (SF stands for the spreading factor).

TDL models. We will indistinctly refer to the oversampled TDL model having a tap spacing of $\Delta_\eta = T/2$ as the $T/2$–spaced TDL model or as the HSSTDL.

Figure 6.3 illustrates the advantages of using $T/2$-spaced TDL models by comparing the absolute value of the FCF of the reference model with that of the FCFs of the T-spaced and $T/2$-spaced TDL models. This figure demonstrates that the aliasing effects are less severe for the $T/2$-spaced TDL model than for the T-spaced TDL models.

As a numerical example of the benefits of using a $T/2$-spaced TDL model for system evaluation, let us consider again the MC-CDMA system described in Section 6.4. We have recalculated the BEP of this system under the same considerations as in Section 6.4, but with the difference that $\Delta_\eta = T/2$, meaning that the tap spacing is equal to $\Delta_\eta = 25$ ns and $\hat{\vec{\boldsymbol{H}}} \in \mathbb{C}^{128\times 1}$ with $N = 33$. The obtained results are shown in Figs. 6.4.

It is clear from Figs. 6.4(a), 6.4(b), and 6.4(c), that the simulation system $\hat{\vec{\boldsymbol{y}}}$ matches better the BEP of the reference system $\vec{\boldsymbol{y}}$ when the $T/2$–spaced TDL model is used. What is more, we can observe from the results obtained for a spreading factor of 64 that the difference between the BEP of $\hat{\vec{\boldsymbol{y}}}$ and $\vec{\boldsymbol{y}}$ is considerably smaller than when we use the T–spaced TDL model (see Figs. 6.2(a), 6.2(b), and 6.2(c)). The reason for such an impressive improvement is that the approximation $R_{\hat{\boldsymbol{H}}\hat{\boldsymbol{H}}}(\varrho) \approx R_{\boldsymbol{HH}}(\varrho)$ is valid for $\varrho \in [-Ws, Ws]$ when we use a $T/2$-spaced TDL model. We shall mention, nonetheless, that the $T/2$-spaced TDL model has been introduced mainly as a solution to enable the approximation of the FCF $R_{\boldsymbol{HH}}(\varrho)$ along the relevant range of frequencies of the system $-W_s \leq \varrho \leq W_s$. It does not remove completely the aliasing effects observed within $\varrho \in [-W/2, W/2]$, which explains the slight differences between the BEP of the reference system and the simulation system when $\sigma = 30$ ns and $M_{\mathrm{SF}} = 64$ [see Fig. 6.4(c)]. Other solutions, more sophisticated than the one discussed here, are necessary to neutralize the aliasing effects, e.g., see [Pae02b].

6.6 Chapter Summary and Conclusions

In this chapter, we showed that important inconsistencies arise when SSTDL models, or $\Delta\eta$-spaced TDL models in general, are used within the context of band-limited systems to model WSSUS channels. Such inconsistencies involve the violation of the US condition. Nevertheless, a Δ_η-spaced TDL model is a valid simulation model for WSSUS channels if it is considered out of the context of band-limited systems.

We showed that the FCF of a Δ_η-spaced TDL model is a periodic function with a period equal to $W = 1/\Delta_\eta$. Because of this characteristic, a Δ_η-spaced TDL models provides just an approximation to the FCF of the reference model,

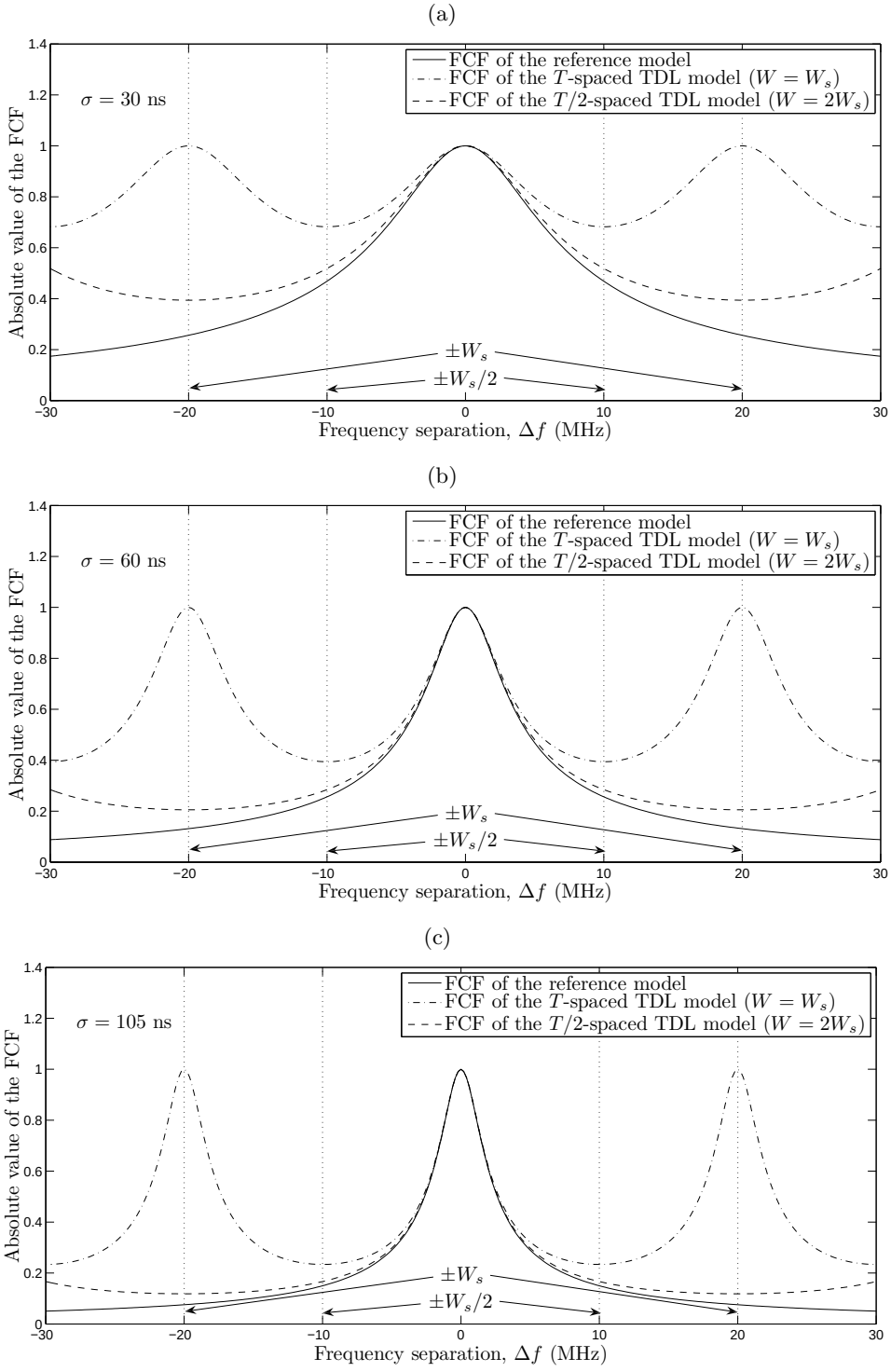

Figure 6.3: Comparison between the absolute value of the FCF of the reference model and the absolute value of the FCF of the HSSTDL by considering the TED-PDP with $\tau_{\max} = 800$ ns, $W_s = 20$ MHz, and different values for the decay factor σ of the PDF.

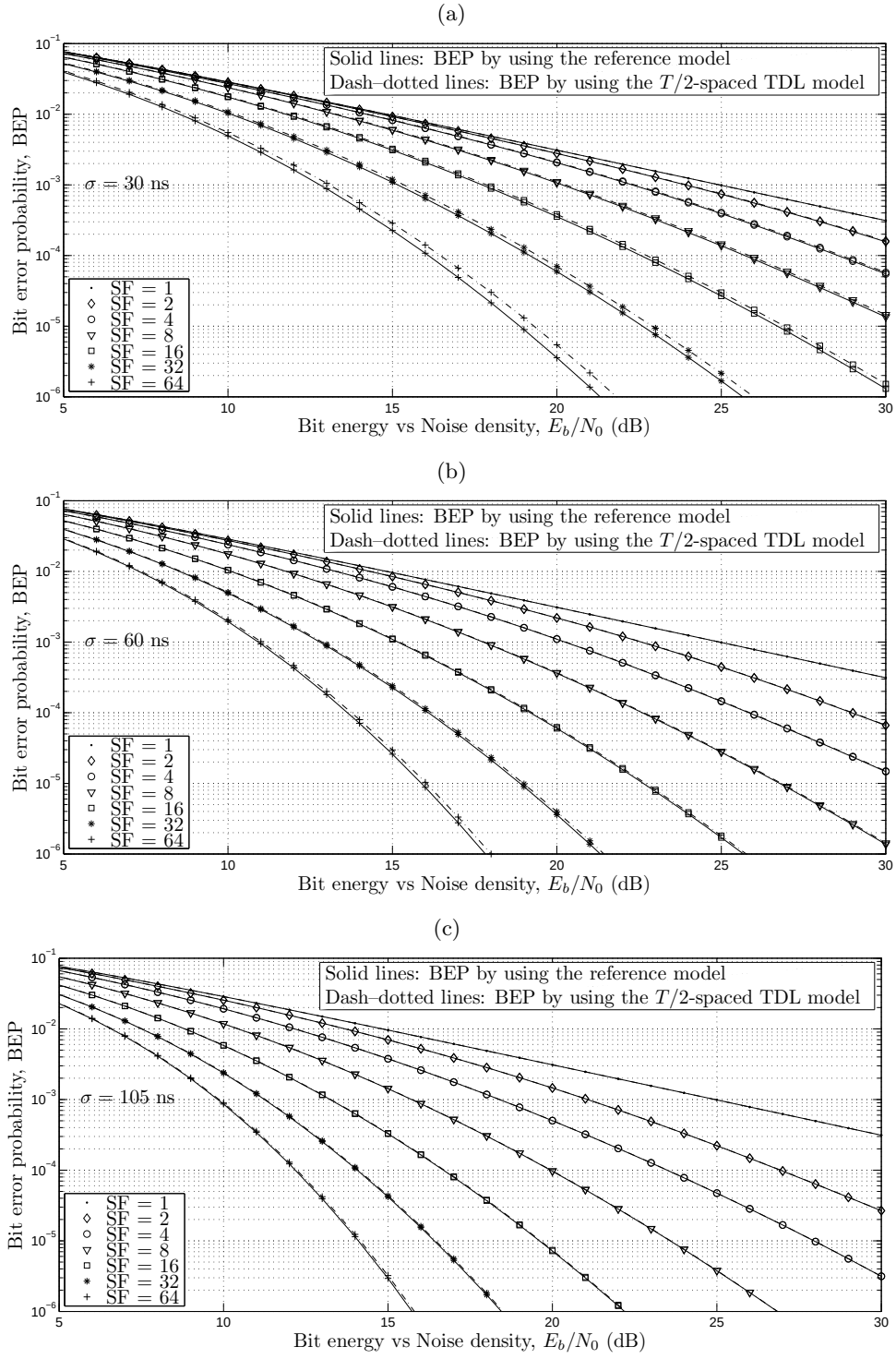

Figure 6.4: Comparison between the theoretical and the empirical BEPs of a MUI-free downlink MC-CDMA system with MRC by considering a $T/2$-spaced TDL model and the TED-PDP with different values of the decay factor σ (SF stands for the spreading factor).

which is valid only within $\varrho \in [-W/2, W/2]$. We also showed that such an approximation is affected by aliasing effects.

The relation $R_{\hat{\boldsymbol{H}}\hat{\boldsymbol{H}}}(\varrho) \approx R_{\boldsymbol{HH}}(\varrho)$ does not hold for $|\varrho| > W/2$ when $\Delta_\eta = T$. For this reason a SSTDL model is not able to emulate the FCF of the reference model within the frequency range of the system's bandwidth. This drawback seriously affects the performance analysis of wireless communication systems sensitive to the FCF.

To avoid the problems caused by T-spaced TDL models, we proposed the use of $T/2$-spaced TDL channel models, which are obtained by sampling the CIR at a rate equal to $2W_s$, i.e., $\Delta_\eta = T/2$. A $T/2$-spaced TDL model is more resilient to the aliasing effects than a T-spaced TDL model provided that the FCF $R_{\boldsymbol{HH}}(\varrho)$ of the reference model approaches to zero as $\varrho \to \infty$. Another advantage of $T/2$ spaced TDL models is that they enable the approximation of the reference model's FCF along the complete frequency range of the system bandwidth. For this reason, using $T/2$-spaced TDL models instead of T-spaced TDL models turns out to be of great advantage for system evaluation purposes.

Chapter 7

Summary of Contributions and Open Problems

7.1 Contributions

The contributions of this doctoral project can be summarized as follows:

- We presented a thorough analysis of the statistical properties of a stochastic SOC simulation model for mobile Rician fading channels having a time-variant LOS component. We analyzed the correlation and spectral properties of the SOC simulator, as well as its envelope and phase PDFs.
- We provided closed-form solutions for the squared envelope ACF of the simulation model. Closed-form expressions were derived for the squared envelope ACF of the ensemble and also for the squared envelope ACF of the sample functions. For this latter function, we provided solutions not only for the case where the IQ components of the SOC model are cross-correlated, but also for the case where they are mutually uncorrelated. The correctness of such expressions was demonstrated by simulations.
- We investigated the stationarity properties of the SOC simulation model. In this respect, we showed that the simulation model is a WSS process provided that its LOS component is time-invariant or equal to zero.
- We analyzed the ergodicity of the stochastic SOC simulation model with respect to the mean value, the power, and the ACF. We found out that the simulation model is always power ergodic and autocorrelation ergodic, but the mean-ergodicity property holds only when the LOS component is time-invariant or equal to zero.
- We also analyzed the mean- and the autocorrelation-ergodicity properties of the simulation model's squared envelope. We showed that the squared en-

velope of the SOC model is a mean-ergodic and an autocorrelation-ergodic process only when its IQ components are uncorrelated.

- We presented a generalized version of the MEA that is well-suited for the design of SOC simulators for narrowband SISO fading channels characterized by any type of DPSDs. We called such a generalized method the GMEA.

- We proposed the RSAM as a suitable method for the design of SOC simulators for narrowband SISO fading channels with arbitrary DPSDs.

- We extended the GMEA and the RSAM with respect to the design of SOC simulators for single-bounce scattering narrowband mobile MIMO fading channels.

- We revisited the concept of the SSTDL model for WSSUS channels. We showed that, from the perspective of band-limited systems, the SSTDL model violates the US condition of the channel. However, the SSTDL model is compatible with the US condition when the model is considered out of the context of band-limited systems. It was shown that a SSTDL suffers from strong limitations in emulating the FCF of WSSUS channels. Such limitations seriously affect the performance analysis of wireless communications systems sensitive to the FCF. A simple solution to avoid the problems produced by SSTDL models was presented by reducing the tap spacing by a factor of two.

7.2 Open Problems

We close this chapter by noticing that closed-form solutions are still lacking for the LCR and the ADF of SOC channel simulation models. Closing this gap is important to determine whether or not a SOC model is able to reproduce the fading coherence of the envelope of mobile fading channels. On the other hand, in this dissertation we focused our attention on the design of SOC simulation models for mobile fading channels in two dimensional single-bounce scattering environments. Further research is necessary to enable the SOC simulation of fading channels in three dimensional multiple-bounce scattering scenarios. This is particularly relevant to investigate the effects that the spatial polarization of the received signal exerts on the system performance.

Appendix A

Derivation of the Squared Envelope ACF of the Reference Model

In this appendix, we derive a closed-form expression for the ACF $r_{\boldsymbol{\xi}^2\boldsymbol{\xi}^2}(t_1,t_2) \triangleq E\{\boldsymbol{\xi}^2(t_1)\boldsymbol{\xi}^2(t_2)\}$ of the squared envelope $\boldsymbol{\xi}^2(t) \triangleq |\boldsymbol{\nu}(t)|^2$ of the narrowband Rician fading channel model described by the complex Gaussian process $\boldsymbol{\nu}(t) = \boldsymbol{\mu}(t) + m_\rho(t)$. The obtained solution is valid irrespective of the PDF characterizing the AOA statistics of the channel's multipath components.

From the definition of $r_{\boldsymbol{\xi}^2\boldsymbol{\xi}^2}(t_1,t_2)$, and taking into account that $E\{\boldsymbol{\mu}(t)\} = 0$ [see Sec. 2.2], one can easily verify that

$$\begin{aligned} r_{\boldsymbol{\xi}^2\boldsymbol{\xi}^2}(t_1,t_2) &\triangleq E\{\boldsymbol{\xi}^2(t_1)\boldsymbol{\xi}^2(t_2)\} \\ &= E\{\, |\boldsymbol{\mu}(t_1) + m_\rho(t_1)|^2\, |\boldsymbol{\mu}(t_2) + m_\rho(t_2)|^2 \,\} \\ &= E\{\, [\, |\boldsymbol{\mu}(t_1)|^2 + |m_\rho(t_1)|^2 + \boldsymbol{\mu}^*(t_1)\, m_\rho(t_1) + \boldsymbol{\mu}(t_1)\, m_\rho^*(t_1)\,] \\ &\qquad [\, |\boldsymbol{\mu}(t_2)|^2 + |m_\rho(t_2)|^2 + \boldsymbol{\mu}^*(t_2)\, m_\rho(t_2) + \boldsymbol{\mu}(t_2)\, m_\rho^*(t_2)\,]\,\} \\ &= r_{\boldsymbol{\zeta}^2\boldsymbol{\zeta}^2}(t_1,t_2) + \rho^4 + 2\sigma_{\boldsymbol{\mu}}^2\,\rho^2 + w_{\boldsymbol{\mu},m_\rho}(t_1,t_2) \\ &\quad + u_{\boldsymbol{\mu},m_\rho}(t_1,t_2) + u_{\boldsymbol{\mu},m_\rho}(t_2,t_1) \end{aligned} \tag{A.1}$$

where $r_{\boldsymbol{\zeta}^2\boldsymbol{\zeta}^2}(t_1,t_2) \triangleq E\{\boldsymbol{\zeta}^2(t_1)\boldsymbol{\zeta}^2(t_2)\}$ is the ACF of the squared envelope $\boldsymbol{\zeta}^2(t) \triangleq |\boldsymbol{\mu}(t)|^2$ of the channel's diffuse component $\boldsymbol{\mu}(t)$, whilst the functions $w_{\boldsymbol{\mu},m_\rho}(t_1,t_2)$ and $u_{\boldsymbol{\mu},m_\rho}(t_1,t_2)$ are equal to

$$\begin{aligned} w_{\boldsymbol{\mu},m_\rho}(t_1,t_2) &= E\{\, [\, \boldsymbol{\mu}^*(t_1)m_\rho(t_1) + \boldsymbol{\mu}(t_1)m_\rho^*(t_1)\,] \\ &\qquad \times [\, \boldsymbol{\mu}^*(t_2)m_\rho(t_2) + \boldsymbol{\mu}^*(t_2)m_\rho^*(t_2)\,]\,\} \end{aligned} \tag{A.2}$$

$$u_{\boldsymbol{\mu},m_\rho}(t_1,t_2) = E\{\, |\boldsymbol{\mu}(t_1)|^2 \cdot [\, \boldsymbol{\mu}^*(t_2)m_\rho(t_2) + \boldsymbol{\mu}(t_2)m_\rho^*(t_2)\,]\,\}. \tag{A.3}$$

A compact expression for $r_{\boldsymbol{\zeta}^2\boldsymbol{\zeta}^2}(t_1,t_2)$ can be obtained by noticing that

$$\begin{aligned} r_{\boldsymbol{\zeta}^2\boldsymbol{\zeta}^2}(t_1,t_2) &\triangleq E\{\,\boldsymbol{\zeta}^2(t_1)\,\boldsymbol{\zeta}^2(t_2)\,\} \\ &= E\{\,|\boldsymbol{\mu}(t_1)|^2|\boldsymbol{\mu}(t_2)|^2\,\} \\ &= E\{\,[\boldsymbol{\mu}_I(t_1)^2+\boldsymbol{\mu}_Q(t_1)^2]\cdot[\boldsymbol{\mu}_I(t_2)^2+\boldsymbol{\mu}_Q(t_2)^2]\,\} \\ &= E\{\boldsymbol{\mu}_I^2(t_1)\boldsymbol{\mu}_I^2(t_2)\}+E\{\boldsymbol{\mu}_Q^2(t_1)\boldsymbol{\mu}_Q^2(t_2)\} \\ &\quad +E\{\boldsymbol{\mu}_I^2(t_1)\boldsymbol{\mu}_Q^2(t_2)\}+E\{\boldsymbol{\mu}_Q^2(t_1)\boldsymbol{\mu}_I^2(t_2)\} \end{aligned} \tag{A.4}$$

where $\boldsymbol{\mu}_I(t)$ and $\boldsymbol{\mu}_Q(t)$ are the inphase and quadrature components of $\boldsymbol{\mu}(t)$, respectively. The expectations in (A.4) satisfy the relationships [Auli79]

$$E\{\boldsymbol{\mu}_I^2(t_1)\,\boldsymbol{\mu}_I^2(t_2)\} = E\{\boldsymbol{\mu}_I^2(t_1)\}\cdot E\{\boldsymbol{\mu}_I^2(t_2)\}+2E^2\{\boldsymbol{\mu}_I(t_1)\boldsymbol{\mu}_I(t_2)\} \tag{A.5a}$$

$$E\{\boldsymbol{\mu}_Q^2(t_1)\,\boldsymbol{\mu}_Q^2(t_2)\} = E\{\boldsymbol{\mu}_Q^2(t_1)\}\cdot E\{\boldsymbol{\mu}_Q^2(t_2)\}+2E^2\{\boldsymbol{\mu}_Q(t_1)\boldsymbol{\mu}_Q(t_2)\} \tag{A.5b}$$

$$E\{\boldsymbol{\mu}_I^2(t_1)\,\boldsymbol{\mu}_Q^2(t_2)\} = E\{\boldsymbol{\mu}_I^2(t_1)\}\cdot E\{\boldsymbol{\mu}_Q^2(t_2)\}+2E^2\{\boldsymbol{\mu}_I(t_1)\boldsymbol{\mu}_Q(t_2)\} \tag{A.5c}$$

$$E\{\boldsymbol{\mu}_Q^2(t_1)\,\boldsymbol{\mu}_I^2(t_2)\} = E\{\boldsymbol{\mu}_Q^2(t_1)\}\cdot E\{\boldsymbol{\mu}_I^2(t_2)\}+2E^2\{\boldsymbol{\mu}_Q(t_1)\boldsymbol{\mu}_I(t_2)\}. \tag{A.5d}$$

Hence, by taking account of the autocorrelation and cross-correlation properties of $\boldsymbol{\mu}_I(t)$ and $\boldsymbol{\mu}_Q(t)$ [see (2.11)], we find that

$$\begin{aligned} r_{\boldsymbol{\zeta}^2\boldsymbol{\zeta}^2}(t_1,t_2) &= E^2\{\boldsymbol{\mu}_I^2(t)\}+E^2\{\boldsymbol{\mu}_Q^2(t)\}+E\{\boldsymbol{\mu}_I^2(t)\}E\{\boldsymbol{\mu}_Q^2(t)\} \\ &\quad +E\{\boldsymbol{\mu}_Q^2(t)\}E\{\boldsymbol{\mu}_I^2(t)\}+2\Big[E^2\{\boldsymbol{\mu}_I(t_1)\boldsymbol{\mu}_I(t_2)\} \\ &\quad +E^2\{\boldsymbol{\mu}_Q(t_1)\boldsymbol{\mu}_Q(t_2)\}+E^2\{\boldsymbol{\mu}_I(t_1)\boldsymbol{\mu}_Q(t_2)\}+E^2\{\boldsymbol{\mu}_Q(t_1)\boldsymbol{\mu}_I(t_2)\}\Big] \\ &= 4r^2_{\boldsymbol{\mu}_I\boldsymbol{\mu}_I}(0)+2\big[r^2_{\boldsymbol{\mu}_I\boldsymbol{\mu}_I}(\tau)+r^2_{\boldsymbol{\mu}_Q\boldsymbol{\mu}_Q}(\tau)+r^2_{\boldsymbol{\mu}_I\boldsymbol{\mu}_Q}(\tau)+r^2_{\boldsymbol{\mu}_Q\boldsymbol{\mu}_I}(\tau)\big] \\ &= \sigma^4_{\boldsymbol{\mu}}+4\big[r^2_{\boldsymbol{\mu}_I\boldsymbol{\mu}_I}(\tau)+r^2_{\boldsymbol{\mu}_I\boldsymbol{\mu}_Q}(\tau)\big] \\ &= \sigma^4_{\boldsymbol{\mu}}+|r_{\boldsymbol{\mu}\boldsymbol{\mu}}(\tau)|^2. \end{aligned} \tag{A.6}$$

This result indicates that the ACF of $\boldsymbol{\zeta}^2(t)$ is not influenced by the choice of the time origin, so that $r_{\boldsymbol{\zeta}^2\boldsymbol{\zeta}^2}(t_1,t_2)=r_{\boldsymbol{\zeta}^2\boldsymbol{\zeta}^2}(\tau)$.

The function $w_{\boldsymbol{\mu},m_\rho}(t_1,t_2)$, on the other hand, may be rewritten as follows

$$\begin{aligned} w_{\boldsymbol{\mu},m_\rho}(t_1,t_2) &= E\big\{\big[\,\boldsymbol{\mu}^*(t_1)m_\rho(t_1)+\boldsymbol{\mu}(t_1)m^*_\rho(t_1)\,\big] \\ &\qquad \times\big[\,\boldsymbol{\mu}^*(t_2)m_\rho(t_2)+\boldsymbol{\mu}(t_2)m^*_\rho(t_2)\,\big]\big\} \\ &= 4\,E\big\{\mathrm{Re}\{\boldsymbol{\mu}^*(t_1)m_\rho(t_1)\}\cdot\mathrm{Re}\{\boldsymbol{\mu}^*(t_2)m_\rho(t_2)\}\big\} \\ &= 4\rho^2\,E\big\{\big[\cos(2\pi f_\rho t_1+\theta_\rho)\boldsymbol{\mu}_I(t_1)+\sin(2\pi f_\rho t_1+\theta_\rho)\boldsymbol{\mu}_Q(t_1)\big] \\ &\qquad \big[\cos(2\pi f_\rho t_2+\theta_\rho)\boldsymbol{\mu}_I(t_2)+\sin(2\pi f_\rho t_2+\theta_\rho)\boldsymbol{\mu}_Q(t_2)\big]\big\}. \end{aligned} \tag{A.7}$$

From (A.7), we obtain after straightforward calculations the result

$$w_{\boldsymbol{\mu},m_\rho}(t_1,t_2) = w_{\boldsymbol{\mu},m_\rho}(\tau) \tag{A.8}$$

$$= \; 4\rho^2\big[\cos(2\pi f_\rho\tau)r_{\boldsymbol{\mu}_I\boldsymbol{\mu}_I}(\tau)+\sin(2\pi f_\rho\tau)r_{\boldsymbol{\mu}_I\boldsymbol{\mu}_Q}(\tau)\big]. \tag{A.9}$$

In turn, the function $u_{\boldsymbol{\mu},m_\rho}(t_1,t_2)$ may be expressed as

$$\begin{aligned}
u_{\boldsymbol{\mu},m_\rho}(t_1,t_2) &\triangleq E\big\{\,|\boldsymbol{\mu}(t_1)|^2\cdot\big[\,\boldsymbol{\mu}^*(t_2)m_\rho(t_2)+\boldsymbol{\mu}(t_2)m_\rho^*(t_2)\,\big]\big\}\\
&= 2\,E\big\{\,|\boldsymbol{\mu}(t_1)|^2\cdot\mathrm{Re}\{\boldsymbol{\mu}^*(t_2)m_\rho(t_2)\}\,\big\}\\
&= 2\,E\big\{\,[\boldsymbol{\mu}_I^2(t_1)+\boldsymbol{\mu}_Q^2(t_1)]\cdot\big[\cos(2\pi f_\rho t_2+\theta_\rho)\boldsymbol{\mu}_I(t_2)\\
&\quad+\sin(2\pi f_\rho t_2+\theta_\rho)\boldsymbol{\mu}_Q(t_2)\big]\,\big\}\\
&= 2\Big\{\cos(2\pi f_\rho t_2+\theta_\rho)\Big[E\big\{\boldsymbol{\mu}_I^2(t_1)\boldsymbol{\mu}_I(t_2)\big\}+E\big\{\boldsymbol{\mu}_Q^2(t_1)\boldsymbol{\mu}_I(t_2)\big\}\Big]\\
&\quad+\sin(2\pi f_\rho t_2+\theta_\rho)\Big[E\big\{\boldsymbol{\mu}_I^2(t_1)\boldsymbol{\mu}_Q(t_2)\big\}+E\big\{\boldsymbol{\mu}_Q^2(t_1)\boldsymbol{\mu}_Q(t_2)\big\}\Big]\Big\}.
\end{aligned} \tag{A.10}$$

It can be shown that the four expectations in (A.10) are equal to zero, so that

$$u_{\boldsymbol{\mu},m_\rho}(t_1,t_2)=0. \tag{A.11}$$

In order to demonstrate the veracity of this result, let us explicitly evaluate the case $E\big\{\boldsymbol{\mu}_I^2(t_1)\boldsymbol{\mu}_I(t_2)\big\}$. To this end, we recall that

$$\boldsymbol{\mu}_I(t) \;=\; \mathrm{Re}\big\{\boldsymbol{\mu}(t)\big\} \;=\; \lim_{\mathcal{N}\to\infty}\sum_{n=1}^{N}\boldsymbol{c}_n\cos(2\pi\boldsymbol{f}_n t+\boldsymbol{\theta}_n). \tag{A.12}$$

The expectation $E\big\{\boldsymbol{\mu}_I^2(t_1)\boldsymbol{\mu}_I(t_2)\big\}$ can then be arranged as an infinite series

$$E\big\{\boldsymbol{\mu}_I^2(t_1)\boldsymbol{\mu}_I(t_2)\big\} \;=\; \lim_{\mathcal{N}\to\infty}\sum_{n=1}^{\mathcal{N}}\sum_{m=1}^{\mathcal{N}}\sum_{p=1}^{\mathcal{N}}E\{\boldsymbol{c}_n\boldsymbol{c}_m\boldsymbol{c}_p\}\cdot E\{\boldsymbol{h}_{n,m,p}(t_1,t_2)\} \tag{A.13}$$

where

$$\begin{aligned}
\boldsymbol{h}_{n,m,p}(t_1,t_2) \;=\;& \big[\cos(2\pi\boldsymbol{f}_n t_1)\cos(\boldsymbol{\theta}_n)-\sin(2\pi\boldsymbol{f}_n t_1)\sin(\boldsymbol{\theta}_n)\big]\\
&\times\big[\cos(2\pi\boldsymbol{f}_m t_1)\cos(\boldsymbol{\theta}_m)-\sin(2\pi\boldsymbol{f}_m t_1)\sin(\boldsymbol{\theta}_m)\big]\\
&\times\big[\cos(2\pi\boldsymbol{f}_p t_2)\cos(\boldsymbol{\theta}_p)-\sin(2\pi\boldsymbol{f}_p t_2)\sin(\boldsymbol{\theta}_p)\big].
\end{aligned} \tag{A.14}$$

The average value of $\boldsymbol{h}_{n,m,p}(t_1,t_2)$ with respect to the random phases proves to be equal to zero, since $E\{\cos(\boldsymbol{\theta}_n)\cos(\boldsymbol{\theta}_m)\cos(\boldsymbol{\theta}_p)\}=E\{\sin(\boldsymbol{\theta}_n)\sin(\boldsymbol{\theta}_m)\sin(\boldsymbol{\theta}_p)\}=E\{\cos(\boldsymbol{\theta}_n)\cos(\boldsymbol{\theta}_m)\sin(\boldsymbol{\theta}_p)\}=E\{\sin(\boldsymbol{\theta}_n)\sin(\boldsymbol{\theta}_m)\cos(\boldsymbol{\theta}_p)\}=0$ for all combinations of n, m, and p (even for $n=m=p$). In view of this, we can state that

$$E\{\boldsymbol{h}_{n,m,p}(t_1,t_2)\}=0,\quad\forall n,m,p \tag{A.15}$$

which in turn implies that $E\big\{\boldsymbol{\mu}_I^2(t_1)\,\boldsymbol{\mu}_I(t_2)\big\}=0$.

Analogously, it can be proved that $E\{\boldsymbol{\mu}_Q^2(t_1)\,\boldsymbol{\mu}_I(t_2)\} = E\{\boldsymbol{\mu}_I^2(t_1)\,\boldsymbol{\mu}_Q(t_2)\} = E\{\boldsymbol{\mu}_Q^2(t_1)\,\boldsymbol{\mu}_Q(t_2)\} = 0$ (we will omit the details for reasons of brevity). Consequently, $u_{\boldsymbol{\mu},m_\rho}(t_1,t_2) = u_{\boldsymbol{\mu},m_\rho}(t_2,t_1) = 0$.

By substituting the results presented in (A.6), (A.9), and (A.11)) into (A.1), we finally obtain the expression

$$\begin{aligned} r_{\boldsymbol{\xi}^2\boldsymbol{\xi}^2}(t_1,t_2) &= r_{\boldsymbol{\zeta}^2\boldsymbol{\zeta}^2}(\tau) + \rho^4 + 2\sigma_{\boldsymbol{\mu}}^2\rho^2 + 4\rho^2\big[r_{\boldsymbol{\mu}_I\boldsymbol{\mu}_I}(\tau)\cos(2\pi f_\rho\tau) \\ &\quad + r_{\boldsymbol{\mu}_I\boldsymbol{\mu}_Q}(\tau)\sin(2\pi f_\rho\tau)\big]. \end{aligned} \tag{A.16}$$

We notice that $r_{\boldsymbol{\xi}^2\boldsymbol{\xi}^2}(t_1,t_2)$ is time-shift insensitive, i.e., $r_{\boldsymbol{\xi}^2\boldsymbol{\xi}^2}(t_1,t_2) = r_{\boldsymbol{\xi}^2\boldsymbol{\xi}^2}(\tau)$. Equation (2.39) follows from (A.16) by rewriting $r_{\boldsymbol{\xi}^2\boldsymbol{\xi}^2}(\tau)$ in terms of the Rician factor $c_R = \rho^2/\sigma_{\boldsymbol{\mu}}^2$.

Appendix B

Derivation of the Squared Envelope ACF of the Stochastic SOC-Based Simulation Model

In this appendix, we derive a closed-form solution for the ACF $r_{\hat{\boldsymbol{\xi}}^2\hat{\boldsymbol{\xi}}^2}(t_1,t_2) \triangleq E\{\hat{\boldsymbol{\xi}}^2(t_1)\hat{\boldsymbol{\xi}}^2(t_2)\}$ of the squared envelope $\hat{\boldsymbol{\xi}}^2(t) \triangleq |\hat{\boldsymbol{\nu}}(t)|^2$ of the stochastic SOC-based simulation model described by the random process $\hat{\boldsymbol{\nu}}(t) = \hat{\boldsymbol{\mu}}(t) + m_\rho(t)$.

Starting from the definition of $r_{\hat{\boldsymbol{\xi}}^2\hat{\boldsymbol{\xi}}^2}(t_1,t_2)$, one can show that [cf. Appx. A]

$$\begin{aligned} r_{\hat{\boldsymbol{\xi}}^2\hat{\boldsymbol{\xi}}^2}(t_1,t_2) &= r_{\hat{\boldsymbol{\zeta}}^2\hat{\boldsymbol{\zeta}}^2}(t_1,t_2) + \rho^4 + 2\sigma_{\boldsymbol{\mu}}^2\,\rho^2 + w_{\hat{\boldsymbol{\mu}},m_\rho}(t_1,t_2) \\ &\quad + u_{\hat{\boldsymbol{\mu}},m_\rho}(t_1,t_2) + u_{\hat{\boldsymbol{\mu}},m_\rho}(t_2,t_1) \end{aligned} \tag{B.1}$$

where $r_{\hat{\boldsymbol{\zeta}}^2\hat{\boldsymbol{\zeta}}^2}(t_1,t_2) \triangleq E\{\hat{\boldsymbol{\zeta}}^2(t_1)\hat{\boldsymbol{\zeta}}^2(t_2)\}$ is the ACF of the squared envelope $\hat{\boldsymbol{\zeta}}^2(t) \triangleq |\hat{\boldsymbol{\mu}}(t)|^2$ of the simulation model's random component $\hat{\boldsymbol{\mu}}(t)$, whereas the functions $w_{\hat{\boldsymbol{\mu}},m_\rho}(t_1,t_2)$ and $u_{\hat{\boldsymbol{\mu}},m_\rho}(t_1,t_2)$ are defined as

$$\begin{aligned} w_{\hat{\boldsymbol{\mu}},m_\rho}(t_1,t_2) &\triangleq E\big\{\big[\,\hat{\boldsymbol{\mu}}^*(t_1)m_\rho(t_1) + \hat{\boldsymbol{\mu}}(t_1)m_\rho^*(t_1)\,\big] \\ &\quad \times\big[\,\hat{\boldsymbol{\mu}}^*(t_2)m_\rho(t_2) + \hat{\boldsymbol{\mu}}^*(t_2)m_\rho^*(t_2)\,\big]\big\} \end{aligned} \tag{B.2}$$

$$u_{\hat{\boldsymbol{\mu}},m_\rho}(t_1,t_2) \triangleq E\big\{\,|\hat{\boldsymbol{\mu}}(t_1)|^2 \cdot \big[\,\hat{\boldsymbol{\mu}}^*(t_2)m_\rho(t_2) + \hat{\boldsymbol{\mu}}(t_2)m_\rho^*(t_2)\,\big]\big\}. \tag{B.3}$$

One can easily verify, by proceeding as we did in Appendix A to obtain the results presented in (A.9) and (A.11), that

$$u_{\hat{\boldsymbol{\mu}},m_\rho}(t_1,t_2) = 0 \tag{B.4}$$

$$\begin{aligned} w_{\hat{\boldsymbol{\mu}},m_\rho}(t_1,t_2) &= w_{\hat{\boldsymbol{\mu}},m_\rho}(\tau) \\ &= 4\rho^2\big[\cos(2\pi f_\rho\tau)\, r_{\hat{\boldsymbol{\mu}}_I\hat{\boldsymbol{\mu}}_I}(\tau) + \sin(2\pi f_\rho\tau)\, r_{\hat{\boldsymbol{\mu}}_I\hat{\boldsymbol{\mu}}_Q}(\tau)\big] \end{aligned} \tag{B.5}$$

where $r_{\hat{\boldsymbol{\mu}}_I\hat{\boldsymbol{\mu}}_I}(\tau)$ and $r_{\hat{\boldsymbol{\mu}}_I\hat{\boldsymbol{\mu}}_Q}(\tau)$ are the correlation functions defined in (3.7). In addition, it is straightforward to show that

$$r_{\hat{\boldsymbol{\zeta}}^2\hat{\boldsymbol{\zeta}}^2}(t_1,t_2) = \sum_{l=1}^{N}\sum_{m=1}^{N}\sum_{n=1}^{N}\sum_{p=1}^{N} \hat{c}_l\,\hat{c}_m\,\hat{c}_n\,\hat{c}_p \cdot \exp\left\{j2\pi(\hat{f}_l-\hat{f}_m)t_1\right\} \times \exp\left\{j2\pi(\hat{f}_n-\hat{f}_p)t_2\right\} \cdot E\Big\{\exp\left\{j(\hat{\boldsymbol{\theta}}_l-\hat{\boldsymbol{\theta}}_m+\hat{\boldsymbol{\theta}}_n-\hat{\boldsymbol{\theta}}_p)\right\}\Big\}. \quad \text{(B.6)}$$

Since the random phases $\hat{\boldsymbol{\theta}}_n$ are mutually independent and uniform over $[-\pi,\pi)$ [Sec. 3.3], the expectation in (B.6) is different from zero only when: $l=m=n=p$; $l=m$, $n=p$, $l\neq n$; and $l=p$, $m=n$, $l\neq m$. Consequently, we have

$$\begin{aligned} r_{\hat{\boldsymbol{\zeta}}^2\hat{\boldsymbol{\zeta}}^2}(t_1,t_2) &= \underbrace{\sum_{l=1}^{N}\hat{c}_l^4}_{\text{Case: } l=m=n=p} + \underbrace{\sum_{m=1}^{N}\sum_{\substack{n=1\\ n\neq m}}^{N}\hat{c}_m^2\hat{c}_n^2}_{\text{Case: } l=m,n=p,l\neq n} \\ &\quad + \underbrace{\sum_{p=1}^{N}\sum_{\substack{q=1\\ q\neq p}}^{N}\hat{c}_p^2\,\hat{c}_q^2\exp\left\{-j2\pi\hat{f}_p(t_2-t_1)\right\}\exp\left\{j2\pi\hat{f}_q(t_2-t_1)\right\}}_{\text{Case: } l=p,m=n,l\neq m} \\ &= \sum_{l=1}^{N}\hat{c}_l^4 + \left[\sum_{m=1}^{N}\hat{c}_m^2\right]^2 - \sum_{n=1}^{N}\hat{c}_n^4 \\ &\quad + \sum_{p=1}^{N}\sum_{q=1}^{N}\hat{c}_p^2\,\hat{c}_q^2\,\exp\{-j2\pi\hat{f}_p\tau\}\exp\{j2\pi\hat{f}_q\tau\} - \sum_{k=1}^{N}\hat{c}_k^4. \end{aligned} \quad \text{(B.7)}$$

It follows from (B.7) that the ACF of $\hat{\boldsymbol{\zeta}}^2(t)$ is time shift insensitive, that is, $r_{\hat{\boldsymbol{\zeta}}^2\hat{\boldsymbol{\zeta}}^2}(t_1,t_2)=r_{\hat{\boldsymbol{\zeta}}^2\hat{\boldsymbol{\zeta}}^2}(\tau)$. Taking account of the property $\sum_{n=1}^{N}\hat{c}_n^2=\sigma_{\boldsymbol{\mu}}^2$ [Sec. 3.3.1], and given that $r_{\hat{\boldsymbol{\mu}}\hat{\boldsymbol{\mu}}}(\tau)=\sum_{n=1}^{N}\hat{c}_n^2\exp\{j2\pi\hat{f}_n\tau\}$ [Eq. (3.5)], we finally obtain

$$r_{\hat{\boldsymbol{\zeta}}^2\hat{\boldsymbol{\zeta}}^2}(\tau) = \sigma_{\boldsymbol{\mu}}^4 + |r_{\hat{\boldsymbol{\mu}}\hat{\boldsymbol{\mu}}}(\tau)|^2 - \sum_{n=1}^{N}\hat{c}_n^4. \quad \text{(B.8)}$$

By substituting the results presented in (B.4), (B.5), and (B.8) into (B.1), we find that the ACF of the simulation model's squared envelope $\hat{\boldsymbol{\xi}}^2(t)$ is equal to

$$\begin{aligned} r_{\hat{\boldsymbol{\xi}}^2\hat{\boldsymbol{\xi}}^2}(t_1,t_2) &= r_{\hat{\boldsymbol{\xi}}^2\hat{\boldsymbol{\xi}}^2}(\tau) \\ &= r_{\hat{\boldsymbol{\zeta}}^2\hat{\boldsymbol{\zeta}}^2}(\tau) + \rho^4 + 2\sigma_{\boldsymbol{\mu}}^2\,\rho^2 + 4\rho^4\big[\cos(2\pi f_\rho\tau)\,r_{\hat{\boldsymbol{\mu}}_I\hat{\boldsymbol{\mu}}_I}(\tau) \\ &\quad + \sin(2\pi f_\rho\tau)\,r_{\hat{\boldsymbol{\mu}}_I\hat{\boldsymbol{\mu}}_Q}(\tau)\big] \end{aligned} \quad \text{(B.9)}$$

where $r_{\hat{\boldsymbol{\zeta}}^2\hat{\boldsymbol{\zeta}}^2}(\tau)$ is given by (B.8). The expression presented in (3.29) follows from (B.9) by rewriting $r_{\hat{\boldsymbol{\xi}}^2\hat{\boldsymbol{\xi}}^2}(\tau)$ in terms of the Rician factor c_R.

Appendix C

Derivation of the Squared Envelope ACF of the Deterministic SOC-Based Simulation Model

In this appendix, we compute a closed-form solution for the time-averaged ACF $r_{\hat{\xi}^2\hat{\xi}^2}(\tau)$ of the squared envelope $\hat{\xi}^2(t) \triangleq |\hat{\nu}(t)|^2$ of the deterministic SOC-based simulation model $\hat{\nu}(t) = \hat{\mu}(t) + m_\rho(t)$ introduced in Section 3.4.1. To that end, we start by noticing that

$$\begin{aligned} r_{\hat{\xi}^2\hat{\xi}^2}(\tau) &\triangleq \big\langle |\hat{\nu}(t)|^2 |\hat{\nu}^2(t+\tau)|^2 \big\rangle \\ &= r_{\hat{\zeta}^2\hat{\zeta}^2}(\tau) + \rho^4 + 2\sigma_{\boldsymbol{\mu}}^2\rho^2 + u_{\hat{\mu},m_\rho}(t,t+\tau) + u_{\hat{\mu},m_\rho}(t+\tau,t) \\ &\quad + z_{\hat{\mu},m_\rho}(t,t+\tau) + z_{\hat{\mu},m_\rho}(t+\tau,t) + w_{\hat{\mu},m_\rho}(\tau) \end{aligned} \tag{C.1}$$

where $r_{\hat{\zeta}^2\hat{\zeta}^2}(\tau) \triangleq \big\langle \hat{\zeta}^2(t)\hat{\zeta}^2(t+\tau) \big\rangle$ is the time averaged ACF of the squared envelope $\hat{\zeta}^2(t) \triangleq |\hat{\mu}(t)|^2$ of $\hat{\mu}(t)$, and:

$$u_{\hat{\mu},m_\rho}(t,t+\tau) \triangleq \big\langle |\hat{\mu}(t)|^2 \cdot \big[\hat{\mu}^*(t+\tau)\, m_\rho(t+\tau) + \hat{\mu}(t+\tau)\, m_\rho^*(t+\tau)\big] \big\rangle \tag{C.2}$$

$$u_{\hat{\mu},m_\rho}(t+\tau,t) \triangleq \big\langle |\hat{\mu}(t+\tau)|^2 \cdot \big[\hat{\mu}^*(t)\, m_\rho(t) + \hat{\mu}(t)\, m_\rho^*(t)\big] \big\rangle \tag{C.3}$$

$$\begin{aligned} z_{\hat{\mu},m_\rho}(t,t+\tau) &\triangleq \big\langle |m_\rho(t)|^2 \cdot \big[\hat{\mu}^*(t+\tau)\, m_\rho(t+\tau) + \hat{\mu}(t+\tau)\, m_\rho^*(t+\tau)\big] \big\rangle \\ &= \rho^2 \big[\big\langle \hat{\mu}^*(t+\tau)\, m_\rho(t+\tau) \big\rangle + \big\langle \hat{\mu}(t+\tau)\, m_\rho^*(t+\tau) \big\rangle\big] \end{aligned} \tag{C.4}$$

$$\begin{aligned} z_{\hat{\mu},m_\rho}(t+\tau,t) &\triangleq \big\langle |m_\rho(t+\tau)|^2 \cdot \big[\hat{\mu}^*(t)\, m_\rho(t) + \hat{\mu}(t)\, m_\rho^*(t)\big] \big\rangle \\ &= \rho^2 \big[\big\langle \hat{\mu}^*(t)\, m_\rho(t) \big\rangle + \big\langle \hat{\mu}(t)\, m_\rho^*(t) \big\rangle\big] \end{aligned} \tag{C.5}$$

$$\begin{aligned} w_{\hat{\mu},m_\rho}(\tau) &\triangleq \big\langle \big[\hat{\mu}^*(t)\, m_\rho(t) + \hat{\mu}(t)\, m_\rho^*(t)\big] \\ &\quad \times \big[\hat{\mu}^*(t+\tau)\, m_\rho(t) + \hat{\mu}(t)\, m_\rho^*(t+\tau)\big] \big\rangle. \end{aligned} \tag{C.6}$$

In order to obtain a compact expression for $r_{\hat{\xi}^2\hat{\xi}^2}(\tau)$, we need first to find a closed-form solution for $r_{\hat{\zeta}^2\hat{\zeta}^2}(\tau)$ and the time-averaged functions defined in (C.2)–(C.6). For that purpose, we will make the following assumptions regarding the Doppler frequencies $\hat{f}_n$ of the SOC model $\hat{\mu}(t) = \sum_n^N \hat{c}_n \exp\left\{j(2\pi\hat{f}_n t + \hat{\theta}_n)\right\}$ and the Doppler frequency f_ρ of the specular wave $m_\rho(t) = \rho \exp\left\{j(2\pi f_\rho t + \theta_\rho)\right\}$:

$$\text{Condition 3.2}: \quad \hat{f}_n \neq 0, \quad \forall n \tag{C.7}$$

$$\text{Condition 3.3}: \quad \hat{f}_n \neq \hat{f}_m, \quad n \neq m \tag{C.8}$$

$$\text{Condition 3.5}: \quad \text{If } N \geq 4, \text{then} \tag{C.9}$$

$$\hat{f}_l + \hat{f}_m = \hat{f}_n + \hat{f}_k, \quad \text{iff} \begin{cases} l = m = n = k; \\ \text{or } l = n, m = k, l \neq m; \\ \text{or } l = k, m = n, l \neq m. \end{cases} \tag{C.10}$$

$$\text{Condition 3.6}: \quad |f_\rho| \neq |\hat{f}_n|, \quad \forall n \tag{C.11}$$

$$\text{Condition 3.7}: \quad \text{If } N \geq 2, \text{ then } f_\rho + \hat{f}_l \neq \hat{f}_m + \hat{f}_n, \quad \forall l, m, n. \tag{C.12}$$

In the case of the function $u_{\hat{\mu},m_\rho}(t, t+\tau)$, we have

$$\begin{aligned} u_{\hat{\mu},m_\rho}(t,t+\tau) &= \left\langle |\hat{\mu}(t)|^2 \cdot \left[\hat{\mu}^*(t+\tau)\, m_\rho(t+\tau) + \hat{\mu}(t+\tau)\, m_\rho^*(t+\tau)\right]\right\rangle \\ &= \sum_{l=1}^{N}\sum_{m=1}^{N}\sum_{n=1}^{N} \hat{c}_l\, \hat{c}_m\, \hat{c}_n\, \rho\, \exp\{j2\pi(f_\rho - \hat{f}_n)\tau\} \\ &\quad \times \exp\{j(\hat{\theta}_l - \hat{\theta}_m - \hat{\theta}_n + \theta_\rho)\} \\ &\quad \times \lim_{T\to\infty} \frac{1}{2T} \int_{-T}^{T} \exp\{j2\pi(\hat{f}_l - \hat{f}_m - \hat{f}_n + f_\rho)t\}\, dt \\ &\quad + \sum_{p=1}^{N}\sum_{q=1}^{N}\sum_{k=1}^{N} \hat{c}_p\, \hat{c}_q\, \hat{c}_k\, \rho\, \exp\{j2\pi(\hat{f}_k - f_\rho)\tau\} \\ &\quad \times \exp\{j(\hat{\theta}_p - \hat{\theta}_q + \hat{\theta}_k + \theta_\rho)\} \\ &\quad \times \lim_{T\to\infty} \frac{1}{2T} \int_{-T}^{T} \exp\{j2\pi(\hat{f}_p - \hat{f}_q + \hat{f}_k - f_\rho)t\}\, dt. \end{aligned}$$

The two integrals above are equal to zero in the limit $T \to \infty$ if the condition established in (C.12) is satisfied. Consequently, we can state that

$$u_{\hat{\mu},m_\rho}(t,t+\tau) = 0, \quad \text{if } f_\rho + \hat{f}_l \neq \hat{f}_m + \hat{f}_n, \forall l, m, n. \tag{C.13}$$

Analogously, one can show that the time average $u_{\hat{\mu},m_\rho}(t+\tau, t)$ equals

$$u_{\hat{\mu},m_\rho}(t+\tau,t) = 0, \quad \text{if } f_\rho + \hat{f}_l \neq \hat{f}_m + \hat{f}_n, \forall l, m, n. \tag{C.14}$$

Notice that $u_{\hat{\mu},m_\rho}(t,t+\tau) = u_{\hat{\mu},m_\rho}(t+\tau,t)$ upon fulfillment of the Condition 3.7. However, such a relationship is in general not valid.

On the other hand, for the time-averaged function $z_{\hat{\mu},m_\rho}(t,t+\tau)$, we have

$$\begin{aligned} z_{\hat{\mu},m_\rho}(t,t+\tau) &= \rho^2\big[\big\langle \hat{\mu}^*(t+\tau)\, m_\rho(t+\tau)\big\rangle + \big\langle \hat{\mu}(t+\tau)\, m_\rho^*(t+\tau)\big\rangle\big] \\ &= \rho^3\Bigg[\sum_{l=1}^{N} \hat{c}_l\, \exp\{j2\pi(f_\rho - \hat{f}_l)\tau\}\, \exp\{j(\theta_\rho - \hat{\theta}_l)\} \\ &\quad \times \lim_{T\to\infty} \frac{1}{2T} \int_{-T}^{T} \exp\{j2\pi(f_\rho - \hat{f}_l)t\}\, dt \\ &\quad + \sum_{m=1}^{N} \hat{c}_m\, \exp\{j2\pi(\hat{f}_m - f_\rho)\tau\}\, \exp\{j(\hat{\theta}_m - \theta_\rho)\} \\ &\quad \times \lim_{T\to\infty} \frac{1}{2T} \int_{-T}^{T} \exp\{j2\pi(\hat{f}_m - f_\rho)t\}\, dt\Bigg]. \end{aligned}$$

If the Condition 3.6 is met, then the integrals introduced in the previous expression are equal to zero in the limit $T \to \infty$, implying that

$$z_{\hat{\mu},m_\rho}(t,t+\tau) = 0, \quad \text{if } |\hat{f}_n| \neq |f_\rho|\ \forall n. \tag{C.15}$$

In a similar way, one can show that

$$z_{\hat{\mu},m_\rho}(t+\tau,t) = 0, \quad \text{if } |\hat{f}_n| \neq |f_\rho|\ \forall n. \tag{C.16}$$

It is worth noticing that the results presented in (C.15) and (C.16) hold even when the absolute value is removed from the Condition 3.6, i.e., if $\hat{f}_n \neq f_\rho\ \forall n$.

In turn, for the function $w_{\hat{\mu},m_\rho}(\tau)$, it can be shown that if the Condition 3.6 is fulfilled, then

$$\begin{aligned} w_{\hat{\mu},m_\rho}(t,t+\tau) &= \big\langle \big[\hat{\mu}^*(t)\, m_\rho(t) + \hat{\mu}(t)\, m_\rho^*(t)\big] \\ &\quad \times \big[\hat{\mu}^*(t+\tau)\, m_\rho(t) + \hat{\mu}(t+\tau)\, m_\rho^*(t+\tau)\big]\big\rangle \\ &= \rho^2\Big[\exp\{-j2\pi f_\rho\tau\}\big\langle \hat{\mu}^*(t)\hat{\mu}(t+\tau)\big\rangle \\ &\quad + \exp\{j2\pi f_\rho\tau\}\big\langle \hat{\mu}(t)\hat{\mu}^*(t+\tau)\big\rangle\Big] \\ &= 2\rho^2\, \mathrm{Re}\big\{\exp\{j2\pi f_\rho\tau\}\cdot r^*_{\hat{\mu}\hat{\mu}}(\tau)\big\} \\ &= 4\rho^2\big\{\cos(2\pi f_\rho\tau)\cdot r_{\hat{\mu}_I\hat{\mu}_I}(\tau) + \sin(2\pi f_\rho\tau)\cdot r_{\hat{\mu}_I\hat{\mu}_Q}(\tau)\big\} \end{aligned} \tag{C.17}$$

where $r_{\hat{\mu}\hat{\mu}}(\tau)$, $r_{\hat{\mu}_I\hat{\mu}_I}(\tau)$, and $r_{\hat{\mu}_I\hat{\mu}_Q}(\tau)$ denote, in that order, the ACF of $\hat{\mu}(t)$ [see (3.33)], the ACF of the inphase component of $\hat{\mu}(t)$ [see (3.35a)], and the CCF between the IQ components of $\hat{\mu}(t)$ [see (3.35b)].

Finally, for the time-averaged ACF $r_{\hat{\zeta}^2\hat{\zeta}^2}(\tau)$ of $\hat{\zeta}^2(t)$, we have

$$\begin{aligned} r_{\hat{\zeta}^2\hat{\zeta}^2}(\tau) &= \left\langle |\hat{\mu}(t)|^2 |\hat{\mu}(t+\tau)|^2 \right\rangle \\ &= \sum_{l=1}^{N}\sum_{m=1}^{N}\sum_{n=1}^{N}\sum_{p=1}^{N} \hat{c}_l\,\hat{c}_m\,\hat{c}_n\,\hat{c}_p \\ &\quad \times \exp\left\{j(\hat{\theta}_l - \hat{\theta}_m + \hat{\theta}_n - \hat{\theta}_p)\right\} \cdot \exp\left\{j2\pi(\hat{f}_n - \hat{f}_p)\tau\right\} \\ &\quad \times \lim_{T\to\infty} \frac{1}{2T} \int_{-T}^{T} \exp\{j2\pi(\hat{f}_l - \hat{f}_m + \hat{f}_n - \hat{f}_p)t\}\, dt. \end{aligned} \tag{C.18}$$

If the condition stated in (C.9) is met, then the integral in (C.18) will be different from zero only when: $l = m = n = p$; $l = n, m = p, l \neq m$; $l = p, m = n, l \neq n$. In such a case, we obtain [cf. Appx. B]

$$\begin{aligned} r_{\hat{\zeta}^2\hat{\zeta}^2}(\tau) &= \underbrace{\sum_{l=1}^{N} \hat{c}_l^4}_{\text{Case: } l=m=n=p} + \underbrace{\sum_{m=1}^{N}\sum_{\substack{n=1\\ n\neq m}}^{N} \hat{c}_m^2 \hat{c}_n^2}_{\text{Case: } l=m, n=p, l\neq n} \\ &\quad \underbrace{+ \sum_{p=1}^{N}\sum_{\substack{q=1\\ q\neq p}}^{N} \hat{c}_p^2\,\hat{c}_q^2 \exp\left\{-j2\pi\hat{f}_p(t_2-t_1)\right\} \exp\left\{j2\pi\hat{f}_q(t_2-t_1)\right\}}_{\text{Case: } l=p, m=n, l\neq m} \\ &= \sum_{l=1}^{N} \hat{c}_l^4 + \left[\sum_{m=1}^{N} \hat{c}_m^2\right]^2 - \sum_{n=1}^{N} \hat{c}_n^4 \\ &\quad + \sum_{p=1}^{N}\sum_{q=1}^{N} \hat{c}_p^2\,\hat{c}_q^2 \exp\{-j2\pi\hat{f}_p\tau\} \exp\{j2\pi\hat{f}_q\tau\} - \sum_{k=1}^{N} \hat{c}_k^4 \\ &= \sigma_{\boldsymbol{\mu}}^4 + |r_{\hat{\mu}\hat{\mu}}(\tau)|^2 - \sum_{n=1}^{N} \hat{c}_n^4. \end{aligned} \tag{C.19}$$

On the basis of the results presented in (C.1), (C.13)–(C.17), and (C.19), we can conclude that

$$\begin{aligned} r_{\hat{\xi}^2\hat{\xi}^2}(\tau) &= r_{\hat{\zeta}^2\hat{\zeta}^2}(\tau) + \rho^4 + 2\sigma_{\boldsymbol{\mu}}^2\,\rho^2 + 4\rho^4\big[\cos(2\pi f_\rho\tau) \cdot r_{\hat{\mu}_I\hat{\mu}_I}(\tau) \\ &\quad + \sin(2\pi f_\rho\tau) \cdot r_{\hat{\mu}_I\hat{\mu}_Q}(\tau)\big] \end{aligned} \tag{C.20}$$

if the conditions established in (C.7)–(C.12) are fulfilled. Notice that the expression in (C.20) does not depend on the set of phases $\{\hat{\theta}_n, \theta_\rho\}$. However, without going into details, we observe that this characteristic does not hold if any of the conditions in (C.7)–(C.12) is not met.

Appendix D

Closed-Form Expression for the Squared Envelope ACF of the Sample Functions of the Stochastic Homogeneous SOC Model with Uncorrelated IQ Components

In this appendix, we outline the derivation of the time-averaged ACF $r_{\hat{\zeta}^2\hat{\zeta}^2}(\tau) \triangleq \left\langle \hat{\zeta}^2(t) \cdot \hat{\zeta}^2(t+\tau) \right\rangle$ of the squared envelope $\hat{\zeta}^2(t) \triangleq |\hat{\mu}(t)|^2$ of the deterministic process $\hat{\mu}(t)$ characterizing the sample functions of the stochastic homogeneous SOC model $\hat{\boldsymbol{\mu}}(t)$. We do so under the assumption that the Conditions 3.1–3.3 are fulfilled, meaning that:

Condition 3.1 :	The number N of cisoids in $\hat{\boldsymbol{\mu}}(t)$ is even, i.e., $N = 2M$, $M \in \mathbb{Z}^+$, and for each pair of parameters $(\hat{c}_n, \hat{f}_n)$ there exist one and only pair $(\hat{c}_m, \hat{f}_m), m \neq n$, such that $\hat{c}_n = \hat{c}_m$ and $\hat{f}_n = -\hat{f}_m$.
Condition 3.2 :	$\hat{f}_n \neq 0, \ \forall n.$
Condition 3.3 :	$\hat{f}_n \neq \hat{f}_m, \quad n \neq m.$

Notice that if these conditions are satisfied, then the IQ components $\hat{\boldsymbol{\mu}}_I(t)$ and $\hat{\boldsymbol{\mu}}_Q(t)$ of $\hat{\boldsymbol{\mu}}(t)$ are uncorrelated [cf. (3.6) and (3.7)]. For notational convenience, and without compromising the generality of our results, we will furthermore assume that the cisoids' parameters are indexed in such a way that $\hat{f}_n < \hat{f}_m \ \forall n < m$.

Our starting point is the expression given in (C.18) for $r_{\hat{\zeta}^2\hat{\zeta}^2}(\tau)$, the which we present again for completeness:

$$\begin{aligned} r_{\hat{\zeta}^2\hat{\zeta}^2}(\tau) &= \left\langle |\hat{\mu}(t)|^2 |\hat{\mu}(t+\tau)|^2 \right\rangle \\ &= \sum_{l=1}^{N}\sum_{m=1}^{N}\sum_{n=1}^{N}\sum_{p=1}^{N} \hat{c}_l\, \hat{c}_m\, \hat{c}_n\, \hat{c}_p \\ &\quad \times \exp\left\{ j(\hat{\theta}_l - \hat{\theta}_m + \hat{\theta}_n - \hat{\theta}_p) \right\} \cdot \exp\left\{ j2\pi(\hat{f}_n - \hat{f}_p)\tau \right\} \\ &\quad \times \lim_{T\to\infty} \frac{1}{2T} \int_{-T}^{T} \exp\{ j2\pi(\hat{f}_l - \hat{f}_m + \hat{f}_n - \hat{f}_p)t \}\, dt. \end{aligned} \tag{D.1}$$

For the case analyzed in Appendix C, the integral in (D.1) is different from zero in the limit $T \to \infty$ only when: $l = m = n = p$; $l = n, m = p, l \neq m$; and $l = p, m = n, l \neq n$. However, for the case at hand, the integral is different from zero also whenever $l \neq m \neq n \neq q$ and: $\hat{f}_l = -\hat{f}_n$, $\hat{f}_m = -\hat{f}_p$; $\hat{f}_l = -\hat{f}_n$, $\hat{f}_p = -\hat{f}_m$; $\hat{f}_n = -\hat{f}_l$, $\hat{f}_m = -\hat{f}_p$; and $\hat{f}_n = -\hat{f}_l$, $\hat{f}_p = -\hat{f}_m$. Under such circumstances, we have

$$\begin{aligned} r_{\hat{\zeta}^2\hat{\zeta}^2}(\tau) &= \sigma_{\boldsymbol{\mu}}^4 + |r_{\hat{\mu}\hat{\mu}}(\tau)|^2 - \sum_{n=1}^{N} \hat{c}_n^4 \\ &\quad + \sum_{l=1}^{N/2} \hat{c}_l^2 \exp\left\{ j\big(\hat{\theta}_l + \hat{\theta}_{N-l+1}\big) \right\} \cdot \exp\left\{ -j2\pi\hat{f}_l\tau \right\} \\ &\quad \times \Bigg\{ \sum_{m=1}^{N/2} \hat{c}_m^2 \exp\left\{ -j\big(\hat{\theta}_m + \hat{\theta}_{N-m+1}\big) \right\} \cdot \exp\left\{ j2\pi\hat{f}_m\tau \right\} \\ &\quad + \sum_{n=1}^{N/2} \hat{c}_n^2 \exp\left\{ -j\big(\hat{\theta}_n + \hat{\theta}_{N-n+1}\big) \right\} \cdot \exp\left\{ -j2\pi\hat{f}_n\tau \right\} \Bigg\} \\ &\quad + \sum_{p=1}^{N/2} \hat{c}_p^2 \exp\left\{ j\big(\hat{\theta}_p + \hat{\theta}_{N-p+1}\big) \right\} \cdot \exp\left\{ j2\pi\hat{f}_p\tau \right\} \\ &\quad \times \Bigg\{ \sum_{q=1}^{N/2} \hat{c}_q^2 \exp\left\{ -j\big(\hat{\theta}_q + \hat{\theta}_{N-q+1}\big) \right\} \cdot \exp\left\{ j2\pi\hat{f}_q\tau \right\} \\ &\quad + \sum_{k=1}^{N/2} \hat{c}_k^2 \exp\left\{ -j\big(\hat{\theta}_k + \hat{\theta}_{N-k+1}\big) \right\} \cdot \exp\left\{ -j2\pi\hat{f}_k\tau \right\} \Bigg\} \end{aligned} \tag{D.2}$$

where $r_{\hat{\mu}\hat{\mu}}(\tau)$ is the ACF defined in (3.8). One can easily verify that

$$r_{\hat{\zeta}^2\hat{\zeta}^2}(\tau) = \sigma_{\boldsymbol{\mu}}^4 + |r_{\hat{\mu}\hat{\mu}}(\tau)|^2 - \sum_{n=1}^{N} \hat{c}_n^4$$

$$
\begin{aligned}
&+\sum_{l=1}^{N/2}\sum_{m=1}^{N/2}\hat{c}_l^2\,\hat{c}_m^2\,\exp\left\{j(\hat{\theta}_l+\hat{\theta}_{N-l+1}-\hat{\theta}_m-\hat{\theta}_{N-m+1})\right\}\\
&\times\left[\exp\left\{-j2\pi(\hat{f}_l-\hat{f}_m)\tau\right\}+\exp\left\{-j2\pi(\hat{f}_l+\hat{f}_m)\tau\right\}\right]\\
&+\sum_{n=1}^{N/2}\sum_{p=1}^{N/2}\hat{c}_n^2\,\hat{c}_p^2\,\exp\left\{j(\hat{\theta}_n+\hat{\theta}_{N-n+1}-\hat{\theta}_p-\hat{\theta}_{N-p+1})\right\}\\
&\times\left[\exp\left\{j2\pi(\hat{f}_n+\hat{f}_p)\tau\right\}+\exp\left\{j2\pi(\hat{f}_n-\hat{f}_p)\tau\right\}\right]\\
=\;&\sigma_{\boldsymbol{\mu}}^4+|r_{\hat{\mu}\hat{\mu}}(\tau)|^2-\sum_{n=1}^{N}\hat{c}_n^4\\
&+\sum_{l=1}^{N/2}\sum_{m=1}^{N/2}\hat{c}_l^2\,\hat{c}_m^2\,\exp\left\{j(\hat{\theta}_l+\hat{\theta}_{N-l+1}-\hat{\theta}_m-\hat{\theta}_{N-m+1})\right\}\\
&\times\Big[\exp\left\{-j2\pi(\hat{f}_l-\hat{f}_m)\tau\right\}+\exp\left\{-j2\pi(\hat{f}_l+\hat{f}_m)\tau\right\}\\
&+\exp\left\{j2\pi(\hat{f}_l+\hat{f}_m)\tau\right\}+\exp\left\{j2\pi(\hat{f}_l-\hat{f}_m)\tau\right\}\Big]\\
=\;&\sigma_{\boldsymbol{\mu}}^4+|r_{\hat{\mu}\hat{\mu}}(\tau)|^2-\sum_{n=1}^{N}\hat{c}_n^4\\
&+4\sum_{l=1}^{N/2}\sum_{\substack{m=1\\m\neq l}}^{N/2}\hat{c}_l^2\,\hat{c}_m^2\,\exp\left\{j(\hat{\theta}_l+\hat{\theta}_{N-l+1}-\hat{\theta}_m-\hat{\theta}_{N-m+1})\right\}\\
&\times\cos\left(2\pi\hat{f}_l\tau\right)\cdot\cos\left(2\pi\hat{f}_m\tau\right).
\end{aligned}
\tag{D.3}
$$

Hence, by taking into account the identity $\sum_{n=1}^{N}\sum_{\substack{m=1\\m\neq n}}^{N}x_n x_m^*=\left|\sum_{n=1}^{N}x_n\right|^2-\sum_{m=1}^{N}|x_m|^2$, we can finally write

$$
\begin{aligned}
r_{\hat{\zeta}^2\hat{\zeta}^2}(\tau)\;=\;&\sigma_{\boldsymbol{\mu}}^4+|r_{\hat{\mu}\hat{\mu}}(\tau)|^2-\sum_{n=1}^{N}\hat{c}_n^4\\
&+4\left\{\left|\sum_{l=1}^{N/2}\hat{c}_l^2\,\exp\left\{j(\hat{\theta}_l+\hat{\theta}_{N-l+1})\right\}\cdot\cos\left(2\pi\hat{f}_l\tau\right)\right|^2\right.\\
&\left.-\sum_{m=1}^{N/2}\hat{c}_m^4\,\cos^2\left(2\pi\hat{f}_m\tau\right)\right\}.
\end{aligned}
\tag{D.4}
$$

Appendix E

Theorems About the Design of SOC-Based Simulation Models with Uncorrelated IQ Components

Theorem E.1 *Let the DPSD of the channel's diffuse component, $S_{\boldsymbol{\mu\mu}}(f)$, be a symmetrical and continuous function in $(-f_{\max}, f_{\max}]$, and suppose that the gains $\hat{c}_n$ and the AOAs $\hat{\alpha}_n$ of the SOC model described by the complex random process $\hat{\boldsymbol{\mu}}(t)$ are given such that*

$$\hat{c}_n = \frac{\sigma_{\boldsymbol{\mu}}}{\sqrt{N}}, \qquad n = 1, \ldots, N \tag{E.1}$$

$$\int_{\hat{\alpha}_{n-1}}^{\hat{\alpha}_n} g_{\boldsymbol{\alpha}}(\alpha) d\alpha = \frac{1}{2N}, \qquad n = 2, \ldots, N. \tag{E.2}$$

Then, the IQ component $\hat{\boldsymbol{\mu}}_I(t)$ and $\hat{\boldsymbol{\mu}}_Q(t)$ of $\hat{\boldsymbol{\mu}}(t)$ are mutually uncorrelated if and only if

$$\int_{0}^{\hat{\alpha}_1} g_{\boldsymbol{\alpha}}(\alpha) d\alpha = \frac{1}{4N}. \tag{E.3}$$

Proof To prove this theorem, we start by noticing from (E.2) that the deterministic AOAs $\hat{\alpha}_n$ fulfill the relationships $0 < \hat{\alpha}_n < \pi \ \forall n$ and $\hat{\alpha}_n \neq \hat{\alpha}_n \ \forall n \neq m$. Consequently, the Doppler frequencies $\hat{f}_n \triangleq f_{\max} \cos(\hat{\alpha}_n)$ of $\hat{\boldsymbol{\mu}}(t)$ satisfy $\hat{f}_n \neq \hat{f}_m$ for all $n \neq m$. Now, if $\hat{f}_n \neq \hat{f}_m$ and $\hat{c}_n = \hat{c}_m$ for all $n \neq m$ (as in the present

case), then $\boldsymbol{\mu}_I(t)$ and $\boldsymbol{\mu}_Q(t)$ are mutually uncorrelated if and only if [see (3.7b)]

$$\hat{f}_n = -\hat{f}_{N-n+1}, \qquad n = 1, \ldots, N. \tag{E.4}$$

For notational convenience, and without loss of generality, we assume that the Doppler frequencies are indexed such that $\hat{f}_n < \hat{f}_m$ for $n < m$. The equality $\hat{f}_n = -\hat{f}_{N-n+1}$ implies that the underlying AOAs satisfy $\hat{\alpha}_n = \pi - \hat{\alpha}_{N-n+1}$, where $\hat{\alpha}_n \in (0, \pi)$. In turn, the symmetry of $S_{\boldsymbol{\mu\mu}}(f)$ implies that $g_{\boldsymbol{\alpha}}(\alpha) = g_{\boldsymbol{\alpha}}(\pi - \alpha)$, for $\alpha \in (0, \pi]$. Consequently, if $S_{\boldsymbol{\mu\mu}}(f) = S_{\boldsymbol{\mu\mu}}(-f)$ and the Doppler frequencies $\hat{f}_n$ satisfy (E.4), then

$$\int_0^{\hat{\alpha}_n} g_{\boldsymbol{\alpha}}(\alpha) d\alpha \;=\; \int_{\hat{\alpha}_{N-n+1}}^{\pi} g_{\boldsymbol{\alpha}}(\alpha) d\alpha, \qquad \forall n. \tag{E.5}$$

Thus, to prove the theorem, it is sufficient to demonstrate that if the AOAs $\hat{\alpha}_n$ fulfill (E.2), then the previous equality holds if and only if (E.3) is met. The proof follows immediately by noticing that the requirement in (E.2) entails that

$$\int_0^{\hat{\alpha}_n} g_{\boldsymbol{\alpha}}(\alpha) d\alpha \;=\; \frac{n-1}{2N} + \int_0^{\hat{\alpha}_1} g_{\boldsymbol{\alpha}}(\alpha) d\alpha \tag{E.6}$$

$$\begin{aligned} \int_{\hat{\alpha}_{N-n+1}}^{\pi} g_{\boldsymbol{\alpha}}(\alpha) d\alpha &= \frac{1}{2} - \int_0^{\hat{\alpha}_{N-n+1}} g_{\boldsymbol{\alpha}}(\alpha) d\alpha \\ &= \frac{n}{2N} - \int_0^{\hat{\alpha}_1} g_{\boldsymbol{\alpha}}(\alpha) d\alpha. \end{aligned} \tag{E.7}$$

Obviously, (E.6) equals (E.7) if and only if $\int_0^{\hat{\alpha}_1} g_{\boldsymbol{\alpha}}(\alpha) d\alpha = 1/(4N)$. ∎

Theorem E.2 *If the DPSD of the channel's diffuse component, $S_{\boldsymbol{\mu\mu}}(f)$, is symmetrical, and the parameters of the SOC simulator described by the random process $\hat{\boldsymbol{\mu}}(t)$ are computed by following the RSAM, then the IQ components of $\hat{\boldsymbol{\mu}}(t)$ are mutually uncorrelated.*

Proof To prove this theorem, it is sufficient to demonstrate that the Doppler frequencies $\hat{f}_n$ and the gains $\hat{c}_n$ of $\hat{\boldsymbol{\mu}}(t)$ satisfy the following condition when the RSAM is applied and $S_{\boldsymbol{\mu\mu}}(f)$ is symmetrical:

Condition E.1 *For each pair of parameters $(\hat{c}_n, \hat{f}_n)$, where $\hat{f}_n \neq 0$, there exists one and only one pair $(\hat{c}_m, \hat{f}_m)$, $n \neq m$, such that $\hat{f}_n = -\hat{f}_m$ and $\hat{c}_n = \hat{c}_m$.*

Notice that the above is a more general condition for the uncorrelatedness of the IQ components of $\hat{\boldsymbol{\mu}}(t)$ than the Condition 3.1 stated in Section 3.3.3.1.

The proof of the theorem follows immediately by noticing that if $S_{\boldsymbol{\mu\mu}}(f) = S_{\boldsymbol{\mu\mu}}(-f)$, and assuming that the even part $g_{\boldsymbol{\alpha}}(\alpha)$ of the AOA distribution has at most one maximum in $[0, \pi)$, then the points α_ℓ and α_u at which $g_{\boldsymbol{\alpha}}(\alpha)$ crosses a threshold $\gamma \in \left(0, \sup\{g_{\boldsymbol{\alpha}}(\alpha)\}_{\alpha\in[0,\pi)}\right)$ from down to up and from up to down, respectively, meet the relation $\alpha_\ell = \pi - \alpha_u$. Consequently, the AOAs $\hat{\alpha}_n$ obtained by applying the RSAM satisfy the equation [cf. (4.31)]

$$\hat{\alpha}_n = \pi - \hat{\alpha}_{N-n+1}, \quad n = 1, \ldots, N. \tag{E.8}$$

Taking account of the relationship $\hat{f}_n = f_{\max}\cos(\hat{\alpha}_n)$, and given that $g_{\boldsymbol{\alpha}}(\alpha) = g_{\boldsymbol{\alpha}}(\pi - \alpha)$ when $S_{\boldsymbol{\mu\mu}}(f)$ is symmetrical, we find that [see 4.28]

$$\begin{aligned}
\hat{f}_n &= f_{\max}\cos(\hat{\alpha}_n) \\
&= f_{\max}\cos(\pi - \hat{\alpha}_{N-n+1}) \\
&= -f_{\max}\cos(\hat{\alpha}_{N-n+1}) \\
&= -\hat{f}_{N-n+1}, \qquad\qquad n = 1, \ldots, N
\end{aligned} \tag{E.9}$$

$$\begin{aligned}
\hat{c}_n &= \sigma_{\boldsymbol{\mu}} \sqrt{\frac{g_{\boldsymbol{\alpha}}(\hat{\alpha}_n)}{\sum_{m=1}^{N} g_{\boldsymbol{\alpha}}(\hat{\alpha}_m)}} \\
&= \sigma_{\boldsymbol{\mu}} \sqrt{\frac{g_{\boldsymbol{\alpha}}(\pi - \hat{\alpha}_{N-n+1})}{\sum_{m=1}^{N} g_{\boldsymbol{\alpha}}(\hat{\alpha}_m)}} \\
&= \sigma_{\boldsymbol{\mu}} \sqrt{\frac{g_{\boldsymbol{\alpha}}(\hat{\alpha}_{N-n+1})}{\sum_{m=1}^{N} g_{\boldsymbol{\alpha}}(\hat{\alpha}_m)}} \\
&= \hat{c}_{N-n+1}, \qquad\qquad n = 1, \ldots, N.
\end{aligned} \tag{E.10}$$

We recall that the Doppler frequencies $\hat{f}_n$ produced by the RSAM fulfill $\hat{f}_n \neq \hat{f}_m$ for $n \neq m$ [see Sec. 4.4.1.3]. Bearing this in mind, and in view of (E.9) and (E.10), we can state that the Condition E.1 is fulfilled when the RSAM is applied and $S_{\boldsymbol{\mu\mu}}(f) = S_{\boldsymbol{\mu\mu}}(-f)$. This concludes the proof. ∎

Appendix F

Validation of the Expressions Obtained for the Squared Envelope ACF of the Deterministic SOC-Based Simulation Model

In order to demonstrate the correctness of the analytical expression presented in Section 3.4.4 for the ACF $r_{\hat{\xi}^2\hat{\xi}^2}(\tau)$ of the squared envelope $\hat{\xi}^2(t)$ of the stochastic SOC model's sample functions, we present in Figs. F.1–F.3 a comparison between the measured ACF of $\hat{\xi}^2(t)$ and the solution given in (3.40) for $r_{\hat{\xi}^2\hat{\xi}^2}(\tau)$. The graphs of $|r_{\hat{\xi}^2\hat{\xi}^2}(\tau)|$ depicted in those figures were generated by applying the RSAM with $N = 20$ to the von Mises PDF of the AOA. The results presented in Figs. F.1–F.3 illustrate the case where the IQ components of the simulation model's random component are mutually uncorrelated as well as the case where they are cross-correlated. One can observe from Figs. F.1–F.3 that the theoretical curves of $r_{\hat{\xi}^2\hat{\xi}^2}(\tau)$ match perfectly the empirical one. This can be taken as a proof of the correctness of the solutions presented in Section 3.4.4 for $r_{\hat{\xi}^2\hat{\xi}^2}(\tau)$.

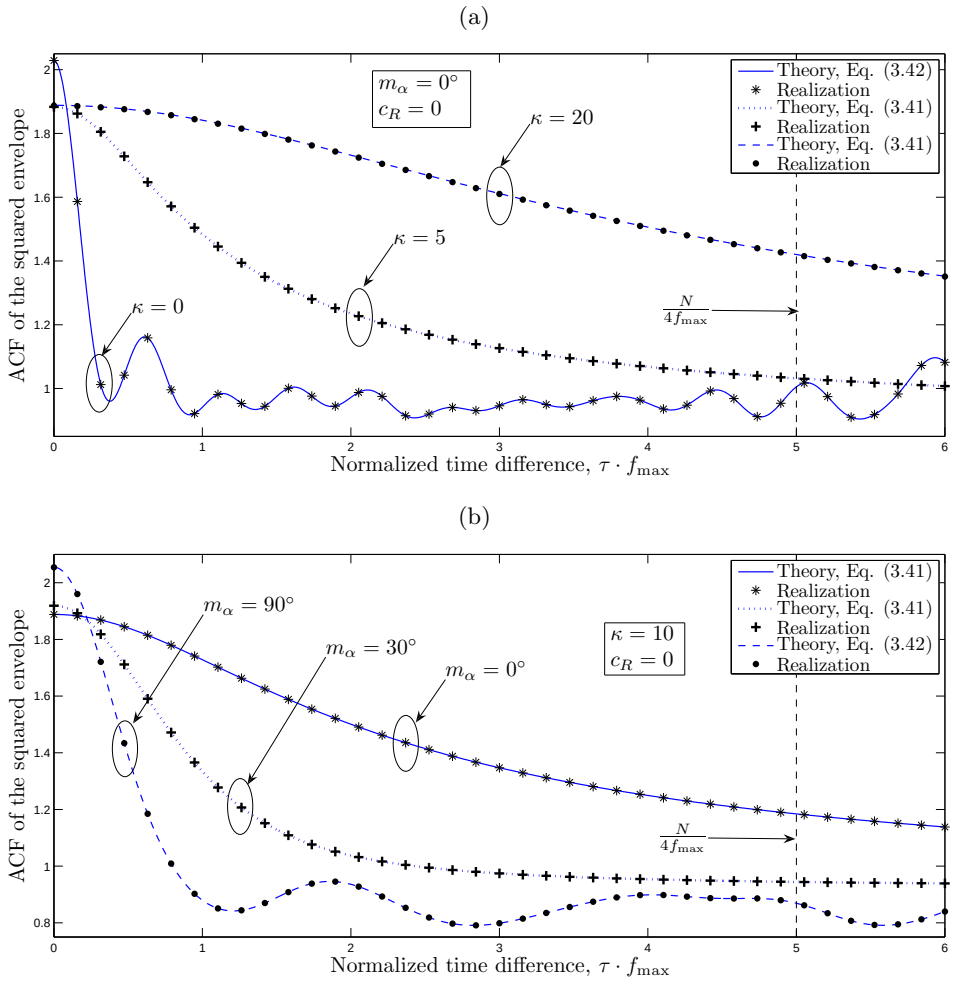

Figure F.1: Comparison between the theoretical and the empirical squared envelope ACFs of the SOC-based simulation model's sample functions by considering a Rician factor equal to $c_R = 0$ and applying the RSAM to the von Mises PDF of the AOA with different pairs of parameters m_α and κ ($f_{\max} = 91$ Hz, $\sigma^2_{\boldsymbol{\nu}} = 1$, $f_p = 65$ Hz, $\theta_\rho = 0°$, and $N = 20$).

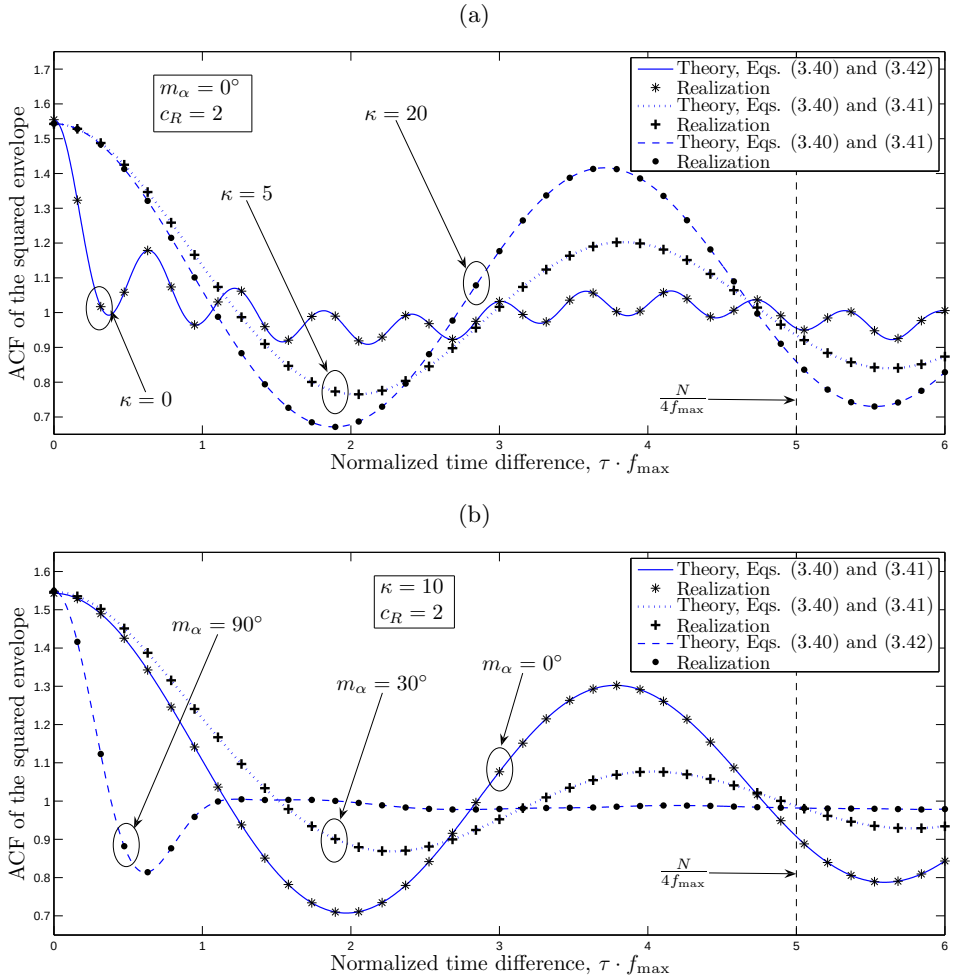

Figure F.2: Comparison between the theoretical and the empirical squared envelope ACFs of the SOC-based simulation model's sample functions by considering a Rician factor equal to $c_R = 2$ and applying the RSAM to the von Mises PDF of the AOA with different pairs of parameters m_α and κ ($f_{\max} = 91$ Hz, $\sigma^2_{\boldsymbol{\nu}} = 1$, $f_p = 65$ Hz, $\theta_\rho = 0°$, and $N = 20$).

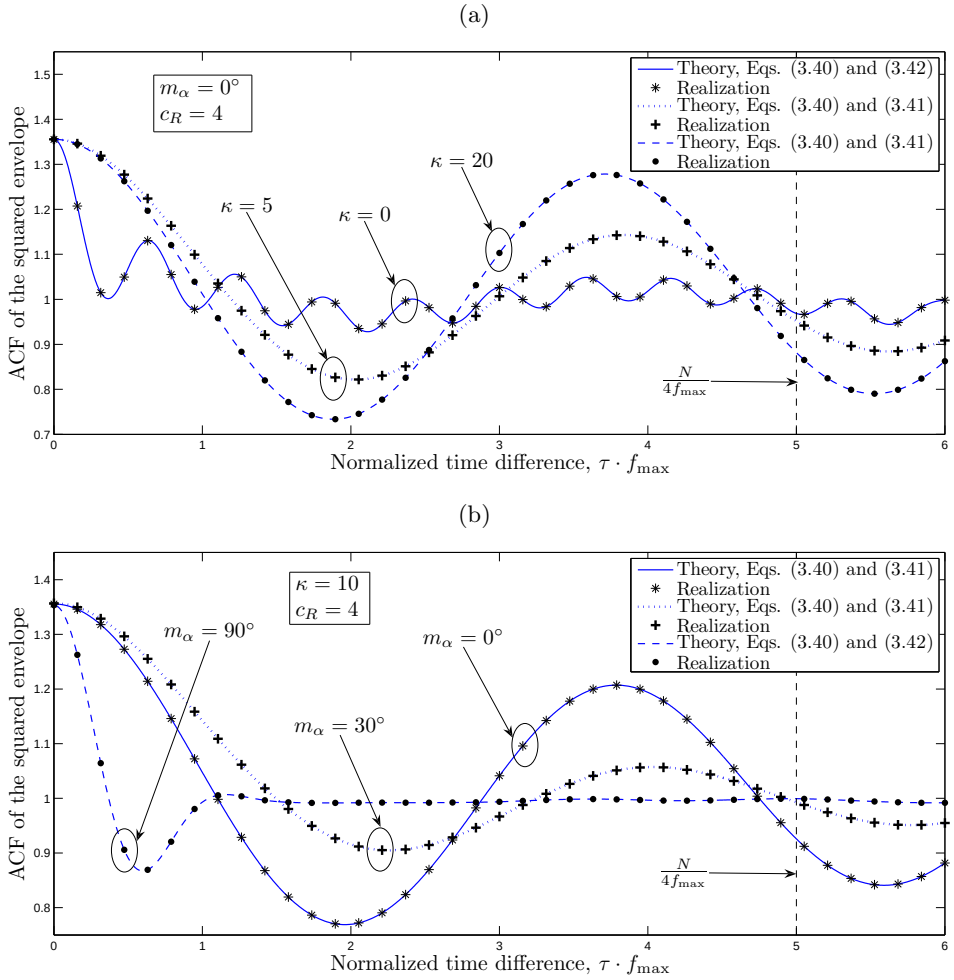

Figure F.3: Comparison between the theoretical and the empirical squared envelope ACFs of the SOC-based simulation model's sample functions by considering a Rician factor equal to $c_R = 4$ and applying the RSAM to the von Mises PDF of the AOA with different pairs of parameters m_α and κ ($f_{\max} = 91$ Hz, $\sigma^2_{\boldsymbol{\nu}} = 1$, $f_p = 65$ Hz, $\theta_\rho = 0°$, and $N = 20$).

Bibliography

[3gpSCM] 3GPP - 3GPP2, *Spatial Channel Model Ad-hoc Group3GPP TR 25.996., Spatial channel model for multiple input multiple output (MIMO) simulations*, v7.0.0, 2003-09.

[3gpUMB] 3GPP2, *Physical Layer for Ultra Mobile Broadband (UMB) Air Interface Specification*, C.S0084-001-0, 3GPP2, Aug. 2007.

[3Gweb1] http://www.3GPP.org

[3Gweb2] http://www.3GPP2.org

[Abd02a] Abdi A., Barger J. A., and Kaveh M., "A parametric model for the distribution of the angle of arrival and the associated correlation function and power spectrum at the mobile station," *IEEE Trans. Veh. Technol.*, vol. 51, no. 3, pp. 425-434, May 2002.

[Abd02b] Abdi A. and Kaveh M., "A space-time correlation model for multielement antenna systems in mobile fading channels," *IEEE J. Sel. Areas Commun.*, vol. 20, no. 3, pp. 550-560, Apr. 2002.

[Abic06] Abichar Z., Peng Y., and Morris Chang J., "WiMAX: The emergence of wireless broadband," *IEEE IT Prof.*, vol. 8, no. 4, pp. 44-48, Jul.-Aug. 2006.

[Alme07] Almers P., Bonek E., Burr A., Czink N., Debbah M., et al., "Survey of channel and radio propagation models for wireless MIMO systems," *EURASIP Journal on Wireless Communications and Networking*, vol. 2007, pp. 1-19, 2007, DOI: 10.1155/2007/19070.

[Aspl06] Asplud H., Alayón Glazunov A., Molisch A. F., Pedersen K. I., Steinbauer M., "The COST 259 directional channel model—Part II: Macrocells," *IEEE Trans. Wirel. Commun.*, vol. 5, no. 12, pp. 3434-3450, Dec. 2006.

[Auli79] Aulin T., "A modified model for the fading signal at a mobile radio channel," *IEEE Trans. Veh. Technol.*, vol. VT-28, no. 3, pp. 182-203, Aug. 1979.

[Badd04] Baddour K. E. and Beaulieu N. C., "Accurate simulation of multiple cross-correlated Rician fading channels," *IEEE Trans. Commun.*, vol. 52, no. 11, pp. 1980-1987, Nov. 2004.

[Badd05] Baddour K. E. and Beaulieu N. C., "Autoregressive modeling for fading channel simulation," *IEEE Trans. Wirel. Commun.*, vol. 4, no. 4, pp. 1650-1662, Jul. 2005.

[Beau04] Beaulieu N. C. and Merani M. L., "Generation of multiple Rayleigh fading sequences with specified cross-correlations," *European Transactions on Telecommunications*, vol. 15, no. 5, pp. 471-476, Sep. 2004.

[Bell63] Bello P. A., "Characterization of randomly time-variant linear channels," *IEEE Trans. Commun. Syst.*, vol. CS-11, no. 4, pp. 360-393, 1963.

[Blau06] Blaunstein N. and Ben-Shimol Y., "Spectral properties of signal fading and Doppler spectra distribution in urban mobile communication links," *Wirel. Commun. Mob. Comput.*, vol. 6, no. 1, pp. 113-126, Feb. 2006.

[Bolt07] Bolton W., Yang X., and Guizani M., "IEEE 802.20: mobile broadband wireless access," *IEEE Wirel. Commun. Mag.*, vol. 14, no. 1, pp. 84-95, Feb. 2007.

[Brig88] Brigham E. O., *The Fast Fourier Transform and its Applications*, New Jersey: Prentice Hall, 1988.

[Brow96] Brown C., Do G., and Feher K., "Digital ultrafast carrier recovery for interactive transmission systems," *IEEE Trans. Consum. Electron.*, vol. 42, no. 1, pp. 132-139, Feb. 1996.

[Cai06] Cai J., Li Z., Hao Y., and J. Cai., "Time-variant Doppler frequency estimation and compensation for mobile OFDM systems," *IEEE Trans. Consum. Electron.*, vol. 52, no. 2, pp. 336-340, May 2006.

[Chen00] Chen T. A., Fitz M. P., Kuo W. Y., Zoltowski M. D., and Grimm J. H., "A space-time model for frequency nonselective Rayleigh fading channels with applications to space-time modems," *IEEE J. Sel. Areas Commun.*, vol. 18, pp. 1175-1190, Jul. 2000.

[Chiz03] Chizhik D., Ling J., Wolniansky P. W., Valenzuela R. A., Costa N., et al., "Multiple-input-multiple-output measurements and modeling in Manhattan," *IEEE J. Sel. Areas Commun.*, vol. 21, no. 3, pp. 321-331, Apr. 2003.

[Choi01] Choi Y. S., Voltz P. J., and Cassara F. A., "On channel estimation and detection for multicarrier signals in fast and selective Rayleigh fading channels," *IEEE Trans. Commun.*, vol. 49, no. 8, pp. 1375-1387, Aug. 2001.

[Chri02] Chryssomallis M., "Simulation of mobile fading channels," *IEEE Antennas Propag. Mag.*, vol. 44, no. 6, pp. 172-183, 2002.

[Clar68] Clarke R. H., "A statistical theory of mobile radio reception," *Bell Syst. Tech. J.*, vol. 47, pp. 957-1000, Jul. 1968.

[Cora97] Corazza G. E., Degli-Esposti V., Frullone M., and Riva G., "A characterization of indoor space and frequency diversity ray-tracing modeling," *IEEE J. on Sel. Areas Commun.*, vol. 14, no. 3, pp. 411-419, Apr. 1996.

[Corr01] Correia L. M., *Wireless Flexible Personalized Communications, COST 259: European Co-operation in Mobile Radio Research*, Chichester: John Wiley & Sons, 2001.

[Corr06] Correia L. M., *Mobile Broadband Multimedia Networks: Techniques, Models and Tools for 4G*, London: Academic Press, 2006.

[Cos207] COST 207, *Digital land mobile radio communications*, Office Official Publ. Eur. Communities, Final Rep., Luxemburg, 1989.

[Edba89] Edbauer F., "Performance of interleaved trellis-coded differential 8-PSK modulation over fading channels," *IEEE J. Sel. Areas Commun.*, vol. 7, no. 9, pp. 1340-1346, Dec. 1989.

[Edwa98] Edwards C. H. and Penney D. E., *Calculus with Analytic Geometry*, New Jersey: Prentice Hall, 5th ed., 1998.

[Erce99] Erceg V., Michelson D. G., Ghassemzadeh S. S., Greenstein L. J., Rustako A. J. Jr., et al., "A model for the multipath delay profile of fixed wireless channels," *IEEE J. Sel. Areas Commun.*, vol. 17, no. 3, pp. 399-410 1999.

[Erce04] Erceg V, Schumacher L, Kyritsi P, Molisch A. F., Baum D. S., et al. "TGn channel models," *Tech. Rep. IEEE P802.11, Wireless LANs*, Garden Grove, Calif, USA, 2004.

[Erte98] Ertel R. and Reed J. H., "Generation of two equal power correlated Rayleigh fading envelopes," *IEEE Commun. Lett.*, vol. 2, no. 10, pp. 276-278, Oct. 1998.

[EtsGSM] ETSI, *Radio Transmission and Reception*, ETSI. GSM 05.05, ETSI EN 300 910 V8.5.1, 2000.

[Etsi99] ETSI, *Broadband radio access networks (BRAN), HIPERLAN Type2 Technical specification: Physical layer*, Ots/bran 0023003, ETSI, Oct. 1999.

[Fleu00] Fleury B. H., "First- and second-order characterization of direction dispersion and space selectivity in the radio channel," *IEEE Trans. Inf. Theory*, vol. 46, no. 6, pp. 2027-2044, Sep. 2000.

[Ghos05] Ghosh A., Wolter D. R., Andrews J. G., and Chen R., "Broadband wireless access with WiMAX/802.16: Current performance benchmarks and future potentials," *IEEE Commun. Mag.*, vol. 43, no. 2, pp. 129-136, Feb. 2005.

[Gold05] Goldsmith A., *Wireless Communications*, New York: Cambridge Univ. Press, 2005.

[Goza06] Gozalvez J., "Mobile WiMAX rollouts announced," *IEEE Veh. Technol. Mag.*, vol. 1, no. 3, pp. 53-59, Sep. 2006.

[Gumb53] Gumbel E. J., Greenwood J. A., and Durand D., "The circular normal distribution: Theory and tables," *Journal of the American Statistical Association*, vol. 48, no. 261, pp. 131-152, Mar. 1953.

[Gumb54] Gumbel E. J., "Applications of the circular normal distribution," *Journal of the American Statistical Association*, vol. 49, no. 266, pp. 267-297, Jun. 1954.

[Guti05] Gutiérrez C. A. and Cabrera M., "Issues of the simulation of wireless channels with exponential-decay power-delay profiles," in *Proc. 16th IEEE International Symposium on Personal, Indoor, and Mobile Radio Communications, PIMRC'05*, Berlin, Germany, Sep. 2005; pp. 507-511.

[Guti06] Gutiérrez C. A., Sanchez J, Cabrera M, and Gutiérrez L. "MC-CDMA based architecture for the downlink of infrastructure WLANs," in *Proc. 17th IEEE International Symposium on Personal, Indoor, and Mobile Radio Communications, PIMRC'06*, Helsinki, Finland, Sept. 2006.

[Gut07a] Gutiérrez C. A. and Cabrera M., "Deterministic simulation of flat-fading MIMO wireless channels under non-isotropic scattering conditions," in *Proc. 17th IEEE International Symposium on Personal, Indoor, and Mobile Radio Communications, PIMRC'07*, Athens, Greece, Sep. 2007.

[Gut07b] Gutiérrez C. A. and Pätzold M., "Sum-of-sinusoids-based simulation of flat-fading wireless propagation channels under non-isotropic scattering conditions," in *Proc. 50th IEEE Global Telecommunications Conference, Globecom 2007*, Washington, U.S.A., Nov. 2007, pp. 3842-3846.

[Gut09a] Gutiérrez C. A. and Pätzold M., "Sum-of-cisoids-based simulation of Rayleigh fading channels in presence of multiple clusters of scatters," *Submitted to the 2009 IEEE CERMA*, Cuernavaca, Mexico.

[Gut09b] Gutiérrez C. A. and Pätzold M., "The Riemann sum method for the design of sum-of-cisoids simulators for Rayleigh fading channels in non-isotropic scattering environments," *Submitted to the 20th IEEE International Symposium on Personal, Indoor, and Mobile Radio Communications, PIMRC'09*, Tokio, Japan.

[Han02] Han J. K., Yook J. G., and Park H. K., "A deterministic channel simulation model for spatially correlated Rayleigh fading," *IEEE Commun. Lett.*, vol. 6, no. 2, pp. 58-60, Feb. 2002.

[Hanz03] Hanzo L., Münster M., Choi B. J., and Keller T., "OFDM and MC-CDMA for Broadband Multi-User Communications, WLANs and Broadcasting," Chichester: *John Wiley & Sons*, 2003.

[Hara97] Hara S. and Prasad R., "Overview of multicarrier CDMA," *IEEE Commun. Mag.*, vol. 35, no. 12, pp. 126-133 1997.

[Hogs05] Hogstad B. O., Pätzold M., Youssef N., and Kim D., "A MIMO mobile-to-mobile channel model: Part II – The simulation model," in *Proc. 16th IEEE International Symposium on Personal, Indoor, and Mobile Radio Communications, PIMRC'05*, Berlin, Germany, Sep. 2005.

[Hogs08] Hogstad B. O. and Pätzold M., "On the stationarity of sum-of-cisoids-based mobile fading channel simulators," in *Proc. 67th IEEE Vehicular Technology Conference, VTC2008-spring*, Singapore, May 2008.

[Hohe92] Höher P., "A statistical discrete-time model for the WSSUS multipath channel," *IEEE Trans. Veh. Technol.*, vol. 41, no. 4, pp. 461-468, Nov. 1992.

[Hou04] Hou Z. and Dubey V. K., "Exact analysis for downlink MC-CDMA in Rayleigh fading channels," *IEEE Commun. Lett.*, vol. 8, no. 2, pp. 90-92, Feb. 2004.

[IEEE06] IEEE 802, *IEEE Standard for Local and Metropolitan Area Networks, Part 16: Air Interface for Fixed and Mobile Broadband Wireless Access Systems, Amendment 2: Physical and Medium Access Control Layers for Combined Fixed and Mobile Operation in Licensed Bands and Corrigendum 2*, 2006.

[Jake74] Jakes W., *Microwave mobile communications*, New York: Wiley, 1974.

[Jeru00] Jeruchim M. C., Balaban P., and Shanmugan K. S., *Simulation of Communication Systems: Modeling, Methodology, and Techniques*, Berlin: Kluwer, 2nd ed., ch. 9, 2000.

[Kail59] Kailath T., *Sampling models for linear time-variant filters*, Report no. 352, M.I.T. Research Lab. of Electronics, Cambridge, Mass, May 1959.

[Kott04] Kotterman W. A. T., Pedersen G. F., and Olsen K., "Diversity properties of multiantenna small handheld terminals," *EURASIP Journal on Applied Signal Processing*, vol. 2004, no. 9, pp. 1340-1353, 2004.

[Kotz01] Kotz S., Kozubowski T. J., and Podgórski K., *The Laplace Distribution and Generalizations: A Revisit with Applications to Communications, Economics, Engineering, and Finance*, Berlin: Birkhäuser, 2001.

[Laga98] Lagarias J. C., Reeds J. A., Wright M. H., and Wright P. E., "Convergence properties of the Nelder–Mead simplex method in low dimensions," *SIAM Journal of Optimization*, vol. 9, no. 1, pp. 112-147, 1998.

[Lapl74] Laplace P. S., "Mémoire sur les probabilité des causes par énvenemènts," *Mém. Acad. Sci. Sav. Étranger*, vol. 6, pp. 621-656, 1774.

[Lee07] Lee K. T., "Create the future with mobile WiMAX," *IEEE Commun. Mag.*, vol. 45, no. 5, pp. 10-14, Mar. 2007.

[Leon94] Leon-Garcia A., *Probability and Random Processes for Electrical Engineering*. Addison-Wesley, 2nd ed., 1994.

[Li07] Li B., Qin Y., Low C. P., and Gwee C. L., "A survey on mobile WiMAX," *IEEE Commun. Mag.*, vol. 45, no. 12, pp. 70-75, Dec. 2007.

[Mard99] Mardia K. V. and Jupp P. E., *Directional Statistics*, Chichester: John Wiley & Sons, 1999.

[Matz05] Matz G., "On non-WSSUS wireless fading channels," *IEEE Trans. Wireless Commun.*, vol. 4, no. 5, pp. 2465-2478, 2005.

[Mayy07] Ma Y. and Pätzold M., "Performance comparison of space-time coded MIMO-OFDM systems using different wideband MIMO channel models," in *Proc. 4th IEEE International Symposium on Wireless Communication Systems, ISWCS 2007*, Trondheim, Norway, Oct. 2007, pp. 762-766.

[Mayy08] Ma Y. and Pätzold M., "A wideband one-ring MIMO channel model under non-isotropic scattering conditions," in *Proc. 67th IEEE Vehicular Technology Conference, VTC2008-Spring*, Singapore, May 2008, pp. 424429.

[Med98a] Medbo J. and Berg J. E., *Measured radio wave propagation characteristics at 5 GHz for typical HIPERLAN/2 scenarios*, Tech. Rep. 3ERI074a, ETSI, Sophia-Antipolis, France, 1998.

[Med98b] Medbo J. and Schramm P., *Channel models for HIPERLAN/2*, Tech. Rep. 3ERI085B, ETSI, Sophia-Antipolis, France, 1998.

[Mill04] Miller S. and Childers D., *Probability and Random Processes: With Applications to Signal Processing and Communications*, London: Elsevier Academic Press, 2nd ed., 2004.

[Miti04] Mitilineos S. A., Varlamos P. K., and Capsalis C. N., "A simulation method for bit-error-rate-performance estimation for arbitrary angle of arrival channel models," *IEEE Antennas Propag. Mag.*, vol. 46, no. 2, pp. 158-163, Apr. 2004.

[Moha05] Mohanty S., "VEPSD: A Novel Velocity Estimation Algorithm for Next-Generation Wireless Systems," *IEEE Trans. Wirel. Commun.*, vol. 4, no. 6, pp. 2655-2660, Nov. 2005.

[Moli05] Molisch A. F., *Wireless Communications*, West Sussex: John Wiley & Sons, 2005.

[Moli06] Molisch A. F., Asplud H., Heddergott R., Steinbauer M., and Zwick T., "The COST 259 directional channel model—Part I: Overview and methodology," *IEEE Trans. Wirel. Commun.*, vol. 5, no. 12, pp. 3421-3433, Dec. 2006.

[Niss06] Nissilä M. and Pasupathy S., "Joint estimation of carrier frequency offset and statistical parameters of the multipath fading channel," *IEEE Trans. Commun.*, vol. 54, no. 6, pp. 1038-1048, Jun. 2006.

[Orti07] Ortiz S., "4G wireless begins to take shape," *IEEE Computer*, vol. 40, no. 11, pp. 18-21, Nov. 2007.

[Pae02a] Pätzold M., *Mobile fading channels*, Chichester: John Wiley & Sons, 2002.

[Pae02b] Pätzold M., Szczepanski A., and Youssef N., "Methods for modeling of specified and measured multipath power-delay profiles," *IEEE Trans. Veh. Technol.*, vol. 51, no. 5, Sep. 2002.

[Pae02c] Pätzold M. and Yao Q., "A Study of stochastic and deterministic procedures for the design of simulation models for spatial channels,," in *Proc. 13th IEEE International Symposium on Personal, Indoor, and Mobile Radio Communications, PIMRC'02*, Lisbon, Portugal, 15-18 Sept. 2002, pp. 1924-1931.

[Pae04a] Pätzold M. and Hogstad B. O., "A space-time simulator for MIMO channels based on the geometrical one-ring scattering model," *Wirel. Commun. Mob. Comput.*, vol. 4, no. 7, pp. 727-737, Nov. 2004.

[Pae04b] Pätzold M., "On the stationarity and ergodicity of fading channel simulators based on Rice's Sum-of-Sinusoids," *Int. J. of Wireless Inf. and Networks*, vol. 11, no. 2, pp. 63-69, Apr. 2004.

[Pae08a] Pätzold M., Hogstad B. O., and Youssef N., "Modeling, analysis, and simulation of MIMO mobile-to-mobile fading channels," *IEEE Trans. Wirel. Commun.*, vol. 7, no. 2, pp. 510-520, Feb. 2008.

[Pae08b] Pätzold M. and Gutiérrez C. A., "Level-crossing rate and average duration of fades of the envelope of a sum-of-cisoids," in *Proc. 67th IEEE Vehicular Technology Conference, VTC2008-spring*, Singapore, Apr. 2008.

[Paet96] Pätzold M., Killat U., and Laue F., "A deterministic digital simulation model for Suzuki processes with application to a shadowed Rayleigh land mobile radio channel," *IEEE Trans. Veh. Tech.*, vol. 45, no. 2, pp. 318-331, May 1996.

[Paet98] Pätzold M., Killat U., Laue F., and Li Y., "On the statistical properties of deterministic simulation models for mobile fading channels," *IEEE Trans. Veh. Tech.*, vol. 47, no. 1, pp. 254-269, Feb. 1998.

[Paet01] Pätzold M. and Youssef N., "Modelling and simulation of direction-selective and frequency-selective mobile radio channels," *International Journal of Electronics and Communications*, vol. AEÜ-55, no. 6, pp. 433-442, Nov. 2001.

[Paet05] Pätzold M. and Hogstad B. O., "Design and performance of MIMO channel simulators derived from the two-ring scattering model," in *Proc. 14th IST Mobile & Communications Summit, IST 2005*, Dresden, Germany, Jun. 2005, pp. 19-23.

[Paet06] Pätzold M. and Hogstad B. O., "A wideband space-time MIMO channel simulator based on the geometrical one-ring model," in *Proc. 64th IEEE Vehicular Technology Conference, VTC 2006-Fall*, Montreal, Canada, Sep. 2006.

[Paet07] Pätzold M. and Talha B., "On the statistical properties of sum-of-cisoids-based mobile radio channel simulators," in *Proc. 10th International Symposium on Wireless Personal Multimedia Communications, WPMC 2007*, Jaipur, India, Dec. 2007.

[Papo02] Papoulis A. and Pillai S. U., *Probability, Random Variables and Stochastic Processes*, New York: McGraw-Hill, 4th ed., 2002.

[Pars00] Parsons J. D., *The Mobile Radio Propagation Channel*, Chichester: John Wiley & Sons, 2000.

[Pate05] Patel C. S., Stüber G. L., and Pratt T. G., "Comparative analysis of statistical models for the simulation of Rayleigh faded cellular channels," *IEEE Trans. Commun.*, vol. 53, no. 6, pp. 1017-1026, Jun. 2005.

[Pede97] Pedersen K. I., Mongensen P. E., and Fleury B. H., "Power azimuth spectrum in outdoor environments," *IEE Electron. Lett.*, vol 33, no. 18, pp. 1583-1584, Aug. 1997.

[Proa01] Proakis J. G., *Digital Communications*, New York: McGraw-Hill, 4th ed., ch. 2, 2001.

[Qua08a] Qualcomm., "3GPP Long-Term Evolution (LTE)," White paper, Jan. 2008.

[Rafi08] Rafiq G. and Pätzold M., "A Study of the Influence of Shadowing on the Statistical Properties of the Capacity of Mobile Radio Channels," *Wireless Per. Commun.*, accepted for publication.

[Rapp02] Rappaport T. S., *Wireless Communications, Principles and Practice*, New York: Prentice-Hall, 2nd ed., 2002.

[Rice44] Rice S. O., "Mathematical analysis of random noise," *Bell Syst. Tech. J.*, vol. 23, pp. 282-332, Jul. 1944.

[Rice45] Rice S. O., "Mathematical analysis of random noise," *Bell Syst. Tech. J.*, vol. 24, pp. 46-156, Jan. 1945.

[Robe06] Roberts M. L., Temple M. A., Mills R. F., and Raines R.A., "Evolution of the air interface of cellular communications systems toward 4G realization," *IEEE Commun. Surveys Tuts.*, vol. 8, no. 1, pp. 2-23, 1st quarter 2006.

[Roys04] Roy S., Foerster J. R., Somayazulu V. S., and Leeper D. G., "Ultrawideband radio design: the promise of high-speed, short-range wireless connectivity," *Proc. IEEE*, vol. 92, no. 2, pp. 295-311, Feb. 2004.

[Saun07] Saunders S. R. and Aragón-Savala A., *Antennas and Propagation for Wireless Communication Systems*, Chichester: John Wiley & Sons, 2nd ed., 2007.

[Schu05] Schulze H. and Lüders C., *Theory and Applications of OFDM and CDMA*, West Sussex: John Wiley & Sons, ch. 2, 2005.

[Shiu00] Shiu D. S., Foschini G. J., Gans M. J., and Kahn J. M., "Fading correlation and its effect on the capacity of multielement antenna systems," *IEEE Trans. Commun.*, vol. 48, pp. 502-513, Mar. 2000.

[Skla88] Sklar B., *Digital communications: Fundamentals and Applications*, Englewood Cliffs, NJ: Prentice-Hall, 1988.

[Soro03] Sorooshyari S. and Daut D. G., "Generation of correlated Rayleigh fading envelopes for accurate performance analysis of diversity systems," in *Proc. 14th IEEE International Symposium on Personal, Indoor, and Mobile Radio Communications, PIMRC'03*, Beijing, China, Sep. 2003.

[Spen00] Spencer Q. H., Jeffs B. D., Jensen M. A., and Swindlehurst A. L., "Modeling the statistical time and angle of arrival characteristics of an indoor multipath channel," *IEEE J. Sel. Areas Commun.*, vol. 18, no. 3, pp. 347-360, Mar. 2000.

[Stal04] Stallings W., "IEEE 802.11: Wireless LANs from *a* to *n*," *IEEE IT Prof.*, vol. 6, no. 5, pp. 32-37, Sep.-Oct. 2004.

[Stei87] Stein S., "Fading channel issues in system engineering," *IEEE J. Sel. Areas Commun.*, vol. SAC-5, no 2, pp. 68-89, 1987.

[Syko00] Sykora J., "Tapped delay line model of linear randomly time-variant WSSUS channel," *Electron. Lett.*, vol. 36, no. 19, pp. 1656-1657, 2000.

[Teo07] Teo K. H., Tao Z., and Zhang J., "The mobile broadband WiMAX standard," *IEEE Signal Process. Mag.*, vol. 24, no. 5, pp. 144-148, Sep. 2007.

[Upto73] Upton G. J. G., "Single-sample tests for the von Mises distribution," *Biometrika*, vol. 60, no. 1, pp. 87-99, Apr. 1973.

[VanN04] Van Nee R., Prasad R., *OFDM for Wireless Multimedia Communications*, Artech House, 2004.

[VonM18] Von Mises R., "Über die 'ganzzahligkeit' det atomgewichte und verwandte fragen," *Physikalische Zeitschrift*, vol. 19, pp. 490-500, 1918.

[Wang07] Wang C.-X., Pätzold M., and Yao Q., "Stochastic modelling and simulation of frequency-correlated wideband fading channels," *IEEE Trans. Veh. Technol.*, vol. 56, no. 3, pp. 1050-1063, May 2007.

[Wats82] Watson G. S., "Distributions on the circle and sphere," *Journal of Applied Probability*, vol. 19, pp. 265-280, 1982.

[Yang02] Yang L L., Hanzo L., "Performance of generalized multicarrier DS-CDMA over Nakagami-m fading channels," *IEEE Trans. Commun.*, vol. 50, no. 6, pp. 956-966, 2002.

[Yang05] Yang H., "A road to future broadband wireless access: MIMO-OFDM-based air interface," *IEEE Commun. Mag.*, vol. 33, pp. 53-60, Jan. 2005.

[Yip95] Yip K.-W. and Ng T.-S., "Efficient simulation of digital transmission over WSSUS channels," *IEEE Trans. Commun.*, vol. 43, no. 12, pp. 2907-2913, Dec. 1995.

[Youn00] Young D. J. and Beaulieu N. C., "The generation of correlated Rayleigh random variates by inverse discrete Fourier transform," *IEEE Trans. Commun.*, vol. 48, pp. 1114-1127, Jul. 2000.

[Zhao03] Zhao X., Kivinen J., Vainikainen P., and Skog K., "Characterization of Doppler Spectra for Mobile Communications at 5.3 GHz," *IEEE Trans. Veh. Technol.*, vol. 52, no. 1, pp. 14-23, Jan. 2003.